

Copyright Undertaking

This thesis is protected by copyright, with all rights reserved.

By reading and using the thesis, the reader understands and agrees to the following terms:

1. The reader will abide by the rules and legal ordinances governing copyright regarding the use of the thesis.
2. The reader will use the thesis for the purpose of research or private study only and not for distribution or further reproduction or any other purpose.
3. The reader agrees to indemnify and hold the University harmless from and against any loss, damage, cost, liability or expenses arising from copyright infringement or unauthorized usage.

IMPORTANT

If you have reasons to believe that any materials in this thesis are deemed not suitable to be distributed in this form, or a copyright owner having difficulty with the material being included in our database, please contact lbsys@polyu.edu.hk providing details. The Library will look into your claim and consider taking remedial action upon receipt of the written requests.

**NUMERICAL INVESTIGATION OF
SINGLE-SIDED NATURAL VENTILATION AND
INTERUNIT DISPERSION IN MULTISTORY
BUILDINGS**

AI ZHENGTAO

Ph.D

The Hong Kong Polytechnic University

2015

The Hong Kong Polytechnic University
Department of Building Services Engineering

**Numerical Investigation of Single-sided Natural
Ventilation and Interunit Dispersion in Multistory
Buildings**

Ai Zhengtao

**A thesis submitted in partial fulfillment of the requirements for the
degree of Doctor of Philosophy**

December, 2014

Certificate of originality

I hereby declare that this thesis is my own work and that, to the best of my knowledge and belief, it reproduces no material previously published or written, nor material that has been accepted for the award of any other degree or diploma, except where due acknowledgement has been made in the text.

_____ (Signed)

Ai Zhengtao (Name of Student)

Department of Building Services Engineering

The Hong Kong Polytechnic University

Hong Kong, China

December, 2014

Abstract

Abstract of thesis entitled: Numerical investigation of single-sided natural ventilation and interunit dispersion in multistory buildings

Submitted by : Ai Zhengtao

For the degree of : Doctor of Philosophy

at The Hong Kong Polytechnic University in Dec, 2014.

Interunit dispersion through opened windows in residential buildings has been attracted more and more attentions since it was first identified in Hong Kong during the outbreak of SARS in 2003. This dispersion is a dangerous pollutant transport route, especially because of the short transport distance and time as well as the possibility of involving the transport of infectious aerosols. Previous studies regarding interunit dispersion were limited to either the solely upward spread or the analyses of envelope concentrations. This thesis therefore provides a systematic investigation of interunit dispersion in multistory buildings with rooms and openings, namely with natural ventilation. Only single-sided natural ventilation was considered, as it is more common in practice than cross ventilation in densely urban areas like Hong Kong. Obviously, an accurate prediction of single-sided natural ventilation is the prerequisite of the successful prediction of interunit dispersion. To achieve the research objective, three sub-works were carried out: (a) an evaluation of predictive methods of single-sided natural ventilation, (b) quality assessments and improvements of CFD prediction of coupled indoor and outdoor flow and dispersion, and (c) CFD simulations of interunit dispersion in multistory buildings.

Several predictive methods of single-sided natural ventilation were evaluated and compared to identify an appropriate predictive method. On-site measurements of ventilation performance were conducted in several multistory residential buildings in Hong Kong, which reveal that previous empirical models established based on simple building models are not reliable to use in multistory buildings, as they cannot account for the effect of room location. The model scale and availability issues as well as the significant difference in ventilation characteristics between rooms in a multistory building post a great difficulty to experimental methods. However, the

CFD method is particularly suitable for predicting single-sided natural ventilation in multistory buildings, despite that its quality must be seriously assured.

The quality of CFD prediction of coupled indoor and outdoor flow and dispersion was assessed and improved. Most of these works have not or not comprehensively been investigated in existing literature. Based on previous high-fidelity experimental data, important influencing factors of both RANS and LES simulation of flow and dispersion around an isolated building were examined and the appropriate selections were recommended. Such sensitivity analyses of influencing factors were conducted also for CFD simulation of single-sided natural ventilation and the implications for its accurate prediction were summarized. Particularly, a simple method of refining the near-wall mesh was proposed and a homogeneous ABL, based on a roughness modified two-layer near-wall model, was developed. Some important issues, such as the inflow fluctuating algorithm of LES simulation, were investigated fundamentally, where novel and useful findings were obtained. These findings provide supplementary information for developing new or updating the current best practice guidelines.

Taking into account wind directions, interunit dispersion in multistory buildings was investigated using both RANS and LES models. A tracer gas was adopted to simulate gaseous and fine particulate pollutants. Using RANS models, the mean dispersion routes were determined and the corresponding reentry ratios from each unit to other units were calculated. Typical dispersion routes and reentry quantities were summarized. Many reentry ratios appear to be within the range from 5.0% to 10.0%, confirming that the interunit dispersion is an important pollutant transmission route. LES results reveal more complex dispersion mechanisms, broader dispersion scopes, and higher dispersion uncertainties than RANS results. The time scales of interunit dispersion are comparable with those of natural ventilation. They are however much smaller than the survival times of most pathogens under ordinary physical environments, implying that the interunit dispersion is highly dangerous. These findings contribute to enhanced understanding of interunit dispersion mechanisms and improved infectious intervention strategies.

Publications arising from this thesis

Journal publications

- [1] Ai, Z.T., Mak, C.M., Niu, J.L., 2013. Numerical investigation of wind-induced airflow and interunit dispersion characteristics in multistory residential buildings. *Indoor Air* 23, 417-429.
- [2] Ai, Z.T., Mak, C.M., 2013. CFD simulation of flow and dispersion around an isolated building: Effect of inhomogeneous ABL and near-wall treatment. *Atmospheric Environment* 77, 568-578.
- [3] Ai, Z.T., Mak, C.M., Cui, D.J., 2013. On-site measurements of ventilation performance and indoor air quality in naturally ventilated high-rise residential buildings in Hong Kong. *Indoor and Built Environment*, In press, Doi: 10.1177/1420326X13508566.
- [4] Ai, Z.T., Mak, C.M., 2014. Determination of single-sided ventilation rates in multistory buildings: Evaluation of methods. *Energy and Buildings* 69, 292-300.
- [5] Ai, Z.T., Mak, C.M., 2014. A study of interunit dispersion around multistory buildings with single-sided ventilation under different wind directions. *Atmospheric Environment* 88, 1-13.
- [6] Ai, Z.T., Mak, C.M., 2014. Modelling of coupled urban wind flow and indoor air flow on a high-density near-wall mesh: sensitivity analyses and case study for single-sided ventilation. *Environmental Modelling and Software* 60, 57-68.
- [7] Ai, Z.T., Mak, C.M., 2014. Analysis of fluctuating characteristics of wind-induced airflow through a single opening using LES modeling and the tracer gas technique. *Building and Environment* 80, 249-258.
- [8] Ai, Z.T., Mak, C.M., 2014. Potential of using reduced-scale models in CFD simulations in saving numerical resources: Theoretical analysis and case study for flow around an isolated building, *Journal of Wind Engineering and Industrial Aerodynamics* 134, 25-29.
- [9] Ai, Z.T., Mak, C.M. Large-eddy simulation of flow and dispersion around an isolated building: Analysis of influencing factors. *Computers and Fluids*, under review.
- [10] Ai, Z.T., Mak, C.M. Large-eddy simulation of wind-induced interunit dispersion around multistory buildings. *Indoor Air*, under review.

Conference publications

- [1] Ai, Z.T., Mak, C.M., 2014. Fluctuating behaviors of airflow through a single opening due to turbulent wind. 6th International Symposium on Computational Wind Engineering. 8-12 June 2014, Hamburg, Germany.
- [2] Ai, Z.T., Mak, C.M., Cui, D.J., 2014. Comparison of single-sided ventilation characteristics between single-room and multistory buildings due to wind effect. 13th International Conferences on Indoor Air Quality and Climate. 7-12 July 2014, Hong Kong.

Acknowledgements

I would like to dedicate this thesis to my family. Without their love, support and understanding, this thesis would not have been written.

Without the financial assistance and research techniques the Department of Building Services Engineering of the Hong Kong Polytechnic University provided, this research would have never been conducted. The Hong Kong ECF is acknowledged for its financial support to the on-site measurements of ventilation and IAQ performance in residential buildings.

My sincere appreciation goes to my Chief supervisor, Prof. Cheuk-ming Mak, for his tireless support, continued inspiration, and valuable suggestions throughout my Ph.D study. His enthusiasm for my research work and incredible rate of proof reading, as well as timely response of my requests are really indispensable components of accomplishing this research and this thesis. The experience of working with him is valuable to me, which trains me to be an independent researcher and lets me know what a good researcher should be.

I would like to thank my co-supervisor, Prof. Jian-lei Niu, for the guidance and opportunities he provided to me. Those precious opportunities allow me to engage into the professional activities in my research field, which greatly extend my knowledge and professional experience.

I thank all my colleagues and friends in Hong Kong, especially Mr. Kenny Hung, Ms. Dong-jin Cui, Mr. Peng Xue, Mr. Yong Cheng, for their valuable help and suggestions.

I would also like to thank those anonymous journal reviewers and the thesis examiners for their constructive comments and useful suggestions which have significantly improved the quality of this thesis.

Last but not least, I express my gratitude to Prof. Zheng-rong Li from Tongji University and Prof. Hai-quan Bi from Southwest Jiaotong University for their care, encouragement and useful discussions throughout.

Table of contents

Certificate of originality	I
Abstract	II
Publications arising from this thesis	IV
Acknowledgements	V
Table of contents	VI
List of Tables	XI
List of Figures	XIII
Nomenclature	XVIII
Chapter 1 Introduction	1
1.1 Background and motivation.....	1
1.2 Objectives and significance	4
1.3 Thesis outline	6
Chapter 2 Literature review	7
2.1 Predictive methods of single-sided natural ventilation.....	7
2.2 CFD simulation of atmospheric flow and dispersion near buildings	11
2.2.1 Issues in RANS simulations	11
2.2.2 Issues in LES simulations	13
2.2.3 Issues in model scale	14
2.3 CFD prediction of single-sided ventilation rate.....	15
2.4 Interunit pollutant dispersion.....	17
2.5 Turbulence and concentration modeling.....	20
2.5.1 RANS models.....	20
2.5.2 LES model.....	22
2.5.3 Concentration model	26
2.6 Determination of single-sided ventilation rate	27
2.7 Summary and research gaps	28
Chapter 3 Evaluation of predictive methods of single-sided ventilation in multistory buildings	31
3.1 Introduction.....	31
3.2 On-site measurements.....	31
3.2.1 Description of measurements	31

3.2.1.1 Measurement sites	31
3.2.1.2 Data collection	35
3.2.2 Results and analyses	35
3.2.2.1 Environmental background of measurements	36
3.2.2.2 Ventilation performance	38
3.3 Validation of past empirical models	41
3.4 Preliminary validation of CFD simulation	43
3.4.1 Airflow involving single-sided natural ventilations	44
3.4.1.1 Experimental model and numerical method	44
3.4.1.2 Results and analyses	46
3.4.2 Pressure distribution on the lateral walls	48
3.5 Difference in ventilation characteristics between single-story and multistory buildings	50
3.5.1 Physical model examined	50
3.5.2 Results and analyses	52
3.5.2.1 Flow and turbulence fields	52
3.5.2.2 Ventilation rates	54
3.6 Summary	56
Chapter 4 Quality assessment and improvement of CFD simulation of atmospheric flow and dispersion	59
4.1 Introduction	59
4.2 RANS simulation of flow and dispersion around an isolated building	59
4.2.1 Modification of inlet conditions and turbulence model	59
4.2.2 Near-wall treatments	61
4.2.2.1 Wall functions modified for rough surfaces	61
4.2.2.2 Two-layer model modified for rough surfaces	63
4.2.3 Experimental and numerical techniques	64
4.2.4 Examining the achievement of the horizontal homogeneity of ABL	70
4.2.5 Effect of inhomogeneous ABL	71
4.2.5.1 Flow field	71
4.2.5.2 Concentration field	74
4.2.6 Effect of near-wall treatment	76

4.2.7 Discussion of the effects.....	77
4.2.8 Summary	78
4.3 Large-eddy simulation of flow and dispersion around an isolated building.....	79
4.3.1 Computational settings and validation: reference case	79
4.3.1.1 Computational domain and mesh generation	79
4.3.1.2 Boundary conditions	80
4.3.1.3 Solution methods	80
4.3.1.4 Results and comparison with wind tunnel experiments	82
4.3.2 Sensitivity analyses of the computational parameters.....	83
4.3.2.1 Effect of upstream distance of computational domain	85
4.3.2.2 Effect of mesh resolution.....	85
4.3.2.3 Effect of length of sampling period	88
4.3.2.4 Effect of inflow fluctuating algorithm	88
4.3.2.5 Effect of subgrid-scale Schmidt number	93
4.3.2.6 Effect of SGS model	95
4.3.2.7 Effect of C_S of the standard Smagorinsky-Lilly model	96
4.3.3 Summary	97
4.4 Potential of using reduced-scale models in CFD simulations	98
4.4.1 Theoretical analysis.....	98
4.4.2 CFD simulations: case setup	101
4.4.3 CFD simulations: results and analyses.....	102
4.4.3.1 Influence of model scale on near-wall y^+ values and numerical accuracy	102
4.4.3.2 Reduced-scale models' potential to save numerical resources	104
4.4.4 Discussion	104
4.4.5 Summary	106
Chapter 5 Quality assessment and improvement of CFD simulation of single-sided natural ventilation	107
5.1 Introduction.....	107
5.2 CFD prediction of single-sided ventilation.....	107
5.2.1 Description of single-sided ventilation measurements.....	107
5.2.2 Computational settings and validation: reference case	108

5.2.2.1 Computational domain and mesh generation	108
5.2.2.2 Boundary conditions.....	111
5.2.2.3 Other computational settings	112
5.2.2.4 Results and comparison with field measurements.....	113
5.2.3 Sensitivity analyses of the computational parameters	115
5.2.3.1 Effect of time interval on calculating $ACH_{LES-tracer}$	115
5.2.3.2 Effect of mesh resolution of the domain	116
5.2.3.3 Effect of near-wall mesh density	117
5.2.3.4 Effect of inlet k	120
5.2.4 Single-sided ventilation rates predicted by various numerical methods..	121
5.2.5 Summary	125
5.3 Fluctuating flow characteristics of single-sided natural ventilation	126
5.3.1 Introduction	126
5.3.2 Fluctuating ventilation rate	126
5.3.3 Relationship between the ventilation rate and interior kinetic energy	128
5.3.4 Instantaneous flow patterns around the opening.....	130
5.3.5 Characteristics of inflow and outflow at a single opening.....	132
5.3.6 Summary	133
Chapter 6 Airflow characteristics and interunit dispersion around multistory buildings.....	135
6.1 Introduction	135
6.2 RANS simulations	135
6.2.1 Modeling method	135
6.2.1.1 Configuration setup	135
6.2.1.2 Numerical details.....	138
6.2.1.3 Interunit dispersion evaluation	139
6.2.2 Normal wind direction ($\theta = 0^\circ$)	140
6.2.2.1 Airflow characteristics.....	140
6.2.2.2 Dispersion characteristics	142
6.2.3 Oblique wind direction ($\theta = 45^\circ$)	147
6.2.3.1 Leeward side.....	147
6.2.3.2 Windward side	149

6.2.4 Parallel wind direction ($\theta = 90^0$)	150
6.2.5 Further discussion	153
6.2.6 Summary	154
6.3 LES simulations	157
6.3.1 Case setup and numerical details	157
6.3.2 Sensitivity test	159
6.3.2.1 Influence of spatial resolution	159
6.3.2.2 Influence of temporal resolution.....	159
6.3.2.3 Influence of inflow conditions.....	160
6.3.2.4 Influence of introducing the concentration equation on solution oscillation.....	161
6.3.3 General flow and dispersion characteristics.....	161
6.3.4 Dispersion routes and reentry ratios.....	165
6.3.5 Time scales of interunit dispersion.....	168
6.3.6 Further discussion	172
6.3.7 Summary	173
Chapter 7 Conclusions and recommendations for future work.....	175
7.1 Summary of main contributions	175
7.2 Predictive methods evaluation	176
7.3 CFD simulation of ABL.....	177
7.3.1 RANS simulations.....	177
7.3.2 LES simulations	178
7.3.3 Reduced-scale model.....	179
7.4 CFD simulation of single-sided ventilation.....	179
7.4.1 Influencing factors.....	179
7.4.2 Fluctuating ventilation characteristics.....	180
7.5 Interunit dispersion	181
7.5.1 RANS simulations.....	181
7.5.2 LES simulations	182
7.6 Recommendations for future work	183
References	185

List of Tables

Table 2.1 Existing empirical models for the determination of single-sided ventilation rate.....	9
Table 3.1 Details of the selected residential rooms.	32
Table 3.2 Summary of the parameters measured and equipment used.....	34
Table 3.3 Indoor and outdoor conditions during the measurement period; the numbers in the brackets are standard deviations.....	37
Table 3.4 Comparison of the measured and predicted ventilation rate for Case 1; the numbers in the brackets are standard deviations.....	42
Table 3.5 Measured ventilation rates (m^3/s) and those predicted by empirical models; the percentiles in the brackets are the deviations of predicted values from measured ones.	42
Table 3.6 Summary of nondimensional ventilation rates of rooms in the single-story and multistory buildings.....	55
Table 4.1 Boundary conditions for examining the effect of inhomogeneous ABL...	68
Table 4.2 Experimental and numerical reattachment lengths and peak k (k_{max}) on the roof; WF indicates wall functions and TL two-layer model.	71
Table 4.3 Percentage deviations of incident profiles and numerical solutions between Gorlé et al. (2009) and other types of inlet conditions.	78
Table 4.4 Summary of influencing factors analyzed in this study, with the reference case highlighted.....	84
Table 4.5 A summary of cases created to examine the influence of model scale....	101
Table 4.6 Influence of model scale on average y^+ value on building surfaces and domain ground. Ψ is the ratio of the increasing ratio of y^+ and the increasing ratio of model scale, based on Case A.....	102
Table 5.1 Comparison of the predicted and measured ACH values (h^{-1}).....	113
Table 5.2 Comparison of measured and predicted mean ACH values (h^{-1}).	116
Table 5.3 Comparison of the ACH values (h^{-1}) predicted using the three types of mesh.	117
Table 5.4 Comparison of the ACH values (h^{-1}) predicted using different near-wall mesh densities.	118
Table 5.5 Comparison of the ACH values (h^{-1}) predicted using the two k profiles.	119
Table 5.6 ACH values (h^{-1}) of the single-sided ventilated room under different wind	

directions. The percentage in brackets indicates the deviations of the ACH value from the $ACH_{LES-tracer}$ 122

Table 6.1 A summary of the cases investigated using LES model; note that two buildings, with and without balconies, are considered for each case. 157

Table 6.2 Comparison of reattachment lengths on the roof and on downstream ground. 162

Table 6.3 A summary of the ranges of the times required to reach specific M_{i-j} values, where t_{γ}^* means the time required to reach the M_{i-j} value of γ ; NB means no balconies and B balconies; NA means no unit reaching this level of M_{i-j} ; and those with only one number mean only one unit reaching this level of M_{i-j} 170.

List of Figures

Figure 1.1 Outdoor pollutants incurring into the interior; route 1 represents special dense sources like carparks, industrial chimneys and construction sites, route 2 traffic exhausts, and route 3 exhausts from other units (interunit dispersion).....	1
Figure 1.2 Schematic diagram of single-sided natural ventilation with two types of openings; the single-sided natural ventilation means that the exchange of the indoor and outdoor flow could occur only at a single opening in one wall of a target room..	3
Figure 1.3 The outline of the research contents.	5
Figure 2.1 Schematic view of the single-sided natural ventilation mechanisms.	7
Figure 2.2 Schematic airflow pattern around a bluff body.....	18
Figure 2.3 Schematic plan view of the building models in a cross (#) floor plan....	19
Figure 3.1 Residential room in Ho Man Tin and equipment locations: (a) room; (b) opening.....	33
Figure 3.2 Tracer gas concentration decay against time and wind speed recorded on the opening during the same period, for the larger floor-extended opening of Case 1.	38
Figure 3.3 Tracer gas concentration decay against time and wind speed recorded on the opening during the same period, for the smaller window-like opening.....	40
Figure 3.4 The building models with one opening on the windward and the leeward wall, respectively, and vertical lines where air velocity is compared.	44
Figure 3.5 Comparison of mean velocity profiles produced using three types of mesh systems at the vertical line of $X=H+H/25$	45
Figure 3.6 Mean velocity distribution at the six vertical lines: RNG + WF indicates RNG $k-\varepsilon$ plus standard wall functions; RNG + TL indicates RNG $k-\varepsilon$ plus two-layer model; MMK + TL indicates MMK $k-\varepsilon$ plus two-layer model.....	46
Figure 3.7 The 6 m building model, locations of pressure tap, and upstream reference position.....	48
Figure 3.8 Pressure coefficients along the centerlines of the cube surface: (a) Normal wind direction; (b) Oblique wind direction.....	49
Figure 3.9 (a) solid block, (b) single-story building, (c) multistory building, (d) computational domain.....	51
Figure 3.10 Velocity and turbulence kinetic energy fields on the vertical centre plane.	52
Figure 3.11 The similar external flow patterns around a single-story and a multistory building; note that here the geometry of the single-story building is stretched for the	

purpose of comparing schematically the flow patterns around the two types of building.....	53
Figure 4.1 Schematic view of the building model and dimensions of the computational domain.....	65
Figure 4.2 Schematic view of the lines on the vertical center plane ($Y = 0$) where simulated results and experimental data are compared.....	66
Figure 4.3 Mesh details of a part of the vertical center plane of the computational domain ($Y = 0$): the coarser for wall functions and the finer for the two-layer model.	66
Figure 4.4 Comparison of inlet and incident profiles in the ABL of an empty domain.	70
Figure 4.5 Comparison of nondimensional velocity along height on the vertical central plane.	72
Figure 4.6 Comparison of turbulence kinetic energy k field on the vertical center plane.	73
Figure 4.7 Comparison of the nondimensional concentration along height on the vertical central plane.	75
Figure 4.8 Comparison of the nondimensional velocity and concentration predicted using the wall functions and two-layer model.	77
Figure 4.9 Comparison of measured and simulated mean velocity profiles.	81
Figure 4.10 Comparison of measured and simulated mean concentration profiles. ..	82
Figure 4.11 Effect of upstream distance of computational domain on mean velocity and concentration fields.	83
Figure 4.12 Schematic view of a part of the five different mesh systems (side view).	85
Figure 4.13 Effect of mesh resolution on mean velocity and concentration fields. ..	86
Figure 4.14 Effect of mesh resolution on streamwise convective flux, $\langle u \rangle \langle Kc \rangle$. ..	87
Figure 4.15 Effect of length of sampling period on mean velocity and concentration field; character 's' in the legend represents Δt^*	88
Figure 4.16 Comparison of the fluctuating characteristics of inlet velocity when using different inflow fluctuating algorithms; the full names of the legends can be found in Section 2.5.2.3.	89
Figure 4.17 Effect of inflow fluctuating algorithm on mean velocity field; the full names of the legends can be found in Section 2.5.2.3; 190, 150 and 230 are number of vortices.....	90
Figure 4.18 Effect of inflow fluctuating algorithm on the concentration field; the	

legends mean the same with those on Figure 4.17.....	91
Figure 4.19 Effect of inflow fluctuating algorithm on streamwise convective flux, $\langle u^{\wedge} \rangle \langle Kc \rangle$	92
Figure 4.20 Contour of streamwise convective flux; dashed red lines mark the interfaces with flux equal to zero; arrows indicate flux directions; and ‘(+)’ ‘(-)’ indicate sign of flux.....	93
Figure 4.21 Effect of SGS Schmidt number on mean concentration field; ‘Sc’ represents Sc_{SGS}	94
Figure 4.22 Effect of SGS model on mean velocity and concentration fields; the full names of the legends can be found in Section 2.5.2.2.	95
Figure 4.23 Effect of C_S on mean velocity and concentration fields.....	96
Figure 4.24 Comparison of y_p between a full-scale case and its reduced-scale case, which use the same mesh system except for a scaling factor of ϕ	99
Figure 4.25 Mean velocity values predicted using different model scales with the same mesh number.	103
Figure 5.1 A schematic view of the building (test cell) used for model validation.	108
Figure 5.2 Schematic view of the computational domain.	109
Figure 5.3 Mesh information on both the building surfaces and the domain ground.	110
Figure 5.4 Comparison of the inlet and incident profiles in an empty computational domain for RANS simulation ($Z_{ref}=1.5$ m).	112
Figure 5.5 Concentration decay and time interval for the calculation of ventilation rates.	114
Figure 5.6 The three mesh systems: (a) finer, (b) basic, and (c) coarser.....	116
Figure 5.7 Schematic view of the change of the near-wall mesh density.	118
Figure 5.8 Comparison of the two inlet k profiles.	119
Figure 5.9 Comparison of the U and the k fields on a horizontal plane ($z = 1.0$ m) produced using the two k profiles based on the RNG model.	120
Figure 5.10 Distribution of velocity vectors and pressure contours on the vertical center plane of the opening for $\theta=0^0$, 90^0 and 180^0	123
Figure 5.11 Transient evolution of ventilation rates under different wind directions.	127
Figure 5.12 Relationship of instantaneous ventilation rates and indoor kinetic energy.	129
Figure 5.13 Distribution of velocity vectors and pressure contours on the vertical	

center plane of the opening for three wind directions.....	131
Figure 5.14 Distribution of the normal-component velocity on the openings.	133
Figure 6.1 Hypothetical building models (a)-(b), cases studied (c), and computational domain (d).	136
Figure 6.2 Mesh information in and around the building model.....	138
Figure 6.3 Mean velocity magnitude and turbulence kinetic energy on the vertical and horizontal center planes of the hypothetical buildings at a wind speed of 1.0 m/s.	141
Figure 6.4 Reentry ratios of tracer gas from the source to other units on the leeward side. Red dot: tracer gas source; ①: Building A, 1.0 m/s; ②: Building B, 1.0 m/s; ③: Building A, 2.0 m/s; ④: Building B, 2.0 m/s.	143
Figure 6.5 Reentry ratios of tracer gas from the source to other units on the windward side. Red dot: tracer gas source; ①: Building A, 1.0 m/s; ②: Building B, 1.0 m/s; ③: Building A, 2.0 m/s; ④: Building B, 2.0 m/s.	144
Figure 6.6 Qualitative comparison of the near-wall airflow pattern around Building A and Building B, under oblique incident wind ($\theta = 45^\circ$).....	146
Figure 6.7 Reentry ratio of tracer gas from a source unit to other units on the leeward side, under oblique incident wind ($\theta = 45^\circ$). Red dot: tracer gas source; ①: Building A; ②: Building B.	147
Figure 6.8 Reentry ratio of tracer gas from a source unit to other units on the windward side, under oblique incident wind ($\theta = 45^\circ$). Red dot: tracer gas source; ①: Building A; ②: Building B.....	149
Figure 6.9 Qualitative comparison of the near-wall airflow pattern around Building A and Building B, under parallel incident wind ($\theta = 90^\circ$).....	152
Figure 6.10 Reentry ratio of tracer gas from a source unit to other units, under parallel incident wind ($\theta = 90^\circ$). Red dot: tracer gas source; ①: Building A; ②: Building B.	153
Figure 6.11 A summary of typical dispersion routes around buildings with and without balconies.....	155
Figure 6.12 Mesh information: (a) $\theta = 0^\circ$ side view with balconies, (b) $\theta = 0^\circ$ plan view without balconies, (c) $\theta = 45^\circ$ plan view without balconies, and (d) $\theta = 45^\circ$ plan view with balconies.	157
Figure 6.13 Power spectra in the frequency domain for the ACH value of unit WM3 under normal wind direction; the legend indicates the nondimensional time step sizes.	160
Figure 6.14 Effect of introducing the concentration equation to the prediction of	

ACH value for unit WM3; the concentration equation is introduced at $t^*=0$	161
Figure 6.15 Time series of ACH values and tracer gas concentrations of some units in the multistory buildings under the normal incident wind.	163
Figure 6.16 Evolution of reentry ratios over time and the maximum, mean, and standard deviation values within the dynamically stable periods; dots mark the moments commencing the dynamically stable periods.....	164
Figure 6.17 Mean and maximum reentry ratios of tracer gas from source units to other units during dynamically stable periods; \overline{R}_k represents mean reentry ratio and \widehat{R}_k maximum reentry ratio.	167
Figure 6.18 Time scales of interunit dispersion from a source unit to its adjacent units; t_m^* and t_h^* represents the nondimensional times for reaching the mean and the half mean M_{i-j} values, respectively, where the mean M_{i-j} values are obtained by taking averages within the dynamically stable periods.....	169
Figure 6.19 Concentration ratio distributions on the windward facades of buildings under normal wind direction at various moments; (a)-(f) present the building without balconies and (g)-(l) present the building with balconies.	171

Nomenclature

List of Abbreviations

ABL	Atmospheric Boundary Layer
ACH	Air Changes per Hour
AIJ	Architectural Institute of Japan
BF	Body Fitted
CFD	Computational Fluid Dynamics
COST	European Cooperation in Science and Technology
DES	Detached Eddy Simulation
DKE	Dynamic Kinetic Energy SGS model
DSL	Dynamic Smagorinsky-Lilly model
GCI	Grid Convergence Index
IAQ	Indoor Air Quality
LES	Large-Eddy Simulation
MMK	Murakami, Mochida and Kondo
NP	No perturbations
PM	Particulate Matter
RANS	Reynolds-Averaged Navier-Stokes
Re	Reynolds number
RNG	Renormalization Group
SARS	Severe Acute Respiratory Syndrome
SGS	Subgrid Scale
SS	Spectral synthesizer
SSL	Standard Smagorinsky-Lilly model
TL	Two-Layer model
TVOCs	Total Volatile Organic Compounds
VM	Vortex method
WALE	Wall-Adapting Local Eddy-viscosity model
WF	Wall Functions

Variable	Description	Unit
A	Area	m^2
A_{eff}	Effective area	m^2
A_o	Opening area	m^2
Ar	Archimedes number	ND
A_μ	Model constant of two-layer model, 70	ND
A_ϵ	Model constant of two-layer model, $2C_l^*$	ND
ACH_{exp}	ACH value measured by experiments	h^{-1}
$ACH_{RNG-mean}$	ACH value calculated by integration method based on steady RNG results	h^{-1}
$ACH_{RNG-tracer}$	ACH value calculated by tracer gas decay method based on unsteady RNG results	h^{-1}
$ACH_{LES-ins,T}$	ACH value calculated by integration method based on LES results	h^{-1}
$ACH_{LES-tracer}$	ACH value calculated by tracer gas decay method based on LES results	h^{-1}
B	Wall additive constant	ND
ΔB	Roughness function	ND
c_i	Concentration of tracer gas i	ppm
C	Concentration	ppm
C_d	Discharge coefficient	ND
C_i, C_j	Tracer gas concentration at unit i and j	ppm
C_{local}	Local concentration	ppm
C_P	Pressure coefficient	ND
C_R	Roughness constant	ND
C_S	Smagorinsky constant	ND
C_{source}	Concentration at the source	ppm
$C_{t_0}, C_{t_i}, C_{t_{i+1}}$	Concentration at the time of t_0, t_i, t_{i+1} , respectively	ppm
C_μ, C_μ^*	Empirical constant	ND

$C_{\varepsilon 1}, C_{\varepsilon 2}$	Model constants	ND
D_t	Turbulent diffusion coefficient	ND
D_X, D_Y, D_Z	Dimensions along X, Y, Z directions, respectively	m
E	Empirical constant, 9.793	ND
f	Frequency	Hz
g	Gravitational acceleration	$\text{m}\cdot\text{s}^{-2}$
G_k	Production of k	$\text{Kg}\cdot\text{m}\cdot\text{s}^{-3}$
H	Building height	m
H_o	Opening height	m
I	Turbulence intensity	ND
I_u	Turbulence intensity in X direction	ND
k	Turbulence kinetic energy	$\text{m}^2\cdot\text{s}^{-2}$
K_C	Nondimensional concentration	ND
$K_{C,H}$	Nondimensional concentration at height H	ND
KE	Kinetic energy	$\text{m}^2\cdot\text{s}^{-2}$
k_{\max}	Peak k on the roof	$\text{m}^2\cdot\text{s}^{-2}$
k_p	Turbulence kinetic energy at the near-wall node P	$\text{m}^2\cdot\text{s}^{-2}$
k_{ref}	Reference turbulence kinetic energy	$\text{m}^2\cdot\text{s}^{-2}$
K_S	Geometrical roughness height	m
K_S^+	Nondimensional geometrical roughness height	ND
l	Turbulence length scale	m
l_μ	Length scale of turbulent viscosity	m
l_ε	Length scale of viscous dissipation rate	m
M_1, M_2	Integration constants for inlet turbulence profiles	ND
M_{i-j}	Mass fraction of air that originates from the source unit i and is present in another unit j	ND
\hat{n}	Frequency of power spectrum	Hz
P	Static pressure	Pa

P_{ref}	Reference static pressure	Pa
ΔP	Pressure difference	Pa
Q	Ventilation rate	$\text{m}^3 \cdot \text{s}^{-1}$
Q^*	Nondimensional ventilation rate	ND
\overline{Q}	Mean ventilation rate	$\text{m}^3 \cdot \text{s}^{-1}$
Q_b	Ventilation rate due to buoyancy effect	$\text{m}^3 \cdot \text{s}^{-1}$
Q_{source}	Flow rate of the source	$\text{m}^3 \cdot \text{s}^{-1}$
Q_t	Mean ventilation rate during a sub period of Δt	$\text{m}^3 \cdot \text{s}^{-1}$
Q_T	Total ventilation rate	$\text{m}^3 \cdot \text{s}^{-1}$
Q_{tracer}	Mean ventilation rate calculated from tracer gas decay method	$\text{m}^3 \cdot \text{s}^{-1}$
Q_w	Ventilation rate due to wind effect	$\text{m}^3 \cdot \text{s}^{-1}$
σ_{Q^*}	Standard deviation of Q^*	ND
Re_y	Wall-distance-based turbulent Re	ND
R_k	Reentry ratio	ND
$\overline{R_k}$	Mean reentry ratio	ND
$\widehat{R_k}$	Maximum reentry ratio	ND
R_ε	Strain-dependent term in the ε equation	ND
S	Scale of strain rate	ND
S_i	Generation rate of source	$\text{ppm} \cdot \text{s}^{-1}$
Sc	Schmidt number	ND
Sc_{SGS}	Turbulent Schmidt number for SGS motions	ND
Sc_t	Turbulent Schmidt number	ND
\widetilde{S}_{ij}	Filtered strain rate tensor for the resolved scales	ND
t	Time	s
Δt	Time step size	s
Δt^*	Nondimensional time step size	ND
t^*	Nondimensional time	ND

t_h^*	Nondimensional time for reaching the half mean M_{i-j} value	ND
t_m^*	Nondimensional time for reaching the mean M_{i-j} value	ND
t_{ft}	Flow-through time	s
T	Temperature	°C
T_{ave}	Mean temperature	°C
ΔT	Temperature difference	°C
u, v, w	Velocity components in the X, Y, Z directions	$m \cdot s^{-1}$
$\hat{u}, \hat{v}, \hat{w}$	Nondimensional u, v, w	ND
u', v', w'	Fluctuating velocities in the X, Y, Z directions	$m \cdot s^{-1}$
u^*	Friction velocity	$m \cdot s^{-1}$
U	Mean streamwise wind speed	$m \cdot s^{-1}$
U^+	Nondimensional streamwise velocity	ND
U_H	Mean streamwise wind speed at the height of H	$m \cdot s^{-1}$
$U_{m,n}$	Mean normal velocity on the cell ($\Delta y_m, \Delta z_n$)	$m \cdot s^{-1}$
U_{obs}	Wind speed recorded at the height of z_{obs}	$m \cdot s^{-1}$
U_P	Mean streamwise wind speed at the near-wall cell P	$m \cdot s^{-1}$
U_{ref}	Reference speed	$m \cdot s^{-1}$
V	Room volume	m^3
W	Width	m
W_o	Opening width	m
y^+, y^*	Dimensionless wall distance	ND
y_P	Distance from point P to the wall	m
z_0	Aerodynamic roughness height	m
z_0^+	Nondimensional aerodynamic roughness height	ND
z_n	Z position of the neutral plane	m
z_{obs}	The height of recording U_{obs}	m

z_p	centroid height of the first cells	m
z_{ref}	Reference Z position	m
Greek symbols		
α, β	power-law index	ND
ε	turbulence dissipation rate	$m^2 \cdot s^{-3}$
ε_{2layer}	turbulent viscous dissipation rate in the near-wall region	$m^2 \cdot s^{-3}$
ϕ	Scaling factor	ND
φ	Scalars	ND
φ_b	Flow variable of the basic case	ND
φ_x	Flow variable of other cases	ND
η_0	Model constant	ND
κ	Von Karman's constant, 0.4187	ND
μ_l	Dynamic laminar viscosity	Pa·s
μ_t	Dynamic turbulent viscosity	Pa·s
$\mu_{t,2layer}$	Dynamic turbulent viscosity in the near-wall region	Pa·s
μ_{SGS}	SGS turbulent viscosity	Pa·s
ν_t	Kinematic turbulent viscosity	$m^2 \cdot s^{-1}$
θ	Wind angle	°
ρ	Air density	$Kg \cdot m^{-3}$
σ_k	Turbulence kinetic energy Prandtl number	ND
σ_ε	Turbulence dissipation Prandtl number	ND
τ_0	Wall shear stress	$m^2 \cdot s^{-2}$
τ_{ij}	SGS stress term	$m^2 \cdot s^{-2}$
Δ	Grid filter width	m
Δ_t	Test filter, its width is twice the Δ	m
Γ_φ	Effective diffusion coefficient	ND
Ω	Scale of vorticity	ND

Ψ	Ratio of the increasing ratio of y^+ and the increasing ratio of model scale	ND
--------	--	----

Note: ND means no dimension.

Chapter 1

Introduction

1.1 Background and motivation

As people spend about 80-90% of their time indoors (Klepeis et al., 2001; Robinson and Nelson, 1995), the factors affecting indoor air quality (IAQ), such as particulate matter (PM) and gaseous concentration level, can have a significant impact on health. Natural ventilation through open windows is a common ventilation strategy in residential buildings, especially during the mild season. People use natural ventilation to condition the indoor environment not only due to its excellence in improving building sustainability (Homod and Sahari, 2013; Schulze and Eicker, 2013), but also due to increased health awareness regarding exposure to outdoor fresh air (Chau et al., 2008; Finnegan et al., 1984).

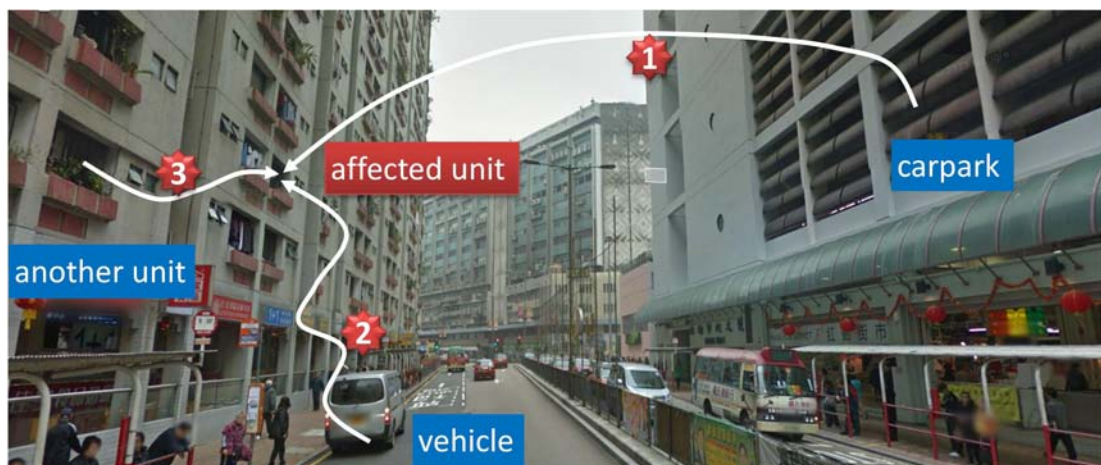


Figure 1.1 Outdoor pollutants incurring into the interior; route 1 represents special dense sources like carparks, industrial chimneys and construction sites, route 2 traffic exhausts, and route 3 exhausts from other units (interunit dispersion).

Despite of the advantages of natural ventilation, it is probably during this ventilation process that outdoor pollutants make their incursion into the interior (Santos et al, 2011), as illustrated in Figure 1.1. Generally speaking, pollutants entering from outdoors due to natural ventilation or envelope infiltration are mainly

traffic exhaust, dust, pollen, smoke, fumes, and mist (ASHRAE Handbook, 2009). They are suspended aerosols in the air, carried by the airflow and transported from the vicinity into the building. Apart from this common route, however, there is another important pollutant transport route: cross transmission between units within the same building, called “interunit dispersion” in the present thesis. Interunit dispersion is a special airborne transmission route (e.g., Barker et al., 2001; Cole and Cook, 1998; Hodgson et al., 2012; Mendell et al., 2002; Morawska et al., 2013; Nicas et al., 2005; Tellier, 2006), which is dangerous, essentially because it is likely to involve the transport of infectious aerosols, such as pathogen-laden respiration droplets. Another consideration is that the transport distance and time are relatively short. Understanding the mechanisms and routes of interunit dispersion thus becomes critically important in developing control measures and ventilation strategies.

Since interunit dispersion was actually observed in Hong Kong during the outbreak of Severe Acute Respiratory Syndrome (SARS) in 2003 (HWFB-HK, 2003), it has begun to attract more and more attention. Previous on-site measurement (Niu and Tung, 2008) and numerical simulations (Gao et al., 2008, 2009) have well explained and quantified the buoyancy-dominated upward transmission of SARS occurring in the Amoy Gardens housing complex (HWFB-HK, 2003). Later, a series of wind tunnel experiments (Liu et al., 2010, 2011a, b; Wang et al., 2010) revealed that wind-induced interunit dispersion could occur along both horizontal and vertical directions. However, based on highly reduced-scale models, the indoor concentration level was difficult to be accurately measured in a wind tunnel experiment (Mfula et al., 2005; Stathopoulos, 1997). Despite of the useful information provided by the previous studies, they are limited to either solely upward transmission or analyses of envelope concentrations. Therefore, a systematic investigation of wind-induced interunit dispersion around multistory buildings with real rooms and openings is still needed.

This thesis only considers single-sided natural ventilation (see Figure 1.2) for the selected multistory building models, as it is more common than cross ventilation in practice, especially in densely populated urban areas like Hong Kong where many rooms are characterized by a single window and a closed door. Obviously, accurate prediction of single-sided natural ventilation is the prerequisite of the successful prediction of interunit dispersion. In general, the single-sided ventilation can be

predicted by empirical models (Caciolo et al., 2013; Larsen and Heiselberg, 2008; Phaff and De Gids, 1982; Warren, 1977; Wang and Chen, 2012), experimental measurements (e.g., Jiang et al., 2003; Caciolo et al., 2011; Dascalaki et al., 1996; Laussmann and Helm, 2011) and Computational Fluid Dynamics (CFD) models (e.g., Allocca et al., 2003; Caciolo et al., 2012, 2013; Evola and Popov, 2006; Jiang and Chen, 2001, 2002, 2003; Papakonstantinou, 2000). However, compared with the former two methods, the CFD modeling has many advantages for the study of single-sided natural ventilation that involves a coupled indoor and outdoor flow (Blocken and Gualtieri, 2012; Chen, 2009; van Hooff and Blocken, 2010, 2013), despite that its quality must be seriously assured. The main advantages of CFD modeling are: (a) it provides whole-flow field data; (b) it allows a strong degree of control over the boundary conditions; (c) it does not suffer from incompatible similarity requirements; and (d) it easily allow parametric studies to evaluate alternative design.

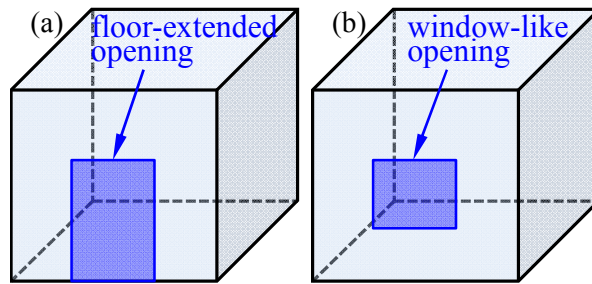


Figure 1.2 Schematic diagram of single-sided natural ventilation with two types of openings; the single-sided natural ventilation means that the exchange of the indoor and outdoor flow could occur only at a single opening in one wall of a target room.

Accurately predicting the single-sided natural ventilation using CFD method requires accurate prediction of outdoor flow and indoor flow, as well as their interaction at the openings. It is now known that many factors, such as turbulence models and grid arrangement, can influence the accuracy and reliability of a CFD simulation of atmospheric flow and dispersion (Franke et al., 2007; Mochida et al., 2006; Tominaga et al., 2008b). For Reynolds-Averaged Navier-Stokes (RANS) simulations, there is a large body of work assessing the effect of different such factors on numerical solutions. However, less attention has been paid to the effect of

the inhomogeneous atmospheric boundary layer (ABL) and near-wall treatment on the simulation of atmospheric flow and pollutant dispersion. For Large-Eddy Simulations (LES), very few such studies exist and thus a comprehensive assessment of the important influencing factors is necessary. In addition, parametric studies for single-sided natural ventilation are not found at time of writing. In particular, no sensitivity test of the near-wall mesh density for both the LES and RANS modeling of natural ventilation has yet been published. However, given the complexity of single-sided ventilation, particularly the constant change of direction of the instantaneous velocity at an opening resulting from the strong interactions between outdoor and indoor flows (Jiang and Chen, 2001), any inappropriate setting of computational parameters may result in incorrect solutions. In order to assure and improve CFD modeling of single-sided ventilation, a comprehensive sensitivity test of the important computational parameters is required.

1.2 Objectives and significance

Owing to the limitations of the previous studies regarding interunit dispersion through opened windows, this thesis aims at providing a systematic investigation of interunit dispersion in multistory buildings with single-sided natural ventilation using numerical method. The numerical studies of this thesis are based on a set of CFD code, namely Ansys Fluent 13.0 (2010), with a series of User Defined Functions (UDF) compiled into the code. Both RANS and LES models are used. As the interunit dispersion occurs in the single-sided natural ventilation system, quality assessment and improvement of CFD prediction of single-sided natural ventilation is conducted, prior to CFD simulation of interunit dispersion. This research objective is achieved through the following works (also see Figure 1.3 in detail):

(a) Evaluate major predictive methods of single-sided natural ventilation to identify an appropriate method for this study. On-site measurements of ventilation performance and IAQ are conducted and past empirical models are evaluated. In addition, CFD methods are preliminarily validated.

(b) Assess and improve the quality of CFD prediction of coupled indoor and outdoor flow and dispersion. Here both RANS and LES models are considered. Necessary modifications and improvements of numerical methods are made and

appropriate selections are recommended.

(c) Study interunit dispersion in multistory buildings using the assured CFD method. Steady simulations using RANS model are conducted to predict the mean dispersion routes and reentry ratios, and transient simulations using LES model to predict the transient dispersion characteristics and time scales.

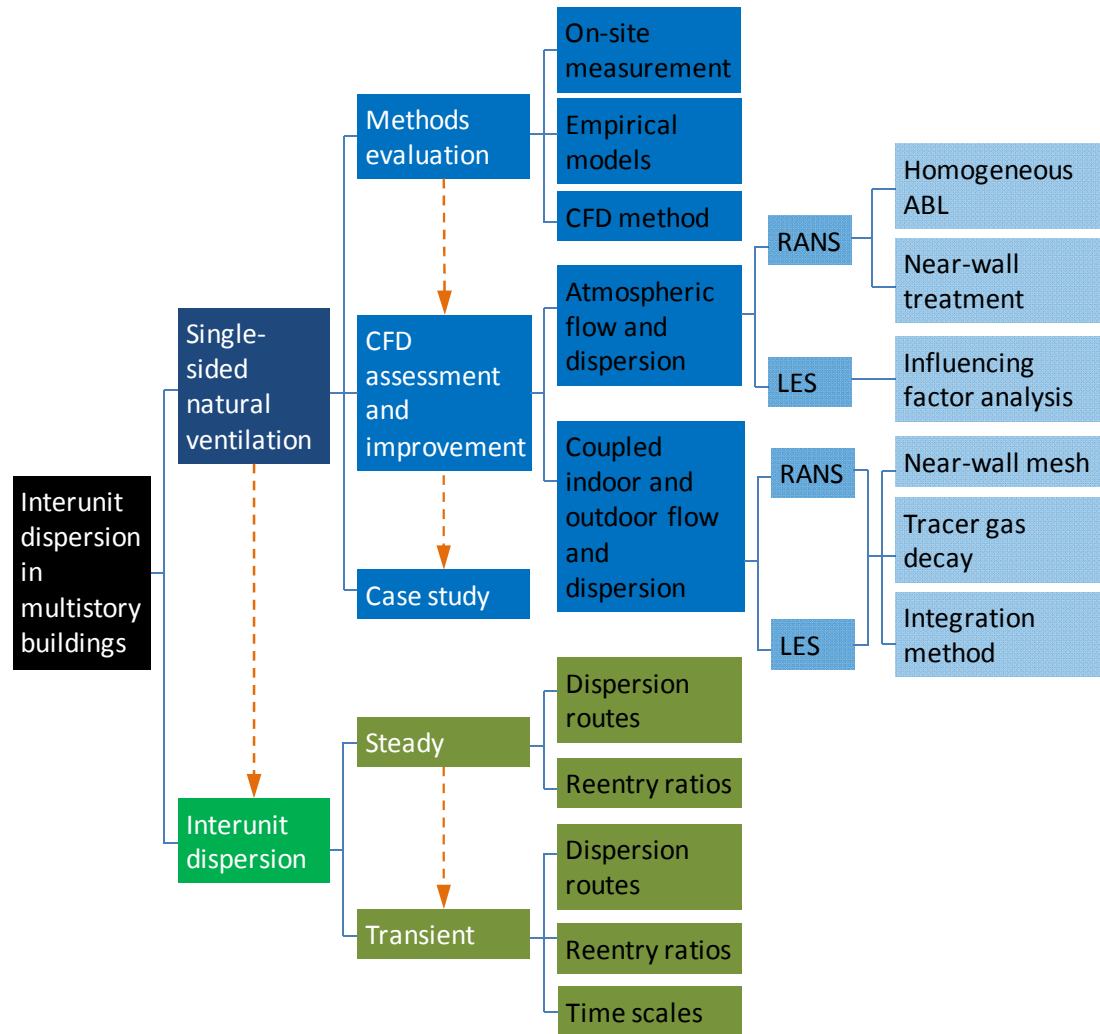


Figure 1.3 The outline of the research contents.

The studies regarding single-sided natural ventilation, particularly CFD method assessment and improvement, should contribute to improved quality of CFD simulation of flow and dispersion problems that involve a coupled indoor and outdoor flow. The transient study of single-sided natural ventilation using LES model extends the current understanding of transient characteristics of flow through a single

opening. The realization of the interunit dispersion routes and quantification of the reentry ratios and the time scales in generic multistory buildings can be useful from both academic and practical points of view. Academically, it enhances the understanding of the pollutant dispersion mechanisms in built environments under such a coupled indoor and outdoor flow condition. Practically, it helps the building officials and designers to implement more effective and immediate infectious intervention strategies. In addition, the modeling and numerical method described in this thesis is useful information for future studies of flow and pollutant dispersion in built environments.

1.3 Thesis outline

This chapter provides a brief introduction of the background and motivation, the objectives and significance, as well as the outline of this thesis.

Chapter 2 presents the literature review, which covers four aspects: predictive methods of single-sided natural ventilation, CFD prediction of flow and dispersion around buildings, CFD prediction of single-sided natural ventilation, and airborne interunit dispersion.

Chapter 3 presents the evaluation of predictive methods of single-sided natural ventilation in multistory buildings including on-site measurements.

Chapter 4 presents the assessment and improvement of the quality of CFD simulation of atmospheric flow and dispersion.

Chapter 5 presents the assessment and improvement of the quality of CFD simulation of single-sided natural ventilation.

Chapter 6 presents the CFD simulation of flow and interunit dispersion in and around multistory buildings.

Chapter 7 concludes this thesis and provides recommendations for future studies.

Chapter 2

Literature review

2.1 Predictive methods of single-sided natural ventilation

Single-sided natural ventilation due to wind effect is a complex process that is strongly influenced by the turbulent nature of the approaching wind and the bi-directional airflow interaction at the opening (Etheridge, 2011; Haghighat et al., 1991, 2000; Linden, 1999; Straw, 2000).

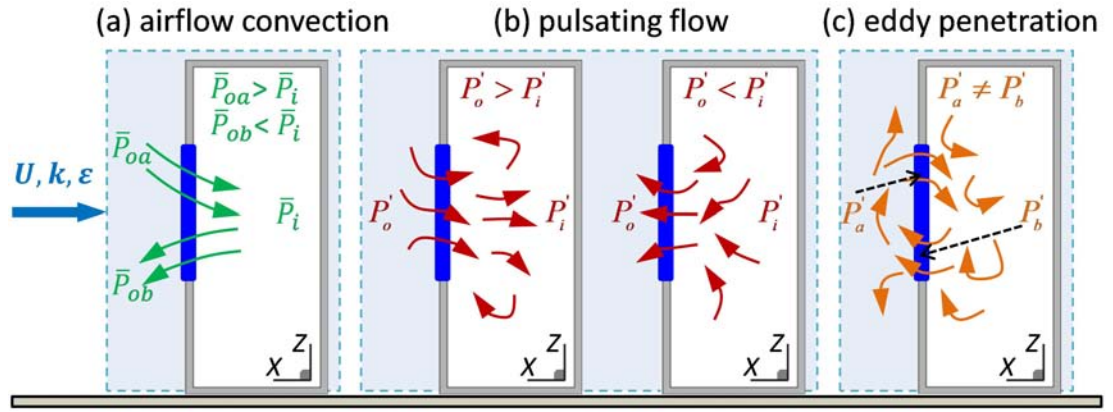


Figure 2.1 Schematic view of the single-sided natural ventilation mechanisms.

The ventilation rate is mainly contributed by three ventilation mechanisms (Etheridge, 2011): mean airflow convection, pulsating flow and eddy penetration, as shown in Figure 2.1. The first one is caused by the mean pressure differences across the opening that induces continuous airflow exchange between the ventilated space and its outside (Ai et al., 2011c; Gao et al., 2008). The mediate one is caused by the temporal change in external pressure, which makes the opening function as an inlet or an outlet at different times. The last one is caused by the pressure fluctuations within the plane of the opening both spatially and temporally. The latter two are essentially caused by the turbulent nature of wind (Haghighat et al., 2000; Wang and Chen, 2012), which are especially significant when the wind fluctuations (turbulent component) are relatively large compared to the mean values. Obviously, the ventilation performance of single-sided natural ventilation is completely determined

by the characteristics of the airflow inside and around the building.

Among the existing prediction methods, the empirical correlations (see Table 2.1) can provide rapid estimations. They are mostly based on the classical orifice equation:

$$Q = C_d A \sqrt{\frac{2|\Delta P|}{\rho}} \quad (2.1)$$

where Q is the ventilation rate, C_d the discharge coefficient, A the opening area, ΔP the pressure difference, and ρ the air density. Warren (1977) proposed a pair of simple equations to calculate the wind-driven (Q_w) and the buoyancy-driven (Q_b) single-sided natural ventilation rate, respectively; the larger of these two ventilation rates is taken as the total ventilation rate due to the combined effect of wind and buoyancy. This model has been widely used (e.g. Warren and Parkins, 1985; Etheridge and Sandberg, 1996; Etheridge, 2002) and has even become a baseline for natural ventilation design (BS5925, 1991). The semi-empirical model developed by Phaff and De Gids (1982) considers the contributions of wind and buoyancy effects together. However, its accuracy is affected by window characteristics as the discharge coefficient of window (C_d) is not included in the model. A common limitation of these two models is that they both ignore wind direction (Larsen et al., 2003), and this inspired Larsen and Heiselberg (2008) to make a new correlation despite the fact that they found that ventilation rate has an unclear relationship with wind direction. Recently, Caciolo et al. (2011) compared the three models above with their full-scale experiments and observed that the equations of Warren (1977) provide the best overall predictions, although all of the models underperform on the leeward side. They (Caciolo et al., 2013) eventually proposed a new equation especially for leeward rooms; however, this equation neglects scenarios where ventilation is purely wind induced. In order to predict the fluctuating ventilation rate, Wang and Chen (2012) used spectrum analysis to derive the contributions of pulsating flow (Haghighat et al., 1991, 2000) and eddy penetration (Straw, 2000). Nevertheless, in addition to omitting wind direction, their model (Wang and Chen, 2012) assumes a uniform velocity distribution along the horizontal direction of a window. In general, these empirical models are established on the basis of a single-room building or a specific room of a building (see Table 2.1). Because few

Table 2.1 Existing empirical models for the determination of single-sided ventilation rate.

Reference	Equations	Technique	Physical model
Warren (1977)	$Q_T = \max(Q_b; Q_w), \quad Q_b = \frac{1}{3} A_{eff} C_d \sqrt{\Delta T H_o g / T_{ave}},$ $Q_w = 0.025 A_{eff} U_{ref}$	Wind tunnel and full-scale experiments	A specific room of a building
Phaff and De Gids (1982)	$Q_T = \frac{1}{2} A \sqrt{D_1 U_{10}^2 + D_2 H_o \Delta T + D_3}$	Full-scale experiments	A specific room of a building
Larsen and Heiselberg (2008)	$Q_T = \frac{1}{2} A \sqrt{C_1 f(\theta)^2 C_p U_{ref}^2 + C_2 H_o \Delta T + C_3 \frac{\Delta C_p \Delta T}{U_{ref}^2}}$	Wind tunnel experiments	A single-room building
Wang and Chen (2012)	$Q_T = Q_a + \sigma_q, \quad Q_a = \frac{C_d l \sqrt{C_p} \int_{z_0}^{H_o} \sqrt{z^{2/7} - z_n^{2/7}} dz}{z_{ref}^{1/7}}, \quad \sigma_q = \sqrt{\sigma_{qp}^2 + \sigma_{qe}^2}$ $\sigma_{qp}^2 = \left(C_d l z_{ref}^{-1/7} \sqrt{C_p} \int_{z_0}^{H_o} \sqrt{z^{2/7} - z_n^{2/7}} dz \right)^2 \sigma_u^2, \quad \sigma_{qe}^2 = C'^2 A^2 U \int_{\bar{U}/l}^{\infty} S_p(\hat{n}) d\hat{n}$	Theoretical analysis	A single-room building
Caciolo et al. (2013)	$Q_T = \frac{1}{3} A C_d \sqrt{\Delta T \Delta T^* H_o g / T_{ave}}, \quad \Delta T^* = 1.355 - 0.179 U_{ref}$	CFD and full-scale experiments	A specific room of a building

structures in urban areas are single rooms (or even single story buildings), an evaluation of their reliability to multistory buildings is necessary.

Experimental measurement is another way to determine single-sided ventilation rates. Measuring the air velocity at an opening (Caciolo et al., 2011; Allard, 1998; Dascalaki et al., 1995, 1996; Li et al., 2014) is one method that can be used. In practice, the constant changes in airflow profiles at an opening mean that a large number of simultaneous high-fidelity velocity measurements are required, which makes this kind of experiment difficult and expensive to conduct. Pressure coefficient measurements on a sealed building model have also been used to estimate ventilation rate (Ai et al., 2011b; Chand et al., 1998; Ernest et al., 1991; Swami and Chandra, 1988). However, this method has many limitations, and numerous assumptions (Straw, 2000; Choiniere et al., 1992; Sandberg, 2004) are required. Some studies (Murakami et al., 1991; Kato et al., 1992; Sandberg, 2004; Karava et al., 2006, 2011; Kobayashi et al., 2009, 2010; Ramponi and Blocken, 2012) show that, in case of wind flow through large openings, the sealed-model assumption is no longer valid. The use of tracer gas techniques (Laussmann and Helm, 2011) should be the most common and reliable experimental method (Caciolo et al., 2011; Dascalaki et al., 1996; Murakami et al., 1991; Katayama et al., 1992). However, it is difficult to use this method simultaneously in many rooms in a multistory building. In addition, wind tunnel experiments are limited by their resolution in the indoor airflow of reduced-scale models (Etheridge, 2011; Mfula et al., 2005; Stathopoulos, 1997), and full-scale measurements are restricted by uncontrollable boundary conditions and model availability, especially in the design stage.

More and more researchers are using CFD to study single-sided natural ventilation (e.g., Caciolo et al., 2013; Papakonstantinou et al., 2000; Jiang and Chen, 2001, 2002, 2003; Allocca et al., 2003; Evola and Popov, 2006; Caciolo et al., 2012), as a CFD simulation can provide detailed information about whole-domain airflow to an acceptable level of accuracy and calculate the ventilation rate for different configurations in an efficient manner. However, these researchers have mostly focused on model validation and parametric analysis using very simple physical models. It is necessary, especially from the viewpoint of ventilation design, to extend their studies to multistory buildings. In addition, previous studies have ignored the difference in envelope airflow pattern between rooms in a multistory building and in

a single-room building. This difference, which could lead to completely different ventilation characteristics in these two types of buildings, can be revealed conveniently using the CFD method.

2.2 CFD simulation of atmospheric flow and dispersion near buildings

2.2.1 Issues in RANS simulations

Accurate prediction of atmospheric flow and dispersion near buildings is very important for the design of a healthy, comfortable, and energy-saving built environment. In recent decades, CFD has been increasingly used to predict such flow and dispersion (e.g., Chen, 2009; Li et al., 2006; Stathopoulos, 1997; Blocken, 2014). It is now known that many factors, such as turbulence models and grid arrangement, can influence the accuracy and reliability of a CFD simulation (Franke et al., 2007; Mochida et al., 2006; Tominaga et al., 2008b), and for RANS simulations there is a large body of work assessing the effect of different such factors on numerical solutions, and some guidelines have been developed based on their findings (Franke et al., 2007; Yoshie et al., 2007; Tominaga et al., 2008b; Tamura et al., 2008; Casey and Wintergerste, 2000). However, less attention has been paid to the effect of the inhomogeneous ABL and near-wall treatment on the simulation of atmospheric flow and pollutant dispersion.

An unexpected problem regarding CFD simulation of flow and dispersion around buildings is the inhomogeneous ABL occurring in the vertical velocity and turbulence profiles throughout the computational domain. In general, a homogeneous ABL can be achieved when the turbulence models, inlet conditions, and applied law of the rough wall are consistent (e.g., Blocken et al., 2007; Franke et al., 2007; Gorlé et al., 2009; Hargreaves and Wright, 2007; Parente et al., 2011; Riddle et al., 2004; Xie et al., 2004; Yang et al., 2009). Some previous studies demonstrate the importance of developing a homogeneous ABL prior to commencing numerical investigations (e.g., Castro and Robins, 1977; Gao and Chow, 2005), given that minor changes to the incident flow profiles can result in significant deviations in the downstream flow fields. Unfortunately, most CFD practitioners are unaware of the importance of this issue and do not confirm whether a homogeneous ABL has been achieved before embarking on numerical investigations (e.g., Lateb et al., 2011;

Mavroidis et al., 2012; Santos et al., 2009; Steffens et al., 2013; Tominaga et al., 2008a; Tominaga and Stathopoulos, 2009). In practice, most atmospheric studies based on outdoor CFD simulations are conducted using an inconsistent combination of inlet conditions and law of the rough wall (e.g., Lateb et al., 2011; Mavroidis et al., 2012; Santos et al., 2009; Steffens et al., 2013; Tominaga and Stathopoulos, 2009). Typically, a smooth domain ground ($K_s = 0$) can result in the horizontal acceleration of a fully developed inlet profile (for example, $U = (u^*/\kappa)\ln(z/z_0)$) towards the streamwise direction. Thus, to develop a homogeneous ABL and to clarify the effect it has on numerical solutions, are matters of urgent importance to studies of atmospheric flow and dispersion processes.

Since the first experimental study (Nikuradse, 1933) of the flow through sand-grain rough pipes, the influence of surface roughness on the overall turbulent boundary layer has received more attention. It has been found that surface roughness can enhance the turbulence (Miyake et al., 1999, 2001) and isotropy (Antonia and Krogstad, 2001; Smalley et al., 2002) of the flow over it, and thus it has an obvious impact on the entire wall-bounded flow (Krogstad and Antonia, 1999). Considering that the bottom of the ABL is always rough (Etheridge and Sandberg, 1996), accurate reproduction of the effect of the ground roughness on the entire ABL should be a basic prerequisite for obtaining an accurate prediction of the flow and dispersion processes. In a CFD simulation, the surface roughness effect can be taken into account using a near-wall model, the most widely used being the standard wall functions (Fluent, 2010). The wall functions directly link the walls and the near-wall logarithmic layer with a series of semi-empirical formulas, and the flow details in the low-Reynolds-number region below the first cells and their effects on the entire wall-bounded flow are thus ignored (Rodi, 1991; Speziale et al., 1992). As an alternative approach, the two-layer model (Fluent, 2010) can integrate the flow variables all the way down to the walls using a one-equation model (Wolfshtein, 1969), and thus the effect of the near-wall flow on the entire flow can be calculated. It has been confirmed, on a smooth domain ground, that the two-layer model gives a better prediction of flow around a cubic obstacle than does the wall function (Lakehal and Rodi, 1997). Recently, modifications of this two-layer model to adapt to rough surfaces have been proposed (Durbin et al., 2001) for RANS simulations. However, it is still expected to develop a homogeneous ABL for this roughed

two-layer model and to clarify the effect of the different types of near-wall treatment approaches on the prediction of flow and dispersion.

2.2.2 Issues in LES simulations

Although previous studies regarding CFD simulation of flow and dispersion near buildings have been conducted mostly using RANS models (e.g., Santos et al., 2009; Chavez et al., 2011; Mavroidis et al., 2012; van Hooff and Blocken, 2013), thanks to advances in computational power, LES simulation has attracted increasing attention in recent years (e.g., Lim et al., 2009; Xie and Castro, 2009; Gousseau et al., 2012; Hu et al., 2008; Chu and Chiang, 2013). A number of earlier studies comparing the performance of RANS and LES models (Murakami, 1993; Rodi, 1997; Tominaga et al., 2008a; Tominaga and Stathopoulos, 2010, 2011; Gousseau et al., 2011; Salim et al., 2011) found that LES models are better for predicting atmospheric flow and concentration fields, although LES modeling requires greater computational resources. The better performance of LES can be attributed to its anisotropic treatment of scalars and its time-resolving feature, which better accounts for the inherently fluctuating characteristics of wind flow.

In LES modeling of flow and dispersion in built environments, a major issue is the treatment of inflow conditions at the inlet of the computational domain. Unlike RANS models, which use time-averaged inflow conditions, generating fluctuating inflow conditions for LES models is difficult, as such inflow conditions should vary randomly, but must be compatible with the governing equations (Tabor and Baba-Ahmadi, 2010). The many methods proposed in the literature to generate the inflow conditions for LES can be roughly categorized into synthesis inlet methods and precursor simulation methods (Tabor and Baba-Ahmadi, 2010; Fluent, 2010). The latter extract fluctuating inflow conditions from a driver domain that presumably exists upstream of the main domain (Bu and Kato, 2011; Hu et al., 2008). This extended domain length could deteriorate the horizontal homogeneity (Blocken et al., 2007; Richards and Hoxey, 1993; Górlé et al., 2009) of the ABL in the main domain. In addition, this inflow generating method is costly and is not convenient to use. Chu and Chiang (2013) compared three different inflow conditions in the simulation of coupled indoor and outdoor flows. Extending such comparisons to dispersion in built

environments would then still be necessary.

It is well known that LES models explicitly resolve large-scale eddies and model the small-scale eddies using a subgrid-scale (SGS) model (Fluent, 2010). Some earlier studies (Cheng and Porté-Agel, 2013; Iizuka and Kondo, 2004; Ghaisas et al., 2013) found that SGS models have obvious influences on the LES prediction of flows in near-wall regions where there are a large number of anisotropic small-scale eddies. Several SGS models have been proposed, most of which are based on the eddy-viscosity approach and use the Boussinesq hypothesis (Fluent, 2010; Cheng and Porté-Agel, 2013; Hinze, 1975). Most of the previous LES studies (e.g., Lim et al., 2009; Chu and Chiang, 2013; Tominaga and Stathopoulos, 2010; Gousseau et al., 2011; Jiang et al., 2003) of the flow and dispersion in built environments selected the standard Smagorinsky-Lilly model (Smagorinsky, 1963) and its dynamic version (Smagorinsky, 1963; Germano et al., 1991; Lilly, 1992). There is still a need to compare the performance of various SGS models in predicting flow and dispersion in built environments.

Many factors, including the aforementioned inflow treatment and SGS model issues, are likely to affect the quality of LES modeling. For a specific flow problem, the optimal model settings and the appropriate selection of many parameters require detailed investigation. Unlike RANS simulation, for LES simulation, to the best of the author's knowledge, only Gousseau et al. (2013) have performed quality studies on external wind flow around an isolated building, based on a few influencing factors. Such studies should be extended to the dispersion problem and should include more influencing factors.

2.2.3 Issues in model scale

Restricted by physical boundaries, reduced-scale models are usually used in wind tunnel experiments in the field of wind engineering. Reduced-scale models have been widely recognized as reasonable and reliable, as long as important similarity criteria are obeyed (Snyder, 1981; Meroney, 2004). For CFD simulations, the standard way of thinking is that they benefit from using full-scale models that have no similarity constraints (Blocken, 2014). Therefore, applied CFD studies of wind flow and related processes have mostly been conducted with full-scale models (e.g.,

Blocken and Persoon, 2009; Lo et al., 2013; van Hooff and Blocken, 2013; Zhang et al., 2012).

It is well known that the prediction accuracy of CFD simulations depends heavily on the appropriateness of mesh resolution. Particularly, predictions of near-field environmental processes always demand for a high-density mesh resolution, as correctly reproducing the separating flows around building obstacles cannot be achieved based on a coarse mesh (Tominaga and Stathopoulos, 2013; Tominaga et al., 2008b; Frank et al., 2007). In fact, specific pairing of a turbulence model and a near-wall treatment approach have specific requirements for near-wall y^+ values (Casey and Wintergerste, 2000; Franke, 2007; Fluent, 2010), namely the nondimensional distance between the centroid of a first cell and its closest wall. The decrease in model scale may decrease the near-wall y^+ value. It is thus hypothesized that the use of reduced-scale models in CFD simulations will require fewer cells to achieve a target near-wall y^+ value and in turn save numerical resources. This is believed not to come at the expense of prediction accuracy, provided that the similarity criteria are met. Verification of this hypothesis is meaningful for future CFD simulations.

2.3 CFD prediction of single-sided ventilation rate

Compared with empirical and experimental methods, CFD modeling has many advantages for the study of single-sided natural ventilation involving coupled atmospheric wind flow and indoor air flow (van Hooff and Blocken, 2010, 2013; Blocken and Gualtieri, 2012). CFD simulation can provide details of the airflow through a single opening in both a steady and a transient way, and again it can provide the whole-domain flow information. Among existing turbulence models, the RANS and LES models (Fluent, 2010) have usually been used to predict the single-sided natural ventilation (e.g. Papakonstantinou, 2000; Jiang and Chen, 2001, 2002, 2003; Allocca et al., 2003; Evola and Popov, 2006; Caciolo et al., 2012, 2013), owing to their reasonable compromise between the numerical accuracy and cost.

Jiang and Chen (2001, 2003) have compared the LES and RANS models against both pure wind-driven and pure buoyancy-driven experiments, demonstrating that

the CFD technique is suitable for the study of single-sided natural ventilation. Recently, Caciolo et al. (2012, 2013) compared the LES and RANS turbulence models with their full-scale measurements and found that the LES model provides more accurate predictions and the RANS models provide acceptable predictions at a computational cost that is at least one order of magnitude lower than that of the LES. These previous studies, however, were conducted without prior sensitivity tests of computational parameters.

Considering the complexity of the single-sided ventilation, namely, the instantaneous velocity at an opening changing direction all the time owing to the strong interactions between outdoor turbulent and indoor laminar flows (Jiang and Chen, 2001), any inappropriate setting of computational parameters may result in incorrect solutions. The detailed guidance for CFD modeling of wind flow around buildings has been provided by the recently established best practice guidelines (e.g., Franke et al., 2007; Yoshie et al., 2007; Tominaga et al., 2008b), which, however, do not provide specific guides for the single-sided ventilation. Up to present, the most related study to the current case should be the generic sensitivity analyses of computational parameters for the CFD modeling of cross ventilation (Ramponi and Blocken, 2012). Particularly, to the best of the author's knowledge, for both the LES and RANS modeling of natural ventilation, the sensitivity test of the near-wall mesh density has not yet been presented in the literature. In order to provide guidance for the improved CFD modeling of single-sided ventilation, a comprehensive sensitivity test of the important computational parameters is required.

In addition to the establishment of the accurate coupled airflow field, the method used to compute the single-sided ventilation rate is another essential element to the successful prediction of the ventilation rate. Built upon CFD technique, there are two commonly used methods for ventilation rate prediction, namely the integration of opening velocity and the tracer gas concentration decay (e.g., Gao et al., 2008; Caciolo et al., 2012). Recent studies (Caciolo et al., 2012, 2013) have shown that the integration method significantly overestimates ventilation rates in the LES context. The reasons are (a) it does not exclude the component contributed by the short-circuiting flow and (b) it does not account for the fluctuating airflow exchange. As an alternative, the tracer gas decay method takes into account all ventilation mechanisms and gives the effective ventilation rate. Caciolo et al. (2012) have

compared these two methods using both RANS and LES turbulence models. However, they did not quantitatively explain the contributions of the mean and fluctuating airflows to the total ventilation rate under different wind directions. In addition, the accuracy of both methods is strongly relied on the velocity and/or turbulence fields established by the selected numerical model.

Previous studies even using the LES models have mostly focused on time-averaged ventilation rates and have not analyzed its fluctuating characteristics. A few studies have examined the fluctuating characteristics of airflow through a single opening. In particular, Hasama et al. (2008) and Yamanaka et al. (2006) have used LES and/or the detached eddy simulation (DES) model to analyze the fluctuating flow through a lateral opening (namely, with a parallel wind direction). Only Yamanaka and colleagues calculate single-sided ventilation rates, which they do using the integration method (integrating opening velocity). In addition, the analysis of the fluctuating airflow characteristics through a single opening facing other wind directions (except for the parallel direction) has not been reported in the literature.

2.4 Interunit pollutant dispersion

A large number of studies have been conducted on pollutant dispersion around the built environment, but most of them focus on dispersion from an upstream pollutant source (e.g., Macdonald et al., 1997; Mfula et al., 2005; Tominaga and Stathopoulos, 2009; Yoshie et al., 2011). Less attention has been paid to interunit transport within a building, despite this having been identified as an important transmission route through observations made in Hong Kong during the 2003 SARS outbreak (HWFB-HK, 2003).

Niu and Tung (2008) conducted on-site measurements in a residential building in Hong Kong to examine vertical interunit transmission mechanisms using the tracer gas technique. They show that under buoyancy effects, the reentry ratio of ventilation exhaust from the lower floor to the one immediately above it can be up to 7%. This implies that windows on the same façade of a building can be a route for the vertical spread of pathogen-laden aerosols. Later, Gao et al. (2008) applied CFD techniques to reexamine this vertical upward transmission and confirmed the importance of this

upward transmission route. They also showed that the wind normally incident to the building either enhances or weakens upward transport depending on the approaching wind speed and the difference in temperature between the indoors and outdoors. However, in their study both the field measurements and numerical modeling were limited to the upward transmission between two vertically adjacent units. In practice, taking into account the wind effect, the airflow pattern around a building-like bluff body (see Figure 2.2), which has been thoroughly examined in the literature (e.g., ASHRAE Handbook, 2011; Liu, 1991; Martinuzzi and Tropea, 1993), contains not only upward but also downward flow, as well as lateral separation and recirculation. This implies that downward and horizontal transmissions, such as those followed by air pollutants released from different locations on a multistory building and taking different dispersion routes, may exist alongside upward trajectories.

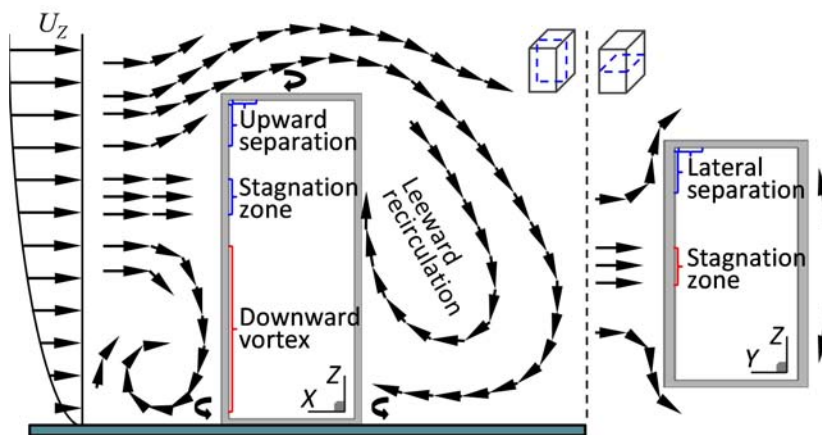


Figure 2.2 Schematic airflow pattern around a bluff body.

More recently, Liu et al. (2010, 2011a, b) and Wang et al. (2010) carried out wind tunnel experiments to study the wind-driven dispersion around 10- and 30-story residential building models in a complicated cross (#) floor plan, see Figure 2.3. By analyzing the tracer gas concentration and wind pressure distributions along the building façades, they show that the pollutant can disperse along the horizontal directions although it mainly spreads vertically in the reentry spaces. Nevertheless, their findings may only be implemented to similar buildings in cross (#) floor plan. For other typical types of buildings, such as slab-like buildings, the pollutant dispersion characteristics are expected to be different, especially for the horizontally

lateral dispersion. In addition, owing to the limitation of experimental resolution on a highly reduced-scale model, the indoor concentration level and the reentry ratio were not analyzed.

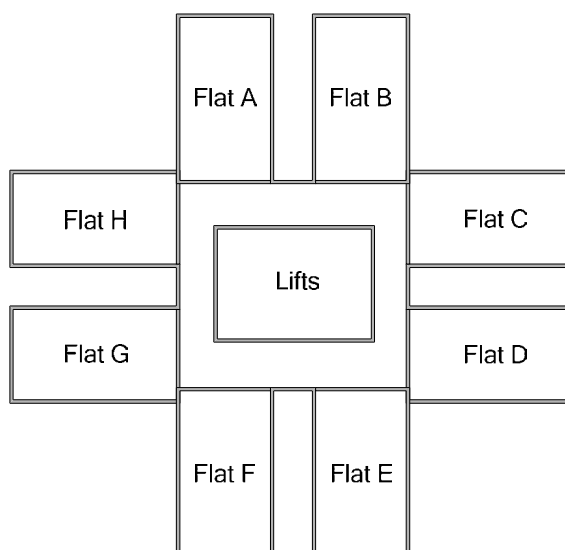


Figure 2.3 Schematic plan view of the building models in a cross (#) floor plan.

Many previous studies of pollutant dispersion used passive tracer gas to simulate pathogen-laden aerosols (Gao et al., 2008; Liu et al., 2010, 2011a, b; Niu and Tung, 2008; Riley et al., 1978; Wang et al., 2010). The rationality of using tracer gas is supported by some studies regarding the size and behavior of respiratory droplet-nuclei (Duguid, 1946; Morawska, 2006; Tellier, 2006; Nicas et al., 2005; Mitman, 1945; CDCP, 1994, Wells, 1934; Brundrett, 1992; Gao et al., 2009). In particular, Duguid (1946) showed that respiratory droplet-nuclei are most commonly between 1 and 2 μm in diameter. A review by Morawska (2006) showed that viruses range from 0.02 to 0.3 μm in diameter; for instance, an individual SARS coronavirus ranges from 0.075 to 0.16 μm and an influenza virus is of a similar size. However, aerosols with diameters less than 3 μm do not settle (Tellier, 2006). Simulations by Gao et al. (2007, 2009) also suggested that aerosols with diameters less than 2.5 μm disperse like gaseous pollutants.

Previous studies on interunit pollutant dispersion have focused on a flat-façade building with flush windows. However, the case of the nonflat façade cannot be

ignored, especially in the light of the latest development projects in Hong Kong which incorporate more and more envelope features. Since 2001, in new residential projects, it has been permitted to exclude envelope features such as balconies from calculations of the Gross Floor Area and/or Site Coverage (Joint Practice Note No. 1., 2001). Previous evaluationS (Ai et al., 2011a, b, c) of the performance of balconies show that their presence modifies the near-façade airflow pattern and creates a unique wind environment that is different from the conventional airflow around a flat-façade block (Lubcke et al., 2001; Sada and Sato, 2002; Burnett et al., 2005; Santos et al., 2009). Therefore, the dispersion of airborne pollutants around this micro-environment, created by the presence of balconies, deserves examination.

2.5 Turbulence and concentration modeling

2.5.1 RANS models

The CFD turbulence models most widely used for the prediction of the flow and concentration field in the built environment are the two-equation RANS models. Numerical solutions are obtained for an isothermal condition by resolving the governing equations describing the fluid field, namely the equations for the conservation of mass and momentum. For incompressible flow, the time-averaged governing equations can be written generally as:

$$\frac{\partial}{\partial t}(\varphi) + \nabla(U_T \varphi) = \nabla(\Gamma_\varphi \nabla \varphi) + S_\varphi \quad (2.2)$$

where φ represents the scalars: the velocity components, u , v , w , the turbulence kinetic energy k , its dissipation rate ε , and the concentration c_i ; term U_T is the mean velocity, Γ_φ the effective diffusion coefficient for each variable, and S_φ the source term of an equation.

The Renormalization group (RNG) $k-\varepsilon$ model presents a number of refinements over the standard $k-\varepsilon$ model (Fluent, 2010). Based on the scale elimination procedure in RNG theory, the turbulent viscosity is described by a more accurate differential equation, which provides an accurate relationship between the turbulent transport and Reynolds number. This feature theoretically allows the RNG model to perform better in predicting the low-Reynolds-number and near-wall flows.

Further, an additional strain-dependent term, R_ε , in the transport equation for ε makes the RNG model more sensitive in dealing with rapid strain and streamline curvature than the standard $k-\varepsilon$ model (Orszag et al., 1993; Yakhot and Orszag, 1986).

$$R_\varepsilon = \frac{C_\mu \rho \eta^3 (1 - \eta/\eta_0)}{1 + \xi \eta^3} \cdot \frac{\varepsilon^2}{k} \quad (2.3)$$

where C_μ , η_0 and ξ are model constants, and $\eta \equiv Sk/\varepsilon$ where S is the scale of strain rate. A more comprehensive description of the RNG model and its empirical numbers is available in (Fluent, 2010; Orszag et al., 1993; Yakhot and Orszag, 1986). As suggested by reference (Fluent, 2010), however, the effective use of these refinements is dependent on an appropriate treatment of the near-wall region, which will be explained later.

One explanation for the deficiencies of the prediction of the wall-bounded flow using most of $k-\varepsilon$ models is the over-prediction of the turbulence kinetic energy (k) in the windward stagnation region. Tsuchiya et al. (1997) have proposed a new correction to the $k-\varepsilon$ model to remove the over-production of k around the frontal corner, referred to here as the MMK $k-\varepsilon$ model. In the MMK $k-\varepsilon$ model, modifications are made to the turbulent viscosity ν_t in the calculation of the production of k as follows:

$$G_k = \nu_t S^2 \quad (2.4)$$

$$\nu_t = C_\mu^* k^2 / \varepsilon, \quad C_\mu^* = C_\mu \Omega / S, \quad (\Omega / S < 1) \quad (2.5)$$

$$\nu_t = C_\mu^* k^2 / \varepsilon, \quad C_\mu^* = C_\mu, \quad (\Omega / S \geq 1) \quad (2.6)$$

where C_μ^* is a function of Ω / S , rather than a constant as in the standard $k-\varepsilon$ model. Given its good performance in predicting k around a bluff body, the MMK $k-\varepsilon$ model has been widely used in the field of computational wind engineering (CWE). It is also used to provide a comparison with the RNG $k-\varepsilon$ model.

It is well known that $k-\varepsilon$ models are primarily valid for high Reynolds-number (Re) flows. In the low-Reynolds near-wall region, the most popular approach is to use semi-empirical wall functions, which bridge the viscosity sublayer between the

walls and the fully developed turbulent region. Since the walls are the main source of mean vorticity and turbulence (Fluent, 2010), an accurate reproduction of the near-wall flow may contribute to more realistic wall-bounded turbulent flows. As an alternative near-wall model to standard wall functions, the two-layer model (Fluent, 2010) can resolve the viscosity-affected sublayer directly, provided that the near-wall mesh is sufficiently fine. Based on a wall-distance-based turbulent Re_y , defined as:

$$Re_y = \frac{\rho y \sqrt{k}}{\mu} \quad (2.7)$$

where y is the wall-normal distance. The two-layer model divides the whole domain into a viscosity-affected region ($Re_y < 200$) and a fully-turbulent region ($Re_y > 200$). In the former, the one-equation model of Wolfshtein (1969) is used and in the latter, the RNG and MMK $k-\varepsilon$ models. In the one-equation model, the momentum and k equations are same with those in $k-\varepsilon$ models. However, the turbulent viscosity $\mu_{t,2layer}$ and the dissipation rate ε_{2layer} are computed from:

$$\mu_{t,2layer} = \rho C_\mu l_\mu \sqrt{k} \quad (2.8)$$

$$\varepsilon_{2layer} = \frac{k^{1.5}}{l_\varepsilon} \quad (2.9)$$

where the length scale l_μ and l_ε are determined by $l_\mu = y C_l^* (1 - e^{-Re_y/A_\mu})$ and $l_\varepsilon = y C_l^* (1 - e^{-Re_y/A_\varepsilon})$, respectively. The constants in these equations for the one-equation model can be taken from Chen and Patel (1988). The solution of the logarithmic layer requires that $C_l^* = \kappa C_\mu^{-3/4}$, where the widely used values of $\kappa = 0.4187$ and $C_\mu = 0.09$ give $C_l^* = 2.5$. $A_\varepsilon = 2C_l^* = 5.0$ and $A_\mu = 70$. A blending function is used to smoothly blend the turbulent variables between the two regions (Fluent, 2010). To ensure that the two-layer model and RNG model are used effectively, the mesh in the near-wall regions must be refined to ensure the y^+ for the first near-wall cells at most wall surfaces being in the order of 1.

2.5.2 LES model

2.5.2.1 LES equations

LES filters a flow in terms of the scale size of eddies and resolves the Navier-Stokes (N-S) equations directly for large eddies. If the filter width is equal to the grid size, the filtered incompressible N-S equations are:

$$\frac{\partial \widetilde{u}_i}{\partial x_i} = 0 \quad (2.10)$$

$$\frac{\partial(\rho \widetilde{u}_i)}{\partial t} + \frac{\partial(\rho \widetilde{u}_i \widetilde{u}_j)}{\partial x_j} = \frac{\partial \sigma_{ij}}{\partial x_j} - \frac{\partial \widetilde{p}}{\partial x_i} - \frac{\partial \tau_{ij}}{\partial x_j} \quad (2.11)$$

where the wavy lines indicate the filtered variables. In the filtration process, an additional term τ_{ij} appears in the momentum equation, which is the SGS stress term, defined as

$$\tau_{ij} \equiv \widetilde{\rho u_i u_j} - \rho \widetilde{u}_i \widetilde{u}_j \quad (2.12)$$

This term represents the effect of non-resolved small-scale eddies on resolved large scales.

2.5.2.2 Subgrid-scale models

As the τ_{ij} in the LES model is unknown, it requires modeling to close the governing equations. Boussinesq hypothesis (Hinze, 1975) is usually used to compute the τ_{ij} using the following expression:

$$3\tau_{ij} - \tau_{kk}\delta_{ij} = -6\mu_{SGS}\widetilde{S}_{ij} \quad (2.13)$$

where μ_{SGS} is the SGS turbulent viscosity. Here the isotropic part τ_{kk} is zero for an incompressible flow and the term \widetilde{S}_{ij} is the filtered strain rate tensor for the resolved scales, computed by:

$$\widetilde{S}_{ij} = \frac{1}{2} \left(\frac{\partial \widetilde{u}_i}{\partial x_j} + \frac{\partial \widetilde{u}_j}{\partial x_i} \right) \quad (2.14)$$

The SGS turbulent flux (q_{SGS}) of a scalar, φ , is modeled using a SGS turbulent Prandtl number by:

$$q_{SGS} = -\frac{\mu_{SGS}}{Sc_{SGS}} \frac{\partial \varphi}{\partial x_j} \quad (2.15)$$

where Sc_{SGS} is the turbulent Schmidt number for SGS motions. Many SGS models (Fluent, 2010) are proposed, which are differentiated based on the methods they adopt to determine μ_{SGS} . There are four popularly used SGS models, which are available in Ansys Fluent (2010): (a) the standard Smagorinsky-Lilly model, (b) the dynamic Smagorinsky-Lilly model, (c) the wall-adapting local eddy-viscosity model, and (d) the dynamic kinetic energy SGS model.

The most popularly used SGS model probably is the Standard Smagorinsky-Lilly model (SSL). In this model (Smagorinsky, 1963), the SGS turbulent viscosity is modeled by:

$$\mu_{SGS} = \rho L_s^2 |\tilde{S}| = \rho (C_s \Delta)^2 \sqrt{2 S_{ij} S_{ij}} \quad (2.16)$$

where Δ is the local grid scale and C_s is the Smagorinsky constant. Lilly (1992) originally derived a value of 0.17 for C_s , which has been found to be inappropriate for flows near walls. In previous studies, C_s has normally been set within the range of 0.1-0.2 (Lim et al., 2009; Chu and Chiang, 2013; Tominaga and Stathopoulos, 2010; Jiang and Chen, 2001; Caciolo et al., 2012; Bu and Kato, 2011; Wang and Chen, 2012). The constant C_s is recognized to be the most serious shortcoming of this model (Fluent, 2010).

To obviate specifying a constant C_s , Germano et al. (1991) and Lilly (1992) proposed a dynamic procedure to compute C_s at each time step based on information offered by the resolved scales of motion. This is the Dynamic Smagorinsky-Lilly model (DSL). The dynamic procedure uses a test filter on the motion equations, and its width, Δ_t , is twice the grid filter width, Δ . The coefficient C_s is computed by:

$$C_s = \sqrt{\frac{(L_{ij} - L_{kk} \delta_{ij} / 3)}{M_{ij} M_{ij}}} \quad (2.17)$$

and the computation methods of L_{ij} , L_{kk} , and M_{ij} can be found in references

(Germano et al., 1991; Lilly, 1992; Kim, 2004). The resultant C_s varies in time and space, but is limited to a range of 0-0.23 to avoid numerical instability (Fluent, 2010). However, it has been reported that this version of the SGS model shows some stability problems and has limitations in reproducing near-wall behavior (Iizuka and Kondo, 2004).

The Wall-Adapting Local Eddy-viscosity model (WALE) model, developed by Nicoud and Ducros (1999), predicts the SGS turbulent viscosity using the following expression:

$$\mu_{SGS} = \rho (C_w \Delta)^2 \frac{(S_{ij}^d S_{ij}^d)^{3/2}}{(\overline{S_{ij} S_{ij}})^{5/2} + (S_{ij}^d S_{ij}^d)^{5/4}} \quad (2.18)$$

where $S_{ij}^d = 0.5 \left(\left(\partial \overline{u_i} / \partial x_j \right)^2 + \left(\partial \overline{u_j} / \partial x_i \right)^2 \right) - 0.33 \delta_{ij} \left(\partial \overline{u_k} / \partial x_k \right)^2$. The WALE constant $C_w = 0.325$. The WALE is expected to reveal the correct wall asymptotic features for a wall-characterized flow. Unlike the Smagorinsky-Lilly model, which returns non-zero turbulent viscosity, the WALE model can correctly model the laminar zones by giving a zero turbulent viscosity to a laminar shear flow. Theoretically, the WALE is more accurate than the Smagorinsky-Lilly model. The WALE model has been used to simulate cavity flows (Barhaghi and Davidson, 2007; Ben-Cheikh et al., 2012). However, up to the present, it has rarely been applied in built environments.

Instead of assuming the local equilibrium, the Dynamic Kinetic Energy SGS model (DKE) predicts the SGS turbulence by taking into account the transport of the SGS turbulence kinetic energy (Kim, 2004; Kim and Menon, 1997). In this model, the SGS turbulent viscosity is determined by:

$$\mu_{SGS} = C_k \rho \Delta \sqrt{\frac{1}{2} (\overline{u_k^2} - \overline{u_k}^2)} \quad (2.19)$$

where the model constant C_k is determined dynamically.

2.5.2.3 Inflow fluctuating algorithms

Three types of inflow fluctuating algorithms are popularly used in previous

studies of flow and dispersion in built environments (e.g., Bu and Kato, 2011, Wang and Chen, 2012), which are also available in Ansys Fluent (2010). The first is the No Perturbations (NP). This option neglects the fluctuating components of the inflow, and thus only the mean velocity profile is imposed on the domain inlet. It is suitable for conditions where the turbulent characteristics of the approaching flow are not obvious. The second type is the Vortex Method (VM). This method introduces perturbations to the mean velocity profile by randomly generating and transporting a certain number of 2D vortices on the inlet (Mathey et al., 2006). The intensity and size of these vortices depend on the local turbulence kinetic energy and dissipation rate (k and ε) that are predefined at the inlet. The third type is the Spectral Synthesizer (SS) method. This method generates fluctuating velocity components by randomly synthesizing a divergence-free velocity field from the summation of Fourier harmonics (Kraichnan, 1970; Smirnov et al., 2001). The number of Fourier harmonics is a constant of 100 (Fluent, 2010). Obviously, for the latter two methods, although fluctuations are added to the mean specified velocity, realistic inlet turbulence conditions (k and ε profiles) are required.

2.5.2.4 Near-wall treatment

LES model automatically adopts different near-wall treatment depending on the near-wall grid density. When the mesh is fine enough to resolve the viscous sublayer ($y^+ \sim 1$, (Fluent, 2010)), the laminar stress-strain relationship is employed to obtain the wall shear stress. If the mesh is too coarse to resolve the laminar sublayer, it is assumed that the centroid of the wall-adjacent cells falls within the logarithmic region of the boundary layer, and the law-of-the-wall is employed. If the mesh is such that the first near-wall point is within the buffer region, the two above laws are blended.

2.5.3 Concentration model

In the simulation of dispersion using RANS models, a concentration equation for the tracer gas (see Equation (2.2)) is solved. Here the turbulent Schmidt number (Sc_t) has a significant impact on the calculation of concentration equation (Tominaga and

Stathopoulos, 2007). This number is defined as the ratio of turbulent momentum diffusivity to concentration diffusivity. It has been observed that the Sc_t strongly depends on dispersion problems and flow structures, which is usually imposed as a constant ranging from 0.2-1.3 (Blocken et al., 2008; Chavez et al., 2011; Hang and Li, 2011; Riddle et al., 2004; Tominaga and Stathopoulos, 2007).

For LES simulations, the filtered concentration equation for the tracer gas is written as:

$$\frac{\partial(\tilde{c}_i)}{\partial t} + \frac{\partial(\tilde{c}_i \tilde{u}_j)}{\partial x_j} = \frac{\partial}{\partial x_j} \left[\left(\frac{\mu}{Sc} + \frac{\mu_{SGS}}{Sc_{SGS}} \right) \cdot \frac{\partial \tilde{c}_i}{\partial x_j} \right] + \tilde{S}_i \quad (2.20)$$

where c_i represents the concentration of tracer gas, μ is the dynamic viscosity coefficient, Sc is the Schmidt number (equal to 1.0), Sc_{SGS} is the turbulent Schmidt number for SGS motions, and S_i is the generation rate of source. The turbulent Schmidt number (Sc_t) for the large eddies is not needed. However, for the SGS motion, the (Sc_{SGS}) number still needs to be decided. Obviously, the scale resolvable turbulent flux is relatively important and the contribution of SGS turbulent flux to total turbulent flux is small.

2.6 Determination of single-sided ventilation rate

The integration of opening velocities is a simple method of calculating the single-sided ventilation rate. Based on the nature of the flow field where the integration is conducted, there are two types of integration method (Jiang and Chen, 2001). One (Q_{mean}) is used to integrate velocities $U_{m,n}$ extracted from a time-averaged flow field generated by a steady simulation.

$$Q_{mean} = \frac{1}{2} \sum_{m=1}^M \sum_{n=1}^N |U_{m,n}| \Delta y_m \Delta z_n \quad (2.21)$$

The other ($Q_{ins,T}$) is used to average the sum of the instantaneous ventilation rates over a time period of $t_T = \sum_{i=1}^b \Delta t^i$; an instantaneous ventilation rate is obtained by integrating the velocities from an instantaneous flow field generated by a transient simulation.

$$Q_{ins,T} = \frac{\frac{1}{2} \sum_{i=1}^b \left(\sum_{m=1}^M \sum_{n=1}^N |U_{m,n}| \Delta y_m \Delta z_n \right) \Delta t^i}{\sum_{i=1}^b \Delta t^i} \quad (2.22)$$

In addition to the integration method, the tracer gas decay method is commonly used to calculate the single-sided ventilation rate based on a transient simulation. Assuming the air and the tracer gas are both incompressible and there is neither a background concentration nor an indoor emission source, the ventilation rate can be determined by the following equation (ISO 12569, 2012; Laussmann and Helm, 2011):

$$Q_{tracer} = \frac{-\ln(C_i/C_{t_0}) \cdot V}{t_i - t_0} \quad (2.23)$$

According to the relationship $ACH = Q/V$, the ventilation rates can be converted to air change per hour (ACH).

2.7 Summary and research gaps

This chapter reviews previous studies that are relevant to the present research topic of single-sided natural ventilation and interunit dispersion. These reviews lead to the following research gaps:

(a) Previous empirical models of predicting single-sided natural ventilation rate have been established based on very simple building models, such as single-room or a specific room of a certain building. It is necessary to verify the reliability of these empirical models used for multistory buildings using on-site measurements. Previous empirical models have ignored the difference in envelope airflow pattern between rooms in a multistory building and a single-room building. This difference, which could lead to completely different ventilation characteristics in these two types of buildings, should be quantitatively examined.

(b) Few CFD practitioners are aware of the importance of establishing a homogenous ABL prior to numerical investigations. Few adopt a correct K_s on the domain ground and a correct z_0 in the inlet profiles, and most use standard wall functions as near-wall treatment approach without taking into account the low-Reynolds-number effect of the viscous sublayer. The effect of the

inhomogeneous ABL and the near-wall treatment on the prediction of flow and dispersion, especially on a quantitative level, remain unclear.

(c) For the RANS modeling of urban wind flow, a large number of parametric studies have conducted sensitivity analyses of influencing factors, and some guidelines have been developed based on their findings. For LES modeling, parametric studies were only conducted for atmospheric flow based on a few influencing factors. Similar studies should be extended to the dispersion problem and should include more influencing factors.

(d) Previous studies and experiences of wind tunnel experiments and CFD simulations lead to a hypothesis that reduced-scale models for CFD simulations of wind flow and related processes can save numerical resources. Qualitative and quantitative verification of this hypothesis using theoretical analysis and numerical simulation is useful for future CFD simulations of wind flow and related processes, particularly over large areas.

(e) Given the complexity of single-sided ventilation, any inappropriate setting of computational parameters may result in incorrect solutions. However, there are no specific guidelines for CFD simulation of single-sided ventilation. In order to provide guidance for the improved CFD modeling of single-sided ventilation, a comprehensive sensitivity test of the most important computational parameters is required. In addition, the predictive method used to compute the single-sided ventilation rate is another essential element in a successful prediction. Examination of the integration and the tracer gas decay methods based on both LES and RANS turbulence models under various wind directions is required.

(f) Most previous studies considered only the time-averaged ventilation rate, while less attention has been paid to the fluctuating ventilation rate. In fact, the description of the ventilation rate using a constant value is insufficient if the root mean square of the fluctuations is too large. In addition, the external airflow patterns could differ widely under different wind directions. Therefore, it is necessary to investigate the fluctuating characteristics of airflow through a single opening under various wind directions using LES model.

(g) It has become evident that the buoyancy-dominated inter-unit pollutant transport, which has been thoroughly studied in previous work, is a unidirectional

dispersion and only significant in conditions of relatively low-speed wind. In addition, the analysis of sole envelope concentration data measured in wind tunnel cannot provide an accurate description of interunit dispersion, as the presence of real rooms and openings could significantly modify the envelope flow pattern and in turn the concentration distribution. Therefore, a systematic investigation of the interunit dispersion in multistory buildings with real rooms and openings is required. In addition, previous studies using RANS models only provide mean dispersion routes and reentry ratios. Considering the highly fluctuating characteristics of a coupled indoor and outdoor flow, the mean results may not be sufficient to describe an interunit dispersion process. Furthermore, time scales of an interunit dispersion, which cannot be obtained from a steady simulation, are important for an infectious risk assessment. Therefore, a transient investigation of interunit dispersion using an advanced numerical model, namely LES, should be necessary.

Chapter 3

Evaluation of predictive methods of single-sided ventilation in multistory buildings

3.1 Introduction

This chapter presents the evaluation of predictive methods of single-sided natural ventilation in multistory buildings. It also serves to identify an appropriate predictive method for this study. On-site measurements of single-sided natural ventilation rate in multistory buildings are described first. The measured results are then used to validate the previous empirical models. Next, validations of RANS simulation of flow and dispersion in built environments are presented, which evaluate preliminarily the appropriateness of CFD simulation. The validated RANS model is used to examine the difference in ventilation characteristics between rooms in single-story and multistory buildings. This provides a further explanation on the unreliability of previous empirical models in multistory buildings.

3.2 On-site measurements

3.2.1 Description of measurements

3.2.1.1 Measurement sites

The on-site measurements were conducted in Hong Kong in early May 2013, when the outdoor temperature and relative humidity were suitable for natural ventilation. Four single-sided, naturally ventilated, residential rooms located in urban areas of Kowloon and Hong Kong Island were selected to study the ventilation performance. These densely populated districts are the most prosperous areas in Hong Kong. Detailed information on the four rooms is given in Table 3.1. In the vertical direction, two rooms are located on a floor below the stagnation region and two above it. The stagnation region represents an area of the building where the approaching wind stagnates and splits such that wind flows downwards below it and upwards above it (ASHRAE Handbook, 2011; Liu, 1991; Martinuzzi and Tropea, 1993). The room dimensions are meant to give a general view of the room size, but are not the dimensions used to calculate the room volumes, due to the irregular

Table 3.1 Details of the selected residential rooms.

Case	Building Location	Surrounding feature	Room location	Room dimensions	Opening orientation	Opening dimensions
Case 1	Ho Man Tin	Light traffic	12 th /27	6.54(L)×3.15(W)×2.94(H) m ³	West 15° to north	a) 1.15(W)×2.3(H) m ² b) 0.8(W)×1.44(H) m ²
Case 2	Mid-level	Light traffic	10 th /22	9.75(L)×6.38(W)×2.65(H) m ³	North 25° to east	a) 1.5(W)×2.3(H) m ² b) 1.0(W)×1.44(H) m ²
Case 3	Hung Hom	Heavy traffic	21 st /22	4.12(L)×3.14(W)×2.94(H) m ³	South 30° to west	a) 0.5(W)×0.8(H) m ²
Case 4	Hung Hom	Heavy traffic	20 th /21	4.5(L)×2.8(W)×2.94(H) m ³	West 35° to south	a) 0.4(W)×0.7(H) m ²

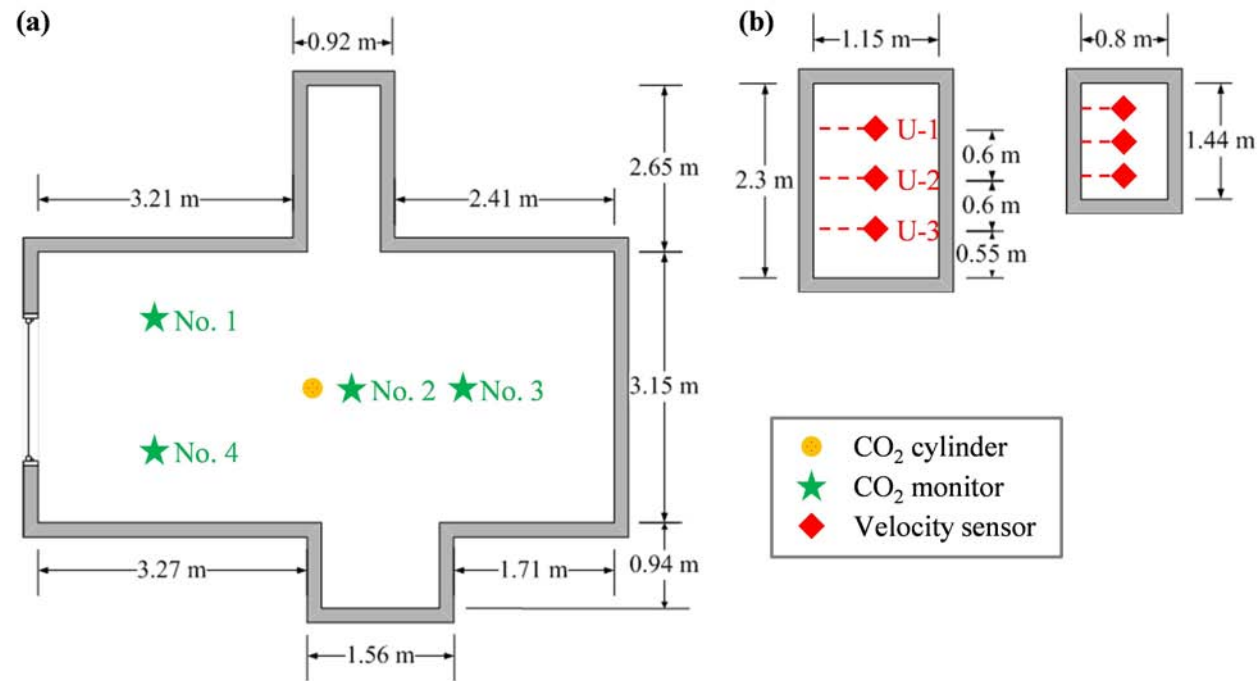


Figure 3.1 Residential room in Ho Man Tin and equipment locations: (a) room; (b) opening.

Table 3.2 Summary of the parameters measured and equipment used.

Parameters	Equipment	Accuracy and range
ACH, T, and RH	Tracer gas CO ₂ Telaire 7001 CO ₂ monitor (Telaire, Goleta, CA, USA)	CO ₂ channel: ± 50 ppm or $\pm 5\%$ of reading in a range of 0 to 10,000 ppm Temperature channel: $\pm 1^\circ\text{C}$ in a range of 0 to 50°C
Wind speed	Model 8475 air velocity transducer (TSI Inc., Shoreview, MN, USA)	$\pm 3.0\%$ of reading in a range of 0.05 to 2.5 m/s

layout of the rooms and the existence of internal objects. Figure 3.1 (a) shows the layout of the room located in Ho Man Tin, where the doors are not presented. ACH was only measured in the rooms located in Ho Man Tin and Mid-level, respectively. For these two rooms, two different opening configurations were compared as shown in Table 3.1 and Figure 3.1(b). The larger one is a floor-extended opening, while the smaller one is a window-like opening with a windowsill height of 0.86 m. This comparison was intended to investigate the effect of the envelope feature on ventilation performance.

3.2.1.2 Data collection

The monitoring parameters, equipment, and their accuracies and ranges are listed in Table 3.2. For the CO₂ monitor and air velocity transducer, additional HOBO data loggers (Onset Computer Corporation, Bourne, MA, USA) were used to record the data. As shown in Figure 3.1 (b), the wind speed was measured at three locations along the vertical centreline of the opening, and analysed for its relationship with the ACH. CO₂ was used as a tracer gas to determine the ACH of the rooms. With the opening closed, the CO₂ was released into a room until the indoor CO₂ concentration was elevated to the level of 3,000~5,000 ppm and mixed uniformly. The window was then opened slowly to allow the concentration to decay freely. During this process, four sets of CO₂ monitors dispersed around the rooms (see Figure 3.1(a)), were used to record the concentration decay against time. The well-known tracer gas concentration decay method (Sherman, 1990; Sherman and Modera 1986) was then used to derive the room ACH, which was obtained by averaging the four ACHs determined by the records of the four CO₂ monitors. In addition, the temperature and relative humidity in the room were simultaneously recorded by the HOBO data logger within the CO₂ monitors. The outdoor climatic data (namely the temperature, humidity, and wind speed and direction) recorded by the nearby observatory station during the measurement periods were extracted for reference and comparison purposes. The data collection method described here for Case 1 was applicable to the other cases.

3.2.2 Results and analyses

3.2.2.1 Environmental background of measurements

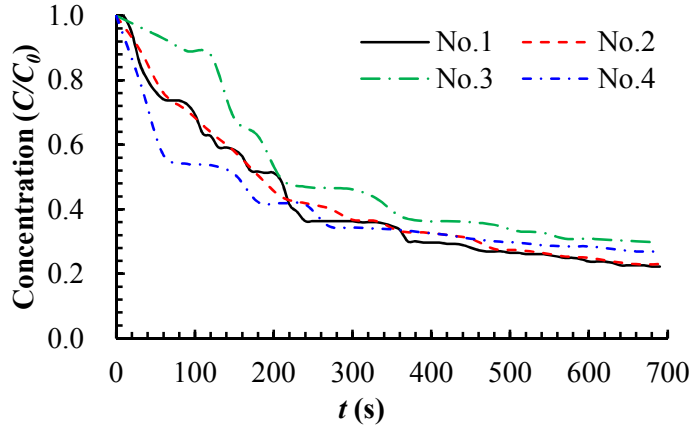
Table 3.3 summarizes the indoor and outdoor conditions during the measurement period, where the detailed fluctuations of the environmental parameters are also presented. It can be seen that the indoor and outdoor temperature differences were small enough to neglect the buoyancy effect (specifically, the value of Ar is negligible, see Equation (3.1)), and the air exchange at the openings was consequently dominated by the wind effect.

$$Ar = \Delta T g H_o / T_{ave} U_T^2 \quad (3.1)$$

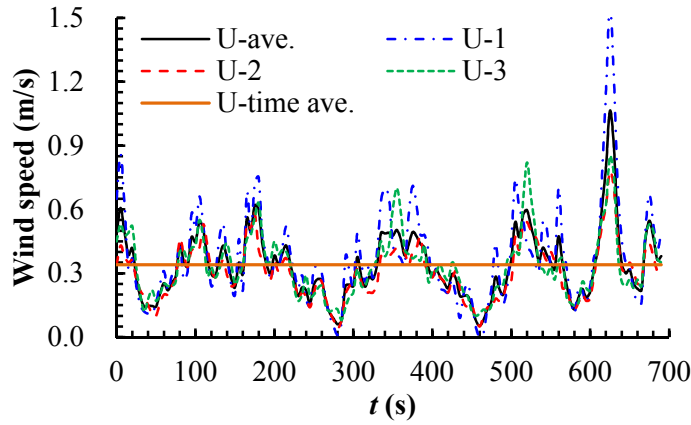
where Ar is the Archimedes number indicating the relative magnitude of buoyancy effect and wind effect, ΔT the indoor and outdoor temperature difference, g the gravitational acceleration, H_o the opening height, T_{ave} the average absolute temperature of the indoor and outdoor airflows, and U_T the mean wind speed at the building height in the free stream. The indoor and outdoor humidity differences indicate that the building envelope has performed well in the moisture control of the indoor environment, except for the last case (Case 4) where the building was close to the Victoria Harbour. The prevailing ambient wind direction was mostly easterly, implying Hong Kong enjoyed a clean marine airflow from the South China Sea during the period of measurement with no incursion of emissions from Mainland China and other neighbouring countries. Although the mean surface wind speed was between 3.0 and 3.5 m/s, the wind speed at the opening was only 0.25 and 0.11 m/s, respectively, when the opening was located in the leeward and lateral sides; see the last column in Table 3.3, where the term “incident” denotes the angle between the outdoor wind direction and the opening normal (i.e. the normal to the surface of the opening), such as 0° for normal incident from the windward side and 90° for parallel incident from the lateral side. This shows that the available wind speed at the opening was extremely small compared to that recorded at the nearby observatory station, which implies that the efficiency of natural ventilation was significantly influenced by urban construction. The difference in wind speed between the openings in Cases 1 and 2 demonstrates the significant influence of the incident wind direction on the available opening wind speed. Rooms such as that of Case 2 with the opening normal almost perpendicular to the incident wind direction should perform worst for natural ventilation.

Table 3.3 Indoor and outdoor conditions during the measurement period; the numbers in the brackets are standard deviations.

Case	T (°C)		RH (%)		Wind speed (m/s)		Wind direction	
	Indoor	Outdoor	Indoor	Outdoor	Opening	Outdoor	Outdoor	Incident
Case 1	22.4±1.2 (1.0)	21.6±1.4 (0.8)	53.0±5.8 (4.2)	63.5±6.7 (5.1)	0.25±0.21 (0.18)	3.02±1.67 (1.65)	East	165°±15 ° (12 °)
Case 2	24.2±2.1 (2.7)	24.7±3.2 (3.0)	57.5±4.2 (3.5)	80.5±7.3 (6.4)	0.11±0.9 (0.7)	3.35±1.43 (1.28)	East 15° to south	80°±13 ° (11 °)
Case 3	23.4±2.4 (1.9)	22.9±3.5 (3.2)	60.3±6.4 (5.7)	90.1±4.2 (3.0)	N.A.	3.83±2.2 (1.8)	East 30 ° to south	90 °±18 ° (15 °)
Case 4	26.5±1.4 (1.1)	27.5±2.5 (2.1)	81.5±7.2 (5.0)	83.3±7.8 (6.3)	N.A.	1.56±1.2 (1.0)	East 15 ° to south	130°±19 ° (14 °)



(a) Tracer gas concentration decay



(b) Wind speed on the opening

Figure 3.2 Tracer gas concentration decay against time and wind speed recorded on the opening during the same period, for the larger floor-extended opening of Case 1.

3.2.2.2 Ventilation performance

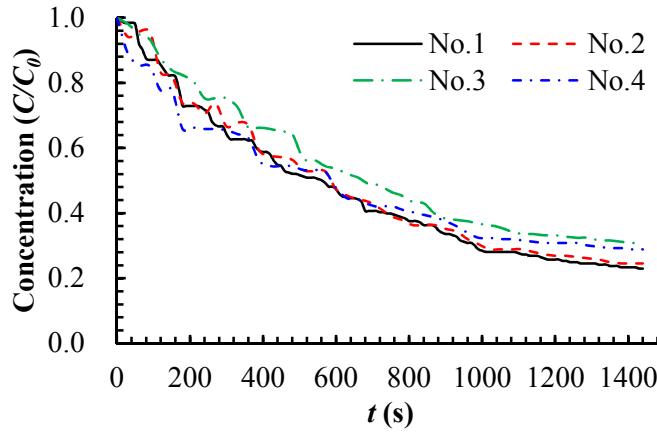
As described, the tracer gas decay technique was used to determine the ACH. In this section, the detailed decay curves and corresponding wind speeds at the openings are presented only for Case 1, while the mean ACH value and wind speed for Case 2 are used for discussion. Figure 3.2 presents the tracer gas concentration decay along time and the wind speeds recorded on the opening during the same period for Case 1, with a larger, floor-extended opening. The two-point method (Sherman, 1990) was used to calculate the ACH value, which used a number (at least five) of concentration-time pairs evenly distributed over the entire measurement period to reduce the statistical error. To correctly use the two-point method, the background

CO₂ concentration in the ambient air must be excluded from the originally measured profiles. The ACHs were, then, determined by the following equation:

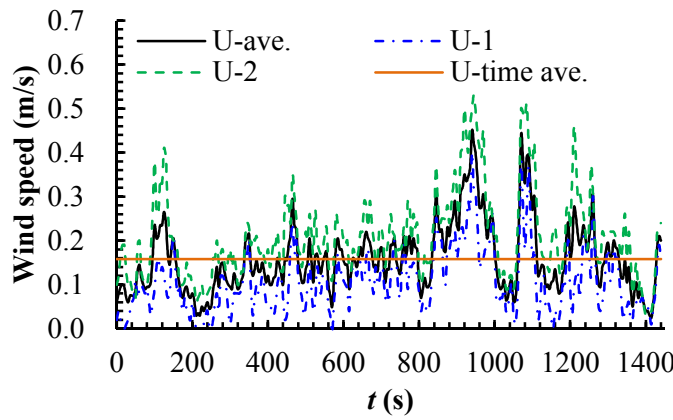
$$\ln(C_{t_{i+1}} - C_a) = \ln(C_{t_i} - C_a) - \text{ACH} \cdot (t_{i+1} - t_i) \quad (3.2)$$

where the $C_{t_{i+1}}$ and C_{t_i} are the measured CO₂ concentrations at the times of t_{i+1} and t_i , respectively; C_a is the background CO₂ concentration in the ambient air (it was around 450 ppm in the measurements). Then, 4 ACH values were obtained based on the records of the 4 CO₂ sensors, and the final average ACH value was 16.1 h⁻¹. This was sufficiently large (ASHRAE Standard 62-2010, 2010) to eliminate the indoor pollutants and overheated air, when the outdoor air quality and climate were at an acceptable level. During this decay process, the time-averaged wind speed on the opening, based on the records of the three velocity sensors, was 0.34 m/s, see Figure 3.2 (b). In Figure 3.2 (b), the legend “U-ave” means the average speed of the records of the three sensors at each time and “U-time ave” the average speed during a period.

Figure 3.3 presents the results of Case 1 with a smaller, window-like opening. Compared to the previous case, this would experience a smaller opening wind speed (0.16 m/s in average, see Figure 3.3 (b)), resulting in a much slower, but more uniform, decay in concentration (see Figure 3.3 (a)). The ACH value derived from these decay curves was 5.5 h⁻¹, which was also sufficient to maintain a comfortable and healthy indoor environment (ASHRAE Standard 62-2010, 2010), if the ambient air quality was acceptable. Comparison of these two scenarios, with different opening configurations, has indicated that having a smaller window-like opening would lower the available wind speed at that location. This was supported by the measurements found in Case 2, where the mean wind speed at the opening was the same between the two scenarios even if the outdoor wind speed was higher during the measurement period of the smaller-opening scenario. This was probably because the pulsating flow and eddy penetration (Haghighat et al., 2000) which had contributed to a larger percentage of the ventilation rate than the wind gust when the opening was smaller. For Case 2, the opening speed of 0.11 m/s had resulted in 4.1 and 1.5 ACHs for the two scenarios, respectively. These results also show that the floor-extended larger opening could produce a much larger ACH than that of a window-like smaller opening, although the percentage increase in ACH was not



(a) Tracer gas concentration decay



(b) Wind speed on the opening

Figure 3.3 Tracer gas concentration decay against time and wind speed recorded on the opening during the same period, for the smaller window-like opening.

necessarily proportional to that in the opening area. This disproportionate change can again be attributed to the fact that the wind-induced single-sided ventilation rate was derived not only from the wind gust, but also the pulsating flow and eddy penetration (Haghighat et al., 2000). The latter two were related to, and determined by, the turbulence and power spectrum characteristics of the approaching wind.

As analyzed above, Case 2, in terms of the incident wind direction, should be the worst case in terms of obtaining air replacement from the outdoor environment. However, it can be seen that this case, even with a smaller window-like opening, can have 1.5 ACH, which is higher than the minimum value (0.35 ACH) recommended by ASHRAE 62-2010 (2010) for indoor pollutants elimination. This suggests that the

single-sided natural ventilation system can be confidently applied in urban areas if the prevailing surface wind speed is acceptable, such as the 3.0~4.0 m/s in Hong Kong in this study.

3.3 Validation of past empirical models

The past empirical models (see Table 2.1) are used to predict the ventilation rate of the measured cases for validation purpose. The prediction of ventilation rates of Case 1 (see Table 3.3) using Warren' model (1977) is described in detail. For other empirical models, only predicted ventilation rates are presented.

The Warren's model is given in Equations (3.3)-(3.5), as:

$$Q_s = \frac{1}{3} A_{eff} C_d \sqrt{\Delta T H_o g / T_{ave}} \quad (3.3)$$

$$Q_w = 0.025 A_{eff} U_{ref} \quad (3.4)$$

$$Q_T = \max(Q_s; Q_w) \quad (3.5)$$

where Q_w is the wind-driven ventilation rate, Q_s the buoyancy-driven ventilation rate, A_{eff} the effective opening area, U_{ref} the reference velocity at the height of the building, and C_d the discharge coefficient. The total ventilation rate due to the combined effect of wind and buoyancy is determined by $Q_T = \max(Q_s; Q_w)$.

As discussed in the previous Section 3.2, the negligible temperature difference means the buoyancy-driven ventilation rate can be neglected, so $Q_T = Q_w$. To calculate Q_w using Equation (3.4), U_{ref} must be correctly determined. According to the definition given by Warren (1977), U_{ref} is the reference velocity at the height of the building. However, for multistory buildings, U_{ref} cannot be the velocity at the building height, as that would give the same ventilation rate for all rooms with the same opening area in the building regardless of their location. In this study, the equivalent wind speed at the height of a room was calculated based on the wind speed provided by the nearby observatory station and a power-law velocity profile (see Equation (3.6)), and then used as U_{ref} to calculate the ventilation rate:

$$U_{ref} = \alpha U_{obs} \left(\frac{z_{ref}}{z_{obs}} \right)^\beta \quad (3.6)$$

where α and β are the coefficients indicating the terrain characteristics, which are 0.67 and 0.25, respectively, for an urban area (Sherman and Modera, 1986; Wang and Chen, 2012); U_{obs} the wind speed recorded at the height of z_{obs} by the nearby observatory station; and z_{ref} the height of the room location.

Table 3.4 Comparison of the measured and predicted ventilation rate for Case 1; the numbers in the brackets are standard deviations.

Opening area (m ²)	Measured Q_T (m ³ /s)	U_{obs} (m/s)	z_{obs} (m)	z_{ref} (m)	U_{ref} (m/s)	Predicted Q_T (m ³ /s)	Q_T -dev. (%)
2.645	0.296±0.24 (0.21)	4.55±1.78 (1.24)	90	74	2.91	0.192	-35.0
1.152	0.101±0.04 (0.03)	3.38±1.63 (1.31)	90	74	2.15	0.062	-38.7

The measured and predicted ventilation rates for Case 1 are presented in Table 3.4, where the term “ Q_T -dev.” means the percentage deviation of the predicted Q_T from the measured Q_T . Using similar methods, ventilation rates predicted with other empirical models are also calculated, which are summarized in Table 3.5. It can be seen that large discrepancies existed between the measured and the predicted results, demonstrating that these empirical models are not reliable to use in multistory buildings. These large discrepancies can be attributed to at least five reasons.

Table 3.5 Measured ventilation rates (m³/s) and those predicted by empirical models; the percentiles in the brackets are the deviations of predicted values from measured ones.

Opening area (m ²)	Warren (1977)	Phaff and De Gids (1982)	Larsen and Heiselberg (2008)	Wang and Chen (2012)	Caciolo et al. (2013)
2.645	0.192 (-35.0%)	0.171 (-42.2%)	0.065 (-78.0%)	0.661 (62.3%)	0.120 (-59.5%)
1.152	0.062 (-38.7%)	0.068 (-32.7%)	0.044 (-56.4%)	0.127 (25.7%)	0.035 (-65.3%)

First, the empirical models were established and validated on the basis of a single-room building (Larsen and Heiselberg, 2008; Wang and Chen, 2012) or a specific room in a two- or three-story building (Warren, 1977; Phaff and De Gids, 1982; Caciolo et al., 2013). Thus, they do not contain a parameter to account for the effect of room location in a multistory building. Particularly, the near-wall airflow pattern around buildings with different height was significantly different (Liu, 1991), even if the presence of envelope features was not considered. For example, in the windward side, the upward flow dominates the 8th floor of a 9-story building, while the same floor of an 18-story building is completely dominated by the downward flow. Therefore, different rooms in a building could have very different ventilation characteristics. This issue will be discussed in detail in Section 3.5.

Second, some models (Warren, 1977; Phaff and De Gids, 1982) do not include the effect of wind direction, but it is well-established that rooms with different opening orientations could experience different envelope flow regimes and have different air exchange rates at the openings (Ai et al., 2011c; Jiang et al., 2003). Note that the room studied in Case 1 was located on the leeward side of the building. Caciolo et al. (2011) also show that Warren's model is inaccurate when predicting leeward ventilation.

Third, most of these models assume that the incoming (or outgoing) flow covers a half opening area (Warren, 1977; Phaff and De Gids, 1982; Larsen and Heiselberg, 2008; Caciolo et al., 2013), which is not necessarily the case as it is not a requirement of mass conservation. Wang and Chen (2012) assume a neutral plane on the opening with uniform height in the horizontal direction. In fact, the airflow could enter into and exhaust from a room from any part of the opening, see Section 5.3.5.

Fourth, all of the models assume that the ventilation rate is in proportion to the wind speed. However, a higher approaching wind speed can sometimes lower the ventilation rate by forming an air curtain blockage near the opening (Gao et al., 2008).

Finally, the models cannot explain the impacts of the forms, surroundings, and interior spaces of buildings on the ventilation performance of a building.

3.4 Preliminary validation of CFD simulation

3.4.1 Airflow involving single-sided natural ventilations

3.4.1.1 Experimental model and numerical method

Airflow inside and around a bluff body was experimentally investigated in a wind tunnel by Jiang et al. (2003). The dimensions of the model are 0.25 m \times 0.25 m \times 0.25 m and the thickness of walls is 0.006 m. An opening of 0.084 m (Y) \times 0.125 m (Z) is fixed on the windward and the leeward wall (Figure 3.4), resulting in wind-driven single-sided windward and leeward ventilation, respectively. The mean air velocities along ten vertical lines were measured using a laser Doppler anemometer, and six of them selected for comparison with the present simulation.

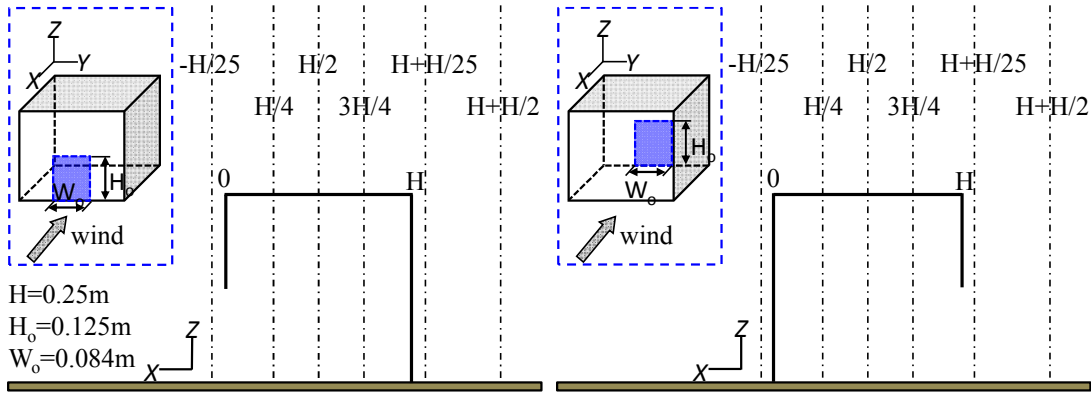


Figure 3.4 The building models with one opening on the windward and the leeward wall, respectively, and vertical lines where air velocity is compared.

The cube is placed in a computational domain with a downstream length of $22H$, an upstream of $11H$, a lateral length of $9H$, and a height of $5H$. The inlet velocity profile in the X direction follows a logarithmic law, $U_z = (U/\kappa)\ln(Z/H)$, and the velocity components in the Y and Z directions are zero. The turbulence on the inlet boundary is specified by the turbulence kinetic energy and its dissipation rate. The turbulence kinetic energy profile (k) is calculated by $k = 1.5(U_{ref}I)^2$ with a turbulent intensity (I) of 10% given the low speeds considered in this study. The turbulence dissipation rate profile (ε) is calculated by $\varepsilon = C_\mu^{0.75} k^{1.5}/l$, where the turbulence length scale l is the characteristic length of the model; that is, 0.25 m. It is assumed that the flow is fully developed at the domain outlet, with zero normal

gradients and zero background pressure, and this condition is referred to pressure outlet later. Non-slip boundary conditions are applied for wall shear stress on domain ground and cube surfaces, while slip conditions (without wall shear stress) on domain top and sides. The structured style hexahedral grid is used to construct the whole computational domain. The minimum grid width is $0.0028H$, which is much smaller than in previous studies of airflow and dispersion around bluff bodies using LES (Tominaga and Stathopoulos, 2010; Tominaga et al., 2008a). Three different mesh systems (in terms of number of meshes) of 2.0 , 2.5 , and 3.0×10^6 , are created and compared. The velocities at the vertical line of $X=H + H/25$ produced using the three types of mesh systems are compared, see Figure 3.5. It is found that the velocity profile produced using the medium mesh has average deviations of 11.8% and 1.9% from the coarser and finer ones, respectively. Thus, the mesh system with around 2.5×10^6 cells is selected eventually, taking a compromise between accuracy and numerical cost.

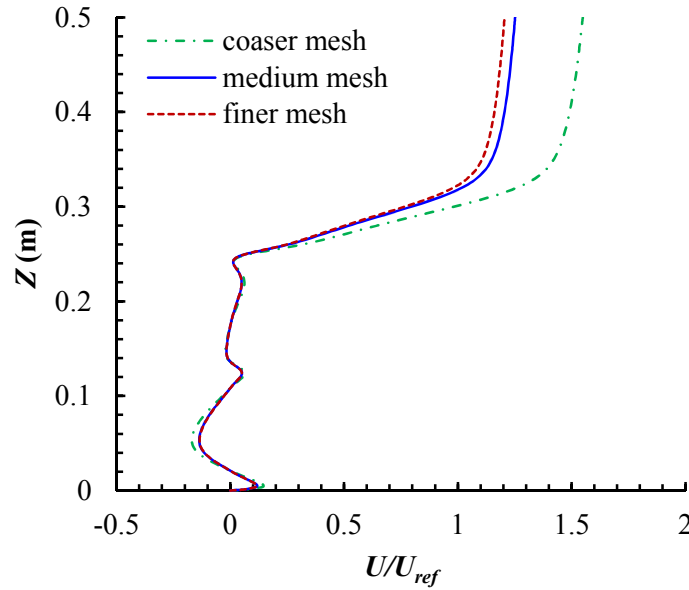


Figure 3.5 Comparison of mean velocity profiles produced using three types of mesh systems at the vertical line of $X=H + H/25$.

For the windward ventilation, three combinations, namely the RNG $k - \varepsilon$ model with standard wall functions, the RNG $k - \varepsilon$ model with the two-layer model, and the MMK $k - \varepsilon$ model with two-layer model, are used and compared. For the

leeward ventilation, only the combination of RNG $k - \varepsilon$ model with the two-layer model is used. With the finite volume method, the governing equations of these numerical models are discretized to algebraic equations on a staggered grid system. The discretization schemes used for the convection and diffusion terms are the second-order upwind scheme and second-order central difference, respectively. Finally, the SIMPLEC algorithm is used to couple pressure and velocity. Simulations are terminated when all residuals are less than 1.0×10^{-5} and the solutions, such as the air velocity at specific points, are stable for dozens of iterations.

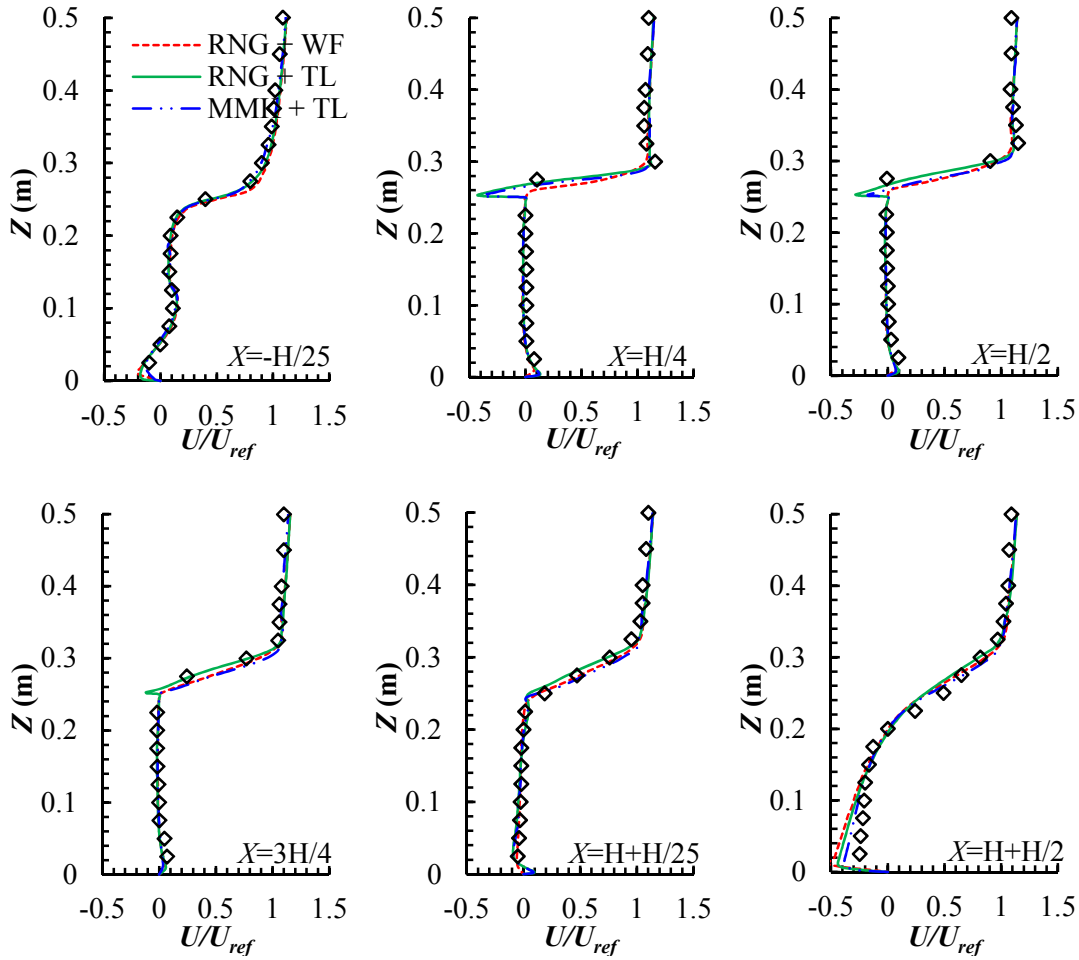


Figure 3.6 Mean velocity distribution at the six vertical lines: RNG + WF indicates RNG $k-\varepsilon$ plus standard wall functions; RNG + TL indicates RNG $k-\varepsilon$ plus two-layer model; MMK + TL indicates MMK $k-\varepsilon$ plus two-layer model.

3.4.1.2 Results and analyses

Figure 3.6 presents the mean air velocity distribution along the six vertical lines under windward ventilation. It can be seen that the RNG $k - \varepsilon$ model with standard wall functions is accurate enough to predict the airflow inside and around a bluff body, except for the reverse flow above the cubic roof and the downstream wake flow (the lower part of line H+H/2). Some researchers attribute these inaccuracies to the reverse flow on the cubic roof being counteracted by the over-predicted large eddy coming from the frontal area (Murakami, 1998) and the vortex-shedding effects in the wake being neglected by $k - \varepsilon$ models (Gao et al., 2008). In this study, with the viscosity-affected near-wall region being completely resolved all the way to the viscous sublayer by the two-layer model, the predictions of the wall-bounded turbulent flows by the RNG $k - \varepsilon$ model are substantially improved, particularly in the cubic roof. The reverse flow above the cube, which disappears in the prediction by standard wall functions, is well reproduced by the two-layer near-wall model. In addition, the two-layer model partially reproduces the vortex-shedding effects in the cubic wake and in turn predicts a more realistic separation region behind the cube (the lower part of line H+H/2) than the standard wall functions. However, owing to the inherent shortcomings of isotropic steady-state $k - \varepsilon$ models, the predicted separation region is still larger than the measured one.

In the present simulation, compared with the RNG $k - \varepsilon$ model, the MMK $k - \varepsilon$ model does demonstrate a slight advantage in the prediction of the cubic wake, but is slightly less accurate in its roof. This implies that the main reason for the disappearance of the reverse flow on the roof of a bluff body is the underperformance of the wall functions instead of the over-prediction of k in the windward impingement area by $k - \varepsilon$ models, given that the latter can be effectively removed by using the MMK $k - \varepsilon$ model (Murakami, 1998). Despite the deficiencies of the RNG and MMK $k - \varepsilon$ models in predicting the vortex-shedding effects in the wake of a bluff body, the simulation of the flow field inside the building (lines H/4, H/2, 3H/4) and in the areas close to the windward and leeward façades (lines -H/25 and H+H/25) agrees well with the measurements. This is sufficient to justify the application of both the RNG and the MMK $k - \varepsilon$ models, combined with the two-layer near-wall model, to establish the flow field involving single-sided natural ventilation. The accuracy of the predicted results under leeward ventilation is very close to these under windward ventilation, which is thus not presented here.

3.4.2 Pressure distribution on the lateral walls

Besides windward and leeward ventilation, lateral ventilation is also involved when the oblique or parallel incident wind directions are considered. However, because experimental data for single-sided ventilation with openings on the lateral walls are rarely available, the measured pressure values on the walls of a bluff body are used to evaluate the numerical models. Richards and Hoxey (2012) have measured the pressures on the vertical and horizontal centerlines of the Silsoe 6 m cube in the atmospheric boundary layer. Figure 3.7 shows the cube model, pressure tap locations, and the reference position.

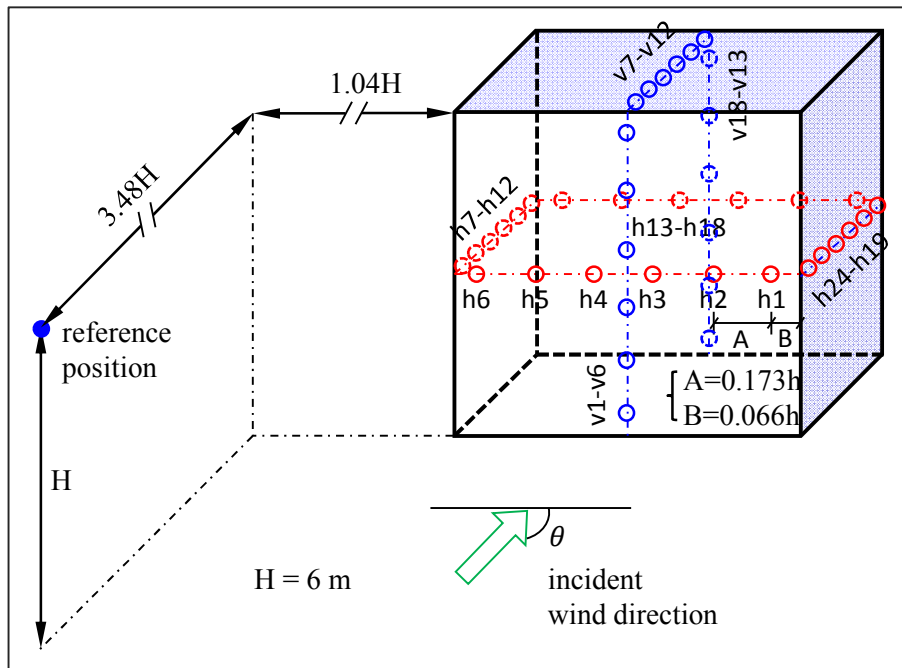


Figure 3.7 The 6 m building model, locations of pressure tap, and upstream reference position.

This cube is simulated in 1:30 reduced-scale model. According to the guidelines by Snyder (1981), the Reynolds independence of the reduced-scale model is achieved. The combination of RNG $k - \varepsilon$ model with the two-layer model is used. Other numerical treatments, including domain dimensions and mesh arrangement method, are similar to those described in Section 3.4.1. As a result, a mesh of around 2.5×10^6 cells is applied. The predicted static pressure values on the cube surfaces

are normalized by the static and dynamic pressures to obtain the pressure coefficients, calculated by the following equation:

$$C_p = \frac{P - P_{ref}}{0.5 \rho U_{ref}^2} \quad (3.7)$$

where P_{ref} is the reference static pressure.

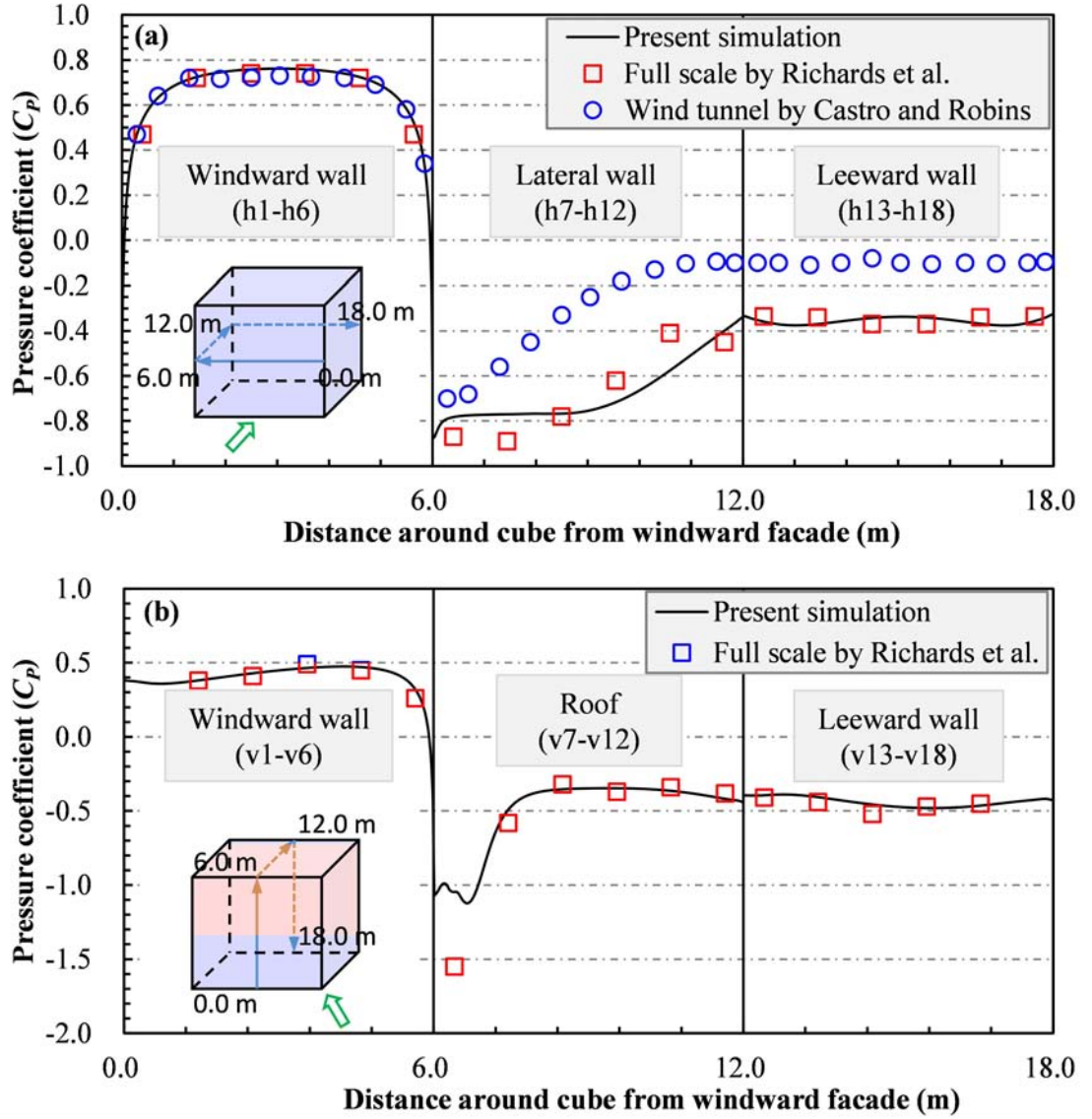


Figure 3.8 Pressure coefficients along the centerlines of the cube surface: (a) Normal wind direction; (b) Oblique wind direction.

The predicted pressure coefficients and full-scale measurements are compared in Figure 3.8, in which the wind tunnel results of Castro and Robin (1977) are also

plotted for reference. It can be seen that the three sets of data are perfectly aligned with each other on the windward wall under normal wind direction (Figure 3.8 (a)), whereas the simulation results and full-scale measurements are much more negative than the wind tunnel data on the lateral and leeward walls. Richards et al. (2001) have compared these full-scale results with a number of wind tunnel data from the Windtechnologische Gesellschaft comparative testing program (Hölscher and Niemann, 1998), and found that, with the exception of the windward wall, the difference between these wind tunnel results is very distinct, and most are larger than these full-scale values. They ascribe this difference to the different approaching flow conditions and model scale. In the present simulation, despite some deviations between the simulation results and full-scale measurements on the lateral wall, they have similar trends and almost the same average C_p value (around -0.67). Under oblique wind direction, as shown in Figure 3.8 (b), the two are aligned perfectly with each other on the windward and leeward walls, although a discrepancy appears near the windward edge on the roof due to the underperformance of the steady-state $k - \varepsilon$ model. Overall, these model evaluations generally justify the later application of the RNG $k - \varepsilon$ model and the two-layer near-wall model to study the flow around the lateral walls of buildings.

3.5 Difference in ventilation characteristics between single-story and multistory buildings

3.5.1 Physical model examined

A solid block, a single-story building and a multistory building are created for purposes of comparison (see Figure 3.9 (a)-(c)). The solid block has the same dimensions as the single-story building, and the dimensions of the rooms in the latter two buildings are the same, extracted from the measurement of a real building in Hong Kong (Niu and Tung, 2008). The room dimensions are 3.1 m (X) \times 2.4 m (Y) \times 2.7 m (Z). The opening dimensions are 0.75 m (Y) \times 1.2 m (Z) on the upper four floors and 0.75 m (Y) \times 2.0 m (Z) on the first floor. The height of the windowsills on the upper four floors is 0.8 m. The solid block is considered as many previous studies have used pressure coefficients on the surfaces of a solid block to estimate ventilation performance (e.g., Chand et al., 1998; Ai et al., 2011b). Some studies

have shown that this method using solid blocks is unreliable (Straw, 2000; Choiniere et al., 1992; Sandberg, 2004). This study compares the difference in flow characteristics between the solid block and a single-story building to explain the unreliability of solid blocks. In order to compare room(s) on the leeward side, both the single-story and multistory models contain leeward room(s), and thus the single-story building has two rooms. The names of the windward rooms can be found in Figure 3.9 (b) and (c), where W represents windward side, R represents room, and the two numbers represent vertical and horizontal locations, respectively. For example, W32 represents the middle room on the third floor on the windward side. This naming method is also applied to the leeward rooms, replacing W with L. The three buildings are separately placed in a computational domain (see Figure 3.9 (d)), which has the similar dimensions as those in the previous validation section.

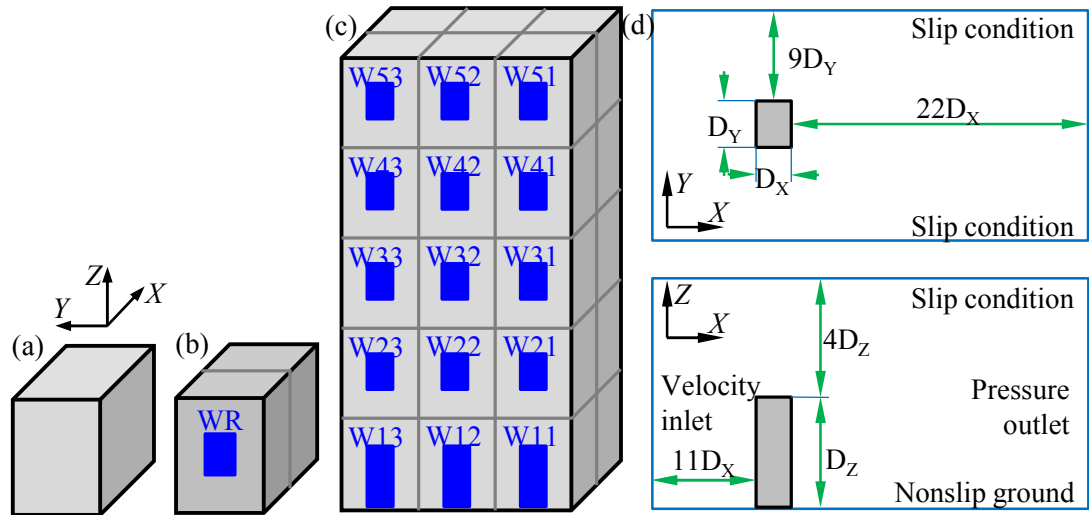


Figure 3.9 (a) solid block, (b) single-story building, (c) multistory building, (d) computational domain.

All the three building models are simulated in 1:30 reduced-scale models, where the Reynolds independence is achieved (Snyder, 1981). The combination of RNG $k - \varepsilon$ model with the two-layer model is used. Other numerical treatments, including mesh arrangement method, used to simulate the three models are similar with those described in the previous validation section. As a result, a mesh of around 2.5×10^6 cells is applied to the solid block and single-story building and a mesh of

around 3.5×10^6 cells is applied to the multistory building.

3.5.2 Results and analyses

3.5.2.1 Flow and turbulence fields

The relative velocity and turbulence kinetic energy field on the vertical centre planes of the three models are presented in Figure 3.10, where the U_{ref} and k_{ref} are the maximum velocity and turbulence kinetic energy near the frontal corner. Comparison of the relative U and k fields leads to the following three observations.

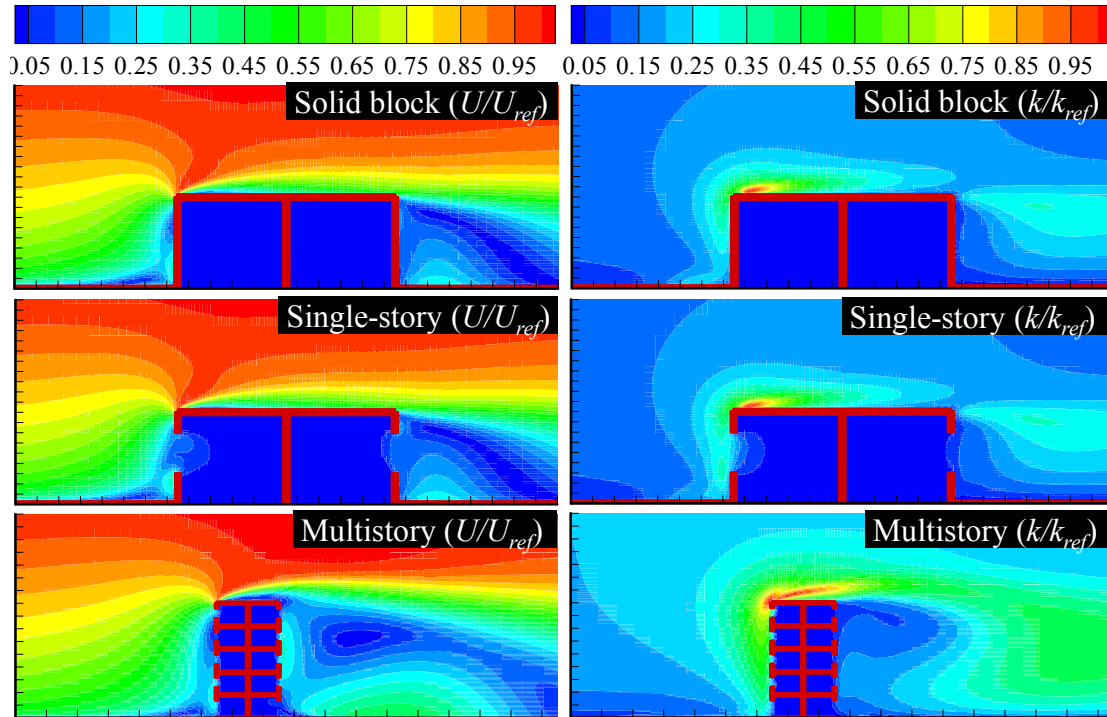


Figure 3.10 Velocity and turbulence kinetic energy fields on the vertical centre plane.

First, it can be seen that the main trends of both the velocity and turbulence kinetic energy fields around the three buildings are very close. Such a basic external flow pattern around a bluff body has been clearly revealed in the field of wind engineering. The former two cases (the solid block and the single-story building)

have almost the same external U and k distributions, as they have the same external configuration. The external U and k distributions of the multistory building are slightly different. This should be attributed to the buildings' different shapes in terms of the height-to-width, height-to-length and width-to-length ratios. However, it is believed that this difference is not important, as the focus of the present comparison is on the envelope flow pattern and ventilation performance.

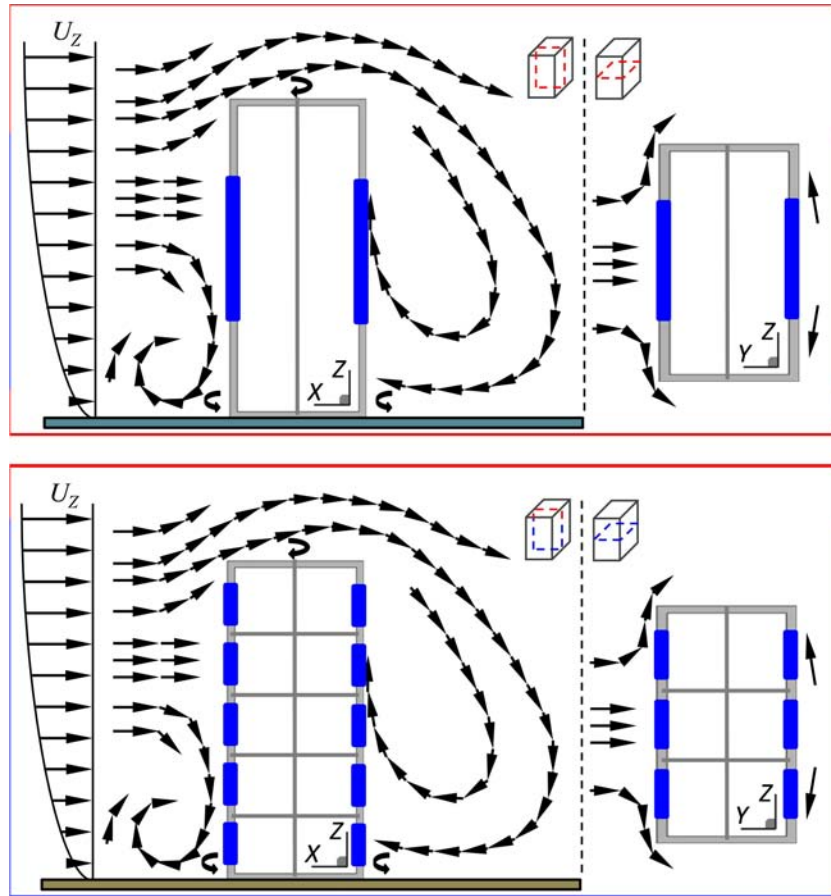


Figure 3.11 The similar external flow patterns around a single-story and a multistory building; note that here the geometry of the single-story building is stretched for the purpose of comparing schematically the flow patterns around the two types of building.

Second, the envelope flow patterns at the location of the opening of the solid block and single-story building are clearly different. This is because the presence of openings increases the roughness of a building's facades and thus disturbs the near-wall airflow pattern through the interaction between outdoor and indoor

airflows. This difference in envelope flow patterns indicates that the surface pressure coefficients measured on a solid block cannot be relied upon to predict indoor and outdoor airflow exchange rates. Review by Ramponi and Blocken (2012) also suggests that, in case of wind flow through large openings, the turbulence kinetic energy cannot be dissipated completely at the windward opening and thus the solid block assumption is not valid. In fact, air can flow into and out of a room through any part of a single opening in a highly random manner (see Section 5.3). This cannot be predicted accurately using a solid block with presumed locations of regularly distributed inlets and outlets.

Third, the envelope flow pattern of a room in a single-story building is completely different from that of a room in a multistory building. As mentioned above, the basic external flow pattern around the two buildings is similar. However, while a room in a single-story building enjoys the whole flow pattern, all of the rooms in a multistory building share this airflow pattern. This eventually leads to rooms at different locations experiencing distinctive envelope flow patterns, namely different velocity and turbulence fields.

Single-story and multistory buildings are further compared in Figure 3.11. It can be seen that, on the windward side of the latter, the top-most room experiences an upward airflow, the room in the fourth floor a stagnation airflow, and the lower three rooms a downward airflow. The different envelope flow patterns between rooms in multistory and single-story buildings justify the argument that the findings derived from a single-story building are not reliable to use in a multistory building, as it is difficult for an empirical model to account for the effect of room location.

3.5.2.2 Ventilation rates

In addition to the flow and turbulence fields, the nondimensional ventilation rates ($Q^* = Q / (U_{ref} A_o)$) of the rooms in the single-story and multistory buildings are also compared (see Table 3.6). The ventilation rates are calculated using the integration method described in Section 2.6. Owing to the aerodynamic symmetry between the end rooms (e.g., W31 and W33), only one is presented in Table 3.6. The comparison of ventilation rates can lead to two principal observations. First, the ventilation rate of neither windward nor leeward rooms in the single-story building can represent that

of any rooms in the multistory building. As explained before, this is basically due to the different envelope flow patterns near the rooms in the two types of building. This implies that one should be cautious in applying the findings from a single-story building to a complex multistory building. Second, it is obvious that the ventilation rates in rooms in a multistory building differ greatly, and that the ventilation rate of a room is strongly dependent on its three-dimensional location in the building. Particularly, along the vertical direction, the ventilation rate of a room does not increase with its height. The rooms located around the intermediate level of the building have relatively smaller ventilation rates. In addition, the ventilation rate of the windward rooms is very different from that of the leeward rooms on the same floor. Unfortunately, this was ignored by past empirical models, which do not contain a parameter to represent the effect of room location, and so cannot account for the difference in ventilation rate between different rooms in the same multistory building.

Table 3.6 Summary of nondimensional ventilation rates of rooms in the single-story and multistory buildings.

	Multistory building					Single-story building
Room	W11	W21	W31	W41	W51	WR
Q^*	0.42	0.29	0.28	0.28	0.31	0.93
Room	W12	W22	W32	W42	W52	
Q^*	0.33	0.25	0.22	0.22	0.34	
Room	L11	L21	L31	L41	L51	LR
Q^*	0.54	0.15	0.10	0.11	0.33	0.35
Room	L12	L22	L32	L42	L52	
Q^*	0.64	0.27	0.09	0.11	0.31	

Overall, the ventilation characteristics of multistory buildings further justify the use of the CFD method as it is convenient to calculate the ventilation rate of many rooms simultaneously and easy to compare the effect of various parameters using this method. In contrast, such calculations and comparisons for multistory buildings are difficult and expensive to achieve using the experimental methods. In addition, it is

quite difficult for experimental methods to explain exactly how the outdoor approaching airflow interacts with a building envelope containing many openings and why the ventilation rates are different between different rooms.

3.6 Summary

Different methods of determining single-sided ventilation rates in multistory buildings have been evaluated. In general, this study demonstrates that compared to the empirical models and the experimental methods, the CFD simulation is very suitable for the determination of ventilation rates in multistory buildings, especially in the design stage. In addition, CFD is a useful tool for understanding the envelope airflow characteristics and ventilation mechanisms of a multistory building.

The on-site measurements of the ventilation performance in multistory residential buildings in Hong Kong were conducted. The measurements are strongly relied on the model availability and are restricted by the uncontrollable boundary conditions. In addition, the measurements of ventilation rates using the tracer gas decay method cannot be conducted in many adjacent rooms simultaneously, as the reentry of tracer gas from one room to other rooms would influence the measured results.

Using the measured ventilation rates, the previous empirical models are validated. None of them are reliable in the prediction of the ventilation rate of rooms in multistory buildings, the main reason for this being that these correlations do not contain a parameter to account for the effect of room location in a multistory building. Both the envelope flow pattern and the ventilation rate of a room in a multistory building are highly dependent on the room's three-dimensional location in the building.

The RNG and MMK $k-\varepsilon$ models combined with the two-layer near-wall approach are preliminarily validated using past experimental data. Good agreements between the predicted and the measured results are achieved, which suggests that the CFD method is a suitable tool for studying single-sided natural ventilation. Any predictive methods reproduced by CFD simulation are compromised by the accuracy of the flow field produced by the selected numerical model. Thus, work on improving the prediction of the flow field is essential to ensure the reliability of CFD predictions of ventilation rate.

Using CFD method, the envelope flow patterns and the ventilation characteristics of a solid block, a single-story building and a multistory building are compared. The envelope flow pattern at the opening of a building is obviously different from that at the same location of a solid block, which indicates that the method of predicting ventilation rates using the pressure coefficients on the surfaces of a solid block is not reliable. The comparison of ventilation characteristics between the latter two models provides both qualitative and quantitative explanation of the unreliability of previous empirical models in multistory buildings.

Chapter 4

Quality assessment and improvement of CFD simulation of atmospheric flow and dispersion

4.1 Introduction

This chapter presents the quality assessment and improvement of CFD simulation of atmospheric flow and dispersion. CFD simulations are known to be very sensitive to the selection of many physical and numerical parameters. Detailed analyses of these influencing factors are necessary to provide information and guidance for improving the quality of future CFD studies. For RANS simulation, based on the two-layer near-wall model, a homogeneous ABL is developed. The effect of the inhomogeneous ABL and near-wall treatment is examined. For LES simulation, totally seven influencing factors are examined. Particularly, the basic difference in fluctuating intensity of the velocity components provided by three commonly used inflow algorithms is identified. In addition, the potential use of reduced-scale models in CFD simulations to save numerical resources is analyzed both qualitatively and quantitatively. For validation purpose, numerical results are compared with high-fidelity wind tunnel experimental data (CEDVAL) (Leitl and Schatzmann, 1998) for the flow (A1-1) and dispersion (A1-5) around a rectangular building placed in the neutral boundary layer.

4.2 RANS simulation of flow and dispersion around an isolated building

4.2.1 Modification of inlet conditions and turbulence model

The standard $k-\varepsilon$ turbulence model (Launder and Spalding, 1972, 1974) and its variants (Tsuchiya et al., 1997; Yakhot and Orsag, 1986) remain the most widely used approaches to modeling wind engineering and atmospheric dispersion problems (Stathopoulos, 1997). Applying the standard $k-\varepsilon$ turbulence model and assuming constant pressure and shear stress and zero vertical velocity, the following equations can be used to describe a neutral, incompressible, and horizontally homogenous two-dimensional ABL flow (Richards and Hoxey, 1993):

$$\mu_t \frac{\partial u}{\partial z} = \tau_0 = \rho u^{*2} \quad (4.1)$$

$$\frac{\partial}{\partial z} \left(\frac{\mu_t}{\sigma_k} \frac{\partial k}{\partial z} \right) + G_k - \rho \varepsilon = 0 \quad (4.2)$$

$$\frac{\partial}{\partial z} \left(\frac{\mu_t}{\sigma_\varepsilon} \frac{\partial \varepsilon}{\partial z} \right) + C_{\varepsilon 1} G_k \frac{\varepsilon}{k} - C_{\varepsilon 2} \rho \frac{\varepsilon^2}{k} = 0 \quad (4.3)$$

where the production of turbulence kinetic energy and the turbulent viscosity are given by $G_k = \mu_t (\partial u / \partial z)^2$ and $\mu_t = \rho C_\mu k^2 / \varepsilon$, respectively. Richards and Hoxey (1993) then suggest the following inlet boundary conditions for a fully developed flow under neutral stratification conditions:

$$U = \frac{u^*}{\kappa} \ln \left(\frac{z + z_0}{z_0} \right) \quad (4.4)$$

$$k = \frac{u^{*2}}{\sqrt{C_\mu}} \quad (4.5)$$

$$\varepsilon = \frac{u^{*3}}{\kappa(z + z_0)} \quad (4.6)$$

where the friction velocity u^* is calculated by $u^* = C_\mu^{1/4} k_p^{1/2}$. It can be shown that these inlet boundary conditions are analytical solutions of the standard $k - \varepsilon$ model if a relation for the model constants is achieved as $\sigma_\varepsilon = k^2 / [(C_{\varepsilon 2} - C_{\varepsilon 1}) \sqrt{C_\mu}]$.

Concerning the impracticality of the constant inlet profile for k , Yang et al. (2009) derive a new set of inlet conditions with a varied k along height. Under a local equilibrium condition, namely a rate of production of k equal to the rate of dissipation (that is, G_k equal to $\rho \varepsilon$), ε can be written as:

$$\varepsilon = C_\mu^{1/2} k (\partial u / \partial z) \quad (4.7)$$

Substituting this relation for ε and the velocity profile (Equation (4.4)) into the governing equation for k (Equation (4.2)), a solution for k can be obtained:

$$k = \sqrt{M_1 \ln(z + z_0) + M_2} \quad (4.8)$$

Substituting Equations (4.8) and (4.4) into Equation (4.7) yields:

$$\varepsilon = \frac{u^* \sqrt{C_\mu}}{\kappa(z+z_0)} \sqrt{M_1 \ln(z+z_0) + M_2} \quad (4.9)$$

It has been shown that these profiles improve the consistency of the horizontal boundary layer (Yang et al., 2009). However, they are just approximate solutions for the equations that govern a fully developed ABL. Gorlé et al. (2009) recently improve on the approach of Yang by modifying the constant C_μ and the turbulent dissipation Prandtl number σ_ε to satisfy the equations for shear stress τ_0 and dissipation rate ε , respectively. Substituting Equations (4.8)-(4.9) into Equation (4.1), the relation for C_μ is derived as:

$$C_\mu = \frac{u^{*4}}{\sqrt{M_1 \ln(z+z_0) + M_2}} \quad (4.10)$$

Substituting Equations (4.8)-(4.9) into Equation (4.3), the relation for σ_ε can be obtained as:

$$\sigma_\varepsilon = \frac{\kappa^2 (k^2 - M_1/2)}{u^{*2} (M_2 - M_1) k} \quad (4.11)$$

The inlet conditions proposed by Yang et al. (2009) together with the modifications of Gorlé et al. (2009) are used in this study to ensure a homogeneous ABL. It should be noted that although these inlet conditions are derived based on the formulations of the standard $k-\varepsilon$ model, they are still compatible with its variants. Here the MMK $k-\varepsilon$ model (Tsuchiya et al., 1997) is employed, which is described in Sections 2.5.1 and 3.4.1.

4.2.2 Near-wall treatments

4.2.2.1 Wall functions modified for rough surfaces

The wall functions in CFD coding are based on the universal law of the wall (Launder and Spalding, 1974; White, 1991). In Ansys Fluent, the wall function (law of the wall for mean velocity) for smooth surfaces is written as:

$$\frac{U_p u^*}{\tau_0 / \rho} = \frac{1}{\kappa} \ln(Ey^*) \quad (4.12)$$

where the nondimensional distance y^* is calculated by $y^* = \rho u^* y_p / \mu_t$, which is approximately equal to y^+ ($y^+ = \rho u y_p / \mu_t$) in the equilibrium of turbulent boundary layers.

Experiments in roughened pipes and channels (Nikuradse, 1933) indicate that the mean velocity distribution near rough walls, when plotted using the usual semi-logarithmic scale, has the same slope ($1/\kappa$) but a different intercept (Blocken et al., 2007; Cebeci and Bradshaw, 1977). Thus, the wall function modified for roughness surfaces has the form:

$$\frac{U_p u^*}{\tau_0 / \rho} = \frac{1}{\kappa} \ln(Ey^*) - \Delta B \quad (4.13)$$

The roughness function ΔB depends, in general, on the type (such as uniform sand, rivets, ribs, or mesh-wire) and size of the roughness. For a sand-grain roughness, ΔB has been found to be well-correlated with the nondimensional roughness height, $K_s^+ = \rho K_s u^* / \mu$. Normally, the whole roughness regime is subdivided into three regimes, and the formulas (Cebeci and Bradshaw, 1977; Raupach et al., 1991) based on Nikuradse's data are adopted to compute ΔB for each regime.

In the hydrodynamically smooth regime ($K_s^+ \leq 2.25$):

$$\Delta B = 0 \quad (4.14)$$

In the transitional regime ($2.25 < K_s^+ \leq 90$):

$$\Delta B = \frac{1}{\kappa} \ln \left[\frac{K_s^+ - 2.25}{87.75} + C_R K_s^+ \right] \times \sin \left[0.4258 (\ln K_s^+ - 0.811) \right] \quad (4.15)$$

In the fully rough regime ($K_s^+ > 90$):

$$\Delta B = \frac{1}{\kappa} \ln \left[1 + C_R K_s^+ \right] \quad (4.16)$$

Note that the previously mentioned aerodynamic roughness z_0 is a function of the geometrical roughness height K_s , rather than a physical length, which will be

explained in the next section. For Ansys Fluent, the relationship between the geometrical roughness height K_s and aerodynamic roughness height z_0 is commonly determined by $K_s = Ez_0/C_R$ (Blocken et al., 2007; Hargreaves and Wright, 2007).

4.2.2.2 Two-layer model modified for rough surfaces

The basic theory of two-layer model can be found in Section 2.5.1. However, that version of two-layer model is only applicable to smooth surfaces. In this section, the methods proposed by Durbin et al. (2001) are used to modify it for rough surfaces.

First, owing to roughness on the surface, the z -origin is shifted to where the mean velocity is zero, namely $U_{(z=0)} = 0$. This location of $z = 0$ is not necessarily the effective origin for the turbulence kinetic energy k . According to the fully developed velocity profile (Equation (4)), the turbulent viscosity can be written as:

$$\mu_t = \rho u^{*2} \partial U / \partial z = \rho u^* \kappa (z + z_0) \quad (4.17)$$

which suggests that the effective origin of the turbulence is $-z_0$. This shifted origin is the aerodynamic roughness z_0 . The z in the damping functions l_ε and l_μ for one-equation model is accordingly replaced with $z + z_0$.

Second, for the damping functions, $A_\varepsilon = 5.0$ is sufficiently small under fully turbulent conditions to yield a negligible effect for the l_ε damping, and thus it need not be modified. However, $A_\mu = 70$ must be reduced with roughness:

$$A_\mu = \max[1; A_\mu^0 (1 - K_s^+ / 90)] \quad (4.18)$$

With the above ‘max’ function, when $K_s^+ > 90$, $l_\mu = (z + z_0) C_l^*$, the damping is effectively deleted.

Third, if the logarithmic layer extends to the origin of z under fully rough conditions, the boundary condition of k should be changed from $k(0) = 0$ to $k(0) = u^{*2} / \sqrt{C_\mu}$. This can be achieved by the following equation:

$$k(0) = \frac{u^{*2}}{\sqrt{C_\mu}} \min \left[1; \left(K_s^+ / 90 \right)^2 \right] \quad (4.19)$$

Apart from the modifications to the l_μ formula and the boundary condition on k , the additive constant B in the log-law should also be decreased by roughness. For sand-grain roughness, this is similar to the wall function modifications (Equations (4.14)-(4.16)). This roughness-modified, two-layer model has been calibrated by solving a practical boundary layer (Durbin et al., 2001), from which a nonlinear relationship between z_0^+ and K_s^+ is obtained:

$$z_0^+ = 0.00001(K_s^+)^3 - 0.0033(K_s^+)^2 + 0.213K_s^+ - 0.52 \quad \text{for } K_s^+ \leq 90 \quad \text{and}$$

$$z_0^+ = 0.0345K_s^+ - 1.529 \quad \text{for } K_s^+ > 90.$$

4.2.3 Experimental and numerical techniques

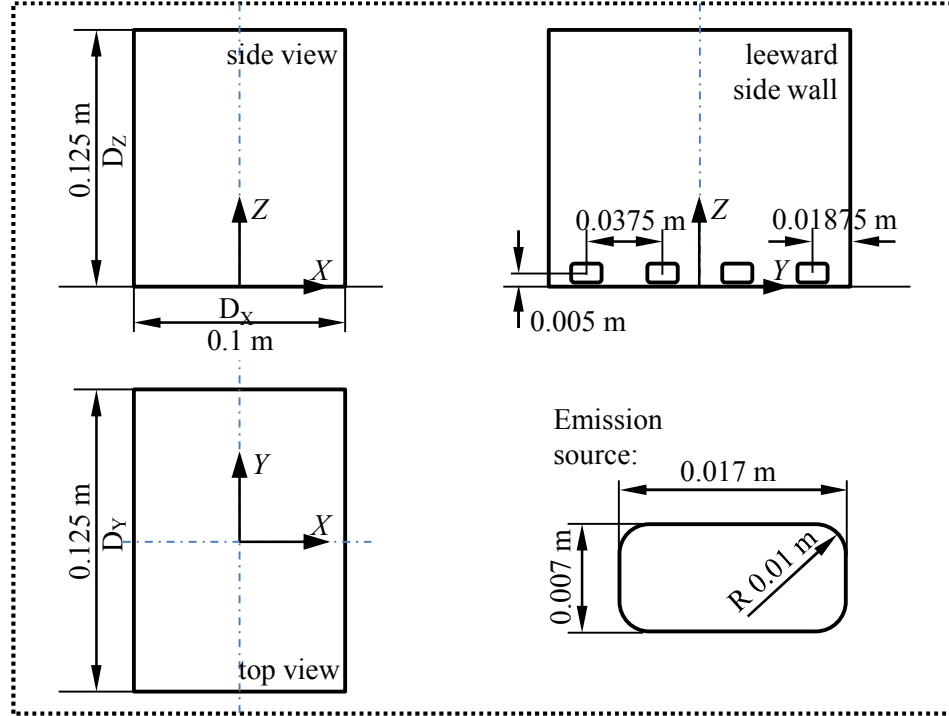
Airflow around a rectangular building (CEDVAL A1-1) and dispersion in the wake of the same building (CEDVAL A1-5) were measured at a scale of 1:200 in the BLASIUS wind tunnel in the University of Hamburg (Leitl and Schatzmann, 1998). The physical model of the building is shown in Figure 4.1 (a), where four facing pollutant sources located on the leeward wall represent the exhaust openings of a hypothesized underground parking garage. The experiments were conducted based on a high quality standard, with the boundary layer flow in the test section validated against full-scale data before the building model was mounted. The measurements were conducted within two planes: a vertical plane at $Y=0$ and a horizontal plane at $Z=0.28H$, see Figure 4.2. The Laser Doppler Velocimetry (LDV) technique was used to measure the velocity and turbulence fields, and the Flame Ionization Detector (FID) the concentration of the pollutant. Note that k was calculated using the measured fluctuating velocities, $k = 0.5(u' + v' + w')$. The concentration field was presented in a nondimensional form as:

$$K_C = \frac{C_{local}}{C_{source}} \frac{U_{ref} H^2}{Q_{source}} \quad (4.20)$$

where K_C is nondimensional concentration, C_{local} local concentration, C_{source} concentration at the source, U_{ref} reference wind speed at the height of 0.5 m, H

height of the building model, and Q_{source} flow rate of the source.

(a) Building model



(b) Computational domain

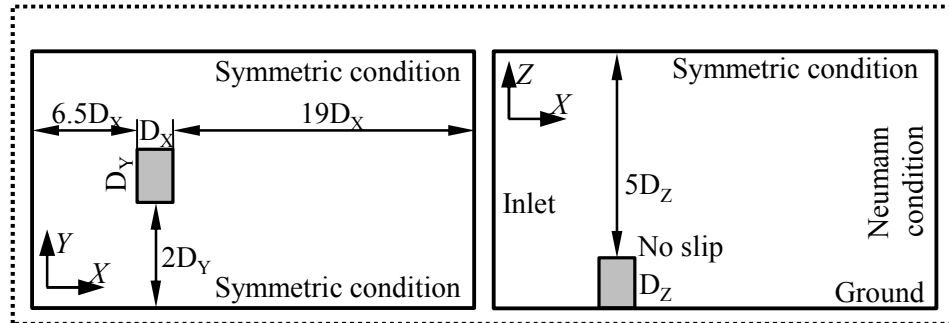


Figure 4.1 Schematic view of the building model and dimensions of the computational domain.

To numerically simulate the flow and dispersion around this building model, a computational domain shown in Figure 4.1 (b) is constructed. The selection of the domain dimensions follows the best practice guidelines for RANS modeling given in previous studies (Tominaga and Stathopoulos, 2009, 2010; Franke et al., 2007; Tominaga et al., 2008b), except for the lateral distances which is taken from the wind tunnel size to ensure an accurate reproduction. The body-fitted (BF) mesh-generation

technique (van Hooff and Blocken, 2010) is used, which has full control of the mesh resolution and stretching ratio in the whole domain. The mesh density, especially in regions close to the building model and domain ground, strongly influences the accuracy of the numerical results. A systematical sensitivity test for the mesh number is conducted by examining the dependence of numerical solutions on mesh number.

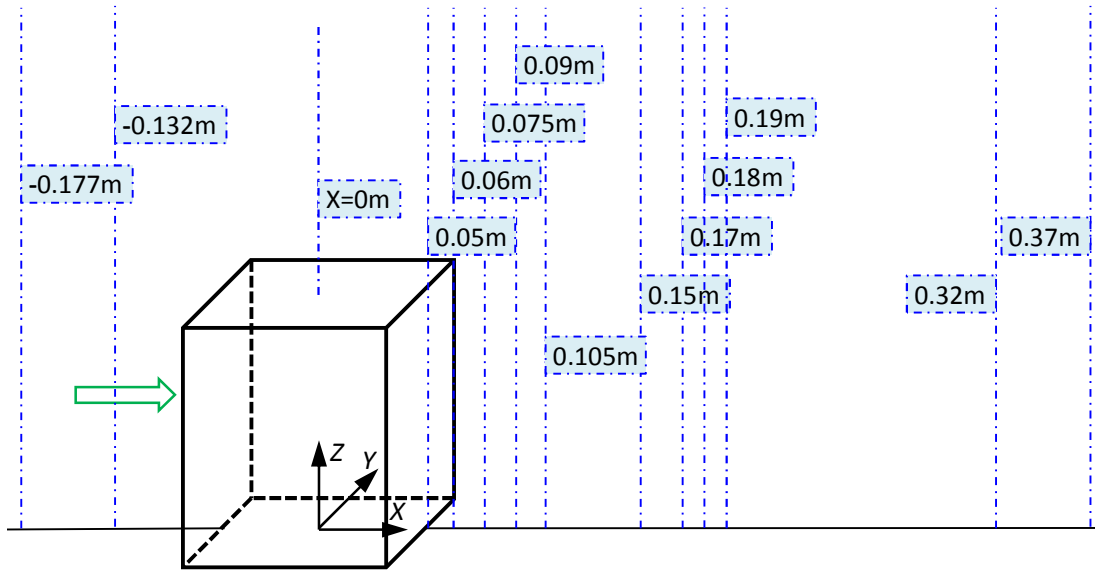


Figure 4.2 Schematic view of the lines on the vertical center plane ($Y = 0$) where simulated results and experimental data are compared.

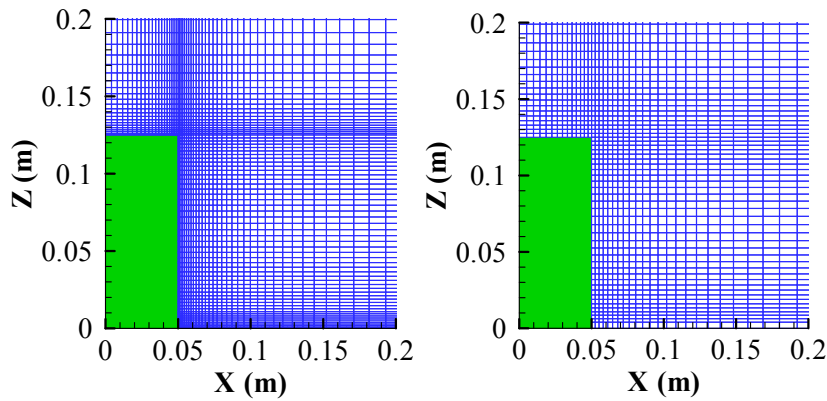


Figure 4.3 Mesh details of a part of the vertical center plane of the computational domain ($Y = 0$): the coarser for wall functions and the finer for the two-layer model.

Consequently, as a compromise between numerical accuracy and cost, two mesh

systems involving 1.5×10^6 and 3.5×10^6 , respectively, of structured hexahedra cells are used to construct the domain for the scenarios using the wall functions and two-layer model, respectively. For these two scenarios, the minimum grid widths near the domain ground and building edges are 0.004 m ($0.032H$, $y^+ \approx 35$) and 0.0002 m ($0.0016H$, y^+ at most walls being in the order of 1), respectively, with a maximum stretching ratio of 1.18 around the building model. A schematic view of the mesh construction can be found in Figure 4.3.

The boundary conditions at the domain's lateral sides, ceiling, and outlet as well as the surfaces of the building model, as described in Figure 4.1 (b) and Table 4.1, are the same for all the cases in this study. To examine the effect of inhomogeneous ABL, the rough wall functions are used at the domain ground, and three sets of inhomogeneous inlet conditions compared with the homogeneous one (that is, following the approach of Gorlé et al. (2009) as described in Section 4.2.2). The three sets are: Richards and Hoxey (1993) with fitting k equation with experimental data, Richards and Hoxey (1993) with fitting U equation with experimental data, and a typical power-law type. All these inlet conditions, together with the homogeneous one, are listed in Table 4.1. The inlet profiles of Gorlé et al. (2009) are obtained by fitting both equations U and k with the experimental data, with model constants $z_0 = 0.00075$ m, $u^* = 0.374$ m/s, $M_1 = 0.025$, $M_2 = 0.41$, and $C_\mu = 0.069$. For the inlet conditions of Richards and Hoxey (1993), when fitting k , $z_0 = 0.00075$ m, $u^* = 0.4078$ m/s, $C_\mu = 0.069$; and when fitting U , $z_0 = 0.00075$ m, $u^* = 0.374$ m/s, $C_\mu = 0.069$. For the inlet conditions of the power-law type, by fitting U , $U_H = 6$ m/s, $z_H = 0.5$ m, and $\alpha = 0.21$. To examine the effect of near-wall treatment, the rough wall functions and two-layer model (see Section 4.2.2), based on the homogeneous inlet conditions of Gorlé et al. (2009), are compared in the simulations of the flow and concentration fields. When the dispersion is simulated, the tracer gas (CO_2) is uniformly released from the four source elements with a constant velocity of 0.025 m/s in the X direction.

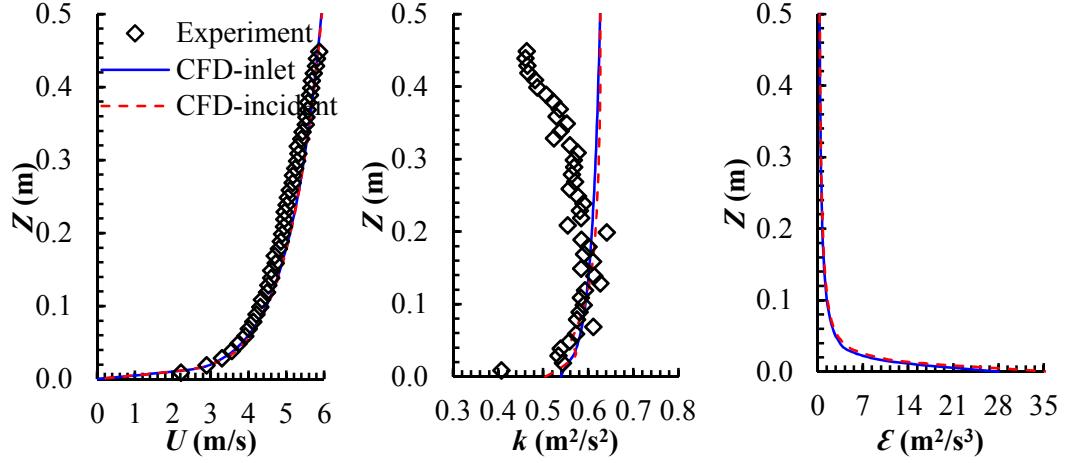
As introduced in Section 2.5.3, the turbulent Schmidt number (Sc_t) has a significant influence on the calculation of the concentration equation in the simulation of dispersion using RANS models. In this study, the optimal value of Sc_t

Table 4.1 Boundary conditions for examining the effect of inhomogeneous ABL.

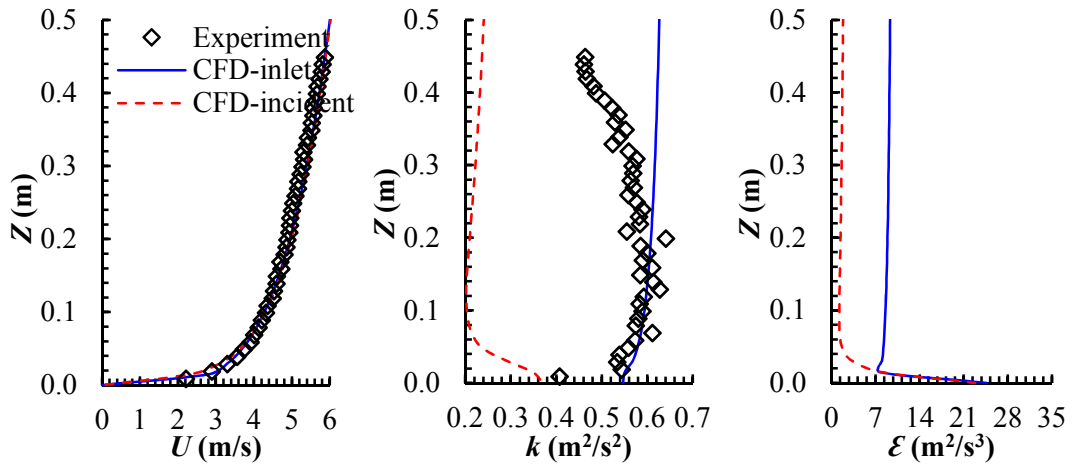
	Gorlé et al. (2009)	Power-law type	Richards and Hoxey (1993) (fitting k or U)
Domain inlet	$U = \frac{u^*}{\kappa} \ln \left(\frac{z + z_0}{z_0} \right)$ $k = \sqrt{M_1 \ln(z + z_0) + M_2}$ $\varepsilon = \frac{u^* \sqrt{C_\mu}}{\kappa(z + z_0)} \sqrt{M_1 \ln(z + z_0) + M_2}$	$U = U_H \left(\frac{z}{z_H} \right)^{0.21}$ $k = 0.5(u'^2 + v'^2 + w'^2)$ $\varepsilon = C_\mu^{0.75} k^{1.5} / l$	$U = \frac{u^*}{\kappa} \ln \left(\frac{z + z_0}{z_0} \right)$ $k = \frac{u^{*2}}{\sqrt{C_\mu}}$ $\varepsilon = \frac{u^{*3}}{\kappa(z + z_0)}$
Domain outlet	$\frac{\partial}{\partial x}(u, v, w, k, \varepsilon) = 0$		
Domain ceiling	$w = 0, \quad \frac{\partial}{\partial x}(u, v, k, \varepsilon) = 0$		
Domain lateral sides	$v = 0, \quad \frac{\partial}{\partial x}(u, w, k, \varepsilon) = 0$		
Domain ground	wall functions, $K_s = 0.002$ m, $C_R = 3.67$		
Building surfaces	non-slip for wall shear stress		
Turbulence model coefficients (for Gorlé et al. (2009))	$C_\mu = \frac{u^{*4}}{\sqrt{M_1 \ln(z + z_0) + M_2}}, \quad \sigma_\varepsilon = \frac{\kappa^2 (k^2 - M_1/2)}{u^{*2} (M_2 - M_1) k}$		

is determined by testing a number of Sc_t values (0.1-0.9) and comparing the simulated concentration fields with experimental data. The value of 0.4 is finally selected since it performed best overall in obtaining a field value close to that of the experiment.

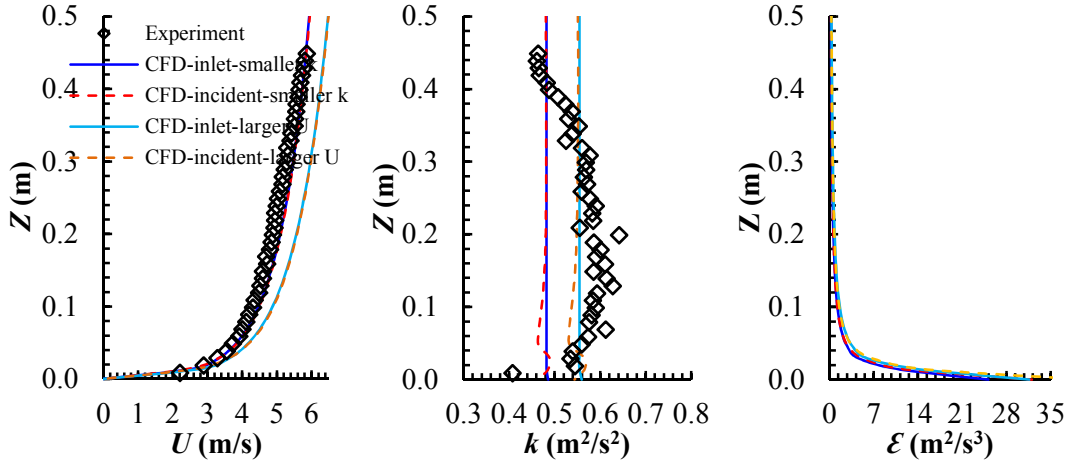
For all simulations conducted in this study, the pressure-velocity coupling is held by the SIMPLEC algorithm, the pressure interpolation is second order, and both the convection and diffusion terms are treated by second-order accuracy discretization schemes. Convergence is assumed to be achieved when all the scalar residuals reached 1.0×10^{-5} and the solutions of the calculation are stable over dozens of iterations.



(a) Inlet conditions of Gorlé et al. (2009)



(b) Inlet conditions of power-law type



(c) Two sets of inlet conditions of Richards and Hoxey (1993)

Figure 4.4 Comparison of inlet and incident profiles in the ABL of an empty domain.

4.2.4 Examining the achievement of the horizontal homogeneity of ABL

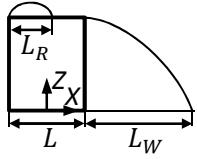
Before any numerical investigations began, simulations are conducted with an empty computational domain to examine the achievement of the horizontal homogeneity of ABL when using the four sets of inlet conditions listed in Table 4.1. Figure 4.4 presents the comparison of the inlet and incident profiles. The incident section refers to the position where the building will be located. It can be seen from Figure 4.4 (a) that the horizontally homogeneous boundary layer is well developed as only negligible streamwise gradients emerge in the k profile, indicating that the horizontally homogeneous ABL can be acceptably achieved by using the inlet conditions of Gorlé et al. (2009). Note that such a homogeneous ABL is also achieved when the roughness modified wall functions are replaced with the rough two-layer model.

Many CFD practitioners use the power-law U profile and theoretical and/or empirical calculated values for k and ε as the inlet conditions, especially when there is no experimental information. From Figure 4.4 (b), it can be seen that the k and ε profiles along the domain length are extremely inhomogeneous. This can be attributed to the inconsistency of these inlet profiles with the wall functions as well as with the governing equations of the $k - \varepsilon$ models.

Two different sets of inlet conditions used by Richards and Hoxey (1993) can be obtained depending on whether the U or k profile is fitted to experimental data.

In a later section, we label the one fitting the U profile as “smaller k ,” and the one fitting the k profile as “larger U .” The comparison of the inlet and incident profiles using the two possible sets of inlet conditions is shown in Figure 4.4 (c). Although the horizontal homogeneity of both sets are acceptably developed, the U or k profile cannot both represent the experimental data. This incompatibility between the U and k profile when simulating the same experiment arises because the inlet conditions of Richards and Hoxey (1993) are not the exact solutions of the governing equations of the $k - \varepsilon$ models. In addition, the constant k profile is always impractical when comparing with experimental observations (Yang et al., 2009).

Table 4.2 Experimental and numerical reattachment lengths and peak k (k_{\max}) on the roof; WF indicates wall functions and TL two-layer model.

	Case	Inlet conditions	Near-wall model	L_R / L	L_W / L	k_{\max} (m^2/s^2)
	Leitl and Schatzmann (1998)	Experiment		0.52	1.8	3.4
	MMK-1	Gorlé et al. (2009)	WF	0.4	3.2	5.5
	MMK-2	Power law	WF	>1.0	4.8	2.9
	MMK-3	Richards and Hoxey (1993): smaller k	WF	0.65	3.6	4.8
	MMK-4	Richards and Hoxey (1993): larger U	WF	0.59	3.3	6.0
	MMK-5	Gorlé et al. (2009)	TL	0.45	3.2	4.1

4.2.5 Effect of inhomogeneous ABL

4.2.5.1 Flow field

Table 4.2 presents the experimental and numerical reattachment lengths on the roof (L_R) and in the wake (L_W). Compared with experimental data, the use of the

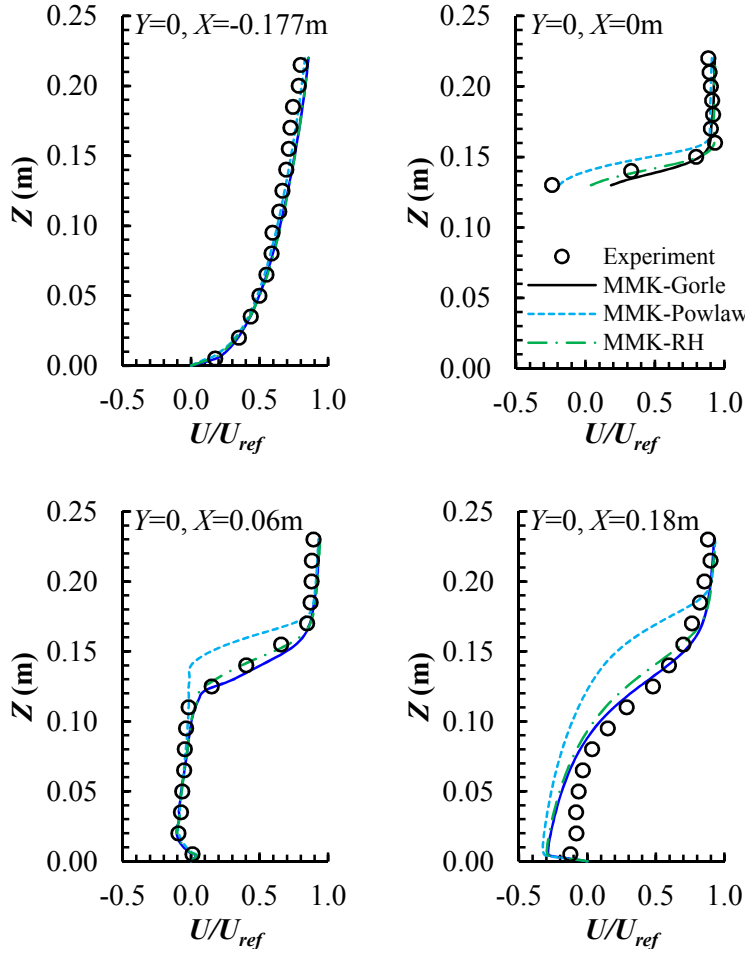


Figure 4.5 Comparison of nondimensional velocity along height on the vertical central plane.

MMK $k - \varepsilon$ model with the inlet conditions of Gorlé et al. (2009) (homogeneous) predicts a shorter reattachment length on the roof and a much larger recirculation region in the wake behind the building. Similar results have been demonstrated by previous studies using $k - \varepsilon$ models (e.g., Murakami, 1993; Tsuchiya et al., 1997; Tominaga et al., 2008a, Tominaga and Stathopoulos, 2009, 2010), which can be attributed to the inadequacy of these turbulence models. In general, all the simulations identify reverse flow on the roof, except for the case with power-law inlet conditions where the lower incident k and ε results in no reattachment on the roof. These lower k and ε also significantly lengthen the wake recirculation region compared to the homogenous case (from 3.2 to 4.8). Similar findings are obtained when the inlet conditions of Richards and Hoxey (1993) with smaller k are used. Compared to the homogeneous case, a larger incident U profile of

Richards and Hoxey (1993) can result in a much larger scope of reverse flow on the roof and a slightly longer wake recirculation region. Comparison of the two sets of inlet conditions of Richards and Hoxey (1993) shows that the one with larger U (that is, obtained by fitting k) predicts the reattachment lengths more closely to the homogenous case.

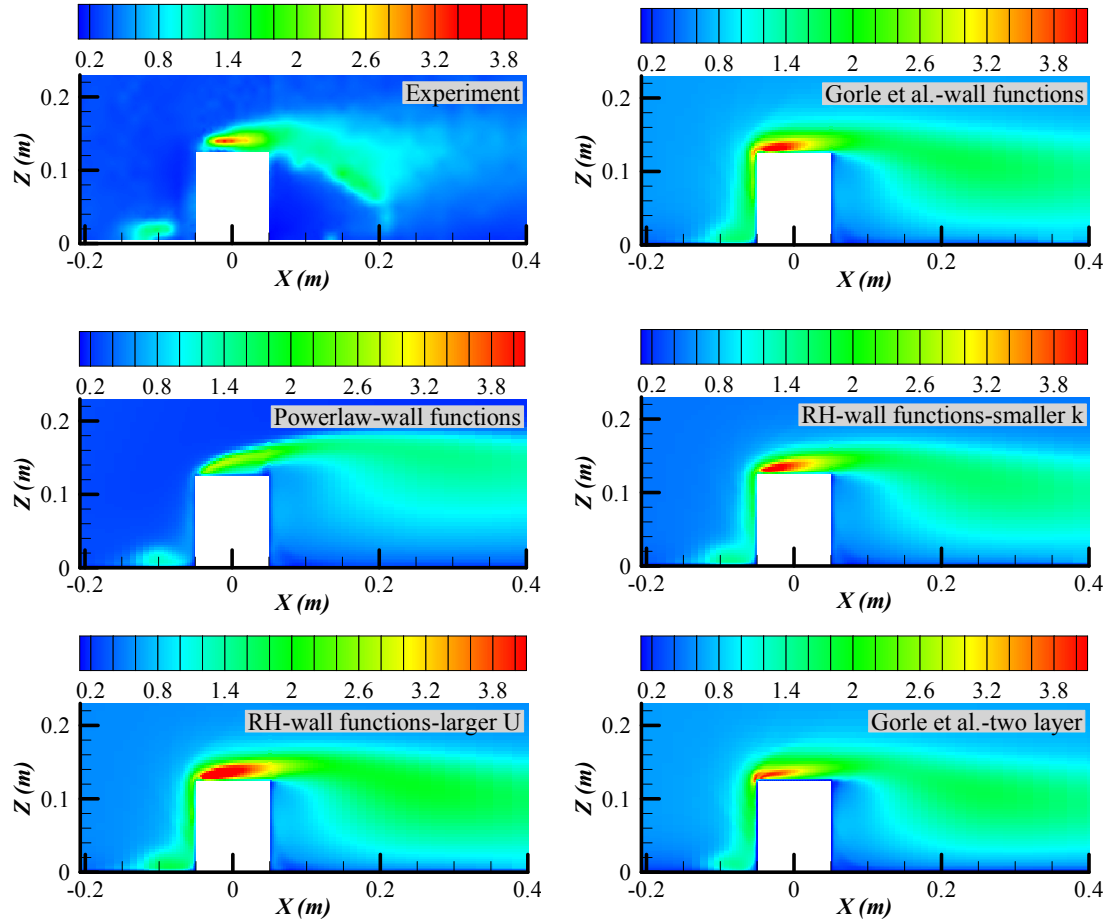


Figure 4.6 Comparison of turbulence kinetic energy k field on the vertical center plane.

Figure 4.5 presents the comparison of nondimensional velocity on the vertical center plane of the computational domain. The two sets of conditions from Richards and Hoxey (1993) produce almost the same nondimensional velocity field, indicated with “RH”. The predicted nondimensional velocity fields are almost the same, except in the regions around the building height as well as in the lower part of the wake. As supported by the analysis of reattachment lengths, the smaller incident k profile

results in a longer recirculation region both on the roof and in the wake. In particular, the power-law inlet conditions, which have a much smaller incident k and ε profiles, give an unrealistic velocity field. This implies that the smaller incident k lowers the mixing effect of the momentum around the building.

Figure 4.6 presents the comparison of the predicted k field within the vertical center planes. The peak of k for all cases appears in the frontal area on the roof, as summarized in the last column of Table 4.2. The predicted k values around the building using the MMK $k - \varepsilon$ model are much larger than those from experimental data. Compared to the homogeneous case (Gorlé et al., 2009), the lower incident k values, given by the power-law inlet conditions, result directly in the underestimation of the k field. This observation is also supported by the prediction using the inlet conditions of Richards and Hoxey (1993) with smaller k . It is this lower k field that enlarges the recirculation regions on the roof and in the wake, since the lateral momentum diffusions consequently become small in the cases of lower incident k (Tominaga et al., 2008a) and the lower velocity fluctuations reduce momentum mixing. However, the larger incident U profile increases the k field, owing to the simultaneous increase in the fluctuating velocity components, u' , v' , w' .

4.2.5.2 Concentration field

The distribution of the nondimensional concentration (K_c) on the vertical center plane is shown in Figure 4.7. In general, the MMK $k - \varepsilon$ model with standard wall functions acceptably predicts the concentration field, except in the wake where the concentration is underestimated. An obvious reason for this is the overprediction of the wake size, leading to dilution of the concentration in the recirculation region as well as limiting of the streamwise diffusion in the ground level. This demonstrates that accurate prediction of the velocity field is not sufficient to obtain an accurate concentration field. Essentially, the parameters governing the pollutant transport, such as the turbulent diffusion coefficient ($D_t = \nu_t / Sc_t = (8/9C_0)k^2 / \varepsilon$), should also be accurately predicted. It is evident that a reasonable calculation of the D_t is based on a correctly predicted turbulence field. However, due to the inherent inability of

$k - \varepsilon$ models to predict the fluctuating velocity components and, in turn, the turbulence diffusions, an accurate turbulence field cannot be reproduced. By comparing the results produced by using different inlet conditions, it is obvious that the lower incident k values accelerate the dispersion of the concentration in the streamwise direction and thus result in a higher concentration field on the vertical center plane. This seems to contradict the common knowledge that the turbulent diffusion coefficient D_t reduces with the decrease of k , when one ignores the fact that the turbulence dissipation rate ε is also significantly reduced. The acceleration of the U profile slightly overpredicts the concentration field in the region around the building height, but slightly underpredicts at ground level. The overprediction can be explained by the fact that the increased momentum diffusion enhances the concentration diffusion towards the streamwise direction, while the underprediction is due to the larger recirculation region produced.

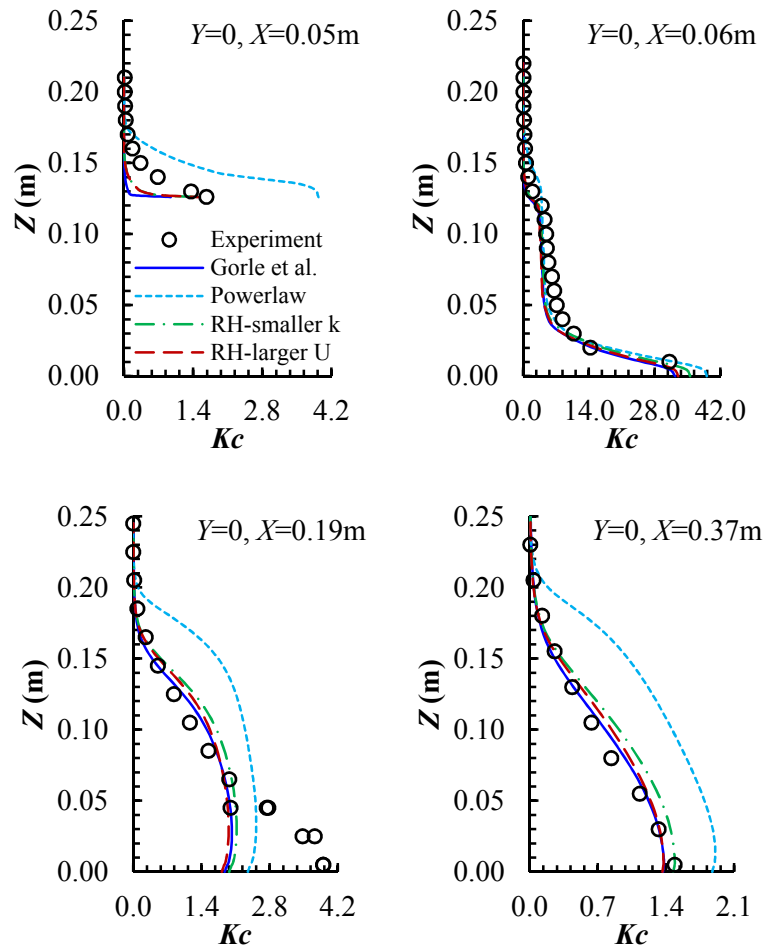
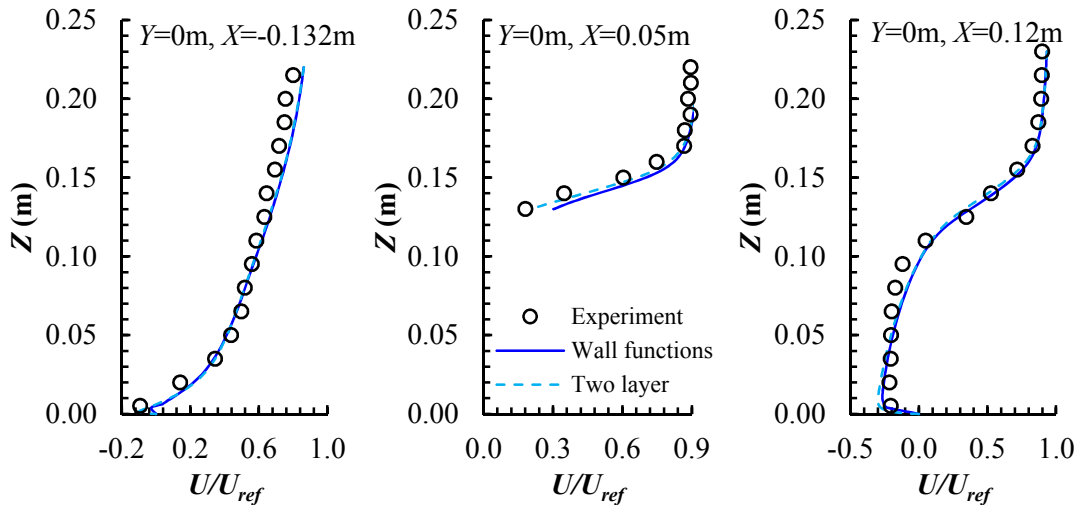


Figure 4.7 Comparison of the nondimensional concentration along height on the vertical central plane.

4.2.6 Effect of near-wall treatment

Based on the inlet conditions of Gorlé et al. (2009), the effect of near-wall treatment is examined by comparing the wall functions and two-layer model in the prediction of the flow and concentration fields. From Table 4.2, it can be seen that, excluding the effect of the horizontal inhomogeneity of ABL, the use of the two-layer model on the domain ground predicts a more accurate reattachment length on the roof than does the use of wall functions, although they give the same recirculation region in the wake. This should be attributed to the fact that the use of the two-layer model effectively lowers the peak of k on the roof and produces a more realistic k field around the building, as shown in Table 4.2 and Figure 4.6. A comparison of the nondimensional velocity and concentration is presented in Figure 4.8. The two-layer model slightly improves the prediction of the velocity field in the region around the building height, by decreasing the momentum and turbulence mixing. These improvements lead to a better concentration field, as shown in Figure 4.8. It is worth noting that the last plot in Figure 4.8 shows a comparison of the concentration on a horizontal line. As suggested by Gorlé et al. (2010), the scale of the lateral separation bubbles largely governs the upstream dispersion of the pollutant. This implies that the two-layer model contributes to producing smaller but more realistic separation bubbles in the lateral sides. However, even if the two-layer model is used to resolve the near-wall viscous region, the concentration field near the ground is still underestimated. This can be explained by the overprediction of the recirculation region in the wake using the $k-\varepsilon$ model.



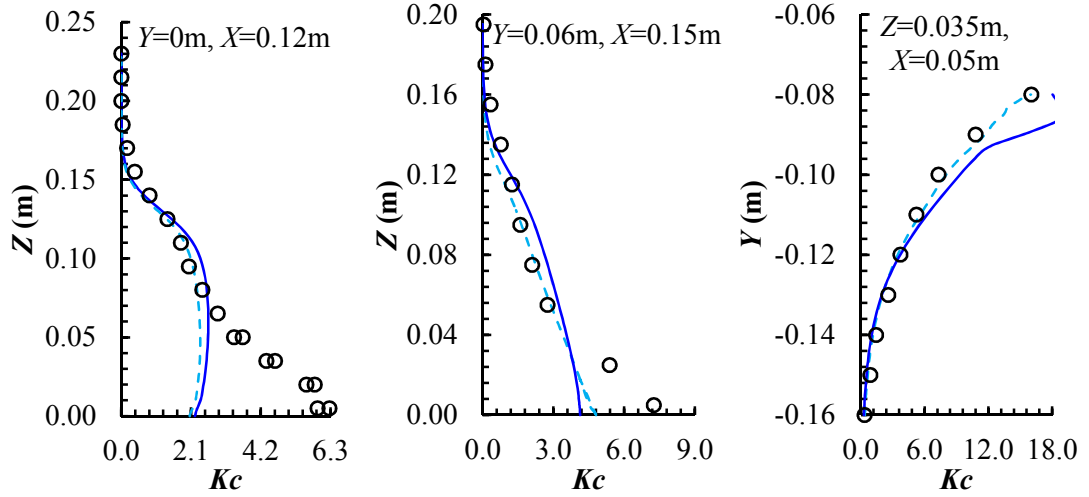


Figure 4.8 Comparison of the nondimensional velocity and concentration predicted using the wall functions and two-layer model.

4.2.7 Discussion of the effects

In this section, the effects of the inhomogeneous ABL and near-wall treatment on the prediction of flow and dispersion around an isolated building are quantified using the basic case of Gorlé et al. (2009). The percentage deviations $((\varphi_x - \varphi_b) / \varphi_b)$ are presented in Table 4.3, where φ_b represents a flow variable of the basic case and φ_x the other cases. Note that except for L_R / L , L_W / L , and k_{\max} , the other flow variables considered are treated averagely before calculating the percentage deviations. From this table, it can be observed that the inhomogeneous ABL has a significant effect on the prediction of flow and dispersion. For example, a reduction of 13.9% in the k profile can result in an overprediction of 62.5% in the roof attachment length and of 23.5% in the concentration at building height level. This suggests that, in order to obtain accurate solutions, one must achieve a homogenous ABL before commencing any numerical investigation. For the effect of the near-wall treatment, the differences in the flow and dispersion fields predicted using the two-layer model and wall functions are obvious. Given that the walls are the main source of mean vorticity and turbulence production, the reproduction of the viscous sublayer can contribute to more realistic wall-bounded turbulent flows. It is expected that the effect of the near-wall treatment might become more significant when the low-Reynolds-number effect of the near-wall regions is more important.

Table 4. 3 Percentage deviations of incident profiles and numerical solutions between Gorlé et al. (2009) and other types of inlet conditions.

	Variables	Gorlé et al. (2009): basic case	Power-law type	Richards and Hoxey (1993): smaller k	Richards and Hoxey (1993): larger U	Gorlé et al. (2009): two-layer model
Incident profiles	U	0%	0%	0%	+9.1%	0%
	k	0%	-60.1%	-13.9%	0%	0%
	ε	0%	-70.1%	0%	0%	0%
Reattachment lengths	L_R / L	0%	>150%	62.5%	47.5%	12.5%
	L_W / L	0%	50%	12.5%	3.1%	3.1%
Peak of k	k_{\max}	0%	-47.3%	-12.7%	9.1%	-25.4%
Velocity at the height of building	U_H / U_{ref}	0%	-94.3%	-27.8%	-26.4%	-7.3%
Concentration at the height of building	$K_{C,H}$	0%	107.4%	23.5%	13.7%	-7.9%

4.2.8 Summary

This section investigates the effect of the inhomogeneous ABL and the near-wall treatment on the RANS simulation of flow and dispersion around an isolated building. The RANS model is validated against two sets of high-quality wind tunnel experimental data. Using the logarithmic-law inlet conditions, the homogeneous ABL is developed based on both standard wall functions and roughness-modified two-layer model. The k and ε profiles of the commonly used power-law inlet conditions decelerate substantially throughout the domain length, although the U profile is well retained.

Generally, the effect of the inhomogeneous ABL on the prediction of flow and dispersion fields is significant. Establishing an accurate turbulence field is very important for the correct prediction of both flow and concentration fields. The lower incident k profile results in a longer reattachment length on the roof and a larger

recirculation region in the wake, but obviously produces a lower k field around the obstacle. This reduces concentration mixing in the lateral directions, which results in the concentrated distribution of pollutant in the streamwise direction. Around the height of the building, the velocity and concentration predicted by using the lower incident k profile are lowered and heightened, respectively. The magnitude of these changes depends on the percentage reduction in the incident k profile from the inlet condition. The larger incident U profile enlarges the reattachment lengths and raises the k field, which produces similar effects on the velocity and concentration fields as the lower k .

Attention should also be paid to the effect of the near-wall treatment on the prediction of flow and dispersion. The use of the two-layer model to solve the near-wall viscous sublayer clearly improves the prediction of both flow and dispersion, since it incorporates the low-Reynolds-number effect of the near-wall region into the calculation of the entire turbulent flow field. However, the time used for mesh and iteration of the two-layer model is around five times that of the wall functions for the current model.

4.3 Large-eddy simulation of flow and dispersion around an isolated building

4.3.1 Computational settings and validation: reference case

The experimental model used here is the same with that described in Section 4.2.3. The LES method is described in Section 2.5. This section describes the detailed computational settings that are used to reproduce the wind tunnel experiments. The numerical results are then compared with the measured data for validation purposes. The numerical settings used in this section are treated as the reference case for the subsequent analyses of influencing factors. Note that the standard Smagorinsky-Lilly model is used in this section and the Smagorinsky constant C_s is set as 0.1.

4.3.1.1 Computational domain and mesh generation

The building model is placed in a computational domain. The domain dimensions are the same with those selected in Section 4.2.3, except for the upstream distance. It is set to $4H$, which is less than that suggested by the best practice guidelines for

RANS modeling. The selection of a smaller upstream distance is based on the consideration that a larger distance could cause an inhomogeneous problem for the ABL in the domain (Blocken et al., 2007). Using the same mesh generation method as that in Section 4.2.3, a mesh system of around 3.5×10^6 structured hexahedral cells is constructed, with a minimum grid width of 0.0002 m (0.0016 H) and a maximum stretching ratio of 1.18 near the building surfaces and domain ground. Such a minimum grid width leads to the y^+ values at most building surfaces and domain ground being in the order of 1.

4.3.1.2 Boundary conditions

The inlet boundary conditions of the domain are prescribed by the profiles of the mean wind speed U , turbulence kinetic energy k , and turbulence dissipation rate ε , as indicated by the inlet conditions of Gorlé et al. (2009) listed in Table 4.1. The coefficients in these equations are determined by fitting them with the experimental data; eventually they are $z_0 = 0.00075$ m, $u^* = 0.374$ m/s, $M_1 = 0.025$, $M_2 = 0.41$, and $C_\mu = 0.069$. Note that here C_μ is only a constant, which has no relationship with the LES model. Based on the predefined k and ε profiles, the fluctuation in the mean velocity profile at the inlet plane is randomly generated using the Vortex method (Mathey et al., 2006) with 190 vortices. The boundary conditions at the domain's lateral sides, ceiling and outlet as well as building surfaces are the same with those listed in Table 4.1. The domain ground is simply defined as wall. As no existing formula for the LES model takes into account the roughness of walls, no special treatment is used for the domain ground. When the dispersion is simulated, the tracer gas (CO_2) is uniformly released from the four source elements with a constant velocity of 0.025 m/s in the X direction. No perturbations are considered for the emissions of tracer gas. The turbulent Schmidt number (Sc_t) for the large eddies is directly and dynamically calculated. However, for the SGS motion, the (Sc_{SGS}) number still needs to be decided. Here, a value of 0.4 is specified for Sc_{SGS} .

4.3.1.3 Solution methods

The initial condition of the transient simulation is a converged mean flow field that is generated by a RANS model. The transient flow and concentration fields are computed simultaneously. The discretization method for the pressure and diffusive terms are a second-order scheme, whereas a second-order bounded central-differencing scheme is used for the convective term. A second-order implicit scheme is used for temporal discretization. Finally, the pressure-velocity coupling method is SIMPLEC. The time step size in nondimensional form ($\Delta t^* = \Delta t \times U_H / H$) is 0.48 and the mean flow and concentration fields are obtained based on averaging during $1200 \Delta t^*$. The convergence of each time step is achieved when both the spatially averaged wind speed and CO₂ concentration at the opening of the test room are stable for at least five iterations.

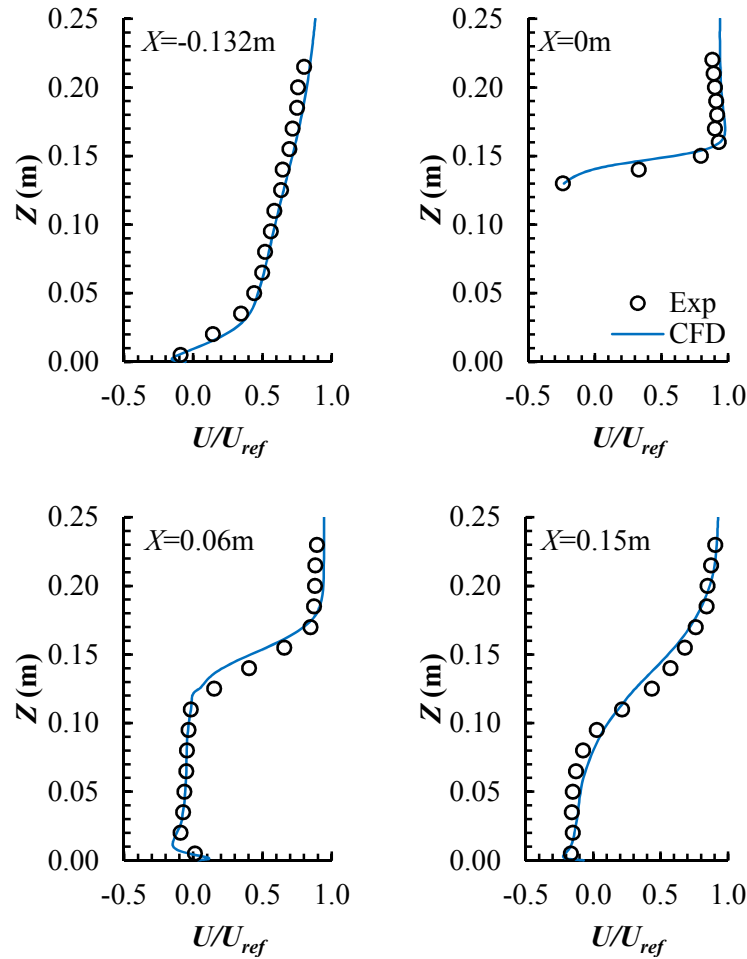


Figure 4.9 Comparison of measured and simulated mean velocity profiles.

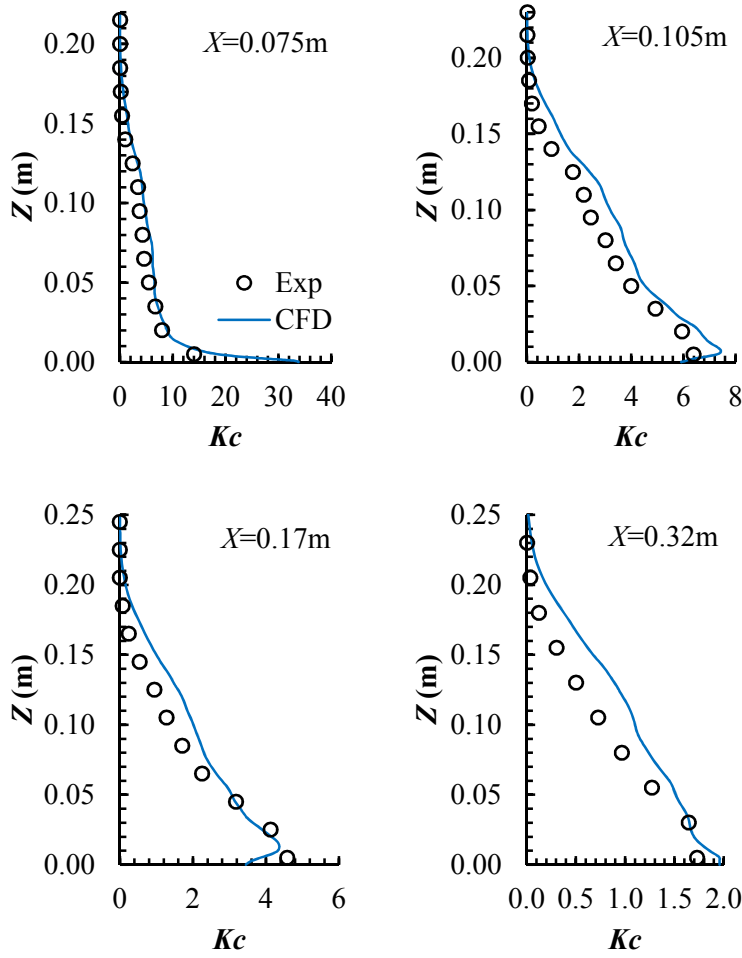


Figure 4.10 Comparison of measured and simulated mean concentration profiles.

4.3.1.4 Results and comparison with wind tunnel experiments

The simulated results of the reference case are compared with Leidl and Schatzmann's wind tunnel measurements (Leidl and Schatzmann, 1998). Figure 4.9 presents the nondimensional mean velocity profiles, which show good agreement between the simulated and measured results. This means that the LES model with the settings used in the reference case can produce a very accurate velocity field. In particular, the reverse flow on the building roof (see $X=0$ m) and the recirculation flow in the building wake (see $X=0.15$ m) are perfectly captured in terms of vortex size and velocity magnitude. Note that intermittent reattachment lengths (Saathoff et al., 1995) are found on the roof and in the wake, as the fluctuation intensity of the approaching flow is relatively small in the sample case. Figure 4.10 presents the nondimensional mean concentration profiles in the building wake. The simulated results generally match well with the measured values, especially in the region

immediately downstream of the building (see $X=0.075$ m). In regions further downstream of the building, the CFD simulation slightly overpredicts the concentration values at the building height level (around $Z=0.125$ m). These overpredictions may be attributed to the underprediction of mass diffusions, which is analyzed in detail in the next section.

4.3.2 Sensitivity analyses of the computational parameters

Based on the reference case, detailed analyses of the seven influencing factors are conducted. A summary of the influencing factors is presented in Table 4.4, with the reference case highlighted.

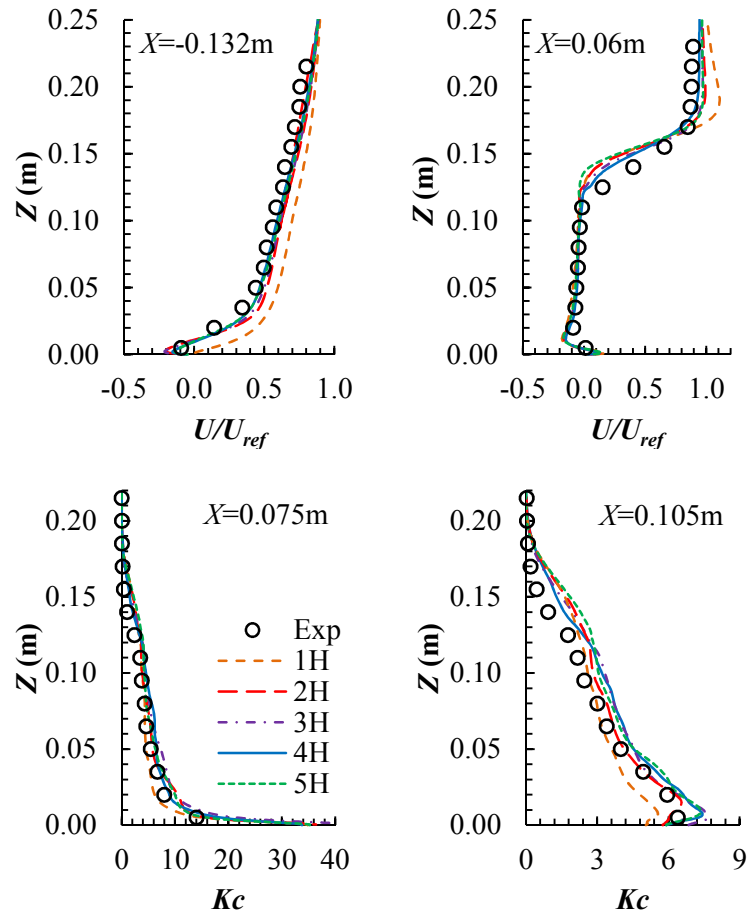


Figure 4.11 Effect of upstream distance of computational domain on mean velocity and concentration fields.

Table 4.4 Summary of influencing factors analyzed in this study, with the reference case highlighted.

Upstream distance of domain (Section 4.3.2.1)	Mesh resolution of domain (Section 4.3.2.2)	Length of sampling period (Section 4.3.2.3)	Fluctuating velocity algorithm (Section 4.3.2.4)	Subgrid-scale Schmidt number (Section 4.3.2.5)	Subgrid-scale model (Section 4.3.2.6)	Smagorinsky constant (Section 4.3.2.7)
4H	$y^+ = 1.6$	$1200\Delta t^*$	VM-190	$Sc_{SGS} = 0.4$	SSL	$C_s = 0.1$
1H	$y^+ = 3.4$	$400\Delta t^*$	NP	$Sc_{SGS} = 0.2$	DSL	$C_s = 0.12$
2H	$y^+ = 7.1$	$800\Delta t^*$	SS	$Sc_{SGS} = 0.3$	WALE	$C_s = 0.15$
3H	$y^+ = 13.8$	$2000\Delta t^*$	VM-150	$Sc_{SGS} = 0.5$	DKE	
5H	$y^+ = 25.4$		VM-230			

4.3.2.1 Effect of upstream distance of computational domain

The selection of the upstream distance between building and domain inlet should balance two issues. A small upstream distance may result in interference in the development of inflow (Franke et al., 2007; Tominaga et al., 2008b); a large upstream distance, however, may cause unintended horizontal gradients in the flow variables and in turn an inhomogeneous ABL in the computational domain. Both issues could deteriorate the accuracy of the simulated results. This section analyzes the influence of upstream distance. In addition to the upstream distance of 4H used in the reference case, four more computational domains with different upstream distances (namely, 1H, 2H, 3H, and 5H) are created for comparison. As shown in Figure 4.11, the influence of upstream distance on mean velocity and concentration fields is not obvious, except for the upstream distance of 1H, which results in some discrepancies in both velocity and concentration fields. These results imply that an upstream distance down to 2H does not obviously interfere with flow and up to 5H does not result in obvious horizontal gradients in the flow.

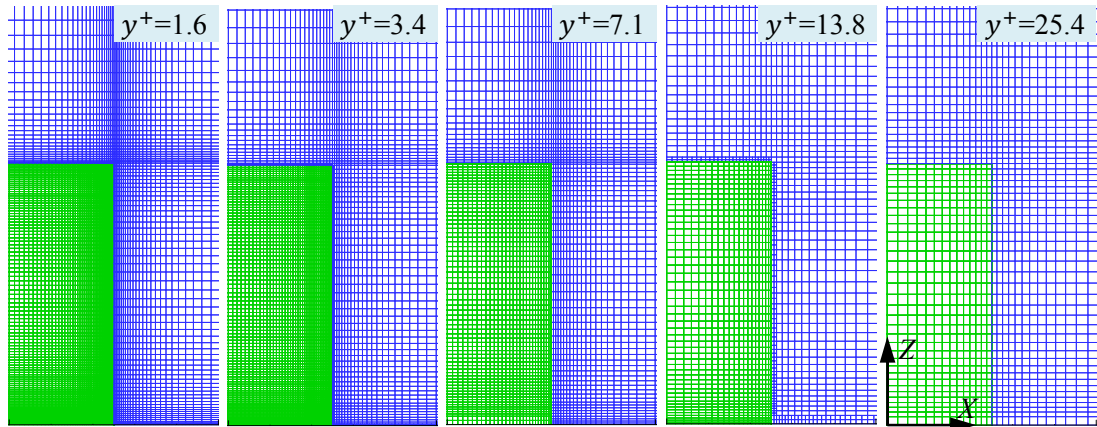


Figure 4.12 Schematic view of a part of the five different mesh systems (side view).

4.3.2.2 Effect of mesh resolution

This section examines the effect of mesh resolution on LES modeling. The aim is not to find an optimal mesh system with grid-independent solutions, as that cannot exist in LES. In addition to the mesh (with an average y^+ of 1.6) in the reference case, four other types of mesh systems are constructed for comparison, as shown in

Figure 4.12. These are obtained by increasing the height of the first cells in the reference case while leaving the stretching ratio unchanged. Given that a near-wall cell with y^+ larger than 30 is generally considered to fall into the fully turbulent outer layer that is outside the viscous-affected inner layer (Fluent, 2010), the coarsest mesh is defined as having an average y^+ of 25.4, which is less than 30.

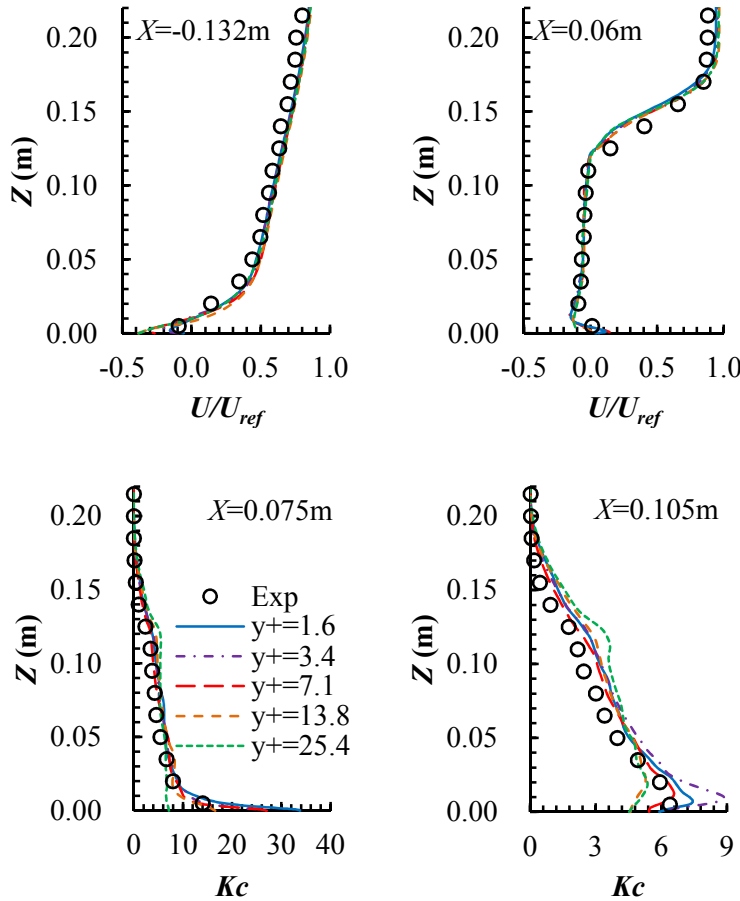


Figure 4.13 Effect of mesh resolution on mean velocity and concentration fields.

The results (see Figure 4.13) show that varying y^+ in the range of 0-30 does not influence the predicted velocity field, but does have an obvious effect on the concentration field, particularly in regions close to the domain ground. It is interesting to find that a finer mesh does not necessarily guarantee a more accurate concentration field. In the present case, the mesh with $y^+ = 7.1$ performs better than the mesh with $y^+ = 3.4$. Mass transport is mainly represented by convective and

turbulent fluxes, with the former normally the dominant transport process (Gousseau et al., 2012; Tominaga and Stathopoulos, 2010; Gousseau et al., 2011). The convective flux at a specific location is defined as the product of local mean velocity and local mean concentration; it is $\langle \hat{u} \rangle \langle Kc \rangle$ for the streamwise direction and $\langle \hat{v} \rangle \langle Kc \rangle$ for the spanwise direction. Figure 4.14 presents the comparison of streamwise convective flux, $\langle \hat{w} \rangle \langle Kc \rangle$, which confirms that a coarser mesh may perform better than a finer mesh. Some previous studies have found this inconsistent relationship between mesh resolution and accuracy of results (Gousseau et al., 2013, Celik et al., 2005; Klein, 2005; Meyers et al., 2003). They pointed out that modeling and numerical errors in some scenarios may have opposite signs and thus may cancel each other out, significantly decreasing the total error on a coarser mesh system, which could be less than that on a finer mesh system.

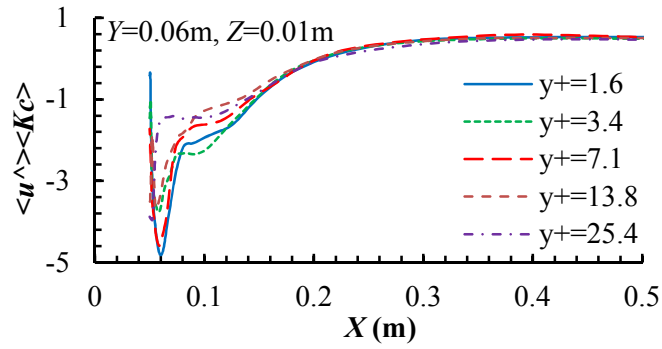
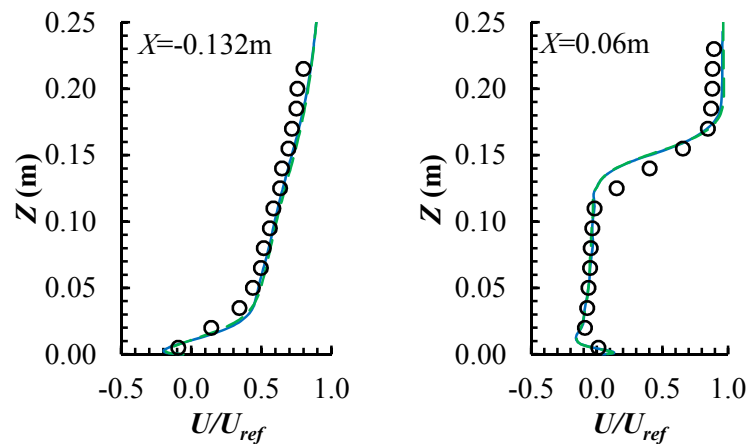


Figure 4.14 Effect of mesh resolution on streamwise convective flux, $\langle \hat{u} \rangle \langle Kc \rangle$.



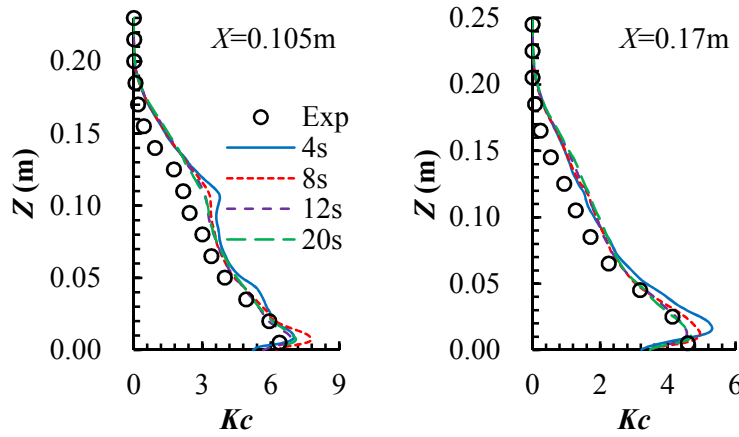


Figure 4.15 Effect of length of sampling period on mean velocity and concentration field; character ‘s’ in the legend represents Δt^* .

4.3.2.3 Effect of length of sampling period

For transient simulations, the mean field of variables is obtained by taking an average over a specific sampling period. The selection of an appropriate period length is important for obtaining accurate mean fields, especially for those variables with high fluctuations. For different flow problems, the time-independent sampling periods should be different; furthermore, they can only be determined through sensitivity tests. In addition to $1200 \Delta t^*$, which is used in the reference case, three more sampling periods, $400 \Delta t^*$, $800 \Delta t^*$, and $2000 \Delta t^*$ are examined. The results are presented in Figure 4.15. They indicate that $400 \Delta t^*$ is sufficiently long to produce a stable mean velocity field around the building; however, $1200 \Delta t^*$ of computation is needed to obtain a stable mean concentration field. This finding is important. It demonstrates that different flow variables may require completely distinctive sampling periods to obtain time-independent fields, which suggests that sensitivity tests of the length of sampling period must be conducted for each variable of interest.

4.3.2.4 Effect of inflow fluctuating algorithm

4.3.2.4.1 Fluctuating characteristics of inlet velocity

Before examining the effect of the inflow fluctuating algorithm (see Section 2.5.2.3) on mean velocity and concentration fields, the fluctuating characteristics of

the inlet velocity profiles are compared. Figure 4.16 presents the evolution of the dimensionless velocity components ($\hat{u} = u/U_b, \hat{v} = v/U_b, \hat{w} = w/U_b$) at the height of the building near the inlet plane with time. The velocity components are almost constant over time when the NP algorithm is used, whereas they have the largest fluctuating intensities under the VM algorithm, although their average values are almost the same. The velocity fluctuations are quantified using the standard deviations ($\sigma_{\hat{u}}$) of the streamwise velocity component \hat{u} (see Figure 4.16). The

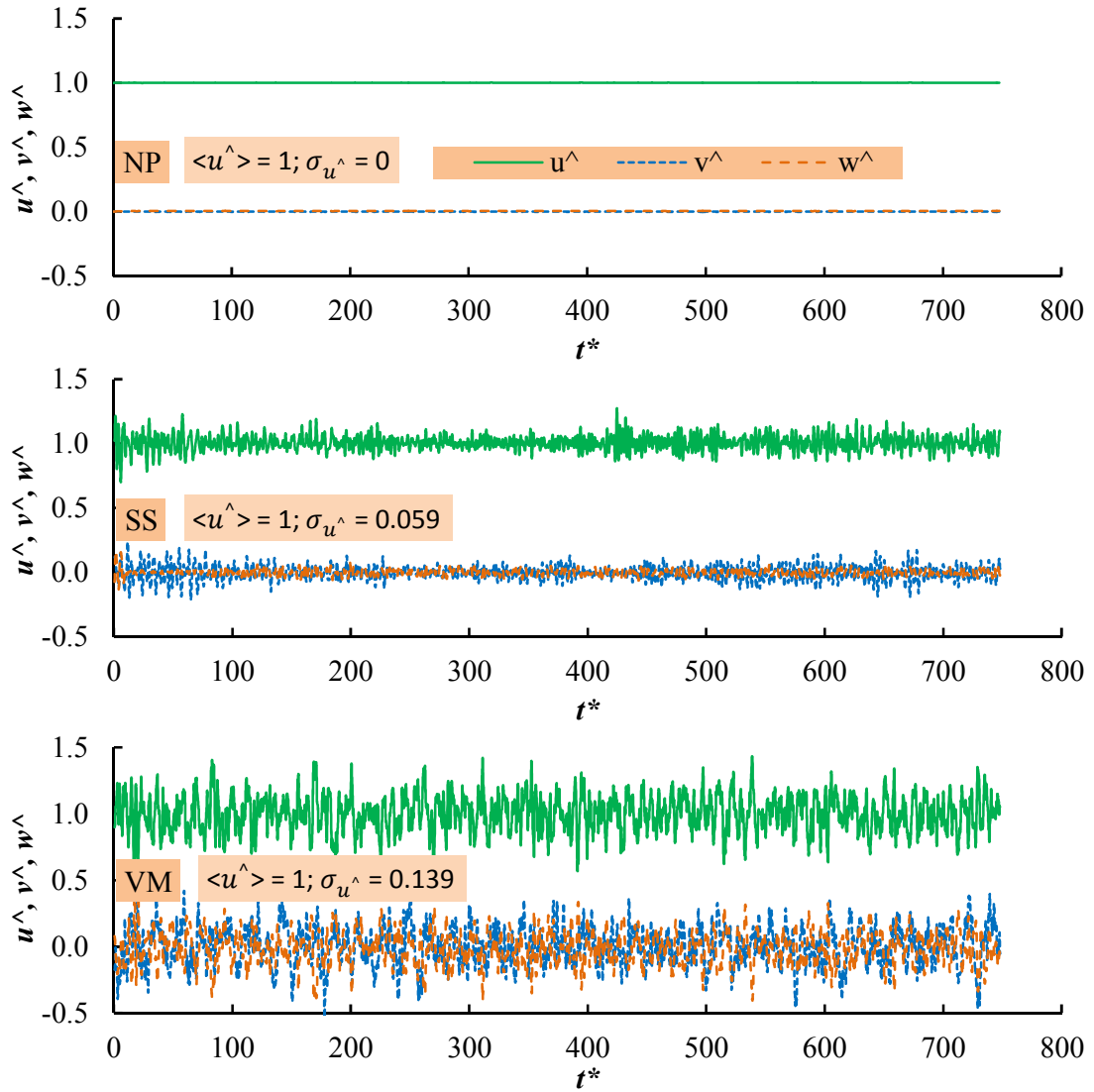


Figure 4.16 Comparison of the fluctuating characteristics of inlet velocity when using different inflow fluctuating algorithms; the full names of the legends can be found in Section 2.5.2.3.

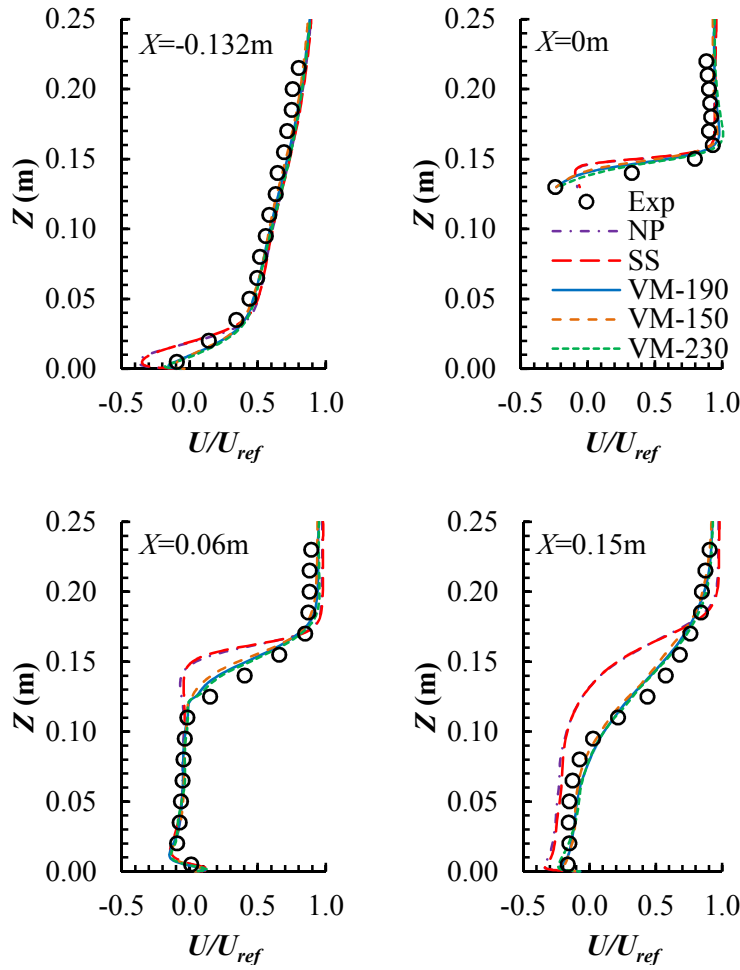


Figure 4.17 Effect of inflow fluctuating algorithm on mean velocity field; the full names of the legends can be found in Section 2.5.2.3; 190, 150 and 230 are number of vortices.

results show that the fluctuating intensity of the velocity components given by the SS algorithm is less than half of that given by the VM algorithm. To the best of the author's knowledge, this difference between SS and VM algorithms has not been previously identified. This is an important finding, which increases the understanding of the different ways the two algorithms introduce perturbations; it provides basic knowledge for further comparisons of the way the two algorithms predict velocity and concentration fields.

4.3.2.4.2 Velocity field

Figure 4.17 presents the comparison of the mean velocity profiles predicted using

different inflow fluctuating algorithms. The results show that the influence of the number of vortices in VM on the predicted velocity field is negligible. The velocity fields given by NP and SS are almost the same; however, they deviate from the experimental data in some areas. Owing to the no or lower perturbations imposed on the inlet velocity profile, the NP and SS predict an unreasonable reverse vortex near the ground in the upstream region (see $X=-0.132$ m) and underpredict velocity magnitudes in regions both above and downstream of the building, although the size of the recirculation region in the wake is not obviously affected. The underprediction of velocity above the building roof means an inaccurate prediction of roof reattachment. Saathoff et al. (1995) have analyzed the effect of free-stream fluctuation intensity on the location of shear layer reattachment on building surfaces. They pointed out that an approaching flow with lower fluctuations may lead to a larger reverse vortex on the roof, delaying the roof reattachment point.

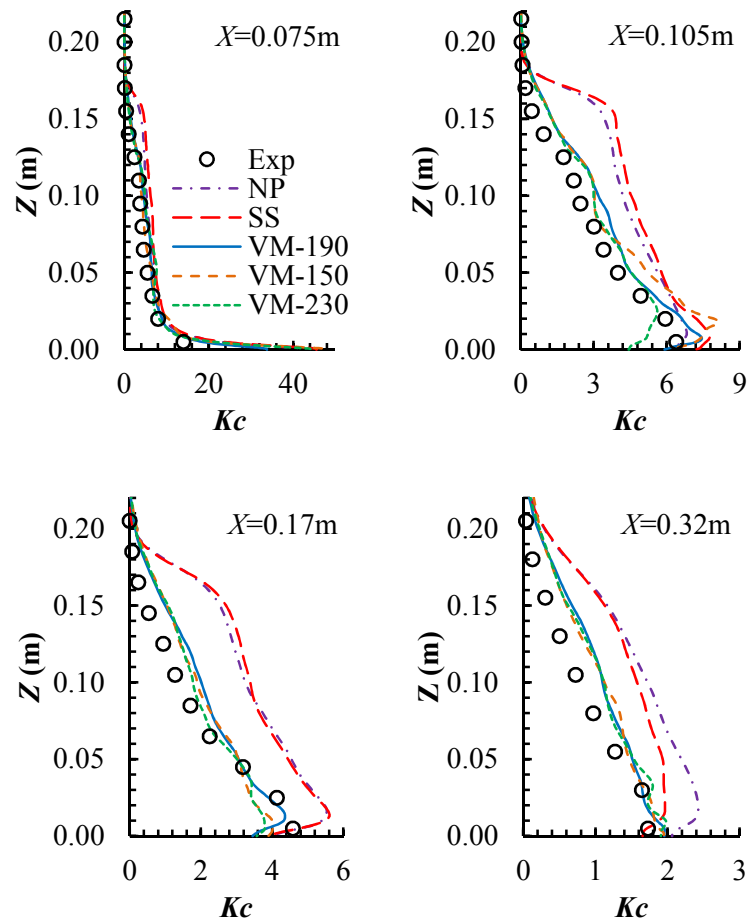


Figure 4.18 Effect of inflow fluctuating algorithm on the concentration field; the legends mean the same with those on Figure 4.17.

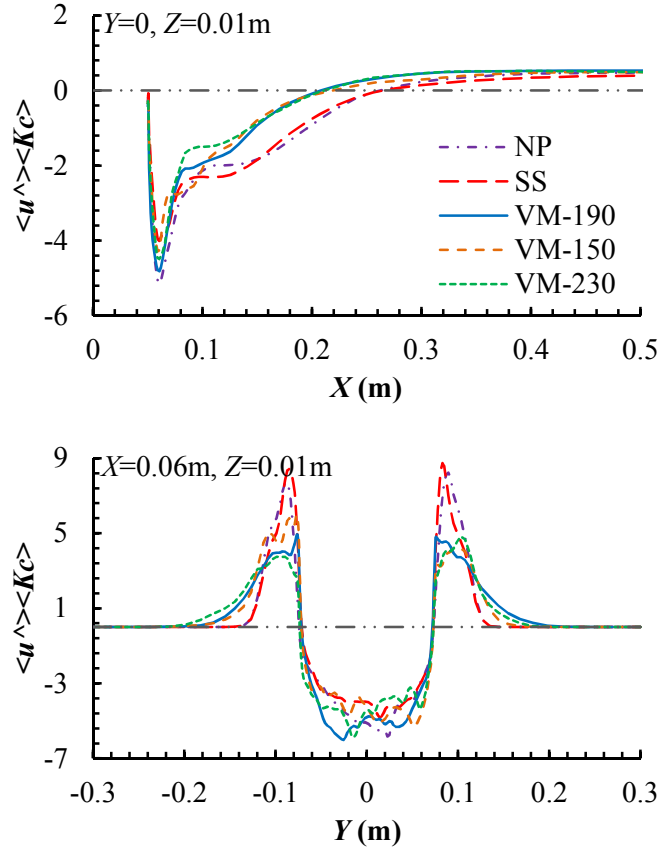


Figure 4.19 Effect of inflow fluctuating algorithm on streamwise convective flux, $\langle \hat{u} \rangle \langle Kc \rangle$.

4.3.2.4.3 Concentration field

Figure 4.18 presents the comparison of the mean concentration profiles produced using different inflow fluctuating algorithms. Again, the number of vortices in the VM algorithm does not have an obvious influence on the concentration field. The lower velocity values given by the NP and SS (see Figure 4.17) algorithms directly result in an overprediction of concentration in the downstream region. However, the essential reason for such an overprediction should be the lower mass and momentum mixings due to the low-fluctuation inflow conditions. Figure 4.19 shows the comparison of streamwise convective flux, where the negative fluxes indicate reverse flows of concentration. It can be seen that the use of NP and SS algorithms leads to a stronger and longer negative-flux region along the streamwise direction (see Figure 4.19 (a)). Gousseau et al. (2011, 2012) have analyzed such negative-flux phenomenon and the counter-gradient mechanism that describes mass flux from a low-concentration region to a high-concentration region. This negative-flux region

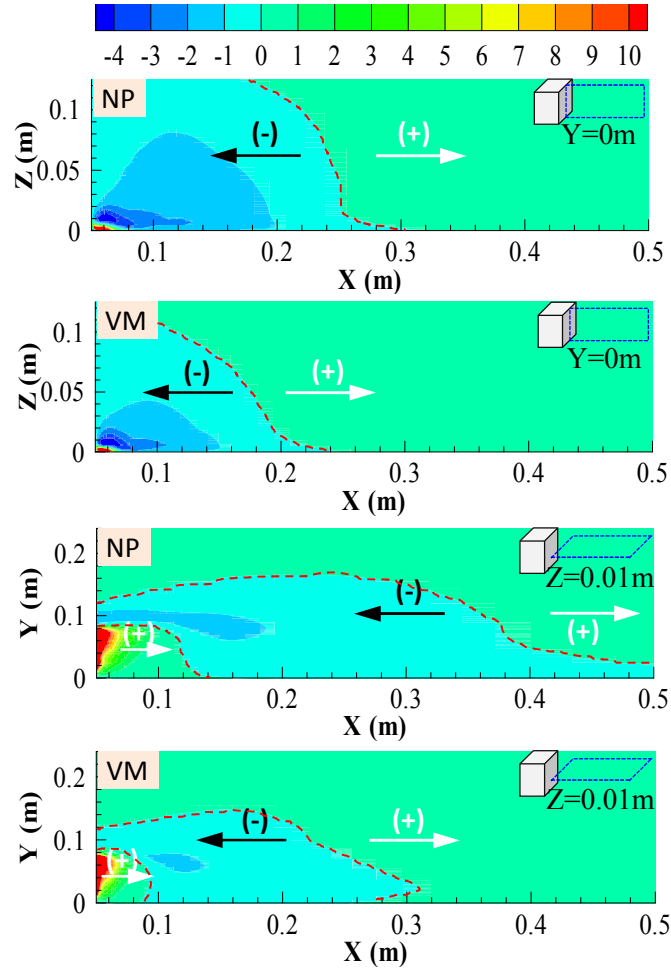


Figure 4.20 Contour of streamwise convective flux; dashed red lines mark the interfaces with flux equal to zero; arrows indicate flux directions; and ‘(+)’ ‘(-)’ indicate sign of flux.

greatly avoids the streamwise diffusion of concentration and thus retains high concentration values (see Figure 4.18). To ensure mass conservation, the use of NP and SS algorithms gives stronger streamwise concentration fluxes in the symmetrical lateral regions (see Figure 4.19 (b)). Figure 4.20 illustrates the contours of the streamwise convective fluxes on both a vertical and a horizontal plane. These contours clearly show that the use of a NP algorithm significantly lowers the mass mixing effect in the wake and in turn produces a much larger high-concentration negative-flux region.

4.3.2.5 Effect of subgrid-scale Schmidt number

To calculate the SGS turbulent mass flux, a Schmidt number for the SGS motion (Sc_{SGS}) is usually required (Fluent, 2010). Few previous studies have examined the effect of Sc_{SGS} on concentration transport (Tominaga and Stathopoulos, 2007). In Ansys Fluent (2010), the default value of Sc_{SGS} is 0.4, and other studies (e.g., Tominaga et al., 1997) have used 0.5. This section analyzes the influence of Sc_{SGS} on the mean concentration field; Figure 4.21 presents the results. It can be observed that the influence of Sc_{SGS} on concentration field is almost negligible. A comparison of the spanwise convective mass flux finds that a larger Sc_{SGS} can provide a longer negative-flux region along the streamwise direction (no figure presented).

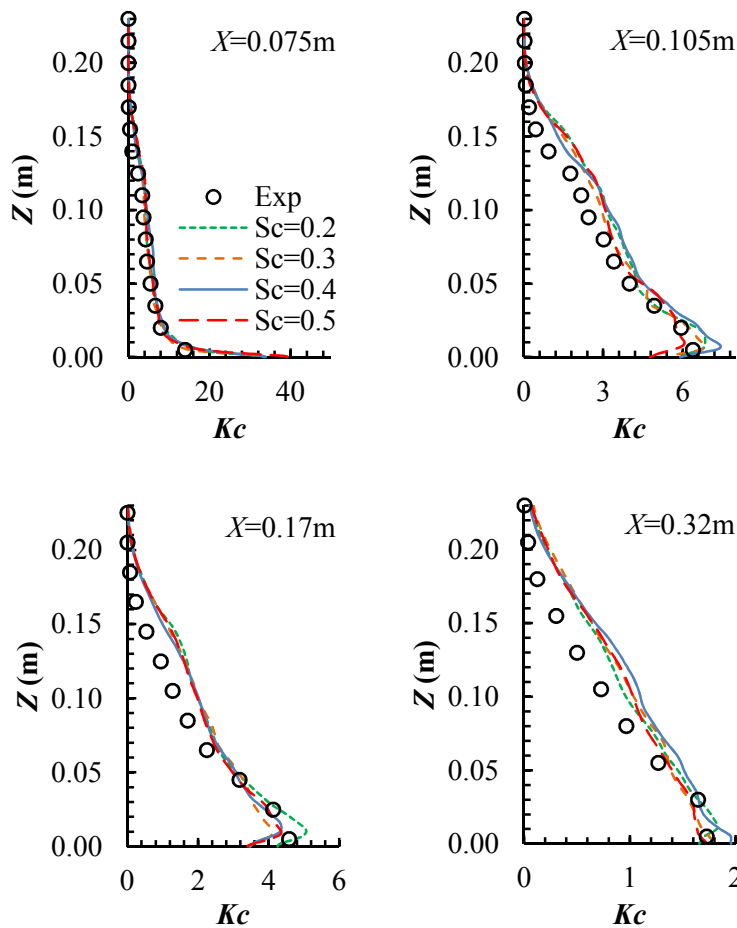


Figure 4.21 Effect of SGS Schmidt number on mean concentration field; ‘Sc’ represents Sc_{SGS} .

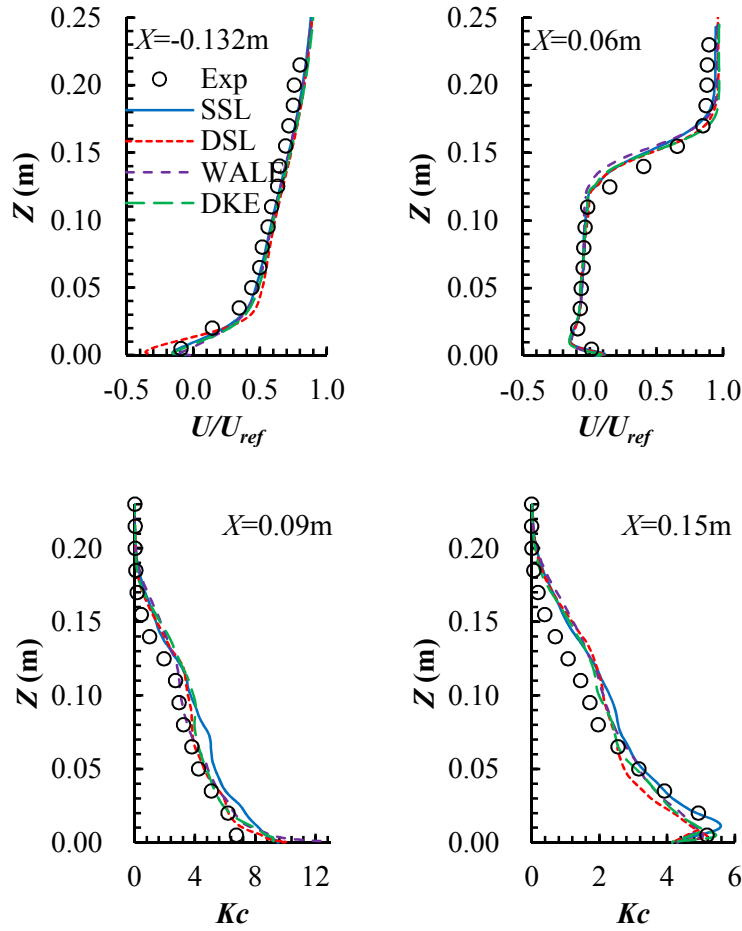


Figure 4.22 Effect of SGS model on mean velocity and concentration fields; the full names of the legends can be found in Section 2.5.2.2.

4.3.2.6 Effect of SGS model

The SGS models described in Section 2.5.2.2 are compared in this section. As shown in Figure 4.22, the influence of the SGS model is not obvious in predicting velocity and concentration fields around the building. This study finds that the DSL model shows some computational instability and a small deficiency in predicting near-wall flows (see $X=-0.132$ m), which supports the findings of Iizuka and Kondo (2004). To treat the stability problem, this study uses a larger time step size in each time step; this uses around 30% more computational time than the SSL model. Theoretically, as explained in Section 2.5.2.2, the WALE and DKE models should be more accurate than the SSL model. However, the simulated results do not show this, probably because the flow problem considered in this study is not appropriate for

examining their superiorities. For example, the WALE model is particularly powerful for predicting flow problems with strong wall effects, such as cavity flows (Barhaghi and Davidson, 2007; Ben-Cheikh et al., 2012). In addition, as modeling error is always convoluted with numerical error in the LES context, improved predictions might not be achieved by using advanced SGS models and/or numerical methods (Meyers et al., 2003; Geurts and Fröhlich, 2002). Overall, the SSL model that is used most frequently in the literature is an appropriate choice for the simulation of flow and dispersion in built environments.

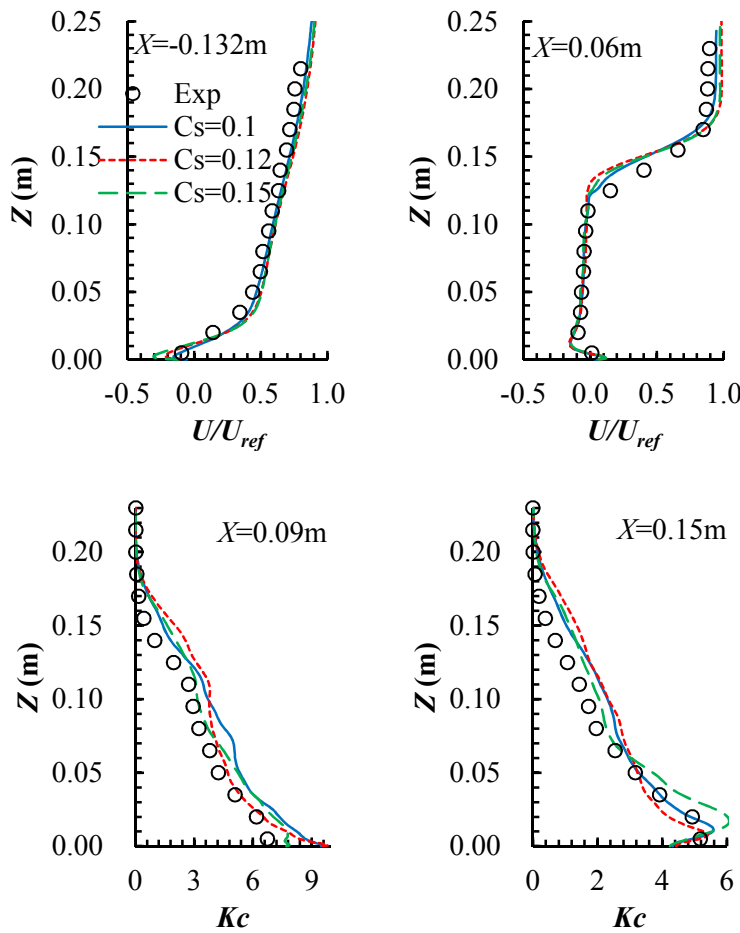


Figure 4.23 Effect of C_s on mean velocity and concentration fields.

4.3.2.7 Effect of C_s of the standard Smagorinsky-Lilly model

Based on a specific mesh system, C_s is the Smagorinsky constant that determines the mixing length of the subgrid scales that in turn influence the

calculation of turbulent viscosity (Fluent, 2010). There is no universal constant for C_s , which can be different for different flow problems. A higher value of C_s may cause excessive damping to large-scale fluctuations when transitional flows are present, as in near-wall flows. In addition to $C_s = 0.1$, this section compares C_s values of 0.12 and 0.15. Figure 4.23 presents the results. Changing C_s within the range of 0.1-0.15 does not have an obvious effect on the flow and concentration fields, except that the use of 0.15 overpredicts concentration values in ground level regions (see $X=0.15$ m). This suggests that further increasing the value of C_s is not reasonable for the present flow problem. Given that a DSL model with a dynamically computed C_s does not necessarily improve the accuracy of the results (see Section 4.3.2.6), a constant C_s of 0.1 is an appropriate choice for the modeling of flow and dispersion in built environments.

4.3.3 Summary

This section presents an investigation of the factors that influence flow and dispersion around an isolated building in a LES model. The LES model is validated against two sets of high-fidelity wind tunnel experimental data. Both velocity and concentration fields predicted with the reference settings show very good agreements with the experimental data, confirming the high accuracy of the LES model. The influencing factors analyzed are upstream distance, mesh resolution, sampling period, inflow condition, SGS model, SGS Schmidt number, and Smagorinsky constant. To the best of the author's knowledge, the analyses of these influencing factors has not (or not comprehensively) been reported in previous studies. These analyses lead to the following observations.

(a) The upstream distances of 3H, 4H, and 5H do not show obvious differences in terms of the accuracy of mean velocity and concentration fields.

(b) Varying y^+ within the range of 0-30 does not obviously change the velocity field, but it greatly changes the concentration field. This suggests that the concentration field is more sensitive to mesh resolution, as the concentration field is generally governed by more complex transport mechanisms than the velocity field. A finer mesh does not necessarily guarantee a better result. A mesh system with an

average y^+ around 1-2 is recommended.

(c) A sampling period of $400 \Delta t^*$ is sufficiently long to produce a stable velocity field, but $1200 \Delta t^*$ is required to achieve a stable concentration field. This again suggests that different variables may have completely different sensitivities to the same influencing factor.

(d) The fluctuating intensity of the velocity components provided by the Spectral synthesizer is less than a half of that provided by the Vortex method. The use of the Vortex method generates accurate velocity and concentration fields, whereas the use of Spectral synthesizer results in inaccurate momentum and mass mixings around the building. This should be an important finding, as the latter is frequently used in similar studies.

(e) The effect of the SGS Schmidt number (Sc_{SGS}) on mass flux is almost negligible. The value of 0.4 is appropriate.

(f) The effect of an SGS model on velocity and concentration fields is not obvious. The standard Smagorinsky-Lilly model is appropriate.

(g) The Smagorinsky constant (C_s) of 0.1 is suggested for the standard Smagorinsky-Lilly model. A large value of C_s (0.15 or larger) overpredicts concentration values at the ground level, as it causes excessive damping of large-scale fluctuations.

4.4 Potential of using reduced-scale models in CFD simulations

4.4.1 Theoretical analysis

This section takes the $k - \varepsilon$ model of RANS simulation as an example to test the hypothesis that the use of reduced-scale models in CFD simulations can save numerical resources. The findings are also applicable to other RANS models and LES models. For a $k - \varepsilon$ turbulence model, there are two commonly used near-wall treatment approaches: the standard wall functions and the two-layer model. The standard wall functions work best with first cells not only being in the fully turbulent outer region but also being close to the viscosity-affected inner region, namely with the y^+ value of first cells larger than but close to 30 (Casey and Wintergerste, 2000;

Blocken et al., 2007). Meanwhile, the two-layer model requires a very fine near-wall mesh (i.e., with y^+ close to 1) to resolve the inner region with a one-equation model (Wolfshtein, 1969). Fulfilling these requirements is a basic prerequisite of a successful CFD simulation.

As an indicator of near-wall mesh density, the nondimensional distance y^+ is defined as:

$$y^+ = \frac{u_P y_P}{\nu_t} \quad (4.21)$$

where y_P the distance between the centroid (P) of a first cell and its closest wall, u_P is the velocity at P , and ν_t the kinematic viscosity. For equilibrium boundary layers, u_P is equal to the friction velocity u^* , which can be computed by:

$$u^* = C_\mu^{1/4} k_P^{1/2} \quad (4.22)$$

where C_μ is a model constant and k_P the turbulence kinetic energy at P . Substituting Equation (4.22) into (4.21) obtains:

$$y^+ = \frac{C_\mu^{1/4} k_P^{1/2} y_P}{\nu_t} \quad (4.23)$$

Under a specific condition, C_μ and ν_t are constants, and thus only k_P and y_P are variables that may influence y^+ .

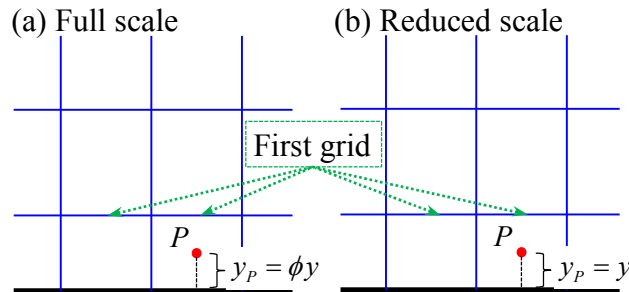


Figure 4.24 Comparison of y_P between a full-scale case and its reduced-scale case, which use the same mesh system except for a scaling factor of ϕ .

Based on similarity criteria, CFD simulations on a full-scale model and its reduced-scale model (assuming a scaling factor of ϕ) should use the same nondimensional inflow conditions, namely the same nondimensional mean velocity (U/U_H), turbulence kinetic energy (k/U_H^2), and dissipation rate ($(\varepsilon \cdot H)/U_H^3$). Here the same reference velocity at the building height (U_H) is used in the two cases to facilitate analysis. It is interesting to consider a scenario in which both cases have the same mesh number and mesh arrangement — in other words, they use the same mesh system except for a scaling factor of ϕ . Obviously, there is a factor of ϕ in y_p between the two cases (see Figure 4.24). In addition, because the two cases have the same k/U_H^2 profile and U_H , the two cases should have the same k_p . Therefore, according to Equation (4.23), the y^+ value of a near-wall cell in the reduced-scale case should be theoretically $1/\phi$ of that of the full-scale case. This implies that fewer cells are needed for a reduced-scale model to achieve a target y^+ than in the full-scale model, and thus the reduced-scale model has the potential to save numerical sources.

In this deduction, there is no doubt that the factor ϕ in y_p is between the full-scale case and its reduced-scale case. However, several factors may influence the relationship of k_p between the two cases. In particular, owing to the change of y^+ , the position of P may shift from a viscosity-affected layer to a fully turbulent layer or the converse. Such a change in position could result in different predictions for k_p , considering the fact that different computing methods are used in different layers.

In addition, with the same U_H , different model scales correspond to different Reynolds numbers. Even though Reynolds numbers are independent, behaviors of small eddies could be different under different Reynolds numbers (Lim et al., 2007). This could also result in different predictions of k_p because near-wall regions contain a large number of small eddies. Therefore, the real difference in y^+ between a full-scale case and its reduced-scale case is probably not accounted for by ϕ . This is further examined in Section 4.4.3.1.

4.4.2 CFD simulations: case setup

The geometrical model, modeling and numerical methods used here are the same with those described in Section 4.2.3. Note that the inlet profiles of Gorlé et al. (2009) and the two-layer model are used, and thus the mesh number is 3.5×10^6 . This section only presents the case setup. Table 4.5 summarizes the cases that are created to examine the influence of model scale on near-wall y^+ values and prediction accuracy of the velocity field. The numerical reproduction of the wind tunnel experiment, as described in Section 4.2.3, is treated as a reference case (Case A). Directly scaling up the building model, mesh system, and computational domain by factors of 4, 13.3, and 200 obtains Cases B, C, and D, respectively. Note that Cases A, B, C, and D have the same mesh number and mesh arrangement method. Cases B, C, and D are conducted using the same numerical method as Case A, except for the inlet boundary conditions. As mentioned before, the same dimensionless velocity (U/U_H), turbulence kinetic energy (k/U_H^2), and dissipation rate ($(\varepsilon \cdot H)/U_H^3$) are used at the domain inlet in the four cases. As a result, the roughness and model coefficients for Case B are: $z_0 = 0.003$ m, $K_s = 0.008$ m, $u^* = 0.374$ m/s, $M_1 = 0.0228$, and $M_2 = 0.3738$; for Case C are: $z_0 = 0.01$ m, $K_s = 0.027$ m, $u^* = 0.374$ m/s, $M_1 = 0.02117$, and $M_2 = 0.3472$; and for Case D are: $z_0 = 0.15$ m, $K_s = 0.4$ m, $u^* = 0.374$ m/s, $M_1 = 0.0183$, and $M_2 = 0.2992$. Note that the U_H is 6 m/s. For these cases, Reynolds independence is checked and is achieved.

Table 4.5 A summary of cases created to examine the influence of model scale.

Case	A	B	C	D	E
Model scale	1:200	1:50	1:15	1:1	1:1
Mesh number ($\times 10^6$)	3.5	3.5	3.5	3.5	6.4

An additional case (Case E) is created, which is the same with Case D, except for its mesh system. Based on the same stretching ratio of Case D, the mesh system of Case E is greatly refined by increasing the mesh number by 83.5%. The intention of creating Case E is to quantitatively test reduced-scale models' potential to save numerical resources.

4.4.3 CFD simulations: results and analyses

4.4.3.1 Influence of model scale on near-wall y^+ values and numerical accuracy

Table 4.6 presents the average y^+ values on building surfaces and domain ground for Cases A, B, C, and D. With the same mesh number, scaling up the model can increase the average y^+ value, which is supported by the previous theoretical analysis. However, their increasing ratios are not equal to, but less than, the corresponding increasing ratios of model scale. Table 4.6 shows the relationship of the two types of increasing ratios, indicated by ψ . The inconsistency between the two types of increasing ratios should be attributed to the different k_p values given by different model scales, as theoretically analyzed in Section 4.4.1.

Table 4.6 Influence of model scale on average y^+ value on building surfaces and domain ground. ψ is the ratio of the increasing ratio of y^+ and the increasing ratio of model scale, based on Case A.

Cases	A	B	C	D
Average y^+	1.6	5.4	15.6	180.1
ψ (%)	-	84.4	73.1	56.3

Comparison of y^+ values clearly shows that an increase of model scale shifts the centroids of first cells far away from walls and in turn coarsens the near-wall mesh. Typically, the full-scale case (Case D) has a very coarse near-wall mesh density ($y^+=180.1$) that cannot be applied to a near-wall model like the two-layer model. Meanwhile, the reduced-scale case (Case A) has a sufficiently fine near-wall mesh ($y^+=1.6$) to be applied to the two-layer model to resolve the viscosity-affected inner layer, even if the two cases have the same mesh number. This implies that more cells must be added to a full-scale case to generate the same y^+ value with a reduced-scale case. Again, this suggests that the use of a reduced-scale model benefits from using fewer cells to achieve a target y^+ value.

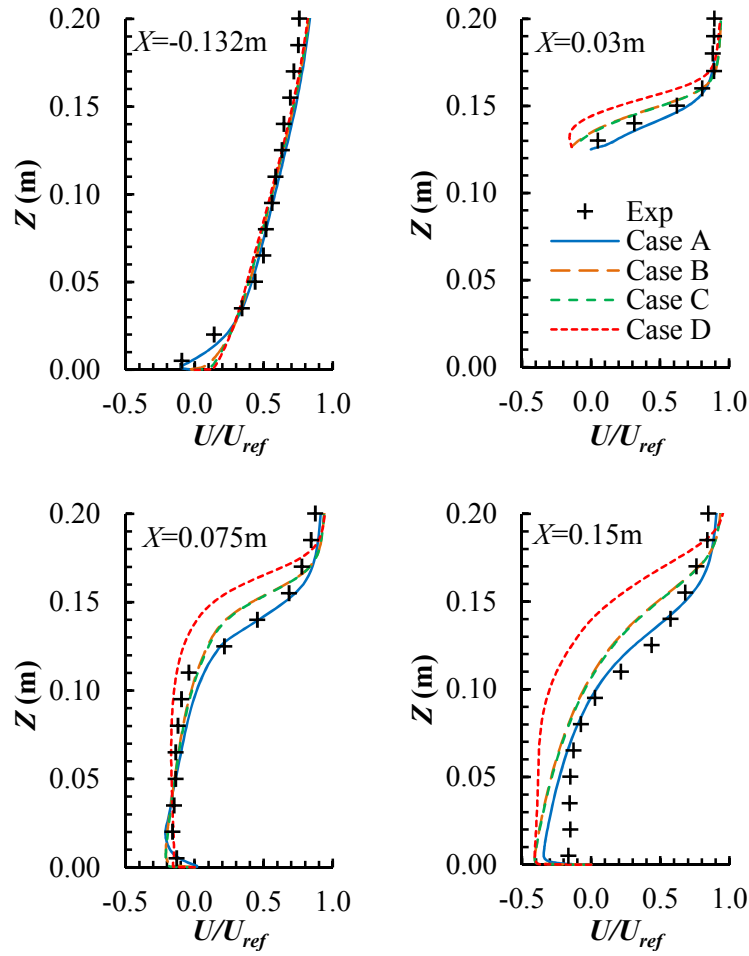


Figure 4.25 Mean velocity values predicted using different model scales with the same mesh number.

Figure 4.25 presents the comparison of mean velocity values predicted using different model scales, where the experimental data is also plotted for validation purposes. It shows that the simulated results of the reference case (Case A) fit well with the experimental data, except in the wake region (see $X=0.15$ m). This deficiency should be attributed to the inherent underperformance of $k-\varepsilon$ models (Murakami, 1998), which has been analyzed in Section 3.4.1. Owing to increased y^+ values, using large-scale models leads to deviations of simulated results from the experimental data, especially in the levels of the roofs of buildings and domain ground. It is clear that results predicted by Case D become unacceptable. It is believed that the mesh system of Case D must be refined to allow a better prediction of the near-wall flow. This indicates that the use of a full-scale model requires more cells to attain the same prediction accuracy as a reduced-scale model.

4.4.3.2 Reduced-scale models' potential to save numerical resources

The above sections demonstrate qualitatively that there is a potential to save on numerical resources by using reduced-scale models. This section explores this potential quantitatively by evaluating the mesh number, y^+ values, and prediction accuracy of the refined full-scale case (Case E). The average y^+ value generated by Case E is 16.3. Comparing Case E with Case D shows that an increase of 83.5% in the mesh number decreases the average y^+ value by 90.9%. It is found that the velocity field given by Case E is very close to that given by Case C (i.e., the 1:15 reduced-scale case), which should be attributed to the similar y^+ value of the two cases. The comparisons above provide a quantitative understanding of the number of cells required to refine a full-scale case to achieve the same y^+ value and prediction accuracy with its reduced-scale case. Obviously, further refining the mesh system of Case E to decrease its y^+ value to that of Case A should require a large number of additional cells, demonstrating reduced-scale models' large potential to save numerical resources.

However, this refinement work is not conducted here because it should be just a mesh independence test and is thus not the interest of this study. In addition, the exact number of cells that can be saved with a reduced-scale model is highly problem-dependent. Factors like the scaling factor, the target y^+ value, and the complexity of the flow problem can influence this number.

4.4.4 Discussion

This section focuses on discussing the limitations of using reduced-scale models in CFD simulations. The possible changes of CFD treatment associated with using reduced-scale models are also discussed.

The use of reduced-scale models in CFD simulations holds almost all limitations and disadvantages of reduced-scale wind tunnel experiments. The main disadvantage of using reduced-scale models in many practical problems is the difficulty of fulfilling similarity requirements. For any specific flow problem, strictly obeying important similarity criteria is the basic prerequisite of using reduced-scale models in

CFD simulations.

In the simulations of environmental processes in complex urban areas that consist of many constructions with different dimensions, largely scaling down the physical model may lead to disappearance of some small constructions aerodynamically, which, however, could have significant influences on the simulated results in a target area. Specifically, based on a same wind speed, a fully rough regime at a full-scale model could be changed to a transitional or even a hydrodynamically smooth regime due to the reduction of roughness heights. With regard to this concern, similarity criteria should be ensured based on not only the target buildings but also those surrounding constructions of pronounced influences.

When scaling down a full-scale model to a reduced-scale model in CFD simulations, the changed mesh resolution, in terms of near-wall y^+ values, may demand for a different near-wall treatment method. As shown in Section 4.4.3.1, based on the same mesh number and mesh arrangement, scaling down the building model could significantly lower the near-wall y^+ value, depending on the scaling factor. For example, the full-scale model (Case D) has an average y^+ value of 180.1, while its 1:200 reduced-scale model (Case A) has an average y^+ value of 1.6. Such a large decrease in y^+ value substantially changes the location of the first cells from fully turbulent region to viscous affected laminar region. In this circumstance, the commonly used standard wall functions that are appropriate to the full-scale case are no longer valid to the reduced-scale case. For those cases with very low y^+ values, advanced near-wall models, such as the two-layer model, should be used.

In addition, this study only discusses the time independent scenarios. For time dependent scenarios, one important aspect is the requirement of limiting Courant number to maintain stability (Fluent, 2010). At a certain local wind speed, Courant number is proportional to the time used to traverse a cell and is inversely proportional to the cell size. Courant number would not be changed by using a reduced-scale model when linear equations are solved, as the flow traverses a smaller computational domain faster. However, for the nonlinear Navier-Stokes equations corresponding to boundary layers and separation regions, the computational domain should have regions with parabolic, elliptic and even hyperbolic flow patterns

simultaneously. In such circumstances, in order to maintain stability at a reduced-scale model, the time step size must decrease by the second power or even third power of the cell size. This significant decrease in time step size may be impractical in CFD simulations, which will limit the use of reduced-scale models.

4.4.5 Summary

Theoretical analysis and numerical case study are employed to examine the hypothesis that reduced-scale models for CFD simulations of wind flow and related processes save numerical resources. This hypothesis is found to be correct. Reduced-scale models require fewer cells than a full-scale model to achieve a target near-wall mesh density (in terms of y^+).

Theoretically, the smaller a model, the more numerical resources can be saved. However, reduced-scale models must not violate similarity criteria. Reduced-scale models' potential to save numerical resources is generally very large, depending mainly on the scaling factor, the target y^+ value, and the flow problem.

Chapter 5

Quality assessment and improvement of CFD simulation of single-sided natural ventilation

5.1 Introduction

This chapter presents the quality assessment and improvement of CFD simulation of single-sided natural ventilation. The sensitivity of several important computational parameters is investigated. Special attention is given to the independence of the near-wall mesh density, a topic that has rarely been studied before. A method is proposed that increases the near-wall mesh density by doubling only the first cells, with no changes to the other non-near-wall cells. The integration and the tracer gas decay methods are examined using both LES and RANS turbulence models under five different wind directions (with a 45° interval), since the performance of single-sided ventilation as a function of the wind direction is still unclear. In addition, the best combination, namely the LES model plus tracer gas decay method, is used to investigate the fluctuating characteristics of single-sided natural ventilation under various wind directions. Special attention is given to determining the dominant contributor (mean flow or fluctuating flow) of the ventilation rate under various wind directions. The full-scale measurements of the single-sided ventilation rate conducted by Dascalaki et al. (1996) are used to validate these studies.

5.2 CFD prediction of single-sided ventilation

5.2.1 Description of single-sided ventilation measurements

Four full-scale measurements of the single-sided ventilation rate were conducted by Dascalaki et al. (1996) in a PASSYS (passive solar components and systems testing) Test Cell, which is a fully equipped outdoor facility for thermal and solar monitoring (Vandaele and Wouters, 1994). The test cell was divided into two rooms, as shown in Figure 5.1; ventilation measurements were carried out in the smaller room (hereafter the “test room”), with the larger room sealed. The tracer gas concentration decay technique, using N₂O, was used to measure ventilation rates. This chapter focuses on one of the four measurements, which had an

occurrence-weighted incident wind angle of 60° (normal incidence being 0°) and a mean approaching wind speed of 1.95 ± 0.52 m/s at a height of 1.5 m. During this measurement, the average outdoor and indoor air temperatures were 23.85°C and 26.59°C , respectively, with the Archimedes number (Ar) equal to $0.02 \ll 1$, thereby the wind effect completely dominated the airflow exchange at the opening. The aerodynamic roughness height (z_0) of the surrounding terrain of the PASSYS Test Cell is not provided in the paper (Dascalaki et al., 1996) although this is a key factor in defining the inlet velocity and turbulence profiles of the CFD simulations. This study assumes an aerodynamic roughness height of $z_0 = 0.255$ mm, which is explained more in Section 5.2.2.2.

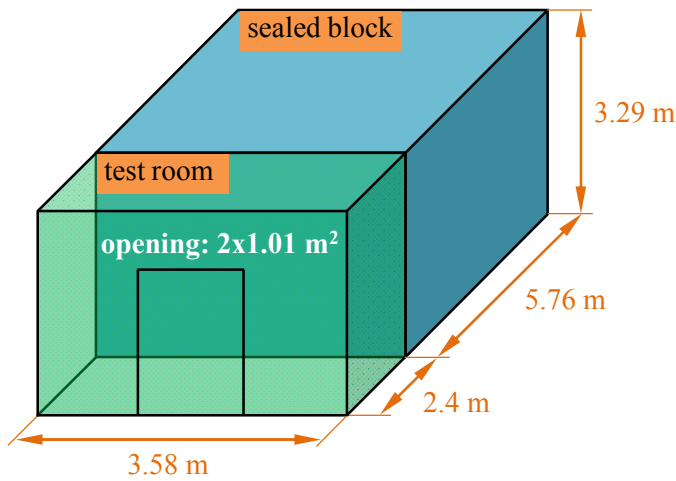


Figure 5.1 A schematic view of the building (test cell) used for model validation.

5.2.2 Computational settings and validation: reference case

This section describes the numerical method and detailed computational settings used to reproduce the full-scale measurement. The numerical results are then compared with the measured data for validation purposes. The computational settings used in this section are treated as the reference case for the subsequent sensitivity analyses.

5.2.2.1 Computational domain and mesh generation

The two-room test cell is placed in a computational domain, as shown in Figure 5.2. The selection of the distances between the domain boundaries and the test cell follows the suggestions of Franke et al. (2007). The resultant maximum blockage ratio is 2.2%, which is less than the maximum of 3% recommended by the best practice guidelines (e.g., Franke et al., 2007; Yoshie et al., 2007; Tominaga et al., 2008b). These domain dimensions are selected also based on the experience obtained from Chapter 4 of this thesis. The façade containing the opening is obliquely oriented to the domain inlet, with an incidence angle $\theta = 60^\circ$, where normal incidence is 0° .

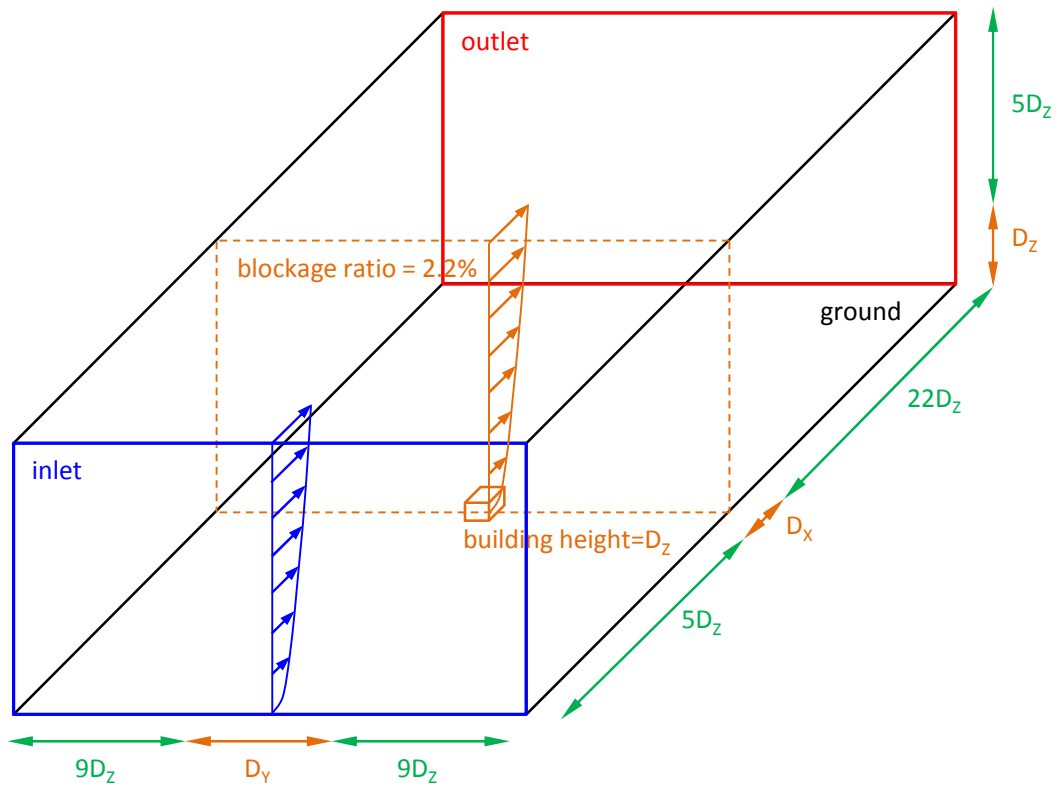


Figure 5.2 Schematic view of the computational domain.

Generating a high-quality mesh for the present case with coupled indoor and outdoor airflow is not easy, owing to the large differences in distance scales in the computational domain, namely the dimensions of the opening of the test room and the domain boundaries. The most important, but also the most difficult, region for high-quality mesh generation is the immediate vicinity of the test cell, so full control of the mesh quality in this region is required. The body-fitted (BF) mesh-generation

technique suggested by van Hooff and Blocken (2010) is used here, which constructs a mesh on the test cell and domain ground with full control of mesh resolution and the stretching ratio before sweeping them along a predefined vertical boundary to generate a mesh for the whole domain. Eventually, the domain is fully constructed with around 3.5×10^6 hexahedral cells, with a minimum grid width of 0.00045 m (around $0.00014 H$) and a maximum stretching ratio of 1.18 around the test cell. The minimum grid width is much smaller than that used in previous studies of natural ventilation (Caciolo et al., 2012, 2013; Bangalee et al., 2012), resulting in an average y^+ value of around 3.8 for the surfaces of the test cell and the domain ground (being in the order of 1.0 near the test cell). Information about the mesh on both the building surfaces and the domain ground is given in Figure 5.3. The sensitivity test of the mesh density, especially for the near wall, is discussed in Section 5.2.3.

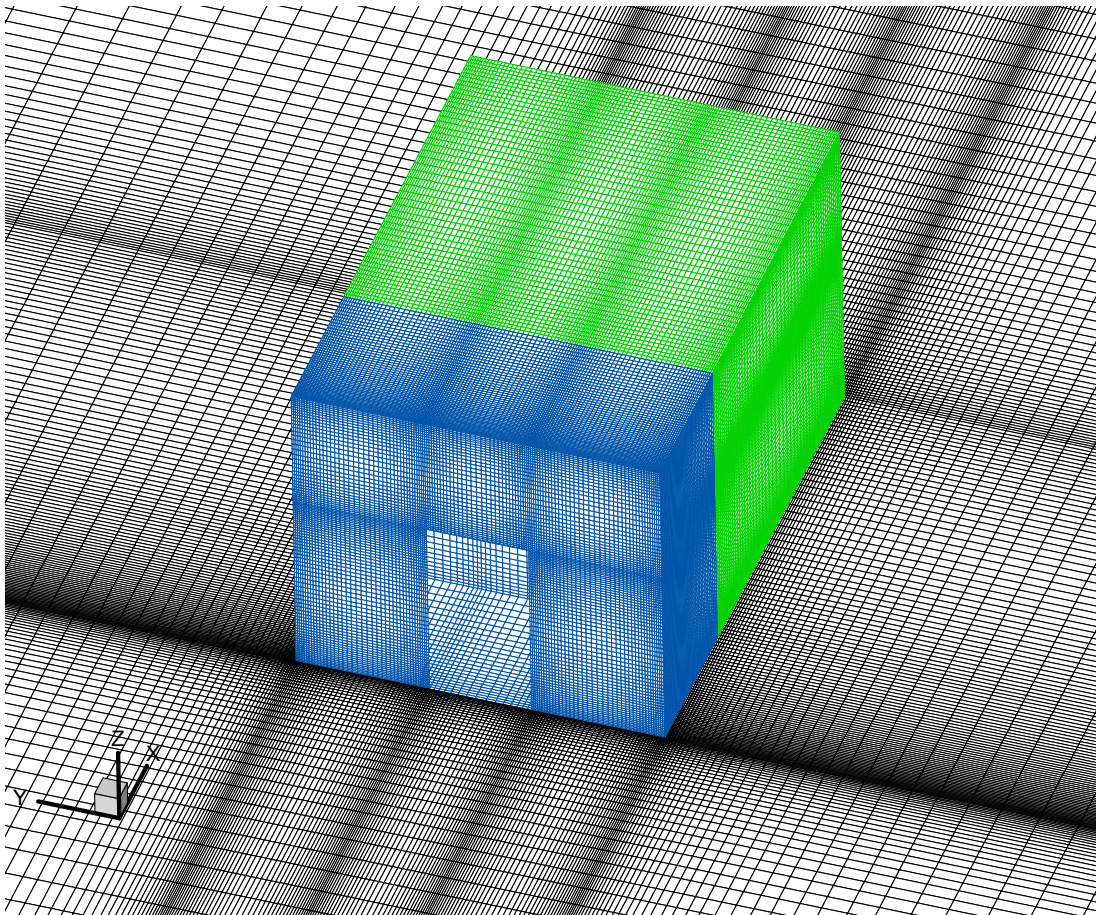


Figure 5.3 Mesh information on both the building surfaces and the domain ground.

5.2.2.2 Boundary conditions

The inlet boundary conditions of the computational domain are specified by the profiles of the mean wind speed U , turbulence kinetic energy k , and turbulence dissipation rate ε , which are the same with the inlet profiles of Gorlé et al. (2009) listed in Table 4.1. Based on $z_0 = 0.255$ mm and $U = 1.95$ m/s at a height of $z = 1.5$ m as well as the von Karman constant $\kappa = 0.4187$, the logarithmic mean wind speed profile (U) is obtained. The friction velocity u^* is then equal to 0.155 m/s. The coefficients M_1 and M_2 are specified as 0.025 and 0.41, making the turbulence profiles identical with those measured in an average wind tunnel (Leitl and Schatzmann, 1998). For RANS simulation, the empirical constant C_μ and turbulence dissipation Prandtl number σ_ε are also determined by the equations listed in Table 4.1. For LES simulation, three types of inflow fluctuating algorithms, namely No perturbations, Spectral synthesizer and Vortex method (explained in Section 2.5.2.3), have been compared. The results show that the use of No perturbations produces the closest result with the measured data. The reason for the best performance of No perturbations should be the fact that the real approaching flow field is relative stable during the measurement. As shown in Section 4.3.2.4, the fluctuating characteristics provided by the three inflow algorithms are largely distinctive, which represent different inflow conditions. Therefore, No perturbations are introduced to the inlet mean velocity profile for remaining consistent with the measurement condition.

On the domain ground, the two-layer model with roughness modifications (Durbin et al., 2001) is used for RANS simulation (see Section 4.2.2). As the aerodynamic roughness height $z_0 = 0.255$ mm, the corresponding geometrical roughness height is $K_s = 5$ mm, given that $K_s = 9.793z_0/C_R$ and $C_R = 0.5$. The selection of such a low-roughness ground is intended to facilitate the subsequent sensitivity test of the near-wall mesh density, taking into account the requirement of the Fluent code (Fluent, 2010) that K_s should not be larger than z_p (namely the half height of the first cells). In addition, another roughness height with $z_0 = 3.29$ mm that is based on a Jensen number (H/z_0) of 1000 (Richards and Hoxey, 2012) is

tested. The deviations in ACH values produced using $z_0 = 3.29$ mm and $z_0 = 0.225$ mm are less than 3%. Both roughnesses give reasonable results, when comparing with the measured values of 9.6~13.18. As the main purpose of this study is to examine the influence of parameters, using a smaller but a same roughness is believed to be acceptable. For LES simulations, no special treatment is used on the domain ground, as currently there are no formula existed to take into account the ground roughness for LES simulations. Other boundary conditions at domain outlet, domain ceiling, domain lateral sides and building surfaces are the same with those listed in Table 4.1. Before commencing the RANS simulation, the homogeneity of these boundary conditions is checked through a comparison of the inlet and incident profiles in an empty computational domain, as shown in Figure 5.4, where the incident indicates the location where the building is placed. It can be seen that a good homogeneous boundary layer is achieved in the computational domain.

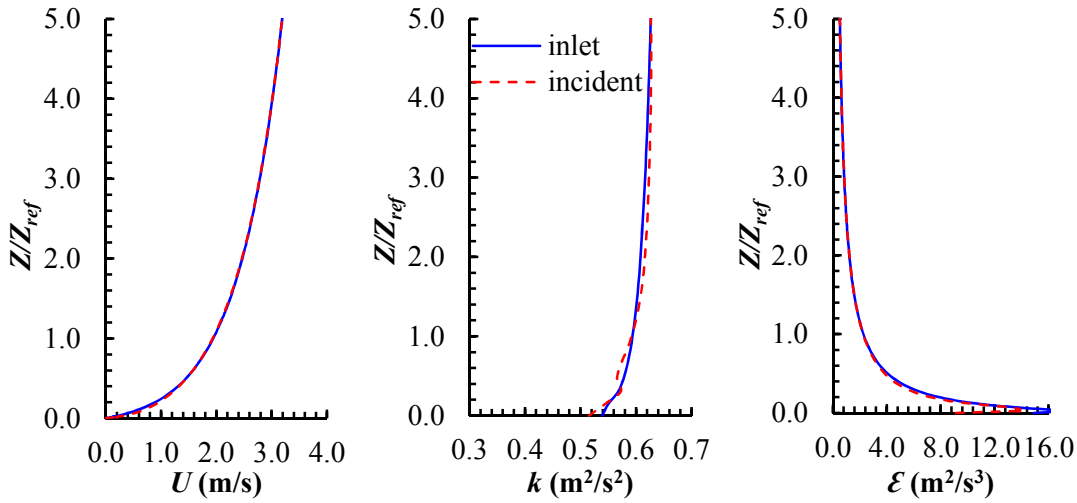


Figure 5.4 Comparison of the inlet and incident profiles in an empty computational domain for RANS simulation ($Z_{ref} = 1.5$ m).

5.2.2.3 Other computational settings

The RNG $k - \varepsilon$ model (Yakhot and Orszag, 1986) is used to predict the steady flow field and the transient concentration decay process. In comparison, the LES model is applied to predict both flow and concentration fields transiently. The standard Smogorinsky-Lilly model (Smagorinsky, 1963; Lilly, 1992) is used to

modeling the subgrid-scale motions, and the Smogorinsky constant (C_s) is set to 0.1 (see Section 4.3.2.7). When the concentration (using CO₂ as a tracer gas) equation is solved, after sensitivity tests, the turbulent Schmidt number (Sc_t) of 0.7 is used for RANS modeling, while the turbulent Schmidt number for SGS motions (Sc_{SGS}) of 0.4 is used for LES modeling.

The general solution methods of both RNG and LES models are similar with those used in Chapter 4. For the steady simulation of the RNG model, convergence is achieved when all scaled residuals (Fluent, 2010) are less than 1.0×10^{-5} and the average wind speed at the opening is stable for around 50 iterations. For the transient simulation of the RNG model, the time step size is 0.5 s and the convergence of each time step is achieved when the average CO₂ concentration at the opening is stable for at least five iterations. For the transient simulation of the LES model, the time step size is 0.01 s and the convergence of each time step is achieved when both the average wind speed and the average CO₂ concentration at the opening are stable for at least five iterations.

Table 5.1 Comparison of the predicted and measured ACH values (h⁻¹).

ACH_{exp}	$ACH_{RNG-mean}$	$ACH_{RNG-tracer}$	$ACH_{LES-ins,T}$	$ACH_{LES-tracer}$
9.60~13.18	11.78	17.02	15.95	12.89

5.2.2.4 Results and comparison with field measurements

The methods used to determine single-sided ventilation rate are described in Section 2.6. In the sections which follow, the terms $ACH_{RNG-mean}$, $ACH_{RNG-tracer}$, $ACH_{LES-ins,T}$, and $ACH_{LES-tracer}$ are used to represent the ACH values calculated using each of the integration and tracer gas decay methods based on the RNG and LES models, respectively. Particularly, using tracer gas decay method, the ventilation rate (Q_i) during a sub-period of $\Delta t = t_{i+1} - t_i$ can be determined by:

$$Q_i = \frac{-\ln(C_{t_{i+1}}/C_{t_i}) \cdot V}{t_{i+1} - t_i} \quad (5.1)$$

The CFD modeling benefits from using time step size (temporal discretization

interval) as the sub period Δt . Therefore, Q_t can be considered the instantaneous ventilation rate at time t . The concentration decay and time interval is shown in Figure 5.5. The mean ventilation rate (\bar{Q}) during the whole decay period is then computed by:

$$\bar{Q} = \frac{\sum_{i=0}^n Q_t}{n} \quad (5.2)$$

where n is the number of sub-periods. $ACH_{LES-tracer}$ is then obtained according to the formula $ACH_{LES-tracer} = \bar{Q}/V$.

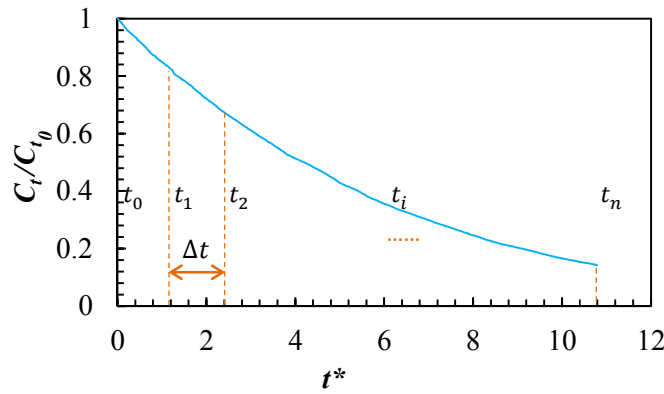


Figure 5.5 Concentration decay and time interval for the calculation of ventilation rates.

Table 5.1 presents the comparison of the measured and predicted ACH values. It can be seen that the $ACH_{RNG-mean}$ and the $ACH_{LES-tracer}$ values agree well with the measured data (ACH_{exp}). One would expect the integration method based on a time-averaged flow field ($ACH_{RNG-mean}$) to underestimate the ventilation rate, as it only takes into account the contribution of the mean airflow convection. The good agreement between $ACH_{RNG-mean}$ and ACH_{exp} in the present simulation may suggest that the airflow convection is the dominant factor when the opening is obliquely (specifically, 60°) oriented to the approaching wind. The work of Caciolo et al. (2012) also shows that the integration method does not necessarily

underestimate the ventilation rate for all scenarios. The reason that the tracer gas decay method used in a RNG context ($ACH_{RNG-tracer}$) overpredicts the ventilation rate should be the overestimation of k in the frontal region of the building (Fluent, 2010; Tominaga et al., 2008a), which results in the overestimation of the turbulence-induced portion of the ventilation rate. The overprediction of the integration method used in a LES context ($ACH_{LES-ins,T}$) can be attributed to the fact that a part of the instantaneous airflow short-circuits at the opening and thus does not contribute to the effective air exchange rate (Cockroft and Robertson, 1976; Larsen and Heiselberg, 2008).

5.2.3 Sensitivity analyses of the computational parameters

Based on the CFD validations presented in Section 5.2.2 and the findings derived from the sensitivity analyses of the CFD modeling of cross ventilation by Ramponi and Blocken (2012), it may be suggested that the computational domain size, discretization scheme, and convergence criteria recommended by the best practice guidelines for wind flow around buildings (Franke et al., 2007; Tominaga et al., 2008b) remain applicable to the CFD modeling of single-sided natural ventilation. It is worth noting that the convergence criteria should be monitored not only by the quantities of scaled residuals, but also that the stability of the numerical solutions involved at the regions of interest is another important criterion. In addition, both the RNG $k - \varepsilon$ and the LES models are compared throughout this study. Therefore, this section reports on detailed sensitivity analyses for only (a) effect of time interval on calculating $ACH_{LES-tracer}$, (b) the mesh resolution of the domain, (c) the near-wall mesh density of the building surfaces and the domain ground, and (d) the inlet turbulence kinetic energy k . The sensitivity analyses of the last two parameters in the prediction of the single-sided ventilation rate have not been reported before.

5.2.3.1 Effect of time interval on calculating $ACH_{LES-tracer}$

The sensitivity analysis concerning the selection of the time interval (Δt) in the calculation of the mean ventilation rate in the whole decay period (\bar{Q}) is conducted

by comparing the $ACH_{LES-tracer}$ values obtained from the calculations using different time intervals. This sensitivity analysis is attempted to identify an appropriate time interval for later calculation of $ACH_{LES-tracer}$. Apart from 0.01s (i.e., the size of the time step of the transient simulations), 1s, 2s, and 4s are also used as comparisons. The results are presented in Table 5.2, which shows that the predicted mean ACH values are nearly independent of the selection of time interval. This finding is useful for the experimental determinations of ACH using the tracer gas decay method because using a larger time interval can save resources. However, in order to reduce random error, the minimum number of sub-time periods should not be less than five, as suggested by previous researchers (Laussmann and Helm, 2011). However, for CFD simulations, $\Delta t = 0.01s$ is used to calculate the ACH values in the rest of this thesis.

Table 5.2 Comparison of measured and predicted mean ACH values (h^{-1}).

Time interval	$\Delta t = 0.01s$	$\Delta t = 1s$	$\Delta t = 2s$	$\Delta t = 4s$
$ACH_{LES-tracer}$	12.89	12.81	12.68	12.68

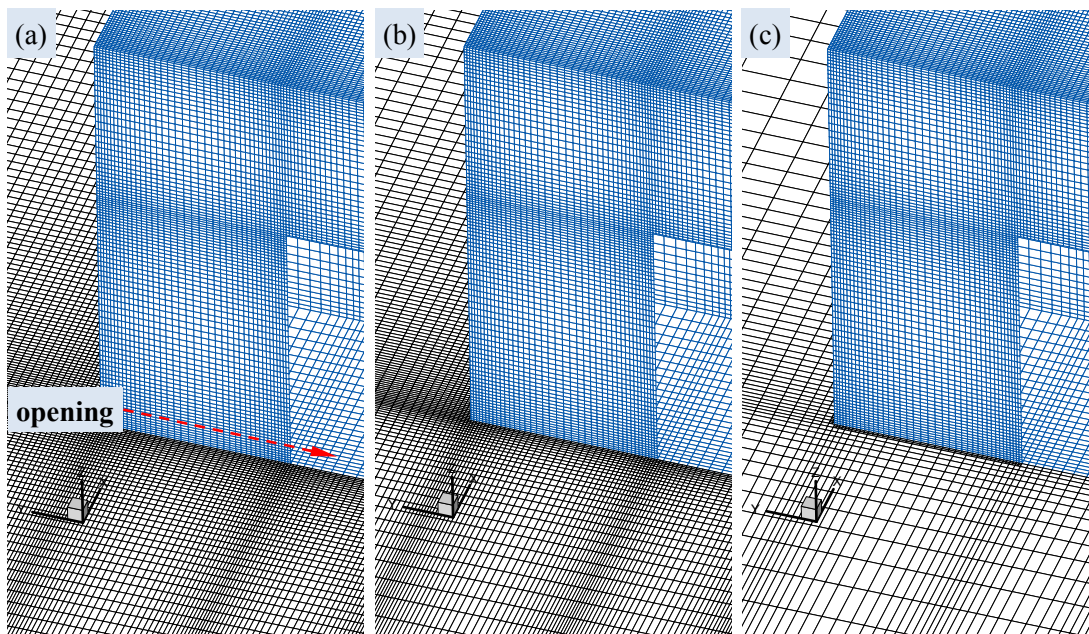


Figure 5.6 The three mesh systems: (a) finer, (b) basic, and (c) coarser.

5.2.3.2 Effect of mesh resolution of the domain

In addition to the basic mesh with around 3.5×10^6 cells, one coarser and one finer mesh are created, containing around 2.0×10^6 and 4.5×10^6 cells, respectively. These are obtained by changing the stretching ratio of the basic case (1.18) to 1.35 and 1.12, respectively, leaving the first cells unchanged. The three mesh systems are illustrated in Figure 5.6 and the results presented in Table 5.3. The average difference in ACH value is 2.7% between the basic and the finer mesh, and 12.1% between the basic and the coarser mesh. This indicates that the basic mesh is suitable, which in turn suggests that the stretching ratio of 1.18 is small enough to achieve independence of the mesh resolution.

Table 5.3 Comparison of the ACH values (h^{-1}) predicted using the three types of mesh.

Grid number	$\text{ACH}_{\text{RNG-mean}}$	$\text{ACH}_{\text{RNG-tracer}}$	$\text{ACH}_{\text{LES-ins},T}$	$\text{ACH}_{\text{LES-tracer}}$
2.0×10^6 (coarser)	9.88	16.19	15.26	9.82
3.5×10^6 (basic)	11.78	17.02	15.95	12.89
4.5×10^6 (finer)	12.02	17.28	15.19	12.70

5.2.3.3 Effect of near-wall mesh density

In addition to the basic near-wall mesh with a y^+ value of 3.8, one finer ($y^+ = 1.8$) and three coarser ($y^+ = 7.4, 18.8$ and 31.2) near-wall meshes are created. Here, the y^+ are the average values for the domain ground and the building surfaces. This section reports on the proposal and testing of a method for increasing the near-wall mesh density. Figure 5.7 (a)-(c) shows schematically the increase of the near-wall mesh density from $y^+ = 7.4$ to 3.8 and from 3.8 to 1.8. This is simply achieved by doubling the mesh number of the first cells both horizontally and vertically in a hemisphere zone. Such an increase does not require any modification of the other non-near-wall cells, potentially saving numerical costs. Figure 5.7 (d) shows a mesh constructed using the conventional method; that is, with the same stretching ratio across the whole computational domain starting from the first cells. The ACH values predicted using the two meshes (see Figure 5.7 (b) and (d)) are almost the same. However, given the larger mesh number, the mesh constructed using the conventional method costs much more numerically. It should also be noted that the

prerequisite of the success of this method is that the mesh resolution in the whole computational domain (as presented in Section 5.2.3.2) is independent.

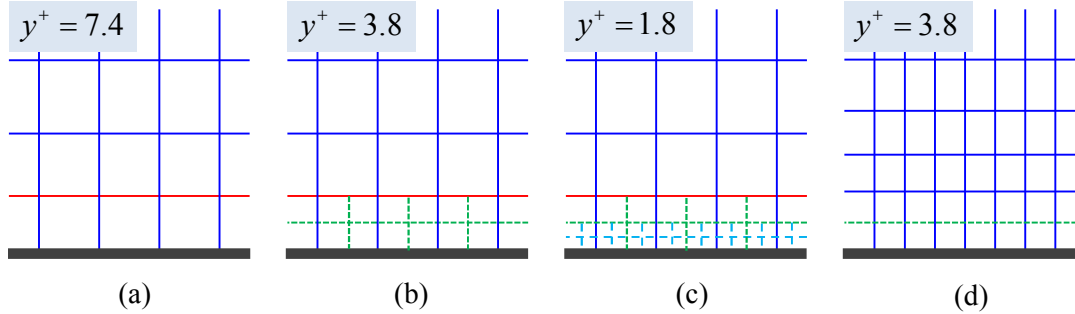


Figure 5.7 Schematic view of the change of the near-wall mesh density.

Table 5.4 Comparison of the ACH values (h^{-1}) predicted using different near-wall mesh densities.

y^+	$ACH_{RNG-mean}$	$ACH_{RNG-tracer}$	$ACH_{LES-ins,T}$	$ACH_{LES-tracer}$
1.8	11.87	16.87	17.69	14.94
3.8	11.78	17.02	15.95	12.89
7.4	11.58	17.03	17.22	14.07
18.8	11.00	18.06	14.16	12.11
31.2	9.07	16.81	16.48	9.19

The results are listed in Table 5.4 from which two main observations can be made. First, the $ACH_{RNG-mean}$ and $ACH_{LES-tracer}$ produced using the mesh with $y^+ = 31.2$ have obvious deviations from those produced using a denser near-wall mesh. This shows that a mesh where the first cells are placed outside the viscosity-affected inner layer could result in large inaccuracies when the near-wall treatment is not the standard wall functions, as $y^+ = 30$ is normally recognized as an indicator of the interface between the viscosity-affected inner layer and the fully turbulent outer layer (Fluent, 2010). Second, when the first cells are located within the inner layer ($y^+ < 30$), the ACH values predicted using the RNG $k-\varepsilon$ turbulence model are insensitive to the near-wall mesh density, especially when using the integration method ($ACH_{RNG-mean}$). However, the predictions of the LES model fluctuate with

the near-wall mesh density. This difference between the RNG and the LES models can be attributed to the distinctive methods they each use to treat the near-wall flow region and to calculate the near-wall flow field at different near-wall mesh densities (Fluent, 2010). For a complex flow problem like the one studied here, it is almost impossible to ensure that the y^+ value is the same for all wall surfaces. The decrease of y^+ from 3.8 to 1.8 occurs mainly as a result of the decrease of y^+ in the regions far from the building (outer regions), as the inner regions in the vicinity of the building already had a very low y^+ value (around 1.0~2.0) in the original mesh ($y^+ = 3.8$). This implies that the near-wall mesh density in the outer regions has a larger impact on the prediction of ACH using the LES model than when using RNG. In addition, the effect of the near-wall mesh density should also rely on the flow problem, namely the role of the low-Reynolds-number regions in the whole wall-bounded flow field.

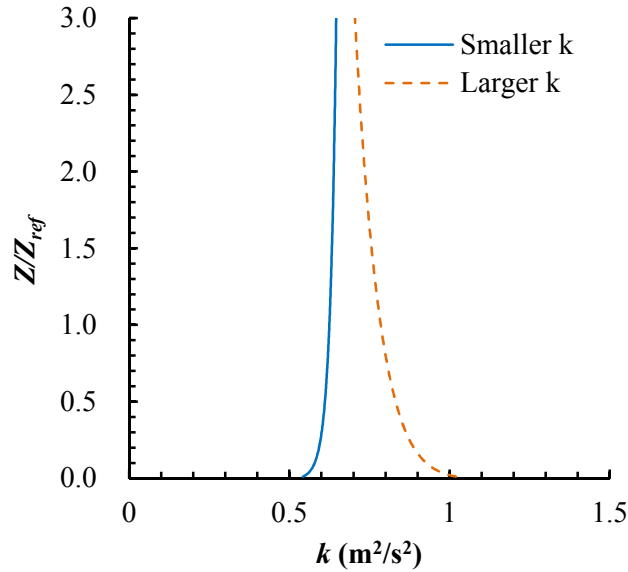


Figure 5.8 Comparison of the two inlet k profiles.

Table 5.5 Comparison of the ACH values (h^{-1}) predicted using the two k profiles.

k profile	$\text{ACH}_{\text{RNG-mean}}$	$\text{ACH}_{\text{RNG-tracer}}$	$\text{ACH}_{\text{LES-ins},T}$	$\text{ACH}_{\text{LES-tracer}}$
Smaller k	11.78	17.02	15.95	12.89
Larger k	12.54	17.78	16.10	12.66

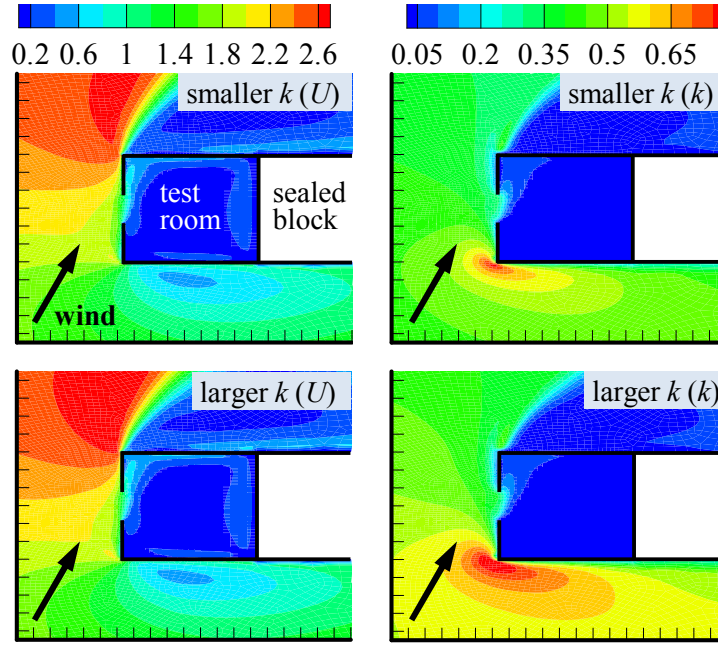


Figure 5.9 Comparison of the U and the k fields on a horizontal plane ($z = 1.0$ m) produced using the two k profiles based on the RNG model.

5.2.3.4 Effect of inlet k

Two methods are commonly used by CFD practitioners to formulate a profile of k (e.g., Blocken et al., 2012; Hussein and El-Shishiny, 2009; Ramponi and Blocken, 2012; Steffens et al., 2013), especially when detailed experimental data about the streamwise turbulence intensity (I_u) or (and) the fluctuating velocity components (u', v', w') is available.

$$k_1 = 0.5(u'^2 + v'^2 + w'^2) \quad (5.3)$$

$$k_2 = 1.5(UI_u)^2 \quad (5.4)$$

This study applies the turbulence intensity (I_u) and the velocity components (u', v', w') measured by Leitl and Schatzmann (1998) in a wind tunnel. In addition to the k profile used in the basic case (smaller k) reported in Section 5.2.2.2, which is fitted from k_1 in Equation (5.3), another k profile (larger k) fitted from k_2 in Equation (5.4) is also formulated for comparison. For the larger k profile, the coefficients M_1 and M_2 in the inlet profiles become -0.11 and 0.53, respectively.

A comparison of the smaller and larger k profiles is illustrated in Figure 5.8, and the results presented in Table 5.5. It can be seen that the ACH value predicted using the RNG turbulence model is more sensitive to the inlet k profile than that predicted using LES. However, even for the RNG model, the differences in ACH values predicted using the two k profiles are very small, since the U and the k fields at the opening they produce are almost the same (see Figure 5.9). The $ACH_{RNG-mean}$ and $ACH_{RNG-tracer}$ predicted using the larger k profile still agree well with the measured ACH value (see Table 5.1). This suggests that the selection of inlet k profile should be based on the availability of experimental data for the turbulence intensity I_u or velocity components u', v', w' .

5.2.4 Single-sided ventilation rates predicted by various numerical methods

Extensive studies on the performance of various numerical methods in predicting the single-sided ventilation rate and its variation under different wind directions have not been reported by other researchers. This section addresses these questions in detail. The $ACH_{LES-tracer}$ values are considered to be the most accurate compared with those obtained using the other three combinations (e.g., Caciolo et al., 2012; Jiang and Chen, 2001). This is due to the fact that theoretically speaking, the LES model can establish a more accurate flow field than the RANS, and the tracer gas decay method can take the ventilation mechanisms into account more comprehensively than the integration method. Therefore, the $ACH_{LES-tracer}$ values are taken as the base in the analysis of the performance of the other predictive methods used. The results are presented in Table 5.6, from which four main observations can be drawn.

First, integrating the time-averaged air speeds on an opening ($ACH_{RNG-mean}$) does not necessarily mean underestimating the ACH for all wind directions. Theoretically, this method does not take into account the turbulence-induced ventilation rate and so will be expected to underestimate the ACH (Caciolo et al., 2012; Jiang and Chen, 2001). However, the time-averaged opening speeds produced by the RNG $k-\varepsilon$ model may not be accurate enough. There is a possibility of overprediction, which will be more likely when the approaching wind direction is

close to the opening normal (Caciolo et al., 2012).

Table 5.6 ACH values (h^{-1}) of the single-sided ventilated room under different wind directions. The percentage in brackets indicates the deviations of the ACH value from the $\text{ACH}_{LES-tracer}$.

Wind angle (θ)	$\text{ACH}_{RNG-mean}$	$\text{ACH}_{RNG-tracer}$	$\text{ACH}_{LES-ins,T}$	$\text{ACH}_{LES-tracer}$
0°	42.34 (208.4%)	17.14 (54.0%)	28.57 (156.7%)	11.13
45°	17.11 (44.8%)	18.63 (57.6%)	14.74 (24.7%)	11.82
60°	11.78 (-8.6%)	17.02 (32.0%)	15.95 (23.7%)	12.89
90°	16.97 (-29.0%)	17.56 (-26.5%)	36.87 (54.3%)	23.89
135°	9.31 (4.7%)	4.68 (-47.4%)	15.73 (76.9%)	8.89
180°	19.38 (-16.9%)	15.60 (-33.1%)	29.78 (27.8%)	23.31

Second, the dominant factor in the accuracy of the $\text{ACH}_{RNG-tracer}$ is the predicted turbulence field. Clearly, this combination overpredicts ACH values for the windward openings (0° , 45° and 60°) and underpredicts for the lateral opening (90°) and leeward openings (135° and 180°). Several studies (e.g., Gao et al., 2008; Murakami, 1998; Tsuchiya et al., 1997) show that most of the isotropic $k-\varepsilon$ models overpredict the turbulence kinetic energy k in the frontal area and underpredict the momentum mixing effects in the wake region. Few studies have assessed the performance of isotropic $k-\varepsilon$ models in predicting the ventilation rate in the lateral areas, but this study shows that it is similar to that in the wake region. The reason for the underprediction of ACH in the lateral areas is therefore likely to be the counteraction of the reverse flows by the large eddy viscosity from the frontal area (Murakami, 1998; Gao et al., 2008).

Third, the method of cumulating and averaging the ACH values ($\text{ACH}_{LES-ins,T}$) derived from the integration of the instantaneous opening velocities will overpredict the room ACH for all wind directions. It is apparent that not all the airflow entering a room can effectively eliminate overheated or polluted indoor air, as some of the incoming air leaves the room immediately after entering. This study shows that on average, around 33% of the airflow short-circuits at the room opening and in turn around 67% of the airflow rate contributes to effective air exchange, as

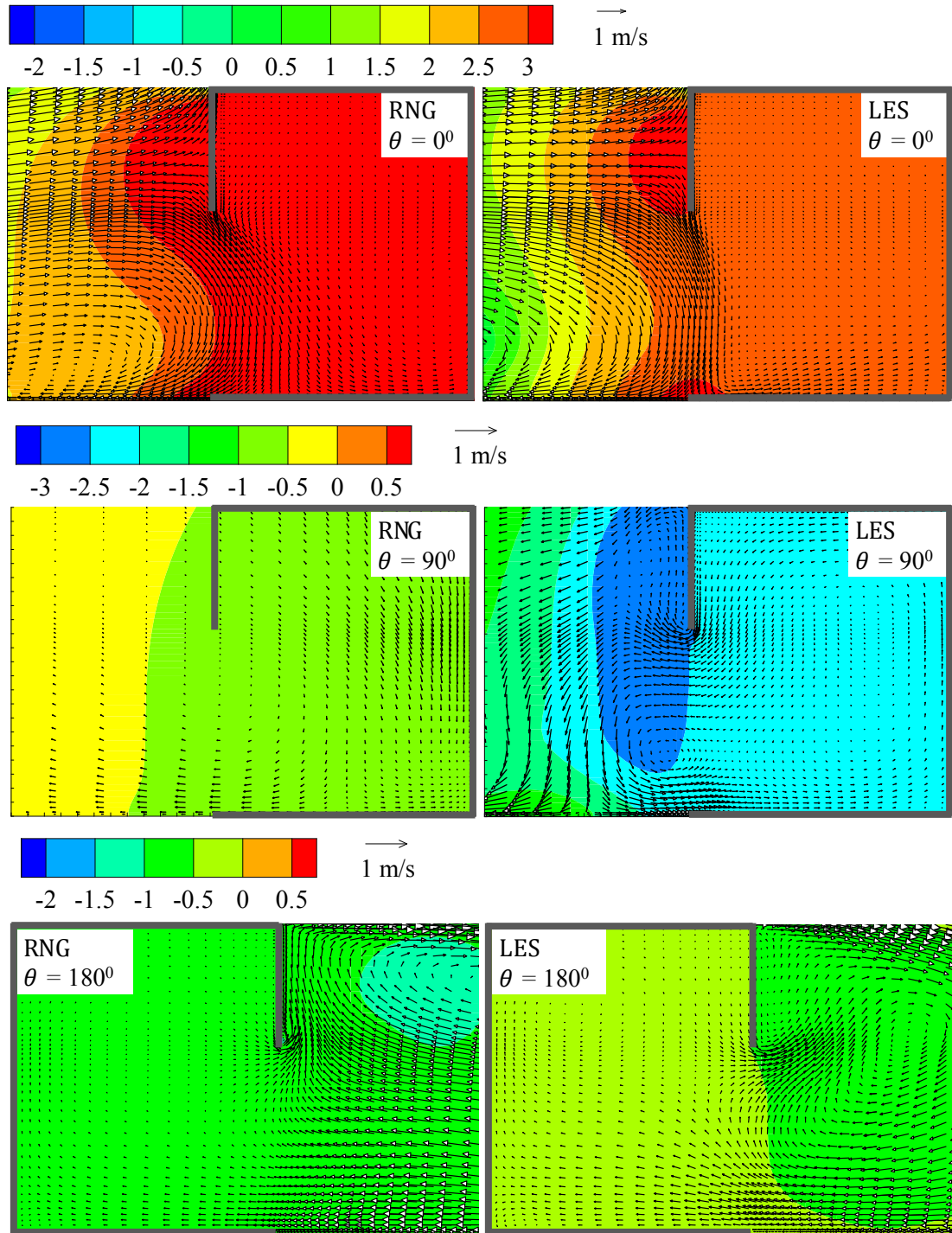


Figure 5.10 Distribution of velocity vectors and pressure contours on the vertical center plane of the opening for $\theta = 0^\circ$, 90° and 180° .

approximately represented by $ACH_{LES-tracer}$. This finding lies in between that of Cockroft and Robertson (1976) and Larsen and Heiselberg (2008), who suggest 37% and 80-90%, respectively, of the airflow rate contributes to effective air exchange.

Note that Larsen and Heiselberg (2008) used a uniform (rather than a logarithmic) velocity profile in their experiments.

Finally, the comparison of ACH values ($ACH_{LES-tracer}$) under different wind directions shows that better single-sided ventilation performance is given with a lateral (90°) and a leeward opening (180°). This contradicts the general belief that the highest ventilation rate is found with windward ventilation (0°), and this common-sense view is more or less supported by RANS simulations as shown here ($ACH_{RNG-mean}$). These observations are supported by the comparison of velocity vectors and pressure contours on the vertical center plane of the openings for the three wind directions, as presented in Figure 5.10. Obviously, a case with a higher pressure difference and with obvious inflow and outflow across the opening holds a higher ventilation rate. In fact, a few studies (Jiang et al., 2003; Melaragno, 1982) show that a higher single-sided ventilation rate should occur in leeward rather than windward ventilation, although insufficient attention has been paid to this finding so far by either CFD practitioners or ventilation designers. Specifically, Melaragno (1982) observes that the mean air speeds in a room with a windward opening are smaller than that with a leeward opening. This observation is supported by the findings of a wind tunnel experiment conducted by Jiang et al. (2003).

Based on the above analyses and discussion, two suggestions can be made for the development of future CFD simulations of single-sided natural ventilation and ventilation design methods. First, the combination of the LES model and tracer gas decay method should be used to predict the single-sided ventilation rate if the numerical resources are available. Here, the time consumed by the simulation of concentration decay using the LES model was at least 20 times higher than that of the RNG model. If the RANS models must be used, the tracer gas decay method is more reliable and controllable than the integration method when seeking an accurate prediction. Before using RANS models to carry out computations, one should conduct a comparison with the LES model and obtain a correcting factor for a specific wind direction. Second, ventilation designers must understand the variation of the single-sided ventilation rate with wind direction, and note in particular that the highest ventilation rate occurs not in a room with a windward but with a lateral or a leeward opening.

5.2.5 Summary

Taking into account wind direction, the problem of accurately predicting single-sided natural ventilation using CFD methods is dealt with. This ventilation rate is attempted to typify generally any airflow exchange rate through a single opening between urban and built environments. Such a study is intended to provide supplementary information for the development of best practice guidelines and to improve future CFD predictions of the coupled urban wind flow and indoor air flow.

According to the current best practice guidelines for the CFD simulation of urban aerodynamics, a basic case is defined to predict the single-sided ventilation rate. The comparison of this basic case with experimental measurements indicates that the recommended computational domain size, discretization scheme, and convergence criteria are still applicable to CFD simulation of coupled urban wind flow and indoor air flow.

The sensitivity analyses show that a mesh with a stretching ratio of 1.18 is sufficiently fine to be insensitive to mesh number. With such a ratio, the sensitivity of the near-wall mesh density in particular is tested, and a method of increasing it by doubling only the first near-wall cells proposed. Requiring fewer numerical resources, this method produces almost the same ACH value as that predicted using conventional methods. When y^+ is less than 30, the ACH values predicted using the RNG model are insensitive to the near-wall mesh density. The LES model is much more sensitive, but a denser near-wall mesh is not necessarily better, suggesting a sensitivity test of the near-wall mesh density should be conducted when attempting to solve a distinctive flow problem.

Four methods of predicting the single-sided ventilation rate are examined under various wind directions. The RNG model plus the integration method ($ACH_{RNG-mean}$) does not necessarily underestimate the ACH value for all wind directions. Such underestimations are more likely to occur when the approaching wind direction is close to the opening normal (0° - 45°). The RNG model used with the tracer gas decay method ($ACH_{RNG-tracer}$) is more reliable than the previous combination, although it overestimates the ACH value for the windward openings and underestimates it for the lateral and leeward openings. The LES model plus the integration method ($ACH_{LES-ins,T}$) overestimates the ACH value in all wind directions, owing to the

short-circuiting effect of airflow. On average, around 33% of the airflow short-circuits at the room opening. The LES model plus the tracer gas decay method ($ACH_{LES-tracer}$) is the best approach, although it requires at least 20 times more computational time than the RNG and tracer gas ($ACH_{RNG-tracer}$) approach. In particular, it is shown that single-sided ventilation performs better in cases with a lateral (90°) and a leeward opening (180°) than with a windward opening (0°).

5.3 Fluctuating flow characteristics of single-sided natural ventilation

5.3.1 Introduction

The validated LES model combined with the tracer gas decay method (described in Section 5.2.2) is used to investigate the fluctuating flow characteristics of single-sided natural ventilation (described in Section 5.2.1). Again, the five wind directions are considered: $\theta = 0^\circ, 45^\circ, 90^\circ, 135^\circ$, and 180° . Comparison between the transient flow and the average flow produced using the RNG model is also made.

5.3.2 Fluctuating ventilation rate

The transient evolution of the ventilation rates through the single opening under different wind directions is presented in Figure 5.11, where the dimensionless ventilation rate Q^* is defined as:

$$Q^* = Q_t / (U_{ref} A_o) \quad (5.5)$$

in which A_o is the opening area (2.02 m^2). In Figure 5.11, $\overline{Q^*}$ represents the mean dimensionless ventilation rate during the whole decay period, and σ_{Q^*} represents the standard deviation of Q^* .

The ratios of the standard deviations to the mean values are also worked out. From Figure 5.11, two observations can be made. First, the ventilation rate through a single opening is always fluctuating, and the fluctuating intensities are distinctive under different wind directions. Larger fluctuations can be found in the lateral and leeward ventilations because the higher-frequency and unsteady small eddies that are generated from the flow separations at the leading edges characterize lateral and

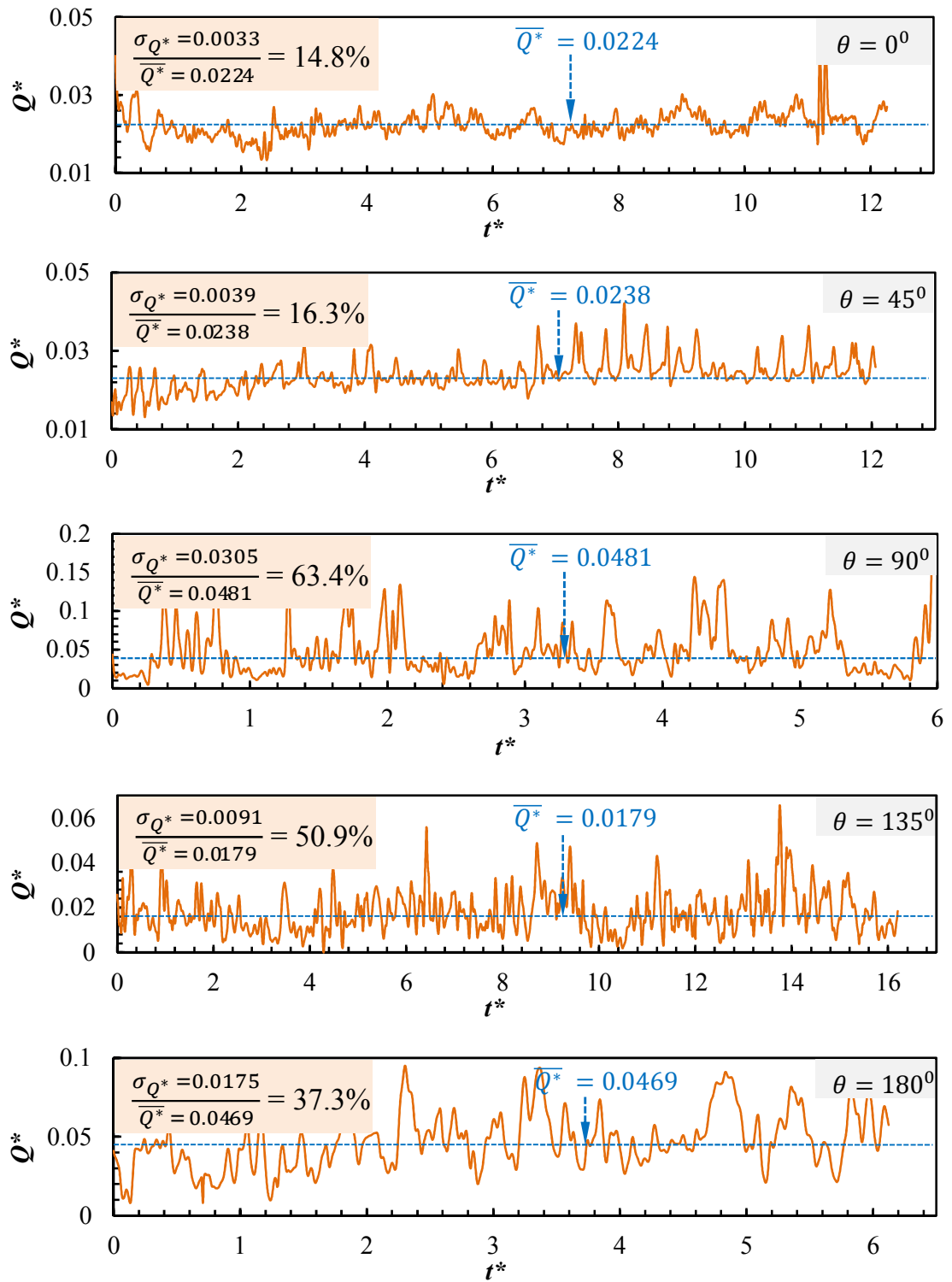


Figure 5.11 Transient evolution of ventilation rates under different wind directions.

leeward flows. Taking the case of 90° as an example, there are many periods when the instantaneous ventilation rates deviate highly from the mean value. This suggests

that the use of a constant ventilation rate cannot fully describe a single-sided ventilation process.

Second, the standard deviation of the ventilation rate is used to indicate the fluctuating intensity of the instantaneous ventilation rates. Because the fluctuation of a wind-induced ventilation rate is caused by the turbulence effect of wind, the standard deviation of ventilation rates can be considered to be turbulence-induced ventilation rates (Straw, 2000; Wang and Chen, 2012). Then, the ratios of σ_{Q^*} to $\overline{Q^*}$ indicate the role of the turbulence-induced component in the total ventilation rate. It can be seen that airflow exchange is dominated by the mean flow for windward ventilation and is dominated by the turbulent flow for the lateral ventilation. For leeward ventilation, the turbulent flow still has an important impact on airflow exchange.

5.3.3 Relationship between the ventilation rate and interior kinetic energy

The ventilation rate only refers to the effective airflow exchange between inside and outside. It cannot indicate indoor airflow characteristics. The air velocity and its fluctuating intensity are important to the evaluation of micro-environmental quality, such as thermal comfort. This section presents the relationship between ventilation rate and indoor airflow characteristics. To quantify the indoor airflow characteristics, this study uses the parameter of kinetic energy (KE) of the indoor air (Bu and Kato, 2011), which is defined as:

$$KE = \frac{\sum_{j=1}^m \left[0.5 \times (u_j^2 + v_j^2 + w_j^2) \times V_j \right]}{\sum_{j=1}^m V_j} \quad (5.6)$$

where j indicates the specific computational cell number in the test room, m is the total number of cells, u_j , v_j , w_j are the instantaneous velocity components, and V_j is the volume of cell j . The dimensionless kinetic energy KE^* is then computed as:

$$KE^* = \frac{KE}{0.5 \times U_{ref}^2} \quad (5.7)$$

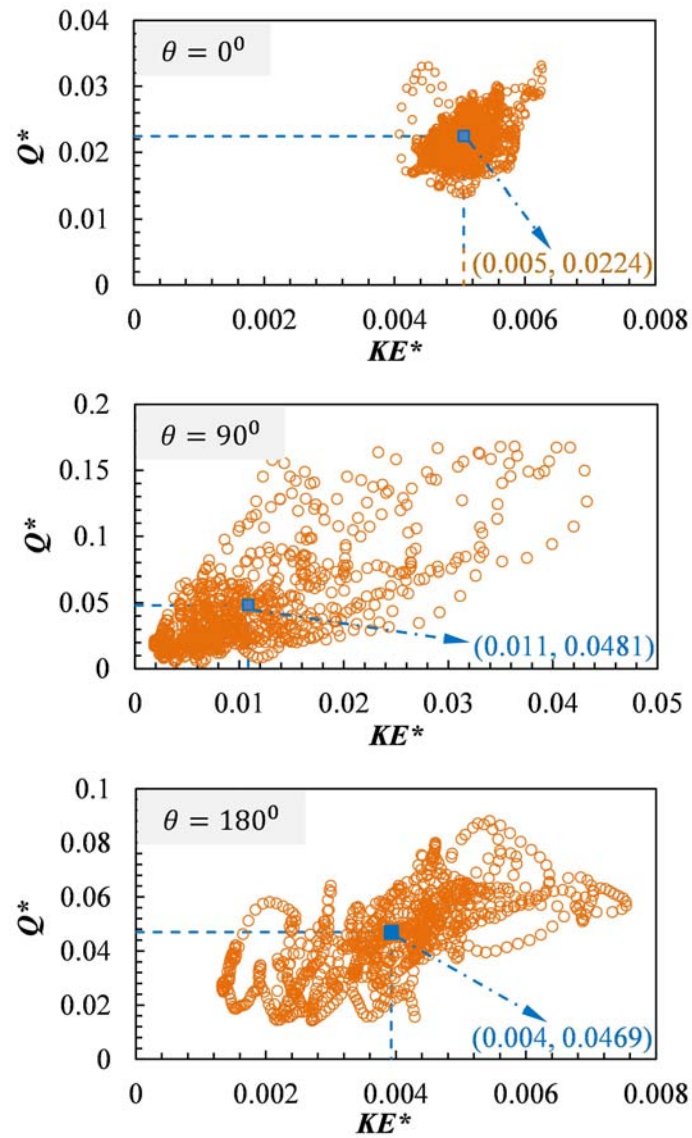


Figure 5.12 Relationship of instantaneous ventilation rates and indoor kinetic energy.

Figure 5.12 presents the relationships between Q^* and KE^* for the wind directions of 0° , 90° , and 180° . Their mean values are also provided in parentheses ($\overline{KE^*}$, $\overline{Q^*}$). Generally, under each wind direction, Q^* increases with KE^* , although not all instantaneous Q^* and KE^* comply with this trend. For mean values, the $\overline{KE^*}$ under 180° is smaller than under 0° , even though $\overline{Q^*}$ has the opposite relation. Such an inconsistency between indoor kinetic energy and ventilation rate implies that a stronger indoor air movement does not guarantee a larger effective airflow exchange. One reason leading to the scenario with a larger

KE^* but a smaller Q^* could be the existence of strong internal recirculation vortexes. Figure 5.12 also shows that the fluctuation of KE^* for windward ventilation is much weaker than for lateral and leeward ventilations. This suggests that a room with lateral or leeward ventilation is much easier to obtain a thermally comfortable indoor environment than that with windward ventilation.

5.3.4 Instantaneous flow patterns around the opening

Most previous studies present only the time-averaged flow field of single-sided ventilation. However, cancelling out the instantaneous flow details, a time-averaged flow field is not helpful for understanding the instantaneous airflow-exchange process through a single opening. This section provides the velocity and pressure fields on the vertical center plane of the opening for the wind directions of 0° , 90° , and 180° . For each wind direction, two instantaneous moments are selected, when the ventilation rates are relatively small and large. Figure 5.13 presents the distributions of velocity vector and the pressure contour for the three wind directions, which can lead to the following three analyses.

First, the instantaneous velocity and pressure fields around a windward opening ($\theta = 0^\circ$) are relatively stable, which do not vary obviously with changes in the ventilation rate. Indoor kinetic energy can also support this statement. Even though the approaching wind speed is high, the impinging airflow towards the windward opening is difficult to penetrate, especially to the deep region. The reason should be the fact that the interior of the room continues to be a high and stable pressure field. Such a pressure field significantly dampens turbulent diffusion through the opening, as the pulsating flows and eddy penetrations can occur only in a time-varied pressure field. As a consequence, the mean flow field dominates the mass transport through the opening. To a large extent, the impinging flow with large momentum forces the outdoor airflow in, while the high interior pressure field pushes the indoor airflow out.

Second, the instantaneous velocity and pressure fields around a lateral opening ($\theta = 90^\circ$) are very distinctive at the two moments when the ventilation rate is largely different. Such unstable airflow exchanges should be attributed to the fact that the reverse vortexes and the reattachment flows at the lateral facades are always

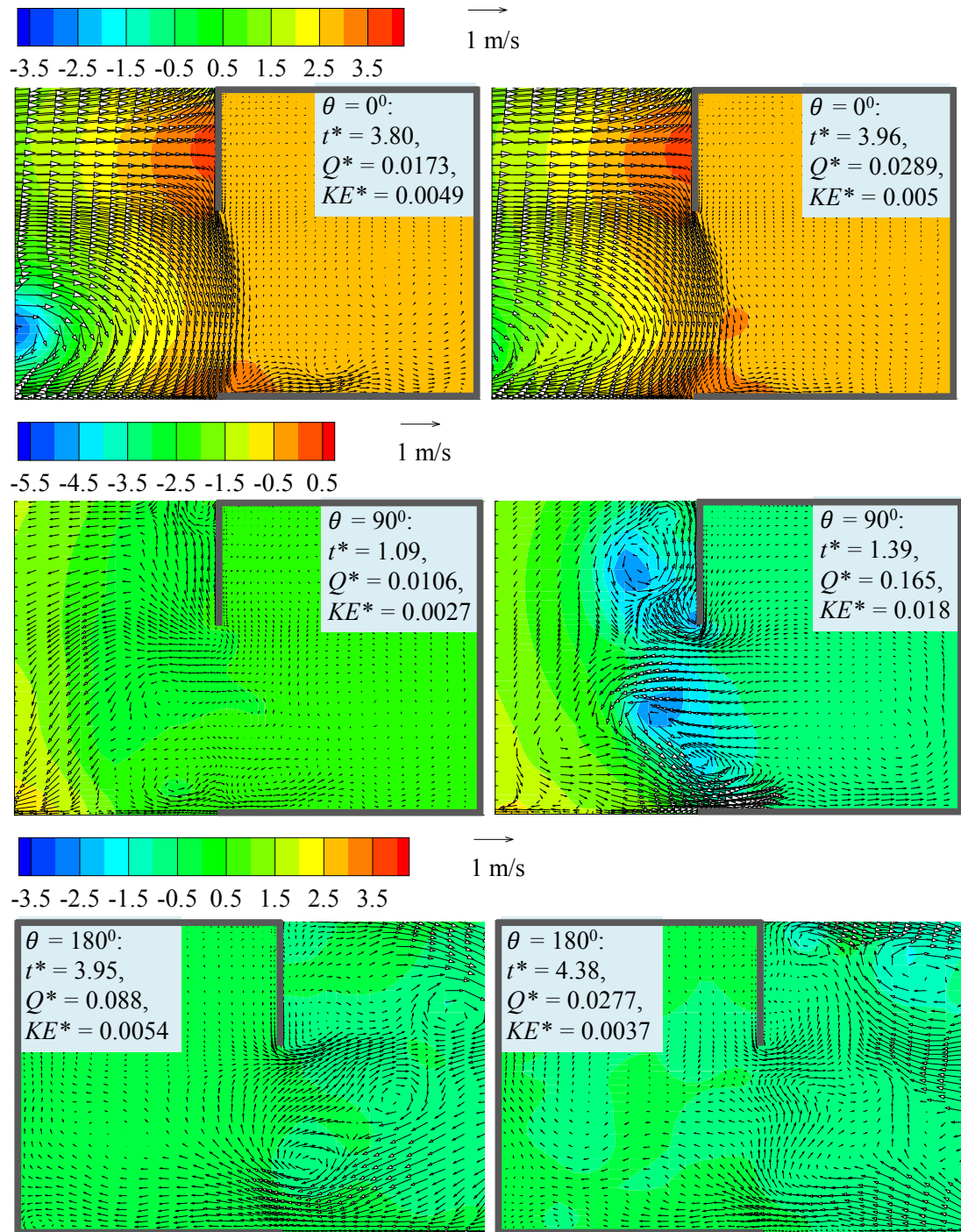


Figure 5.13 Distribution of velocity vectors and pressure contours on the vertical center plane of the opening for three wind directions.

fluctuating (ASHRAE Handbook, 2011; Martinuzzi and Tropea, 1993). In particular, in the moment with a large ventilation rate, at least three low-pressure vortexes are formed near the opening, which induce strong airflow exchanges between the inside and outside. For a lateral opening, it is the highly unsteady envelope flow that

dominates the airflow exchange.

Third, the fluctuating intensity of the velocity and pressure fields around a leeward opening ($\theta = 180^\circ$) is in between those in the windward and lateral sides. It can be observed that instantaneous vortices that formed near the opening induce effective inflows and outflows at the lower and upper part of the opening and thus enhance airflow exchange. In contrast, the relatively stable pressure field is not suitable for creating these effective airflows that are normal to the opening plane. However, for both moments, the basic airflow pattern around the opening is almost the same, which is that the large low-pressure, fluctuating, recirculation vortex behind the building drives the airflow to the inside through the lower part of the opening and vacuums the indoor air to the outside from the upper part of the opening. This basic airflow pattern should be the dominant driver of the airflow exchange through the leeward opening.

As shown above, the airflow pattern around a single opening always changes with time, and these changes are particularly significant for lateral and leeward openings. This demonstrates that the transient analyses of airflow exchange processes are necessary. As a comparison, these transient flow characteristics are compared with those produced using the RNG $k-\varepsilon$ turbulence model (see Figure 5.10). The time-independent velocity and pressure fields seem to be close to the instantaneous ones (as shown in Figure 5.13) for the windward opening, but largely different for the lateral and leeward openings, where the fluctuation of airflow exchange is significant. In addition, these comparisons also provide evidence that the RANS models normally overestimate the ventilation rate for windward ventilation and underestimate lateral and leeward ventilations (Caciolo et al., 2012).

5.3.5 Characteristics of inflow and outflow at a single opening

Figure 5.14 presents the distributions of the velocity component that is normal to the opening at two selected moments for wind directions of 90° and 180° . As the legends note, the positive values indicate inflows and the negative values indicate outflows. From this figure, three things can be observed. First, for a certain wind direction, the velocity distributions on the opening are very different in the two moments. The moment with a larger ventilation rate shows obvious areas of inflow

and outflow on the opening, but they are less obvious for moments with a smaller ventilation rate.

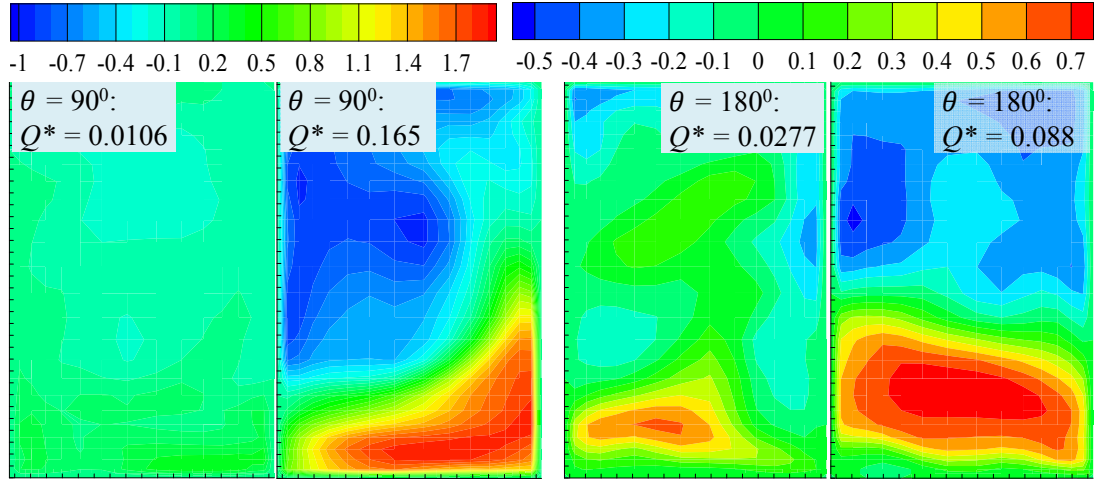


Figure 5.14 Distribution of the normal-component velocity on the openings.

Second, the locations of inlets and outlets on an opening are different under different wind directions. Even for the same wind direction, these locations could change with time. That is, an inlet at a previous moment could be an outlet at a later moment.

Third, the inlets and outlets are not necessarily located at the upper and lower halves of an opening, which could be very irregular in geometry. These observations imply that it is unreliable to predict ventilation rates through a single opening with a presumption that the inlet and outlet are regularly located on the upper and lower parts of an opening and are fixed with time. Examples of such predictions can be found in the empirical and experimental methods that use pressure coefficients on a building surface to estimate ventilated forces (Chand et al., 1998; Ai et al., 2011b) and the theoretical methods developed based on the upper-lower distribution of inlet and outlet (Wang and Chen, 2012).

5.3.6 Summary

The fluctuating ventilation characteristics of single-sided natural ventilation under five different wind directions are investigated. The tracer gas concentration decay

method based on the LES model is used to predict transient ventilation rates. The indoor kinetic energy and the airflow patterns around the openings are also analyzed.

For windward ventilation, the velocity and pressure fields around the opening are relatively stable, hindering turbulence diffusion across the opening. The airflow exchange through the windward opening is mainly driven by the large momentum of the impinging mean flow. The turbulent flow contributes only an average of 14.8% to the total ventilation rate.

For lateral ventilation, the velocity and pressure fields around the opening are very unsteady and highly time-dependent. The fluctuating reverse and reattachment flows dominate the lateral flow field and, in turn, the airflow exchange through the opening, leading to a highly fluctuating ventilation rate. The turbulent flow contributes an average of 63.4% to the total ventilation rate.

For leeward ventilation, the fluctuating intensity of the velocity, pressure fields, and the ventilation rate fall in between those of the windward and lateral ventilations. The airflow exchange through the opening is mainly driven by the low-pressure, fluctuating, recirculation vortex behind the building. Turbulent flow still plays an important role in airflow exchange, which contributes an average of 37.3% to the total ventilation rate.

The locations of inlets and outlets on an opening can change frequently with time, and they are not necessarily located at the upper and lower parts. This implies that it is not reliable to use a predictive method of single-sided ventilation rates that assumes that the inlet and outlet are regularly located on the upper and lower parts of an opening.

Indoor kinetic energy generally increases with the ventilation rate. However, abnormal trends can be found. Namely, stronger indoor air movement does not guarantee a larger effective airflow exchange. Owing to higher indoor air movements, a room with lateral or leeward ventilation is much easier to achieve a thermally comfort indoor environment than that with windward ventilation.

Chapter 6

Airflow characteristics and interunit dispersion around multistory buildings

6.1 Introduction

This chapter presents the investigation of wind-induced airflow pattern and interunit dispersion characteristics around multistory buildings using both RANS and LES models. The RANS model is used to predict and quantify the reentry phenomenon under three wind directions, namely normal, oblique and parallel wind directions. The interunit dispersion pattern characterized by the airflow field is investigated by generating tracer gas in each unit of the buildings. The tracer gas concentration distribution in all units is then analyzed to visualize the dispersion routes and to quantify reentry possibilities. The dispersion pattern around a building with non-flush walls (with the presence of balconies) is also examined. Based on the RANS results, selected typical cases are further investigated transiently using a LES model. For LES simulation, two aspects are paid special attentions: (a) comparison of dispersion routes with those provided by previous RANS simulations and (b) comparison of time scales with those of natural ventilation and survival times of pathogens.

6.2 RANS simulations

6.2.1 Modeling method

6.2.1.1 Configuration setup

In order to study the wind-induced interunit pollutant dispersion via envelope openings in multistory residential buildings, a 1:30 scaled five-story hypothetical building (Building A) with six units on each floor is constructed (see Figure 6.1 (a)). For isothermal flow and pollutant dispersion around an isolated building, as studied here, the Re similarity is relatively important and it is suggested to be followed (Snyder, 1981). In this study, even though the wind speed at the height (H) of hypothetical buildings is as low as 1.0 m/s, Re ($Re = (\rho U_{ref} H) / \mu_t$) is around

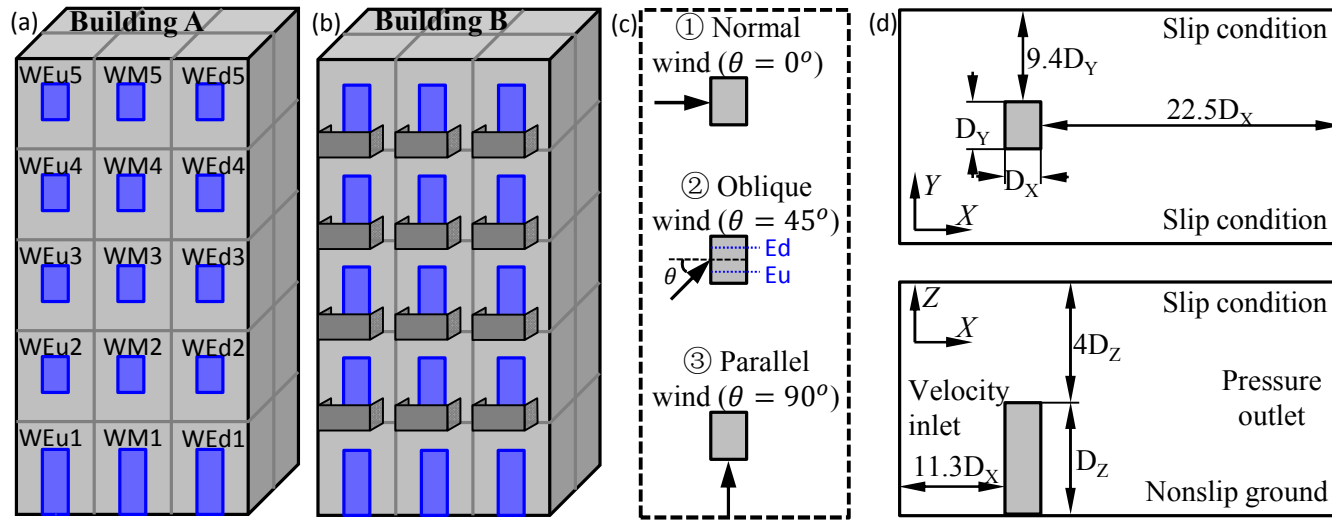


Figure 6.1 Hypothetical building models (a)-(b), cases studied (c), and computational domain (d).

30,000, which is sufficiently large to make Re independent ($>15,000$).

The room dimensions in the prototype are 3.1 m (X) \times 2.4 m (Y) \times 2.7 m (Z). The opening dimensions are 0.75 m (Y) \times 1.2 m (Z) on the upper four floors and 0.75 m (Y) \times 2.0 m (Z) on the first floor. The height of the windowsills on the upper four floors is 0.8 m. All of these dimensions match those measured by Niu and Tung (2008) in a real building in Hong Kong. The choice of this hypothetical building is derived from the following considerations:

- The slab-like block is one of the most typical forms of residential building in Hong Kong (Niu and Tung, 2008; Gao et al., 2008).
- It is suspected that the leeward side may exhibit serious upward dispersion since it is close to the strong downstream recirculation zone. Thus, the leeward units are constructed.
- The scale of present hypothetical models (five stories vertically and three units horizontally per side) is chosen, as a result of the compromise between the computational costs and the capability to revealing and capturing the upward, downward and lateral dispersion phenomena.

To further evaluate the effect of an envelope feature on pollutant dispersion, another hypothetical building with balconies (Building B) is created (see Figure 6.1 (b)). The dimensions of the balcony in the prototype are 0.9 m (X) \times 1.8 m (Y) \times 0.9 m (Z). In Building B, the opening dimensions for all units are 0.75 m (Y) \times 2.0 m (Z). This treatment is based on the assumption that a room with a balcony benefits from a larger, floor-extended opening. Apart from normal incident wind direction (0°), this study also considers oblique (45°) and parallel (90°) wind directions (see Figure 6.1 (c)). The effect of wind direction on the interunit pollutant dispersion characteristics will be discussed comparatively. The units are named as shown in Figure 6.1 (a), W indicating windward side, Eu upstream end units, M middle units, Ed downstream end units, and numbers 1 to 5 the story levels. The naming system in the leeward side is identical to the windward side, except that W is replaced by L. The two lateral sides are aerodynamically identical for the cases under parallel wind direction, and W and L are omitted from the names.

6.2.1.2 Numerical details

The two hypothetical buildings are separately placed in a computational domain, as shown in Figure 6.1 (d). The domain dimensions are selected based on the best practice guidelines (e.g., Franke et al., 2007; Tominaga et al., 2008b, Yoshie et al., 2007) as well as the findings arisen from Chapters 4 and 5, resulting in a maximum blockage ratio of 1.01%. According to Niu and Tung (2008), for current building configurations and an indoor/outdoor temperature difference of 3-5 °C, the turbulence effect of a wind speed over 0.9 m/s can overwhelm the thermally driven force. Measurements by Georgakis and Santamouris (2006) show that the most common range of wind speeds in the urban environment is 1.0 to 2.0 m/s, which is supported by the findings of a numerical study on a residential estate of 52 blocks in Hong Kong (Gao, 2011). Based on this information, two reference wind speeds, U_{ref} , at the height of the building roof, at 1.0 and 2.0 m/s are considered when studying the wind-dominated pollutant dispersion.

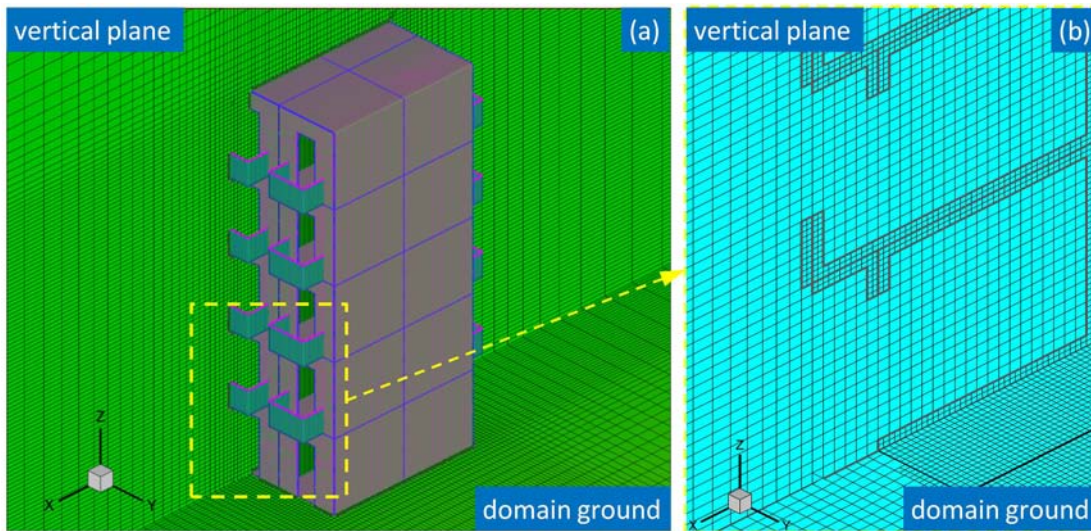


Figure 6.2 Mesh information in and around the building model.

The body-fitted mesh-generation technique suggested by van Hooff and Blocken (2010) is adopted to take a full control of the mesh quality, particularly in the region immediately close to the building. Near the domain ground and the building surfaces, a locally refining method (see Section 5.2.3.3) that doubles the mesh number of the first cells both horizontally and vertically in a hemisphere zone is used. The

sensitivity of the mesh number has been tested, and eventually a mesh system with around 3.5×10^6 cells is used because it produces a similar flow field with a finer mesh system. The grid width of the minimum cells is $0.0028H$ and a maximum stretching ratio around the building models is 1.18. The resultant average y^+ value on the building surfaces and domain ground is around 4.0. A schematic view of numerical grid in and around the building model is given in Figure 6.2.

The inlet boundary conditions are specified with U , k and ε , which are the same with those of Gorlé et al. (2009) listed in Table 4.1. In order to obtain the expected reference wind speeds at the roof height, the friction velocity u^* in the inlet velocity profile is changed, when maintaining the roughness height z_0 to be a constant. Consequently, the parameters and model coefficients used are: for $U_{ref}=1$ m/s: $u^*=0.065$ m/s, $z_0=0.00075$ m, $M_1=0.025$, $M_2=0.41$, $C_\mu=0.001$ and $C_R=1.0$; for $U_{ref}=2$ m/s: $u^*=0.13$ m/s, $z_0=0.00075$ m, $M_1=0.025$, $M_2=0.41$, $C_\mu=0.001$ and $C_R=1.0$. On the domain ground, the roughness modified two-layer model is used. Other boundary conditions at domain outlet, domain ceiling, domain lateral sides, building surfaces and turbulence model coefficients are the same with those listed in Table 4.1. Based on the converged airflow field, the tracer gas (CO_2) is generated and its governing equations are then solved alone. Each time, the CO_2 is released in the geometrical center (point source) of one unit at a rate of 8.0 mg/s, and its concentration in all units is then examined to determine its dispersion characteristics. When concentration equations are solved, the turbulent Schmidt number (Sc_t) of 0.7 is used. Solution methods are the same with those for RANS simulations of flow and concentration fields in Chapters 4 and 5. The convergence is achieved when both the area averaged wind speed and CO_2 concentration at the opening of the source unit are stable for around 50 iterations.

6.2.1.3 Interunit dispersion evaluation

To evaluate the potential interunit pollutant dispersion, that is, the possibility of reentry, the quantifying method proposed by Niu and Tung (2008) is used, but with some changes based on the different airflow patterns between the buoyancy and wind dominated conditions. The reentry ratio, R_k , is defined as the fraction of the exhaust

air from a source unit i which reenters another unit j . It can be calculated by the following equation:

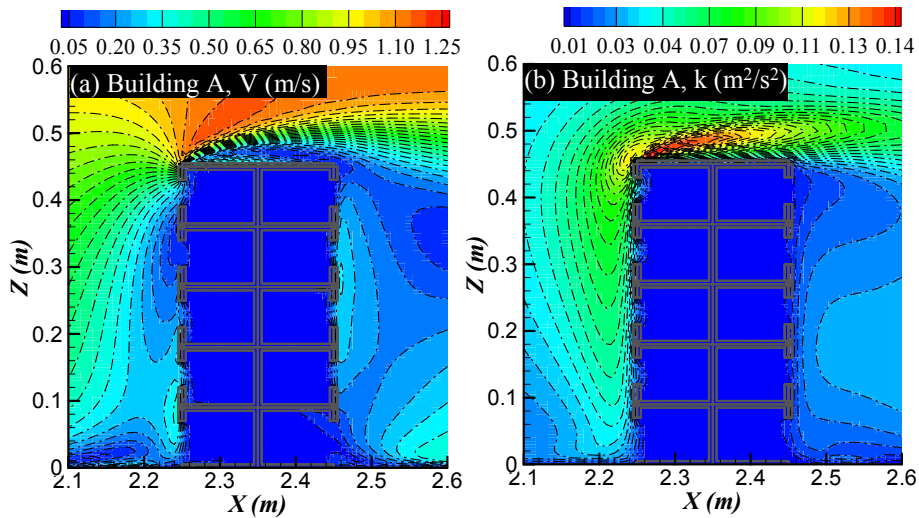
$$R_k = M_{i-j} \frac{V_j (\text{ACH})_j}{V_i (\text{ACH})_i} \quad (6.1)$$

A detailed deduction of this equation can be found in (Niu and Tung, 2008). The mass fraction, M_{i-j} , is defined as the mass fraction of air that originates from the source unit i and is present in another unit j . Here, the pollutant concentration in a room is represented by that found on the respiration plane (in the standing situation) at the height of 1.6 m above the floor. M_{i-j} can be directly calculated from the predicted mean concentrations of the tracer gas CO_2 on the two planes, $M_{i-j} = C_j / C_i$.

6.2.2 Normal wind direction ($\theta = 0^\circ$)

6.2.2.1 Airflow characteristics

The airflow pattern in and around a building is the key to influence the airborne dispersion of pollutant between units. Although the airflow pattern around a bluff body has been well studied, little work has been done on the envelope flow of a multistory windows-opened building.



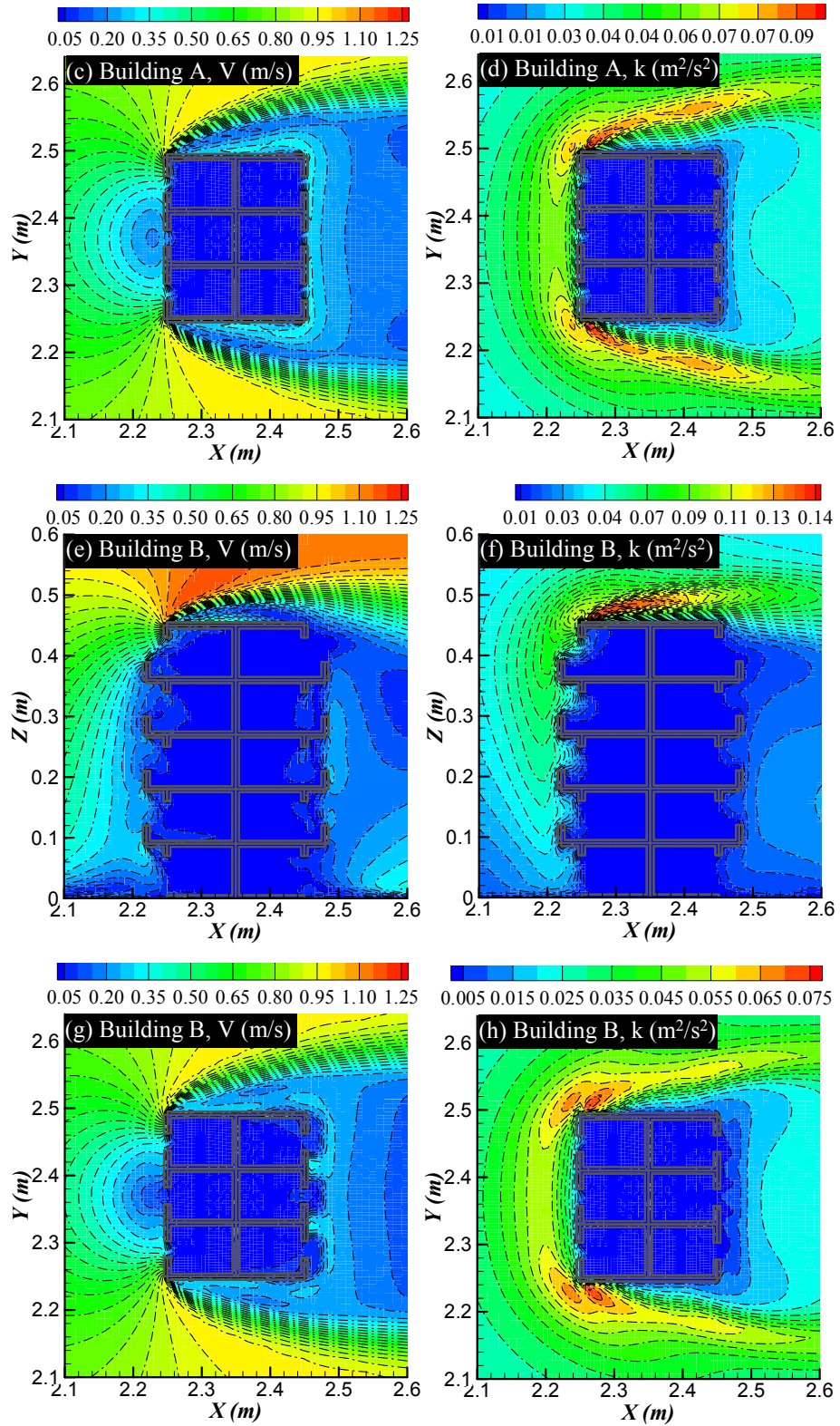


Figure 6.3 Mean velocity magnitude and turbulence kinetic energy on the vertical and horizontal center planes of the hypothetical buildings at a wind speed of 1.0 m/s.

Figure 6.3 shows the mean velocity magnitude and turbulence kinetic energy on

the vertical and horizontal center planes of the hypothetical buildings under the wind speed of 1.0 m/s. The mean velocity and turbulence kinetic energy values of the mainstream are very similar to those around a bluff body (Santos et al., 2009; ASHRAE Handbook, 2011; Liu, 1991; Martinuzzi and Tropea, 1993). However, because of the stronger interaction between the approaching wind and the building envelope, the opening-mounted façades here introduce more resistance to the sweeping airflow (the airflows that are almost parallel to the walls in the near-wall regions) and in turn create a more rough and dynamic near-wall flow field than that formed in nonslip, smooth surfaces. This near-wall turbulent wind fluctuation continuously drives the indoor/outdoor air exchange (Haghighat et al., 1991). The presence of balconies further roughens the façades. Their presence effectively breaks up the vertical downwash and uprush near the windward and leeward façades, which consequently extends the airflow penetrations into the interior (see Figure 6.3 (e) and (g)). From Figure 6.3 (f) and (h), it appears that the turbulence kinetic energy in the mainstream is lowered by the roughness of balconies, but in the near-wall areas, it still remains larger due to the impingement of wind.

6.2.2.2 Dispersion characteristics

6.2.2.2.1 Leeward side

On the leeward side, the near-wall flow pattern is characterized by two recirculation flows, namely one large building-height recirculation and one small corner recirculation near the bottom floor. Figure 6.4 shows the reentry ratios of tracer gas from a source to other units on the leeward side. As the two end units are aerodynamically identical under normal incident wind direction, only one end's results are presented. In the figure, the arrows (in background) are used to schematically indicate the important dispersion directions (with a reentry ratio larger than 1.0%). Their lengths represent the dispersion scope in these important dispersion directions. The meaning of these arrows is the same in later figures.

First, pollutants generated from the first floor can only affect the bottom two floors and are more serious on the first level; see Figure 6.4 (a) and (f). This implies that the small corner recirculation could extend across the lowest two floors. Most of the pollutant generated from LE1 is effectively diluted and transported downstream,

with a small stream reentering the adjacent units. In contrast, the pollutant emitted from the middle unit LE2 has a larger scope of contamination, since it disperses round all adjacent units before entering the main downstream. The presence of balconies generally increases the reentry ratios, since it restricts the upward dilution and maintains a higher concentration in the region of corner recirculation.

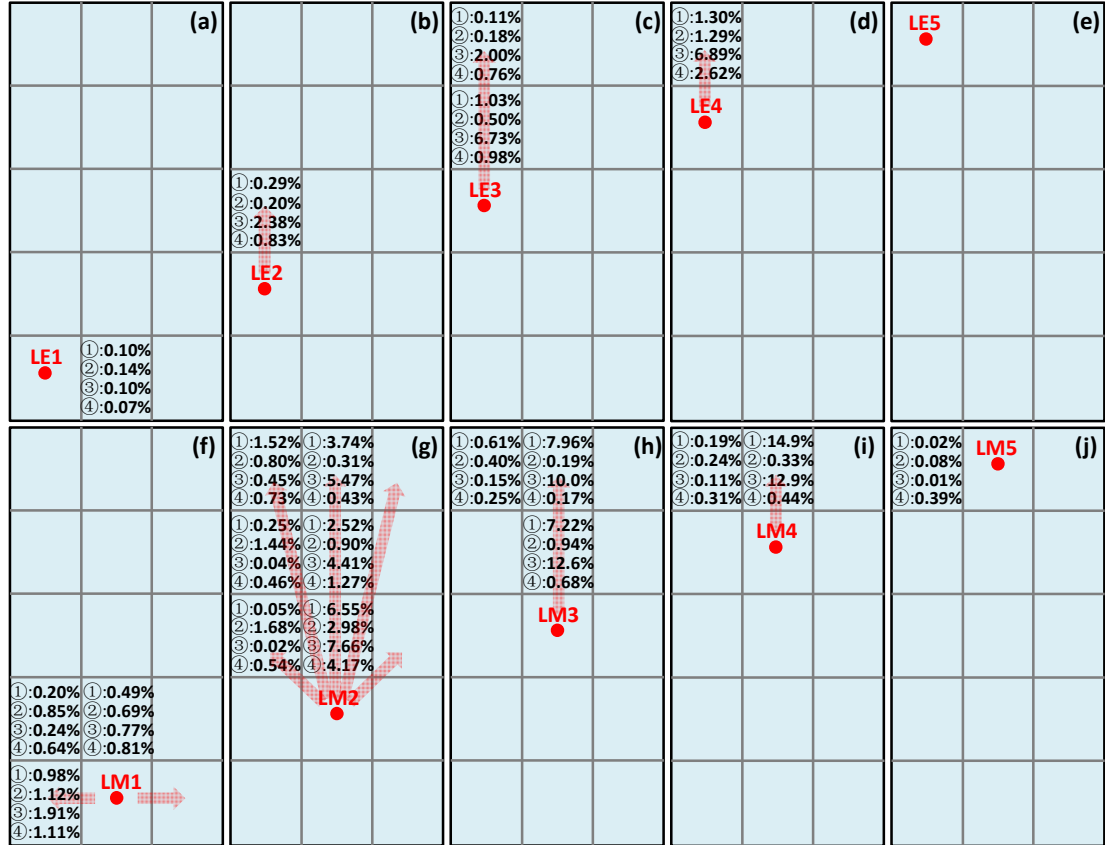


Figure 6.4 Reentry ratios of tracer gas from the source to other units on the leeward side. Red dot: tracer gas source; ①: Building A, 1.0 m/s; ②: Building B, 1.0 m/s; ③: Building A, 2.0 m/s; ④: Building B, 2.0 m/s.

Second, almost solely upward transmission (almost no dispersions towards other directions) is found when the pollutant is released from the middle three floors (Figure 6.4 (b)-(d) and (g)-(i)), where the strong upward flow is fully developed. Pollutant emitted from the end units (LE2, LE3, and LE4), pushed by weak lateral flows, has no or negligible effect on the middle units. On the contrary, pollutant from the middle units LM2, LM3, and LM4, reenters all the units above them, with the

effect being more serious for the center units. When the tracer gas is released from LM4 (Figure 6.4 (i)), the reentry ratio in the upper unit LM5 reaches as high as 14.9% at a wind speed of 1.0 m/s. This means that the units vertically above the source should be included on the high-infection list. The presence of balconies can effectively obstruct the vertical upward development of flows and accelerate their dilution to the downstream flow, which in turn significantly decreases the vertically upward transmission and lowers the interunit infection risk. This implies that the high reentry ratios in the scenario without balconies are being generated by the direct reentry carried by upward flow, rather than a high concentration caused by the negative-pressure recirculation.

Finally, the pollutant released from the topmost floor is easily diluted by both the upward flow in the leeward side and the horizontal flow from the upstream, so very little reenters the neighboring units.

6.2.2.2.2 Windward side

On the windward side, the exhaust air from the end units does not reenter other windward units and reenters the leeward units with negligible reentry ratios ($<0.1\%$). This basically means the gaseous pollutants generated from the end units, driven by the lateral separation flows, directly disperse downstream.

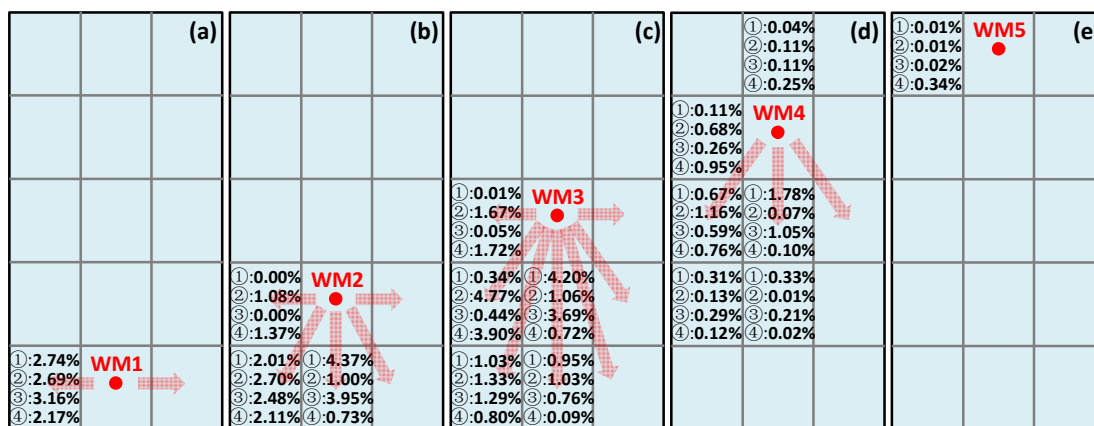


Figure 6.5 Reentry ratios of tracer gas from the source to other units on the windward side. Red dot: tracer gas source; ①: Building A, 1.0 m/s; ②: Building B, 1.0 m/s; ③: Building A, 2.0 m/s; ④: Building B, 2.0 m/s.

For the middle units, although the lateral flows are also important, the upward and downward separations dominate the tracer gas dispersion. In this study, the stagnation zone is located at the fourth floor, which is consistent with the common knowledge that it occurs at the 2/3 height of a bluff body. The reentry ratios of the tracer gas from a source to the other units in the windward side are shown in Figure 6.5. From this summary of the reentry ratios under the four scenarios, namely, hypothetical buildings A and B under wind speeds of 1.0 and 2.0 m/s, several observations can be made.

First, when the gaseous pollutant is released in the unit WM1 (Figure 6.5 (a)), only lateral dispersions result. The first floor is located at the bottom of the downward flow. As this is close to the ground, the momentum of the downward flow is partially transferred to the frontal recirculation and partially to the lateral separations. It is the latter which carry pollutants back into the lateral units.

Second, when the source is located in the units WM2 and WM3 (Figure 6.5 (b)-(c)), both downward and lateral dispersions result. The second and third floors are covered by the strong downward flow. Here, the near-wall flow pattern is very different between the cases with and without balconies. For the latter, most momentum is transferred to the vertical and oblique downward flows, leaving very weak horizontal flows. Thus, almost all the tracer gas is carried to the lower regions, giving larger reentry ratios for the units on the lower floors (up to 4.37% in the unit immediately beneath the source). Traveling with the downward flow, the tracer gas is rapidly diluted; taking the source unit WM3 as an example, the reentry ratio of 3.69%-4.20% in WM2 decreases to 0.76%-0.95% in WM1. In contrast, the vertical downward flow is effectively broken up by the presence of balconies, which results in a significant reduction (up to 82%) in the reentry ratio in the vertical lower floors, from 3.95% to 0.73% (see Figure 6.5 (b)). However, this allows more tracer gas to disperse in the lateral and oblique downward directions. Owing to the blockage created by balconies, the largest reentry ratios do not occur in the unit beneath the source, but in the end unit of the floor immediately below (up to 4.77% in WE2 in Figure 6.5 (c)). This is because the downward flow, blocked by the balconies, flows downwards through the spaces between the two horizontal balconies, and hence easily reaches the end unit of the lower floor. The effect of wind speed on the tracer gas dispersion is complex. The reason for this complexity is likely to be the conflict

between the dispersion and dilution momentums of the tracer gas as wind speed increases. Generally, the units on the floor immediately beneath the source should be included in the high-infection list in the event of a disease outbreak.

Third, when the pollutant is released in the unit WM4, all windward units can be affected; see Figure 6.5 (d). Since WM4 is located in the stagnation region, the released tracer gas disperses in all directions, though reducing the reentry ratios. From these ratios, it is clear that the downward and lateral rather than the upward separations dominate the envelope flow pattern of the fourth floor.

Finally, most of the pollutant released from WM5, driven by the upward flow, directly disperses downstream and does not reenter other units.

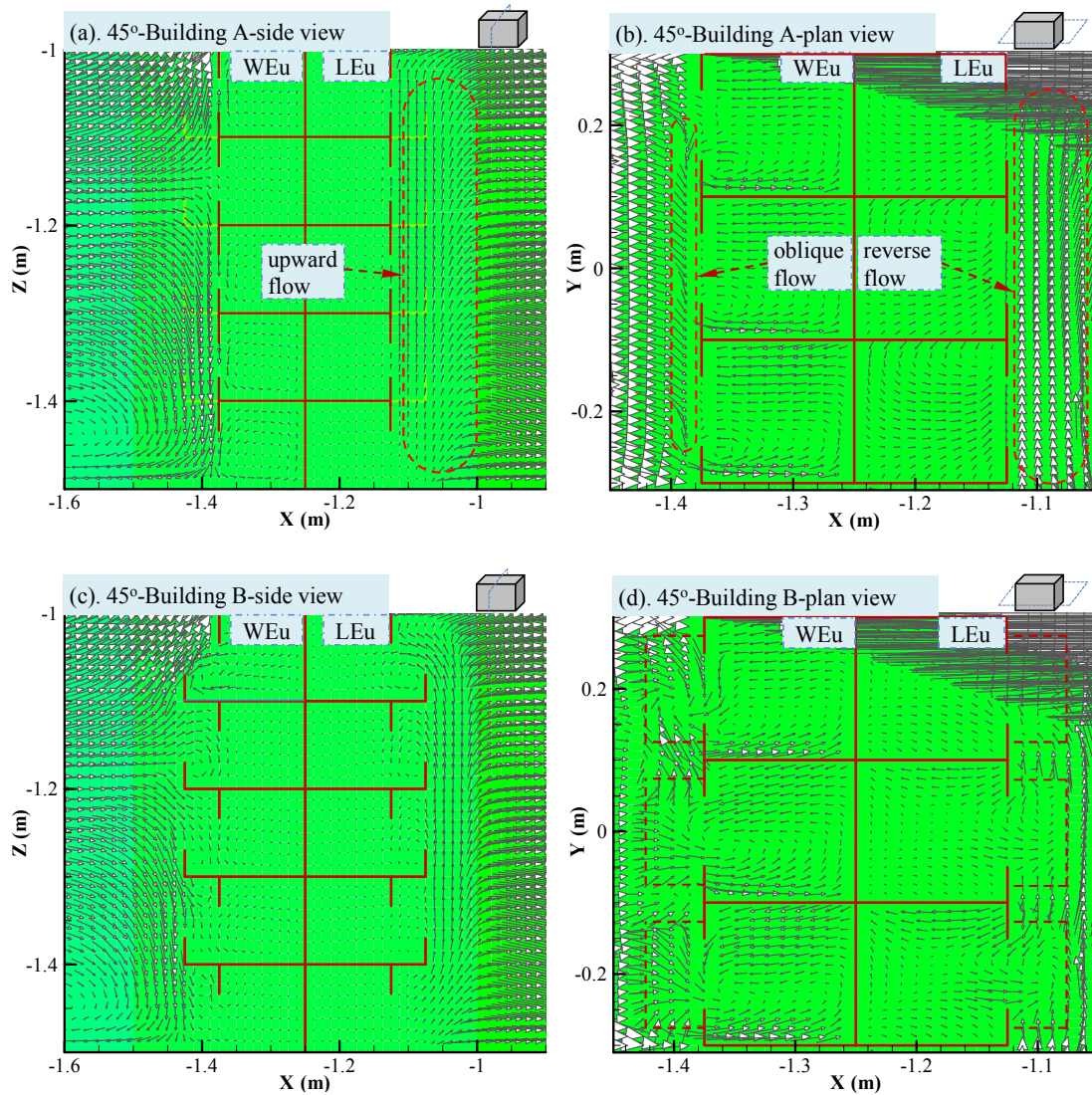


Figure 6.6 Qualitative comparison of the near-wall airflow pattern around Building A and Building B, under oblique incident wind ($\theta = 45^\circ$).

6.2.3 Oblique wind direction ($\theta = 45^\circ$)

6.2.3.1 Leeward side

In spite of the complexity of the effect of wind speed, the results under normal wind direction show that the dispersion characteristics at the wind speeds of 1 m/s and 2 m/s are mostly similar. In order to focus on analyzing the interunit dispersion characteristics under oblique and parallel wind directions, the later sections only present velocity fields and reentry ratios at the wind speed of 2 m/s.

In general, the flow pattern near the leeward facade under oblique wind direction is mainly characterized by the combination of a strong upward airflow, a strong horizontal reverse flow from downstream to the upstream units, and a weak reattachment flow, as shown in Figure 6.6. Again, the presence of balconies roughens the building surfaces and in turn results in a more turbulent and dynamic near-wall flow field.

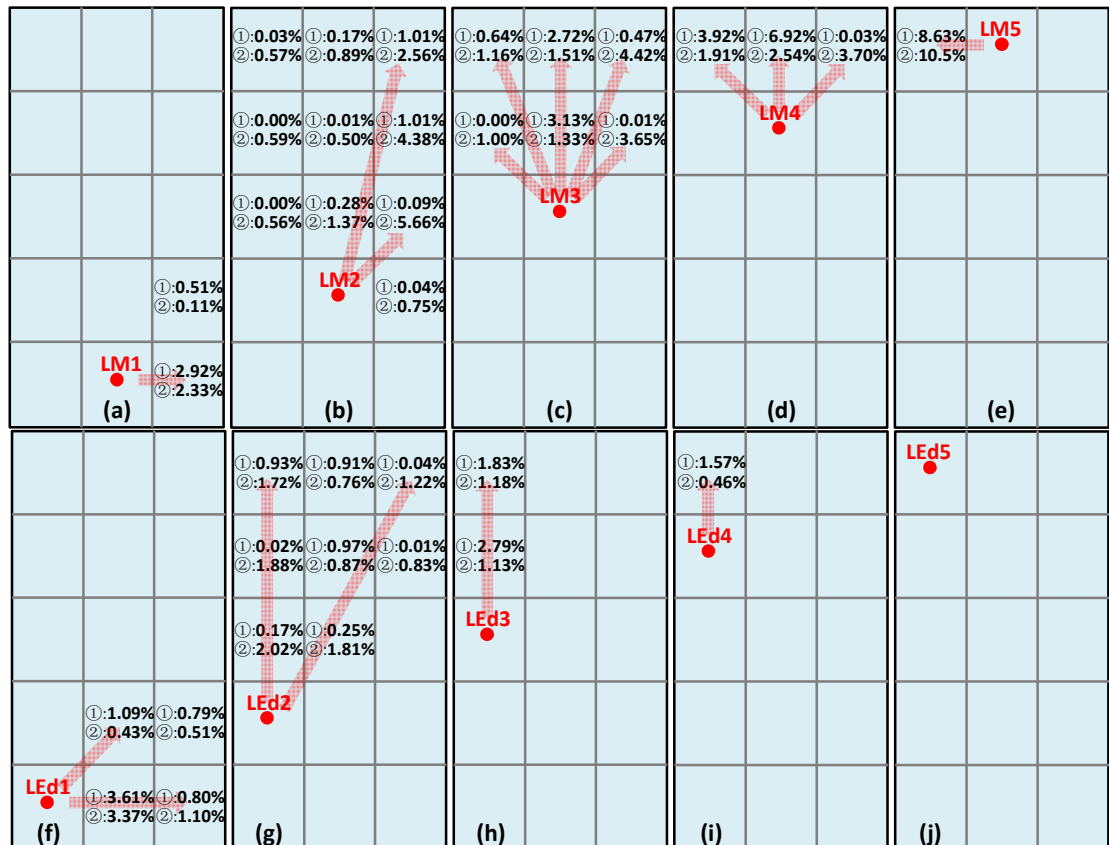


Figure 6.7 Reentry ratio of tracer gas from a source unit to other units on the leeward side, under oblique incident wind ($\theta = 45^\circ$). Red dot: tracer gas source; ①: Building A; ②: Building B.

The reentry ratios on the leeward side, with and without balconies, are summarized comparatively in Figure 6.7. The pollutant generated in the upstream units (LEu-) is effectively diluted into the mainstream and reenter into other downstream units negligibly, owing to the strong reverse flow. The dispersion in the middle units on the leeward side is complex (see Figure 6.7 (a)-(e)): different locations are dominated by different types of airflow. The lowest unit (LM1) is dominated by the reverse flow, leaving a large reentry ratio to its upstream unit, up to 2.92%. The dispersion of pollutant generated in the upper four units (LM2, LM3, LM4, LM5) is controlled by all three types of flow; namely, the upward, reverse, and reattachment flows. However, with an increase in height and in horizontal direction, the momentum of the reverse flow is gradually transferred to the reattachment flow. The reason for this is due to the mixing, near the top of the building, of the leeward flows and the strong streamwise flow coming from upstream. This flow trend is similar to those found near a solid body (ASHRAE Handbook, 2011). Here the dispersion pattern is very different between the cases with and without the presence of balconies. When there are no balconies, the upward airflow along the facade is very smooth, inducing a remarkable reentry ratio to the upper floors, especially vertically upper units, up to 6.92%. However, the presence of balconies breaks up this vertically upward development and in turn substantially reduces the reentry ratio to the vertical upper units. Instead, their presence forces the airflow to develop obliquely upward from the space between two balconies, resulting in significant increase of reentry into the oblique upper units, up to 5.66%. For the source unit LM4, the presence of balconies alters the dominance of the type of near-wall airflow on the topmost floor; namely, from reattachment to reverse flows. Finally, there is a great possibility that the pollutant released from unit LM5 will reenter into its downstream unit, which confirms that here the reattachment airflow completely dominates the dispersion.

The pollutant dispersion from the downstream end units (LEd-) is also driven by the combination of the strong upward and attachment flows, as well as a weak reverse diffusion (see Figure 6.7 (f)-(j)). The reverse flow on the bottom floor is very strong, with almost no occurrence of reattachment. Thus, obvious reentry into the adjacent upstream units is found when the tracer gas is generated in unit LEd1. Similar to that in the middle section, along the height of the building, the reverse

momentum quickly decreases and the reattachment momentum increases. The difference from the middle section is that here a large part of the pollutant exhausted from the downstream units is diluted into the downstream of buildings, leaving a little stream to reenter the upper floors. For the source unit LEd2, the presence of balconies decreases the dilution of a pollutant and in turn results in larger reentry ratios in most of its upper units. The reattachment airflow diffusion dominates the upper three floors, where the presence of balconies effectively reduces the upward reentry possibilities.

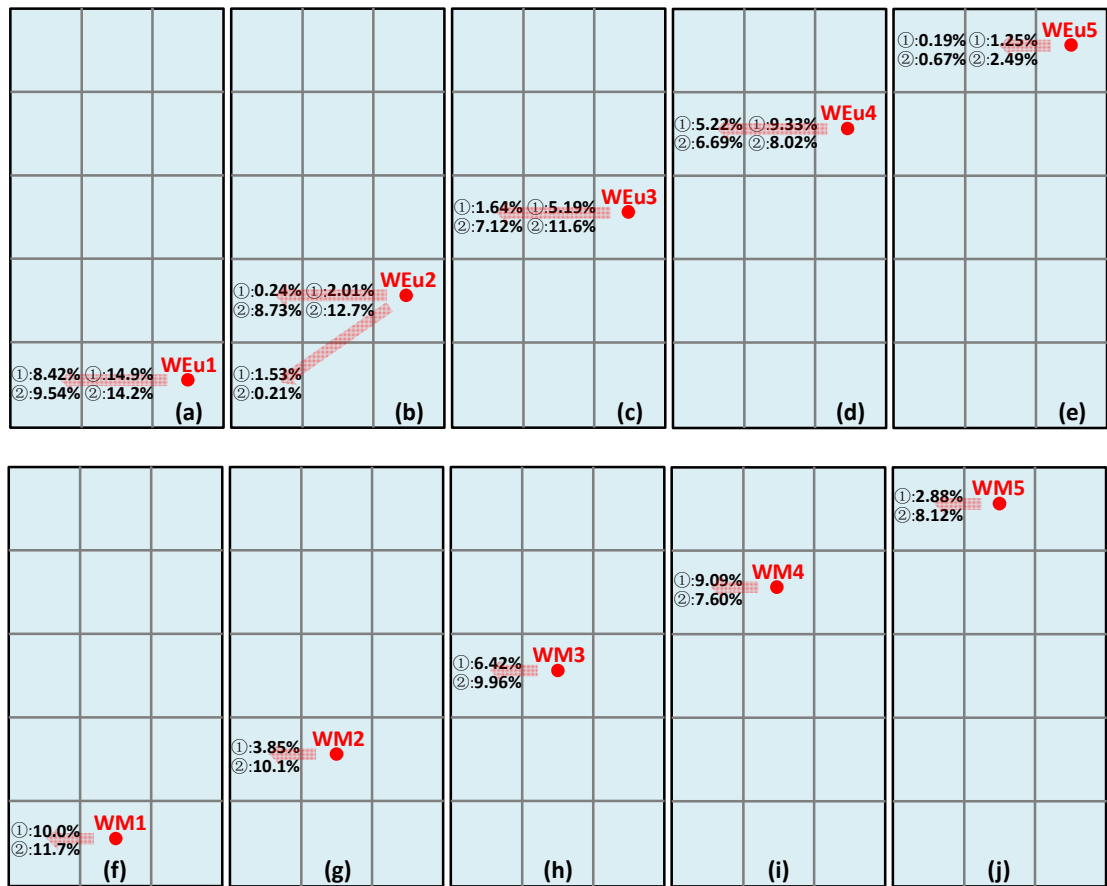


Figure 6.8 Reentry ratio of tracer gas from a source unit to other units on the windward side, under oblique incident wind ($\theta = 45^\circ$). Red dot: tracer gas source; ①: Building A; ②: Building B.

6.2.3.2 Windward side

The reentry ratios on the windward side are summarized in Figure 6.8. On this

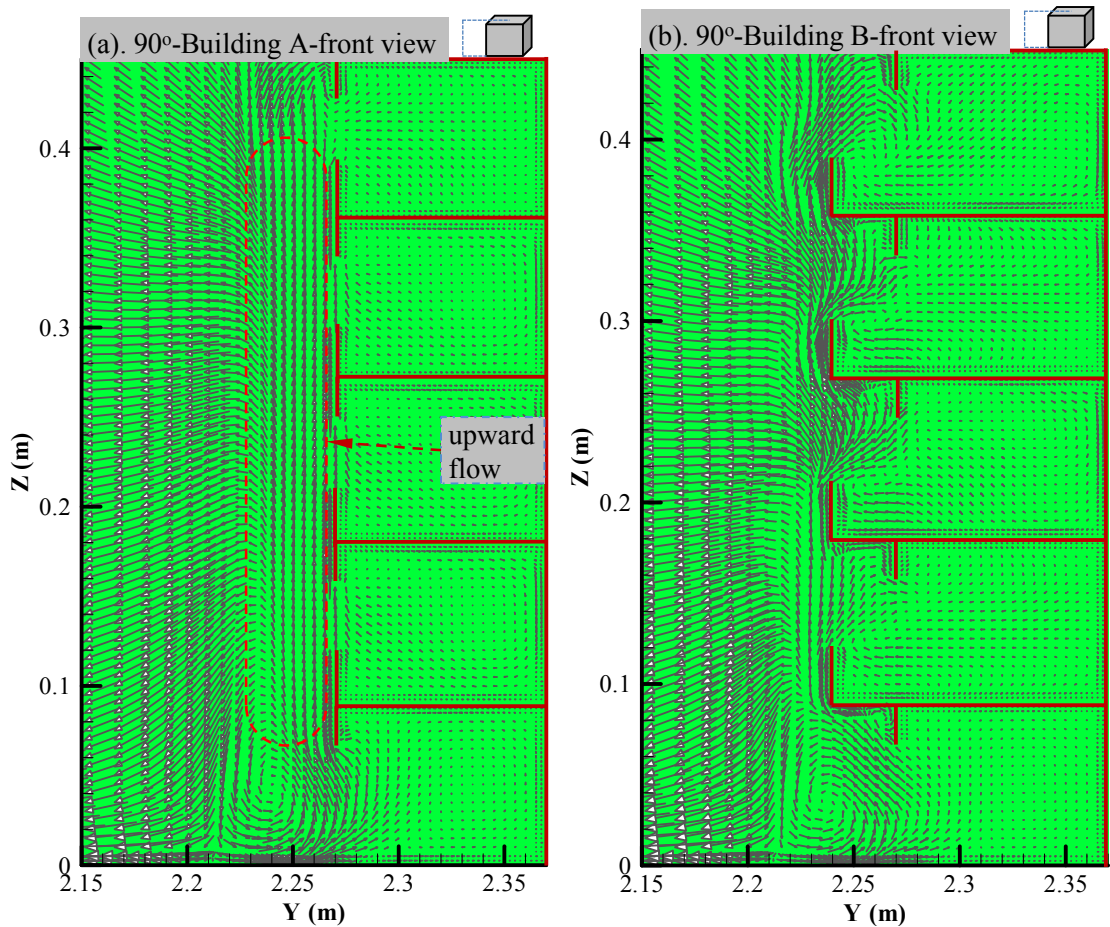
side, the strong sweeping flow from the upstream to the downstream units dominates the interunit dispersion. The bilateral diffusions, as found in any case under normal wind direction, have disappeared. The upward and downward separations are very weak, and do not have enough energy to affect the pollutant dispersion. A special case appears in the lower part of the building, see Figure 6.8 (b), where the combination of the relatively lower sweeping speed and the corner recirculation near the ground results in a downward dispersion. Generally, the reentry ratios on the windward side are large, owing to the unidirectional dispersion containing high-concentration airflow. It is interesting to observe from the figure that the presence of balconies significantly enlarges the reentry ratios for all cases except for the source located in the fourth floor (Figure 6.8 (d) and (i)). This should be explained by the fact that the fourth floor is located in the stagnation region, where the airflow is parallel to the facade, whereas both upward and downward flows exist on other floors. Therefore, on the fourth floor, the vertical parapets of balconies obstruct the spread of a pollutant, resulting in a lower reentry ratio to the adjacent downstream unit, but still a higher ratio in the secondary downstream unit due to the accumulation of a higher concentration. On the other floors, however, the horizontal floors of balconies on the neighboring two stories function as two physical boundaries to reduce the dilution by the upward or downward airflow, and in turn result in a higher reentry ratio to the downstream units. The pollutant exhausted from the downstream end units (WE_d-) is effectively diluted into the downstream, without reentering into other units.

6.2.4 Parallel wind direction ($\theta = 90^\circ$)

Under parallel incident wind direction, the two lateral sides are aerodynamically identical, and thus only one side's results are presented. The flow pattern near the lateral walls is mainly characterized by the combination of an upward flow and a strong reverse flow, see Figure 6.9. Again, it can be seen that the presence of balconies greatly changes the near-wall flow pattern.

The reentry ratios on the lateral side are summarized in Figure 6.10. When the pollutant is exhausted from the upstream end units (Eu-), a large portion, driven by the reverse flow, is diluted into the mainstream coming from upstream, resulting in a

very small reentry ratio to most downstream units. The dispersion of pollutant generated in the middle units (M-) (Figure 6.10 (a)-(e)) is dominated by the reverse flow, with more serious reentry infection in the upper floors, due to a higher reverse wind speed. In the middle section, the presence of balconies can either increase or decrease the reentry ratio to the upstream units. This is essentially due to the fact that the near-wall flow pattern in the middle section is not stable, where the reverse flow, more or less, conflicts with the reattachment flow. Generally, when the reverse flow is dominant, the presence of balconies can increase the reentry ratio, such as in the upper two floors. The reason for this is, as explained before, that the horizontal floors of balconies function as physical boundaries to channel the spread of the pollutant, which lowers its dilution speed and causes high reentry ratios. On the lower floors, the relatively lower wind speed is probably not strong enough to create such parallel flows, and thus the complex diffusion and mixing due to the interactions between flows and boundaries dominates the dispersion. Transient studies are required to explore the details of the dispersion process.



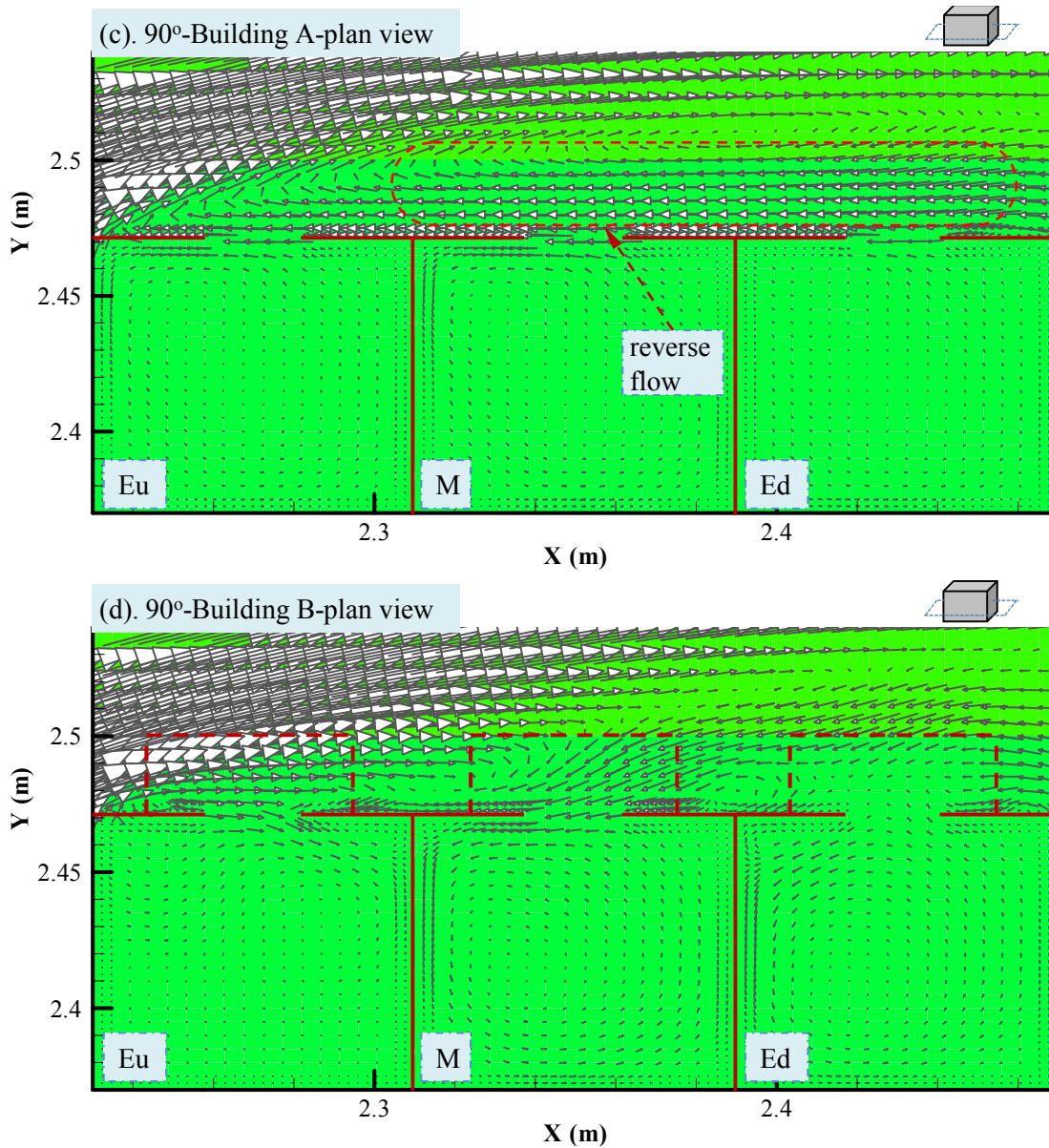


Figure 6.9 Qualitative comparison of the near-wall airflow pattern around Building A and Building B, under parallel incident wind ($\theta = 90^\circ$).

When the pollutant is released from the downstream end units (Ed-), it disperses upstream horizontally and obliquely. The most affected unit is its adjacent upstream one, followed by the floor immediately above. Here, the presence of balconies substantially increases the reentry possibilities. In general, the presence of balconies decreases the dilution of a pollutant and then is not helpful in the prevention of interunit contamination, when there is a crosswind.

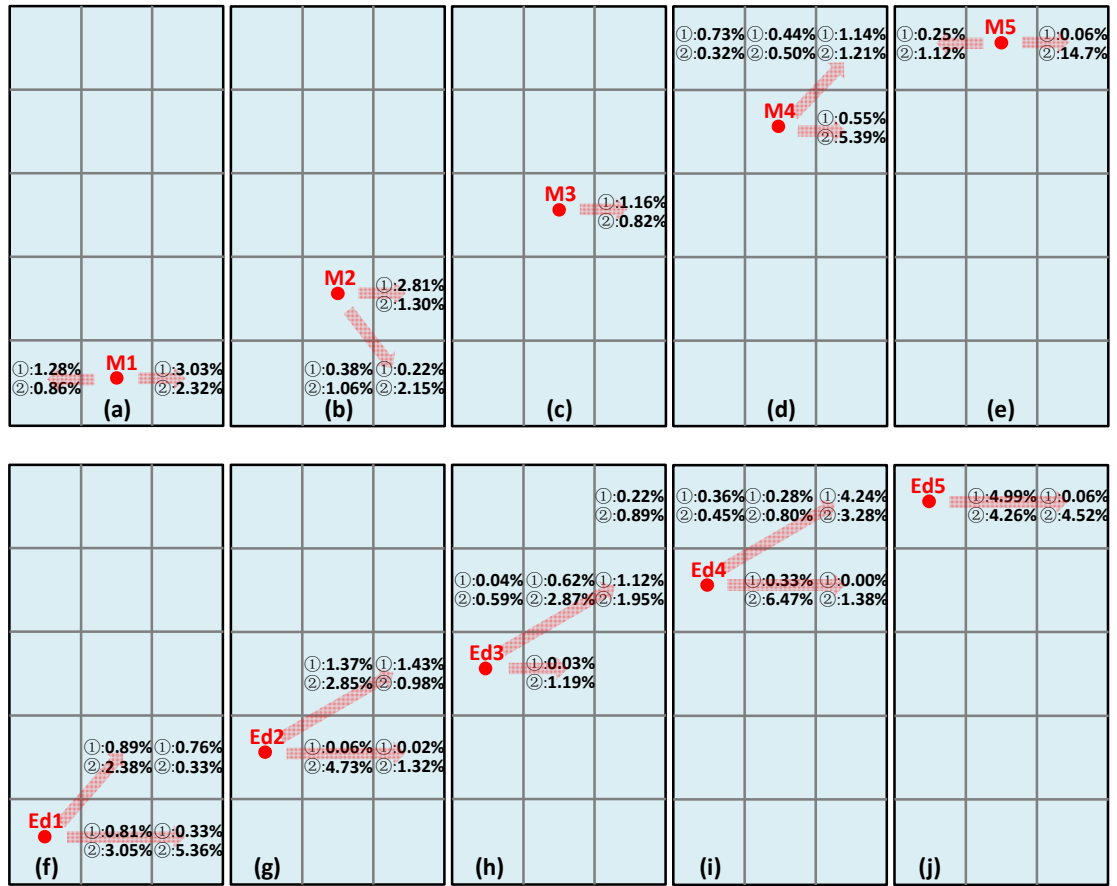


Figure 6.10 Reentry ratio of tracer gas from a source unit to other units, under parallel incident wind ($\theta = 90^\circ$). Red dot: tracer gas source; ①: Building A; ②: Building B.

6.2.5 Further discussion

As the foregoing analysis demonstrates, the dispersion mechanisms of gaseous pollutant in both the vertical and horizontal directions are determined by the near-wall airflow pattern around the building. In the previous wind tunnel experiment by Liu et al. (2010), similar dispersion characteristics are observed under the wind effect; for example under normal incident wind direction, all possible dispersion directions occur on the windward side with upward-dominated dispersion on the leeward. However, the vertical dilution speed observed in their experiment is almost several orders of magnitude lower than in this study, and the horizontal dilution is lower still. This is mainly due to the different building models used in the two studies. In their experiment, the building model is a complex high-rise residential building with a cross (#) floor plan shape in Hong Kong, where the tracer gas is released in

the reentry space. The two lateral boundaries of the reentry space confine the horizontal dispersion of the tracer gas, leading to a high concentration and lower dilution speed. In contrast, the slab-like building used in this study is better for achieving dilution of the pollutant, since there is no obstruction in either the vertical and horizontal directions. Another reason for this difference is likely to be the effect of the presence of real units and openings in this study, whereas Liu et al. (2010) used a solid model. On the one hand, their presence gives rise to a more complex and turbulent near-wall airflow field. On the other, the units can accommodate some of the tracer gas, further reducing the near-wall concentration. By comparing the dispersion mechanism in these two typical building models, it should be apparent to designers and building officials that the different types have different possibilities for cross contamination, in terms of the scope and extent of infectious transmission. Accordingly, they should apply distinctive ventilation strategies and control measures as appropriate.

One of the main findings in this section is the possible dispersion routes and reentry ratios under specific near-wall flow patterns (e.g. upward and downward flows). Thus, for a specific building, once the near-wall flow patterns are determined, the possible interunit dispersion conditions can be estimated. For stand-alone buildings, the near-wall flow pattern can be easily estimated using the local prevailing wind condition. For those buildings located in the street canyons, the near-wall flow pattern should be determined by further on-site measurement or numerical simulation. Based on the estimation of dispersion conditions, the building officials and designers can formulate strategies.

6.2.6 Summary

Taking into account the effect of balconies, the mean reentry ratios of pollutant between units in the same building under three wind directions are quantified, and then the mean dispersion routes are revealed. As a summary, Figure 6.11 presents the typical dispersion patterns around the multistory buildings under the three wind directions, where the corresponding reentry ratios are also provided.

Under a normal incident wind ($\theta = 0^\circ$), the pollutant disperses mainly downwards on the windward side and upwards on the leeward side, respectively. The presence

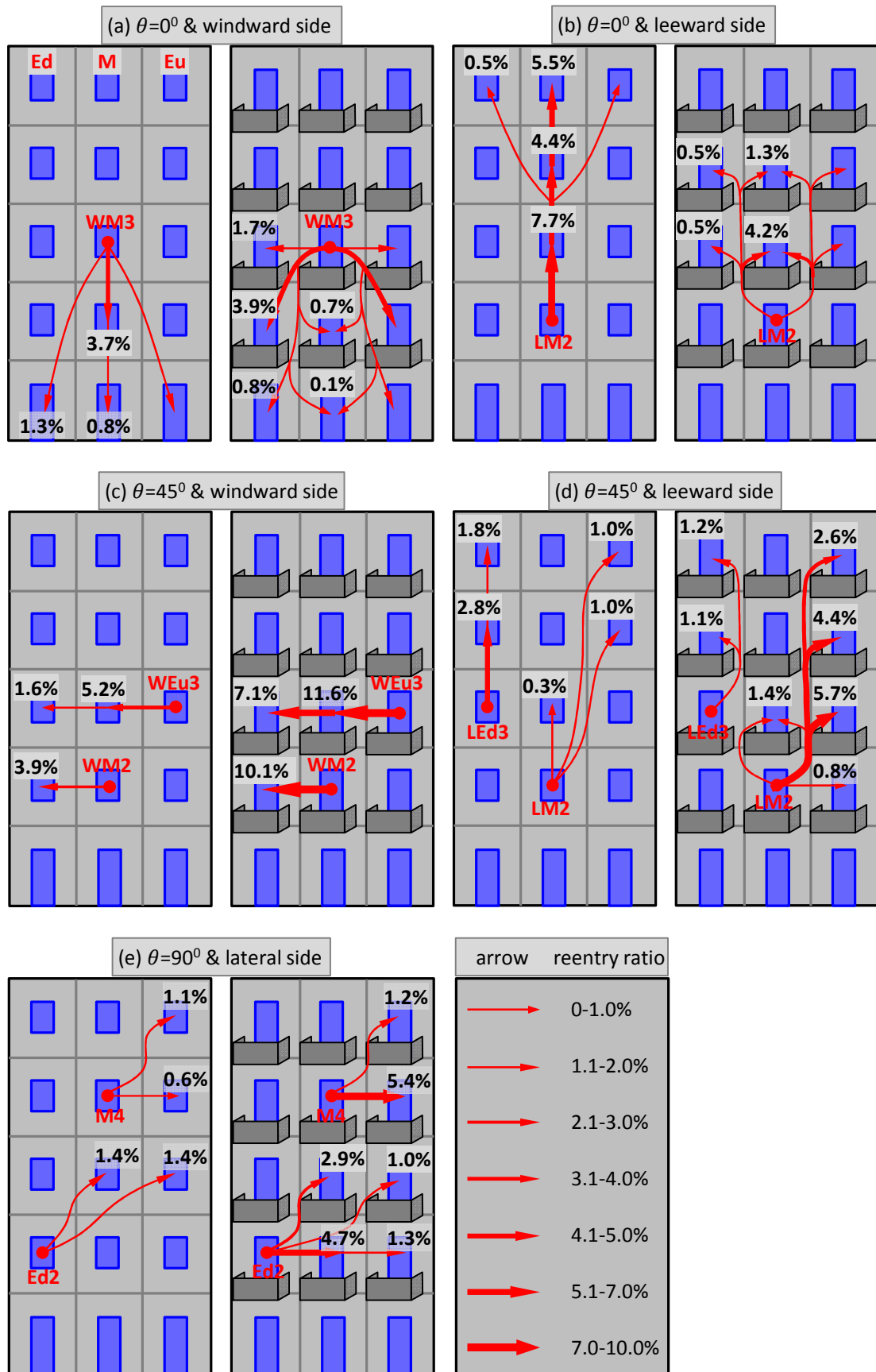


Figure 6.11 A summary of typical dispersion routes around buildings with and without balconies.

of balconies shifts the most affected units obliquely on the windward side, without obviously increasing the reentry ratios. On the leeward side, their presence significantly decreases the reentry ratios from a source unit to its upper units, as the vertical parapet of a balcony induces and assists the dilution of pollutant into the downstream low-pressure recirculation vortex.

- Under an oblique incident wind ($\theta = 45^\circ$), the pollutant disperses mainly towards its downstream units on the windward side and upstream units on the leeward side, respectively. The presence of balconies strongly intensifies the reentry. On the windward side, the balconies function as dispersion channels and restrict the dilution of pollutant along vertical directions. On the leeward side, the intensification of such channel effects is still existed, although their presence lowers the vertical reentry largely when the pollutant is generated from the downstream units (Ed-).
- Under a parallel incident wind ($\theta = 90^\circ$), the pollutant disperses mainly towards its upper and upstream units. The presence of balconies greatly intensifies the dispersion and decreases the pollutant dilution. The reason is similar with that under oblique incident wind.

In general, many reentry ratios appear to be within the range between 5.0% and 10.0%, which suggests that the interunit dispersion is an important pollutant transmission route. On average, the strongest interunit dispersion occurs on the windward wall of the buildings under oblique wind direction (45° & windward side), due to the high ACH values and the unidirectional spread routes. It should be highlighted that the role of protrusive envelope features in interunit dispersion cannot be ignored. The presence of balconies significantly modifies the near-wall flow pattern and the dispersion characteristics. Except under a normal incident wind (0°), a balcony intensifies the interunit dispersion by increasing the reentry ratios. Overall, in case of an outbreak of an infectious disease, distinctive control measures should be implemented depending on the incident wind direction and the fact whether the building has envelope features.

Under a certain wind direction, the source location is a factor to determine the infectious scope and extent, and a distinctive dispersion route may be found when the pollutant is generated in a different unit on the same façade. In addition, the size (height and width) of a building may also influence the dispersion scope and extent.

However, the typical dispersion patterns around the five-story buildings revealed using RANS model in this study are still useful in developing control measures of infection.

6.3 LES simulations

6.3.1 Case setup and numerical details

The building geometry, incident wind directions and computational domain are the same with those in the previous Section 6.2. In this section, totally ten cases are investigated, as listed in Table 6.1. These cases are selected, as they represent the typical dispersion patterns around façades under specific wind directions (see Section 6.2.6).

Table 6.1 A summary of the cases investigated using LES model; note that two buildings, with and without balconies, are considered for each case.

Case	$\theta = 0^\circ$ & windward side	$\theta = 0^\circ$ & leeward side	$\theta = 45^\circ$ & windward side	$\theta = 45^\circ$ & leeward side	$\theta = 90^\circ$ & lateral side
Source unit	WM3	LM2	WEu3	LM2	Ed2

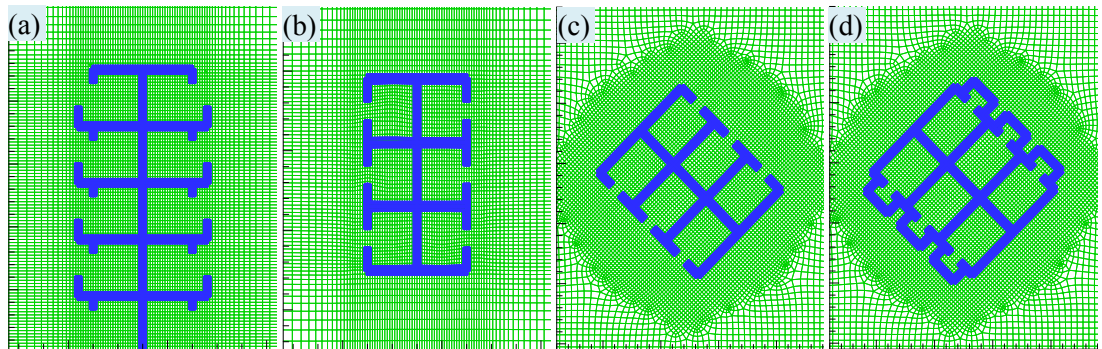


Figure 6.12 Mesh information: (a) $\theta = 0^\circ$ side view with balconies, (b) $\theta = 0^\circ$ plan view without balconies, (c) $\theta = 45^\circ$ plan view without balconies, and (d) $\theta = 45^\circ$ plan view with balconies.

The mesh generation method is the same with those in Section 6.2.1. Eventually,

the computational domain is constructed with around 6.0×10^6 hexahedral cells, with a minimum cell width of $1 \times 10^{-4} H$ and a maximum stretching ratio of 1.16 (1.18 in Section 6.2.1). Such a small minimum cell width in combination with a reference wind speed of 2 m/s results in an average y^+ value of around 2.0 for the domain ground and the building surfaces (around 1.0 at most walls). A schematic view of mesh information in and around the buildings is given in Figure 6.12. The sensitivity analysis of the mesh resolution is described in Section 6.3.2.

The inlet boundary conditions of the computational domain are defined using the profiles of U , k and ε , which are the same with those of Gorlé et al. (2009) listed in Table 4.1. As deduced in Section 6.2.1, the eventually used parameters and coefficients for $U_{ref} = 2$ m/s are: $u^* = 0.13$ m/s, $z_0 = 0.00075$ m, $M_1 = 0.025$, $M_2 = 0.41$, and $C_\mu = 0.001$. Based on the predefined k and ε profiles, the fluctuation in the mean velocity profile at the inlet plane is generated using the Vortex method (Mathey, 2006) with 190 vortices. The domain ground is simply set as walls. Other boundary conditions at the domain outlet, domain ceiling, domain lateral sides, and building surfaces are the same with those listed in Table 4.1. With regard to dispersion simulation, the tracer gas CO_2 is released in the center of a source unit and the evolution of concentrations in all units then examined to record its dispersion characteristics. The CO_2 is generated constantly at a rate of 8.0 mg/s.

The general solution methods are the same with those for LES simulations, as described in Chapters 4 and 5. The convergence of each time step is achieved when both the area averaged wind speed and CO_2 concentration at the opening of the source unit are stable for at least five iterations. Based on converged mean flow and concentration fields that are generated by a RANS model, the transient simulation of flow and concentration fields using LES model continues to conduct for a sufficient period of time (around 3 flow-through time t_{ft} , namely $1200 \Delta t^*$ in this study) to avoid the influence of initial conditions, where $t_{ft} = D_L / U_H$ with D_L the domain length, and Δt^* is the nondimensional time step size, defined as $\Delta t^* = \Delta t \times U_H / H$ with Δt the time step size. Here Δt^* is equal to 0.044. Note that at this stage the concentration field corresponds to a background tracer gas, which is O_2 in this study. Then tracer gas CO_2 is generated in the source unit, and the transient flow and

concentration fields are computed simultaneously. Both the ACHs of units and the average concentration at respiration planes for standing position (at the height of 1.6 m from a floor) are then continuously recorded.

In LES simulations, the concentration ratio, M_{i-j} , and the reentry ratio, R_k , are still used to evaluate the interunit dispersion, see Section 6.2.1.3. An instantaneous R_k can be calculated from the predicted instantaneous mean flow and concentration fields. ACH values are calculated using the integration method.

6.3.2 Sensitivity test

The LES validation and some general sensitivity test can be found in Sections 4.3 and 5.2. This section describes sensitivity analyses of some important computational parameters that may influence the reliability of the LES simulation of interunit dispersion.

6.3.2.1 Influence of spatial resolution

The mesh quality is assured in three aspects. First, the mesh is arranged based on our previous mesh sensitivity test (against experimental data) on a similar flow problem (see Sections 4.3.2 and 5.2.3). Second, the mesh resolution, especially in regions on and close to building surfaces, strictly follows the best practice guidelines, such as the COST (Franke, 2007) and AIJ (Tominaga, 2008b). Third, for each wind direction, two grids with different resolutions (y^+ around 2.0 and 4.0) are created, and then the Grid Convergence Index (GCI) (Roache, 1994) that is based on the Richardson extrapolation method (Richardson, 1910) is calculated to show the relative errors of the grids. The ACH values of the 30 units in the multistory buildings are used to represent numerical solutions. The values of the finer mesh based $GCI_{(ACH)}$ are all below 3.0%, indicating that the finer grid (with y^+ around 2.0) is generally grid converged.

6.3.2.2 Influence of temporal resolution

Besides 0.044, two other time step sizes (indicated by Δt^*), namely 0.022 and

0.22, are also tested. The power spectra in the frequency domain for ACH values generated using the three time step sizes are compared. Figure 6.13 presents the comparison for unit WM3 under normal wind direction. Generally, the two smaller time steps, 0.044 and 0.022, predict very close dominant frequencies with similar amplitudes, which deviate significantly from those given by 0.22. This comparison demonstrates that the time step 0.044 is small enough to cover the high frequencies that have pronounced influence on interunit dispersion (Franke, 2007), and thus further reduction down to 0.022 is unnecessary, while 0.22 is too large to realize the effect of those important high-frequency flows.

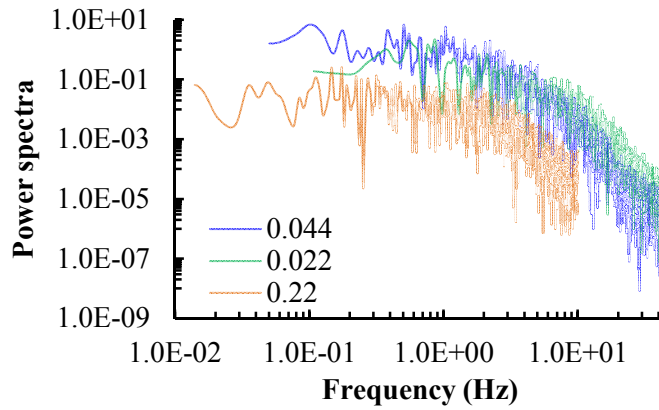


Figure 6.13 Power spectra in the frequency domain for the ACH value of unit WM3 under normal wind direction; the legend indicates the nondimensional time step sizes.

6.3.2.3 Influence of inflow conditions

The turbulent characteristics of inflow conditions are always an important issue of concern for LES modeling. Tabor and Baba-Ahmadi (2010) systematically reviewed the generating methods of the inflow condition for LES, suggesting that each method has its advantages and disadvantages. Studies in Section 5.2 indicate that there is no universal inflow generating method and the optimum method should be flow problem dependent. Section 4.3 compares the fluctuating characteristics of the nondimensional velocity components ($\hat{u} = u/U_{ref}$, $\hat{v} = v/U_{ref}$, $\hat{w} = w/U_{ref}$) that are produced by several inflow generating methods, demonstrating that a specific type of generating method represents a specific type of inflow condition. In this study,

the Vortex method (Fluent, 2010) is selected to consider a highly fluctuating inflow condition.

6.3.2.4 Influence of introducing the concentration equation on solution oscillation

It is found that a sudden introduction of the concentration equation initially causes abnormal solutions to the flow field, specifically short-period, largely overpredicted ACH values for all units. An example is provided in Figure 6.14. Such abnormal predictions of ACH values could lead to inaccurate predictions of the transient characteristics of interunit dispersion and in turn to inaccurate estimations of its time scales. Fortunately, it is found that this unexpected period can be avoided by pre-charging a background tracer gas that is different from CO₂ into the whole domain. The whole implementing procedure is described in detail in Section 6.3.1. This method should be useful to any transient studies involving a dispersion problem.

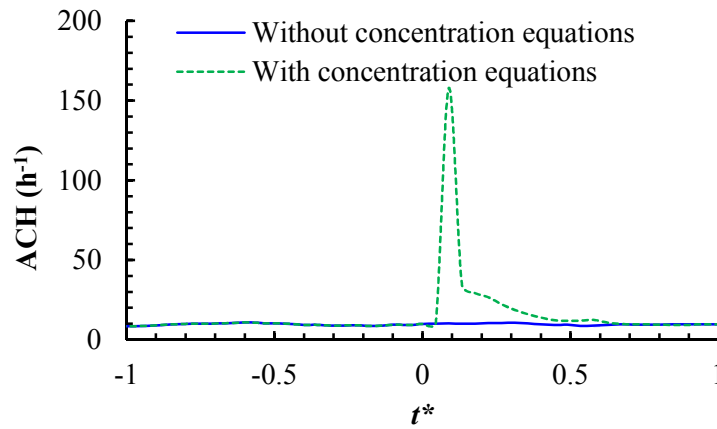


Figure 6.14 Effect of introducing the concentration equation to the prediction of ACH value for unit WM3; the concentration equation is introduced at $t^* = 0$.

6.3.3 General flow and dispersion characteristics

This section presents the general flow and dispersion characteristics around the multistory buildings, which are intended to provide background flow and dispersion information for the later analyses of interunit dispersion routes and time scales.

Table 6.2 compares the reattachment lengths on the roof and on downstream ground of bluff bodies under a normal wind condition. Comparison between the LES results with the two sets of experimental data generally justifies the present LES simulations of flow field around the multistory buildings. The deviations between the LES predictions and the experiments could be attributed to two reasons: (a) the configurations of the physical models are different and (b) there are real units and openings in the present building models, whereas the experimental models are solid blocks.

Table 6.2 Comparison of reattachment lengths on the roof and on downstream ground.

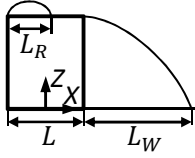
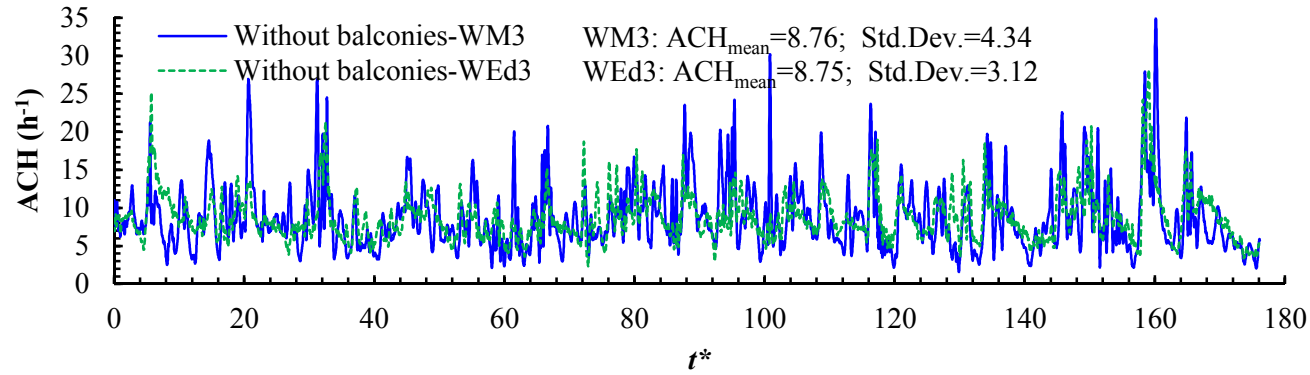
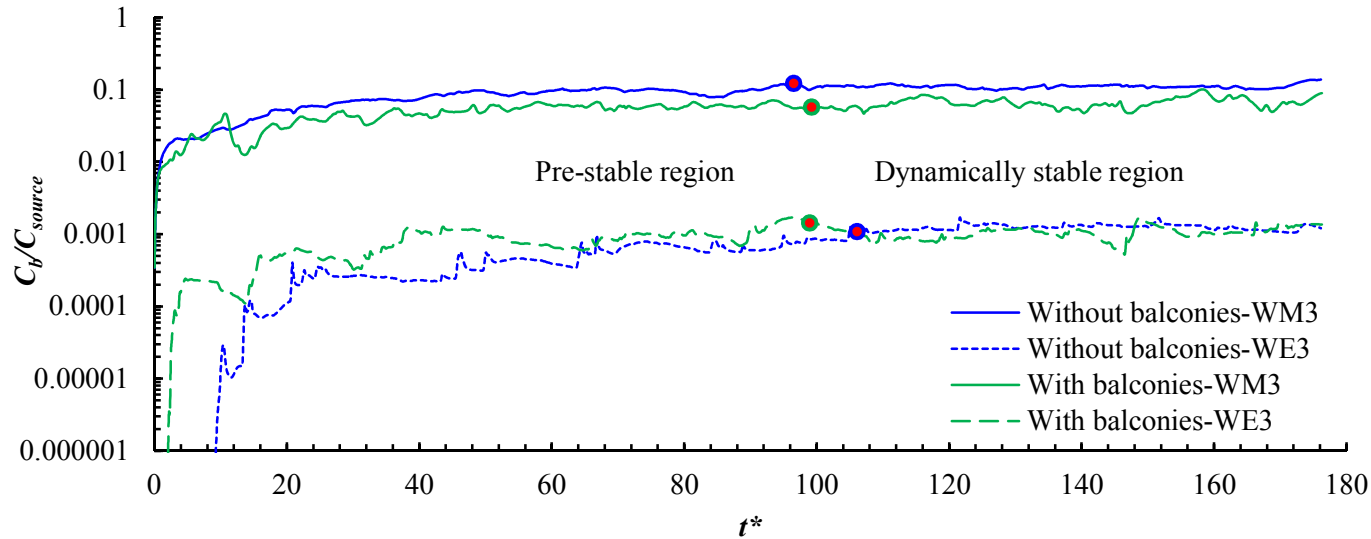
		Method	Physical model (X:Y:Z)	L_R/L	L_W/L
	Leitl and Schatzmann (1998)	Experiment	1:1.25:1.25	0.52	1.8
	Li and Meroney (1983)	Experiment	1:1:1	0.64	1.33
	Section 4.2	CFD-RANS	1:1.25:1.25	0.45	3.2
	This section	CFD-LES	1:1.2:2.25	0.51	1.95

Figure 6.15 provides examples of the time series of ACH values and tracer gas concentrations of certain units in the multistory buildings. It can be seen from Figure 6.15(a) that the ACH value of a unit is always highly fluctuating. Detailed analyses of the fluctuating behaviors of a single-sided ventilation rate as well as the transient flow patterns around a single opening, under various wind directions, can be found in Section 5.3. Owing to the highly fluctuating flow field, it is necessary to analyze the interunit dispersion transiently. As shown in Figure 6.15(b), the continuous release of tracer gas in a source unit (namely, WM3) results in a quick elevation of the concentration level in that unit, and the accumulated tracer gas then starts to transmit to adjacent units (e.g., WEd3) at a later moment. Such interunit dispersion would eventually achieve a dynamically stable state. The moments that separate the whole evolution period into the pre-stable period and the dynamically stable period are



(a) Evolution of ACH values over time



(b) Evolution of tracer gas concentrations over time and the moments (marked with dots) commencing the dynamically stable region

Figure 6.15 Time series of ACH values and tracer gas concentrations of some units in the multistory buildings under the normal incident wind.

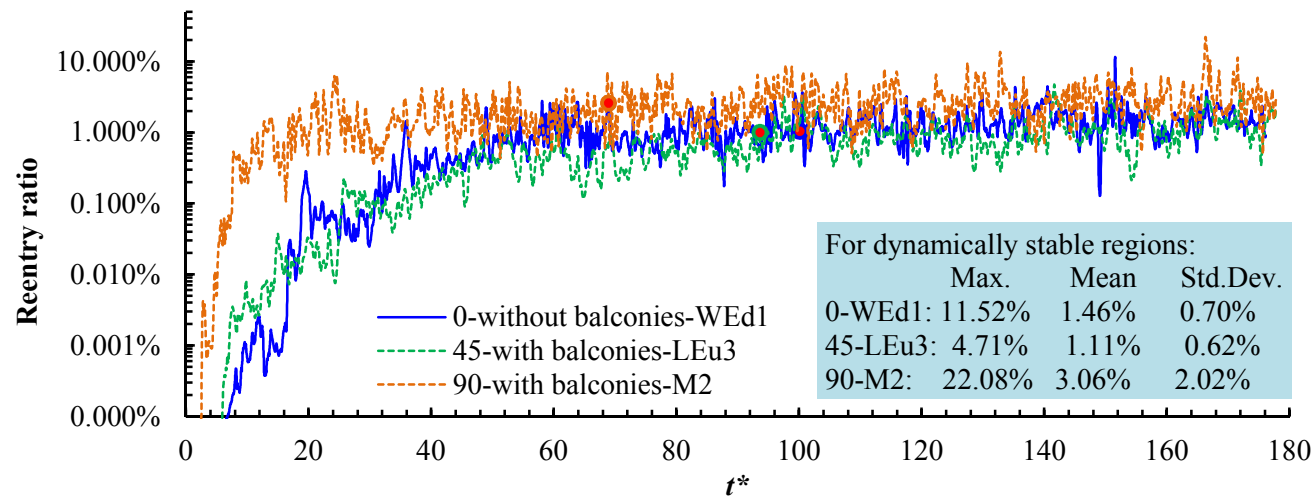


Figure 6.16 Evolution of reentry ratios over time and the maximum, mean, and standard deviation values within the dynamically stable periods; dots mark the moments commencing the dynamically stable periods.

carefully identified through sensitivity tests. When a moment is identified, the linear regression is made on a concentration curve within the dynamically stable period. A final moment is selected if further changing this moment does not result in obvious changes to both the coefficient and the R^2 value of the regressed linear equation. For all wind directions, these final concentration levels in other units are, on average, two to four orders of magnitude lower than those in the corresponding source units.

Figure 6.16 provides examples of the evolution of reentry ratios over time after releasing tracer gas, where the maximum, mean, and standard deviation values of reentry ratios within the dynamically stable periods are also calculated. Three observations can be made based on these time series of reentry ratios. First, the reentry ratio of a specific unit is always fluctuating, implying that using a mean reentry ratio to describe an interunit dispersion is inaccurate. Second, the fluctuating densities of reentry ratios within the dynamically stable periods differ between different units, as indicated by the standard deviation values. The reentry characteristics during the dynamically stable periods are analyzed in Section 6.3.4. Third, there may be a large difference in the moments when the reentry ratios reach the mean value in different units. Such time scales of interunit dispersion are analyzed in Section 6.3.5.

6.3.4 Dispersion routes and reentry ratios

This section analyzes the interunit dispersion characteristics during the dynamically stable periods. Figure 6.17 presents the mean and maximum reentry ratios of the tracer gas from source units to other units. The maximum values are provided, given that they are important to the infectious risk assessment.

Figure 6.17(a) presents the results on the windward side under a normal wind direction, when the tracer gas is released from unit WM3. These results may lead to three conclusions. First, without balconies, the tracer gas disperses in all directions around the source unit, namely upward, downward, and lateral directions. This finding is inconsistent with previous RANS results (see Section 6.2), which show only downward dispersion. Such a difference between the findings of the RANS and LES simulations could be attributed to the inability of the RANS models to interpret the transiently fluctuating flows that deviate from the mean flow. Second, a unit with

a very small mean reentry ratio could occasionally experience very large reentry ratios, such as unit WEd2 with $\overline{R_k}$ and $\widehat{R_k}$ equal to 0.9% and 16.5%, respectively. This is an important finding, demonstrating that the mean RANS results are insufficient to describe real infectious risk circumstances. Third, the presence of balconies significantly aggravates the transmission to the two lateral units on the same floor of the source unit. Their presence shrinks the infectious scope, evidently because of their blockage and channel effects.

Figure 6.17(b) presents the results on the leeward side under a normal wind direction, when the tracer gas is released from unit LM2. Similar to the windward side, the stochastic and fluctuating flows induce dispersion in all directions around the source unit. This, again, does not accord with previous RANS results, which suggest only upward dispersion. In particular, downward dispersion is found, which is produced by unsteady interaction between the large recirculation vortex behind the building and the small corner vortex at ground level (see Section 5.3). Unlike on the windward side, the presence of balconies broadens the infectious scope and elevates the reentry ratios. This should be attributed to the fact that the negative wake region helps the leeward balconies accumulate and preserve the tracer gas.

Figure 6.17(c) presents the results on the windward side under an oblique wind direction, when the tracer gas is released from unit WEu3. Without balconies, the tracer gas mainly disperses downstream, along which many units could be dangerous. This finding updates previous RANS simulations, which detected infections only in the two downstream units on the same floor as the source unit. Through the channel effect, the presence of balconies limits the dispersion to a smaller number of units, particularly to those on the same floor, which is very useful for the control of infection.

Figure 6.17(d) presents the results on the leeward side under an oblique wind direction, when the tracer gas is released from unit LM2. Although the dispersion is only limited to the units on the floor above the source unit in the building without balconies, it is dangerous for almost all units in the building with balconies, except for those on the floor below the source unit. As under normal wind direction, the presence of balconies has the disadvantage of diluting the tracer gas. Such a large difference in dispersion characteristics between buildings with and without balconies

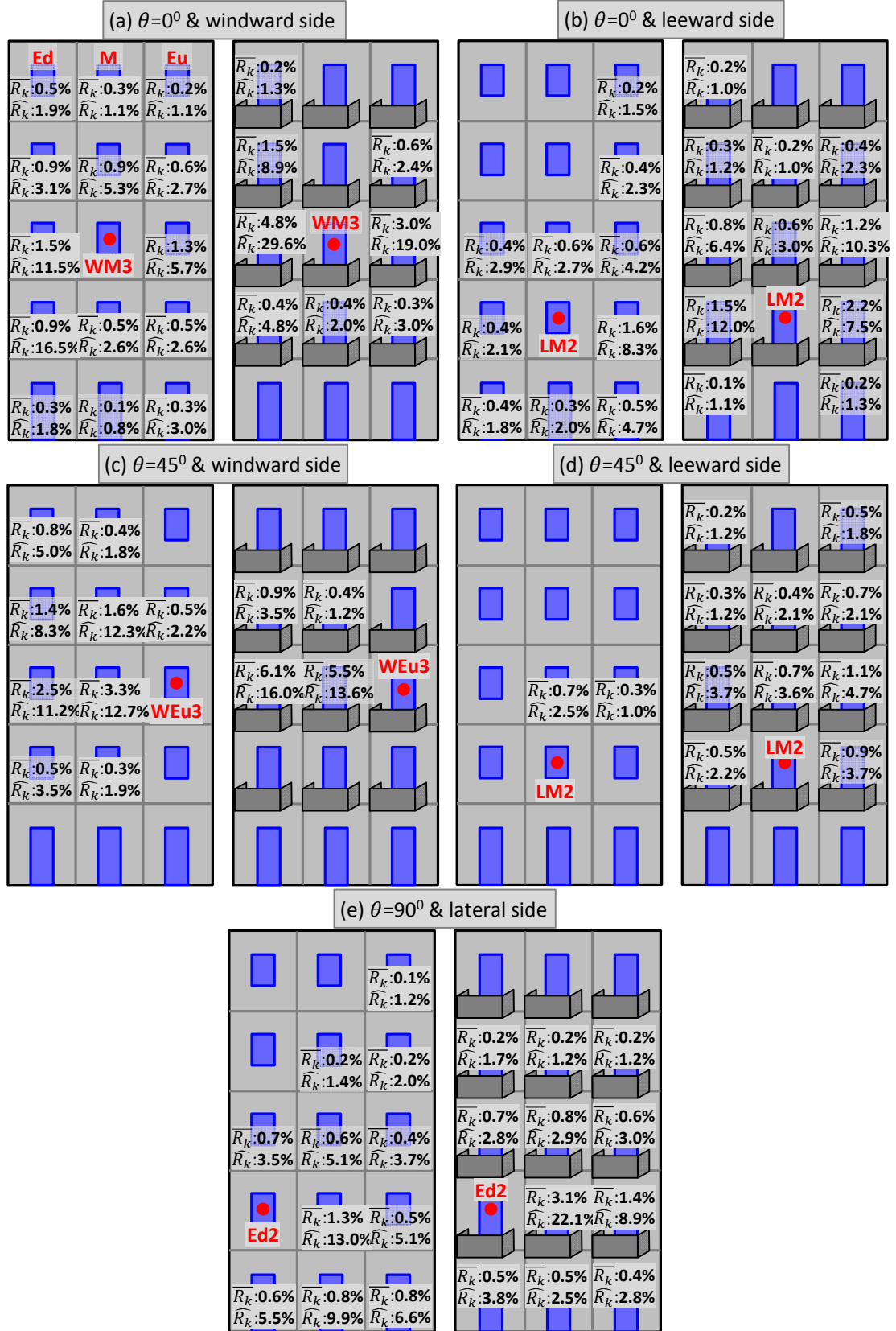


Figure 6.17 Mean and maximum reentry ratios of tracer gas from source units to other units during dynamically stable periods; \bar{R}_k represents mean reentry ratio and

\hat{R}_k maximum reentry ratio.

(also other similar envelope features) should be given special attention in developing control measures.

Figure 6.17(e) presents the results on a lateral side under a parallel wind direction, when the tracer gas is released from unit Ed2. The tracer gas released from the source unit disperses mainly in upward and upstream directions, though the downward dispersion is still significant. Units along these directions could suffer from reentry and thus be dangerous. The presence of balconies dramatically intensifies the dispersion in the downstream units, while it slightly mitigates the dispersion in other units. For both buildings, the infectious scopes predicted by LES simulations are much larger than those given by RANS simulations.

In addition to reentry ratios, the standard deviations of reentry ratios are also calculated to indicate their fluctuations (these figures are not presented). It is found that, for many units, the standard deviations are large enough to be comparable with the mean reentry ratios. These levels of fluctuation in reentry ratios should be considered when assessing infectious risk.

6.3.5 Time scales of interunit dispersion

This section analyzes the time scales of interunit dispersion during the pre-stable periods. As reentry ratio R_k is related to an ACH ratio, it could be very large even at the beginning of tracer gas release, see Figure 6.16. Therefore, although R_k is useful to evaluate the dispersion characteristics during the dynamically stable periods, it is not sensitive to reveal time characteristics. This section uses the concentration ratio M_{i-j} between an infected unit and the source unit to examine the time scales of interunit dispersion.

Figure 6.18 presents the nondimensional times required to reach both the mean and the half mean M_{i-j} values of the relevant units. The figure shows two aspects worthy of discussion. The first is the influencing factors of the distribution and magnitude of the time scales. For a specific unit, the time scales do not show an obvious relation with its distance to the source unit and the approaching wind direction. However, the time scales on the buildings without balconies scatter at a larger range than those with balconies. The relatively uniform distribution of time

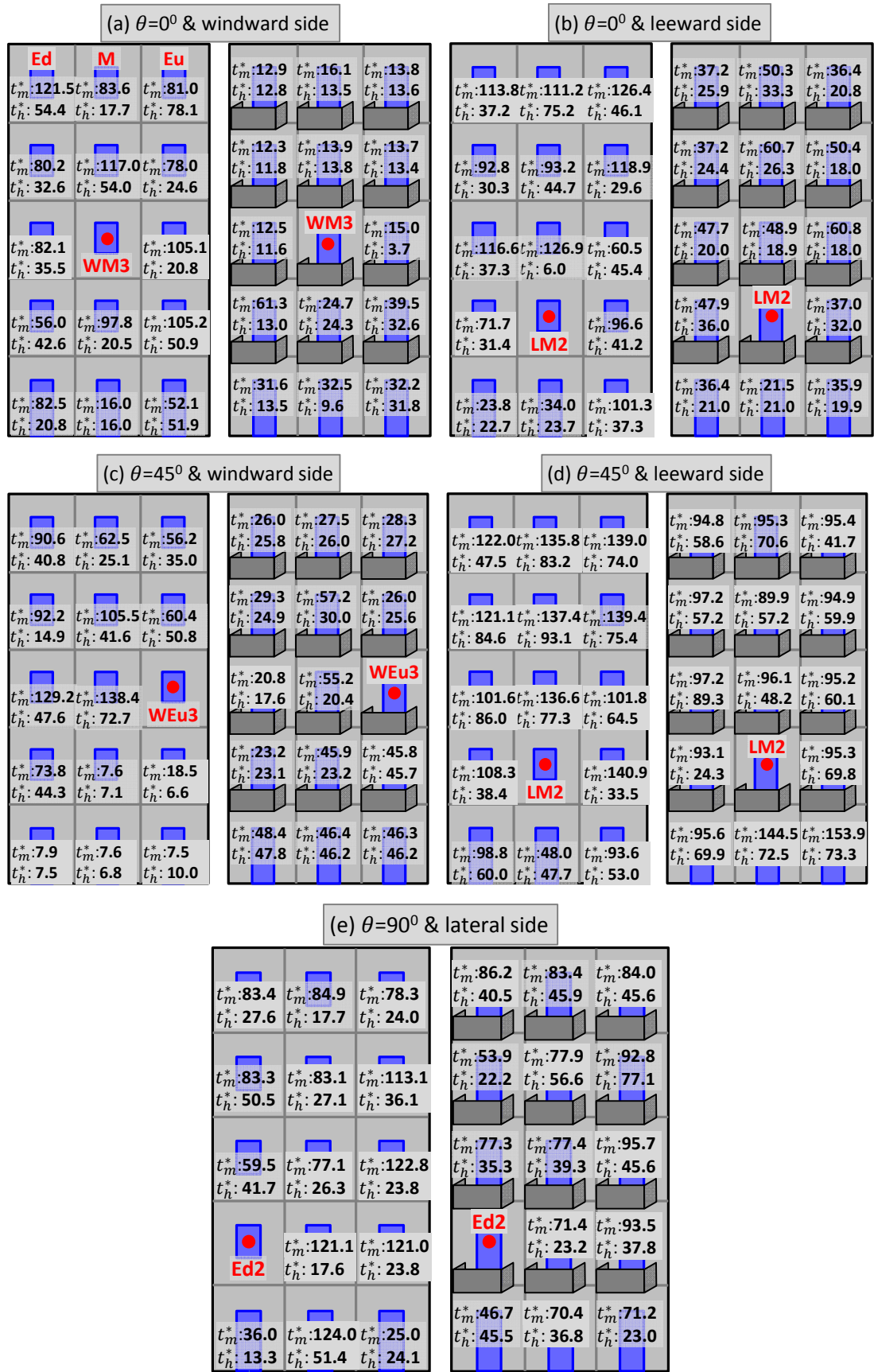


Figure 6.18 Time scales of interunit dispersion from a source unit to its adjacent

units; t_m^* and t_h^* represents the nondimensional times for reaching the mean and the half mean M_{i-j} values, respectively, where the mean M_{i-j} values are obtained by taking averages within the dynamically stable periods.

scales on the buildings with balconies should be ascribed to the fact that the balconies disturb the near-wall flow, resulting in a more dynamically stable envelope concentration field. Generally, under the normal and oblique wind directions, the time scales on windward sides are shorter than those on leeward sides, as larger pressure fields near the windward sides intensify quick dispersion of the tracer gas. The second aspect is the magnitudes of these time scales. The magnitudes of t_h^* values are mostly comparable with those of natural ventilation. Based on the present physical model, the nondimensional times required to achieve one whole-unit air replacement for the typical naturally ventilated ACH values of 5, 10, and 20 are 53.3, 26.7, and 13.3, respectively. Such comparable magnitudes are to be expected as interunit dispersion occurs based on the natural ventilation system and the interunit dispersion is governed by the indoor and outdoor airflow exchange mechanisms.

Table 6.3 A summary of the ranges of the times required to reach specific M_{i-j} values, where t_γ^* means the time required to reach the M_{i-j} value of γ ; NB means no balconies and B balconies; NA means no unit reaching this level of M_{i-j} ; and those with only one number mean only one unit reaching this level of M_{i-j} .

	$\theta = 0^\circ$ & windward side		$\theta = 0^\circ$ & leeward side		$\theta = 45^\circ$ & windward side		$\theta = 45^\circ$ & leeward side		$\theta = 90^\circ$ & lateral side	
	NB	B	NB	B	NB	B	NB	B	NB	B
$t_{0.001}^*$	[4.4, 18.1]	[2.1, 31.8]	[3.2, 18.3]	[5.4, 19.6]	[6.4, 46.5]	[2.8, 48.2]	[13.2, 57.9]	[2.3, 69.6]	[9.7, 18.2]	[4.9, 17.4]
$t_{0.01}^*$	[13.5, 78.8]	[2.4, 32.6]	[4.8, 75.0]	[8.8, 35.7]	[7.2, 58.2]	[5.9, 59.6]	[26.6, 94.9]	[24.1, 84.4]	[9.9, 108.6]	[6.5, 103.5]
$t_{0.1}^*$	[82.5, 84.4]	[3.8, 12.6]	60.3	[32.1, 61.2]	[99.3, 174.4]	[14.4, 129.8]	NA	97.3	24.8	[16.7, 113.5]

Table 6.3 provides a summary of the time scales required to reach specific M_{i-j} values. From the viewpoint of the control of infection, there is a negligible difference in the time scales between different cases. Among these time scales, the ranges of $t_{0.0001}^*$ are particularly interesting, representing the times required to achieve M_{i-j} values of 1:10,000. Considering that a respiratory process, such as coughing and sneezing, can produce millions of aerosols (Duguid, 1946), $t_{0.0001}^*$ may represent the times required by the first stream of pathogen-laden aerosols to reach an infected unit. Previous particle simulations by Gao et al. (2009) suggested a comparable time scale to the first arrivals with the $t_{0.0001}^*$ values listed in Table 6.3. Generally, a shorter time is required to reach a specific M_{i-j} in a unit that is closer to the source unit (these figures are not presented).

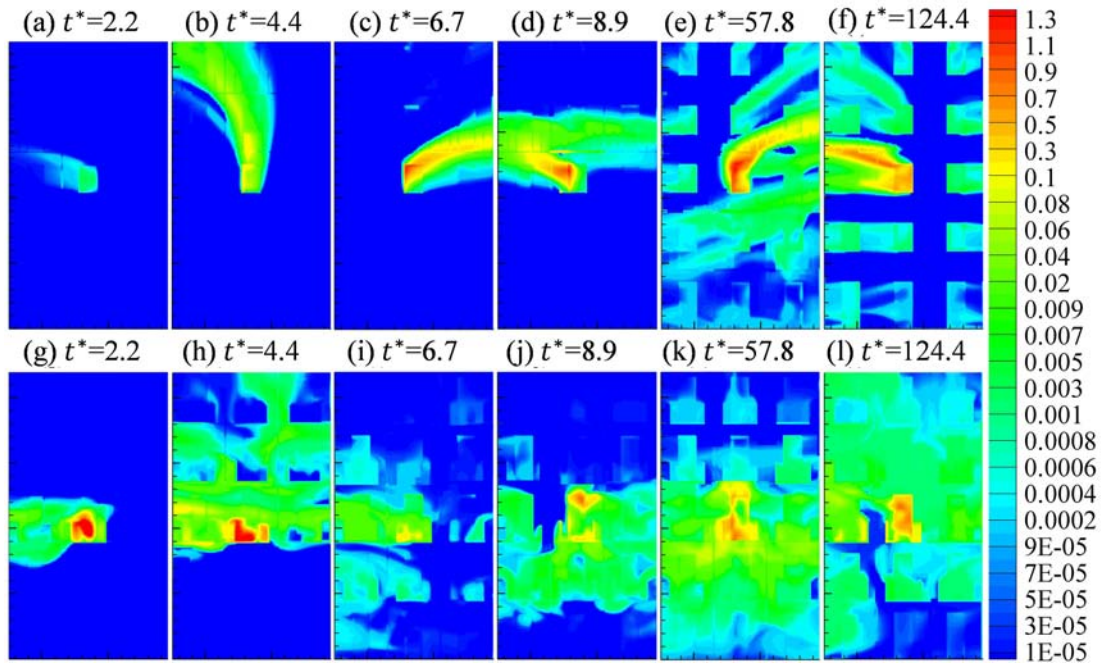


Figure 6.19 Concentration ratio distributions on the windward facades of buildings under normal wind direction at various moments; (a)-(f) present the building without balconies and (g)-(l) present the building with balconies.

In order to further examine the time characteristics of interunit dispersion, the concentration distributions on building facades at various moments are analyzed.

Figure 6.19 presents M_{i-j} distributions on the windward facades of the buildings under normal wind direction at six different moments. Based on Figure 6.19, three observations can be made. First, dispersion route is not constant; the main dispersion direction varies with time. This variation is stochastic, implying that the incursion of pollutants into a specific unit is intermittent. Such characteristics significantly broaden the dispersion scope and thus increase the difficulty of control. Second, there could be secondary interunit dispersions around multistory buildings, as shown clearly in Figure 6.19 (e) and (f). Secondary dispersion could be an important mechanism of interunit dispersion. It indicates that a portion of pollutants entering a specific unit could come from an infected unit, rather than directly from the source unit. This feature also contributes to extending dispersion scope and increases dispersion uncertainty. Third, the presence of balconies helps increase the uniformity of pollutant distribution on the buildings' facades, as their presence hinders the development of main dispersion directions. These envelope dispersion characteristics under normal wind direction represent the general dispersion circumstances of other cases not presented here.

6.3.6 Further discussion

The results and analyses presented in the previous sections provide an overview of the characteristics of transient interunit dispersion around multistory buildings. This section presents further discussion of the infectious risk of this dispersion more broadly within the field of epidemiology and building ventilation.

According to the well-known Wells-Riley model (Riley et al., 1978), the number of infectious quanta produced by infector(s) and the duration of exposure time are two key factors influencing the infectious risk of a susceptible person. Within a specific unit, the number of infectious quanta may be estimated by the reentry quantity of infected air originating from the source unit, based on the concentration of pathogens. Such reentry quantities in various circumstances are provided in this study. However, this study cannot provide a universal safe threshold for the reentry ratio to estimate the infectious risk for a specific unit, as the size of a quantum is strongly related to the type of pathogen and the physical condition of susceptible persons. Previous studies by Franz et al. (1997) showed that many pathogens can

cause disease with several to dozens of organisms, such as viral hemorrhagic fevers (1-10), Q fever (1-10), tularemia (10-50), brucellosis (10-100), and smallpox (10-100). For highly infectious bacteria like *M. tuberculosis*, even a single organism is sufficient to cause disease, while a cough may produce around 3,000 organisms (Fitzgerald and Haas, 2005; Duguid, 1946). When exposed to a certain concentration level of a pathogen, the exposure time should be controlled. Isolating the infectors as early as possible to reduce exposure time and ventilating the suspected regions sufficiently are effective methods (Tang et al., 2006) to control infection.

Another aspect that is important to the estimation of airborne infectious risk is the ratio of two time scales: the time scale required to accumulate a quantum and the time scale of the pathogen's survival. To the best of the author's knowledge, the two time scales have not been compared previously. The prerequisite of the occurrence of an airborne infection is that at least a quantum of organisms produced by an infector must remain both airborne and survive to be inhaled by a susceptible person (Tang et al., 2006). If the pathogen's survival time is shorter than the time scale needed to accumulate a quantum of this pathogen in a target unit, the occupants in this unit are safe and thus no protective measures are required. Unfortunately, previous data have shown that many pathogens can survive in aerosols for a very long time, such as human coronavirus 229E, which survives for several to dozens of hours (Ijaz et al., 1985); influenza viruses, which survives for up to 24 hours (Loosli et al., 1943); and SARS coronavirus, which survives for more than seven days (Lai et al., 2005). These survival times are much longer than the time scales of interunit dispersion. However, the survival time of a pathogen is affected by many factors (Tang et al., 2006; Morawska, 2006). In certain circumstances, the survival time of a SARS virus is only several minutes (WHO, 2003), a period comparable with most interunit dispersion time scales. Therefore, for a specific pathogen under a certain physical environment, it is meaningful and necessary to make a comparison of its survival time and the time scales of interunit dispersion in order to take more accurate and effective intervention measures.

6.3.7 Summary

Wind-induced interunit dispersion around multistory buildings is investigated

using the LES model. The reliability of the LES model is assured with experimental validation and sensitivity tests. This study proposes a method that avoids the occurrence of solution oscillation after the introduction of the concentration equation.

Continuous release of tracer gas in a source unit results in a quick elevation of concentration level in this unit, and the accumulated tracer gas starts to transmit to adjacent units at a later moment. Such an interunit dispersion would eventually achieve a dynamically stable state, with reentry ratios always fluctuating around their mean values. The main dispersion routes always vary with time, implying that the incursion of pollutants into a specific unit is intermittent. In addition, secondary dispersions are observed. These two dispersion route features contribute to extended dispersion scope and increased dispersion uncertainty.

In order to facilitate analyses, the transient interunit dispersion processes are divided into two periods, namely pre-stable and dynamically stable periods. For the pre-stable periods, the nondimensional times required to reach the mean and half mean M_{i-j} values are analyzed. These time scales of a unit are influenced negligibly by distance from the source unit and the approaching wind direction, which, generally, are larger on the windward sides than the leeward sides. The magnitudes of the time scales of reaching the half mean M_{i-j} values are mostly comparable with those of natural ventilation.

For dynamically stable periods, the mean and maximum reentry ratios as well as their standard deviations are analyzed. LES simulations reveal much broader infectious scopes than previous RANS simulations. A unit with a very small mean reentry ratio could occasionally experience very large reentry ratios. For many units, the standard deviations of reentry ratios are large enough to be comparable with the mean reentry ratios. These findings demonstrate that the previous RANS results are insufficient to describe the actual infectious risk circumstances. In addition, the presence of balconies helps shrink and broaden the infectious scope on the windward and leeward sides, respectively, which also helps create more stable and uniform envelope concentration fields.

The general reentry ratios and dispersion time scales provided by this study are useful for infectious risk assessment and the development of control measures, based on the infectious and survival characteristics of a certain type of pathogen.

Chapter 7

Conclusions and recommendations for future work

7.1 Summary of main contributions

This thesis has investigated the single-sided natural ventilation and interunit dispersion around multistory buildings using CFD methods. The main contributions are summarized as follows:

(a) On-site measurements of ventilation rates have been conducted, which prove that previous empirical models established on the basis of very simple building models are unreliable to use in complex multistory buildings. CFD simulation provides an explanation of this unreliability, namely those empirical models cannot account for the effect of room location.

(b) For RANS simulation of atmospheric flow and dispersion, a homogeneous ABL based on the roughness modified two-layer near-wall model is developed. The effect of inhomogeneous ABL and near-wall treatment is then quantitatively examined.

(c) For LES simulation of atmospheric flow and dispersion, the effect of several important parameters is examined and the appropriate selections are recommended. Particularly, it is found that different inflow algorithms generate very distinctive fluctuating intensities to the velocity components. A flow field is generally less sensitive to some of the parameters than a concentration field.

(d) Theoretical analysis and numerical case study confirm the hypothesis that reduced-scale models for CFD simulations of wind flow and related processes save numerical resources. Reduced-scale models require fewer cells than a full-scale model to achieve a target near-wall mesh density (in terms of y^+ value).

(e) Several influencing factors on CFD prediction of single-sided ventilation rate are examined and appropriate selections are recommended. Particularly, a simple method that is used to increase the near-wall mesh density is proposed. The main ventilation mechanisms of single-sided natural ventilation under five wind directions are identified.

(f) RANS simulation reveals the mean interunit dispersion routes around multistory buildings and quantifies the corresponding reentry ratios. The RANS results confirm that the interunit dispersion is an important pollutant transmission route.

(g) LES simulation extends the RANS results, which reveals a broader dispersion scope, with fluctuating and intermittent dispersion characteristics. The time scales of interunit dispersion are generally comparable with those of natural ventilation, which are less than the survival times of most pathogens. This suggests that the interunit dispersion is very dangerous.

7.2 Predictive methods evaluation

Different methods of determining single-sided ventilation rates in multistory buildings have been evaluated. In general, this study demonstrates that compared to the empirical models and the experimental methods, the CFD simulation is more suitable for the determination of ventilation rate in multistory buildings, especially in the design stage. In addition, CFD is a useful tool for understanding the envelope airflow characteristics and ventilation mechanisms of a multistory building.

The on-site measurements of the ventilation performance in four multistory residential buildings in Hong Kong were conducted. The measurements are strongly relied on the model availability and are restricted by the uncontrollable boundary conditions. The measurements of ventilation rates using the tracer gas decay method cannot be conducted in many adjacent rooms simultaneously, as the reentry of tracer gas between rooms would influence the measured results.

Using the measured ventilation rates, the previous empirical models are validated. None of them are reliable to the prediction of the ventilation rate of rooms in multistory buildings, the main reason for this being that these correlations do not contain a parameter to account for the effect of room location in a multistory building. Both the envelope flow pattern and the ventilation rate of a room in a multistory building are highly dependent on the room's three-dimensional location in the building.

The RNG and MMK $k-\varepsilon$ models combined with the two-layer near-wall model are preliminarily validated using past experimental data. Good agreements

between the predicted and the measured results are generally achieved, which suggests that the CFD method is a useful tool for studying single-sided natural ventilation. Any methods reproduced by CFD simulation are compromised by the accuracy of the velocity and turbulence fields produced by the selected numerical model. Thus, work on improving the prediction of the flow field is essential to ensure the reliability of CFD predictions of ventilation rate.

Using CFD method, the envelope flow patterns and the ventilation characteristics of a solid block, a single-story building and a multistory building are compared. The envelope flow pattern at the opening of a building is obviously different from that at the same location of a solid block, which indicates that the method of predicting ventilation rates using the pressure coefficients on the surfaces of a solid block is not reliable. A room in a single-story building enjoys the whole flow field, whereas many rooms in a multistory building share the whole flow field. This difference in envelope flow characteristics explains basically the unreliability of previous empirical models in multistory buildings.

7.3 CFD simulation of ABL

7.3.1 RANS simulations

Based on wind tunnel experimental data, the effect of the inhomogeneous ABL and the near-wall treatment on the prediction of flow and dispersion around an isolated building immersed in a neutral ABL is investigated. A homogeneous ABL based on the $k-\varepsilon$ turbulence model and the roughness modified two-layer near-wall model is developed.

Generally, the effect of the inhomogeneous ABL on the prediction of flow and dispersion fields is significant. Establishing an accurate turbulence field is very important for the correct prediction of both flow and concentration fields. A lower incident k profile results in a longer reattachment length on the roof and a larger recirculation region in the wake, but obviously produces a lower k field around the building. This reduces concentration mixing in the lateral directions, which results in the concentrated distribution of pollutant in the streamwise direction. Around the height of the building, the velocity and concentration predicted by using the lower incident k profile are lowered and heightened, respectively. The magnitude of these

changes depends on the percentage reduction in the incident k profile from the inlet condition. A larger incident U profile enlarges the reattachment lengths and raises the k field, which produces similar effects on the velocity and concentration fields as the lower k .

Attention should also be paid to the effect of the near-wall treatment on the prediction of flow and dispersion. The use of the two-layer model to solve the near-wall viscous sublayer clearly improves the prediction of both flow and dispersion, since it incorporates the low-Reynolds-number effect of the near-wall region into the calculation of the entire turbulent flow field. However, the time used for mesh and iteration of the two-layer model is around five times that of the wall functions for the current model.

7.3.2 LES simulations

Based on wind tunnel experimental data, seven factors that influence flow and dispersion around an isolated building in a LES model are investigated, namely upstream distance, mesh resolution, sampling period, inflow condition, SGS model, SGS Schmidt number, and Smagorinsky constant. Up to present, the analyses of these influencing factors have not (or not comprehensively) been reported in previous studies.

- The upstream distances of 3H, 4H, and 5H do not show obvious differences in terms of the accuracy of mean velocity and concentration fields.
- Varying y^+ within the range of 0-30 does not obviously change the velocity field, but it greatly changes the concentration field. This suggests that the concentration field is more sensitive to mesh resolution. A finer mesh does not necessarily guarantee a better result. A mesh system with an average y^+ around 1-2 is recommended.
- A computing period of $400 \Delta t^*$ is sufficiently long to produce a stable velocity field, but $1200 \Delta t^*$ is required to achieve a stable concentration field. This again suggests that different variables may have completely different sensitivities to the same influencing factor.
- The fluctuating intensity of the velocity components provided by the Spectral

synthesizer is less than a half of that provided by the Vortex method. The selection of the inflow algorithm should be based on the actual flow characteristics.

- The effect of the SGS Schmidt number (Sc_{SGS}) on mass flux is almost negligible. The value of 0.4 is appropriate.
- The effect of an SGS model on velocity and concentration fields is not obvious. The standard Smagorinsky-Lilly model is appropriate.
- The Smagorinsky constant (C_s) of 0.1 is suggested for the standard Smagorinsky-Lilly model. A large value of C_s (0.15 or larger) overpredicts concentration values at the ground level, as it causes excessive damping of large-scale fluctuations.

7.3.3 Reduced-scale model

Theoretical analysis and numerical case study confirm the hypothesis that reduced-scale models for CFD simulations of wind flow and related processes save numerical resources. Reduced-scale models require fewer cells than a full-scale model to achieve a target near-wall mesh density (in terms of y^+).

Theoretically, the smaller a model, the more numerical resources can be saved. However, reduced-scale models must not violate similarity criteria. Reduced-scale models' potential to save numerical resources is generally very large, depending mainly on the scaling factor, the target y^+ value, and the flow problem.

7.4 CFD simulation of single-sided ventilation

7.4.1 Influencing factors

Based on full-scale measurements, the problem of accurately predicting single-sided natural ventilation using CFD methods is dealt with. This study confirms that the computational domain size, discretization scheme, and convergence criteria recommended by the best practice guidelines for the CFD simulation of urban aerodynamics are still applicable to CFD simulation of single-sided natural ventilation.

The sensitivity analyses show that a mesh with a stretching ratio of 1.18 is sufficiently fine to be insensitive to mesh number. With such a ratio, the sensitivity of the near-wall mesh density in particular is tested, and a method of increasing it by doubling only the first near-wall cells proposed. Requiring fewer numerical resources, this method produces almost the same ACH value as that predicted using conventional methods. When y^+ is less than 30, the ACH values predicted using the RNG model are insensitive to the near-wall mesh density. The LES model is much more sensitive, but again a denser near-wall mesh is not necessarily better.

Four methods of predicting the single-sided ventilation rate are examined under various wind directions. The RNG $k-\varepsilon$ model plus the integration method ($ACH_{RNG-mean}$) does not necessarily underestimate the ACH value for all wind directions. Such underestimations are more likely to occur when the approaching wind direction is close to the opening normal (0° - 45°). The RNG model used with the tracer gas decay method ($ACH_{RNG-tracer}$) is more reliable than the previous combination, although it overestimates the ACH value for the windward openings and underestimates it for the lateral and leeward openings. The LES model plus the integration method ($ACH_{LES-ins,T}$) overestimates the ACH value in all wind directions, owing to the short-circuiting effect of airflow. On average, around 33% of the airflow short-circuits at the room opening. The LES model plus the tracer gas decay method ($ACH_{LES-tracer}$) is the best approach, although it requires at least 20 times more computational time than the RNG and tracer gas ($ACH_{RNG-tracer}$) approach. In particular, it is shown that single-sided ventilation performs better in cases with a lateral (90°) and a leeward opening (180°) than with a windward opening (0°).

7.4.2 Fluctuating ventilation characteristics

Using the best approach, namely the LES model plus the tracer gas decay method, the fluctuating ventilation characteristics of single-sided natural ventilation under five different wind directions are investigated.

For windward ventilation, the velocity and pressure fields around the opening are relatively stable, hindering turbulence diffusion across the opening. The airflow

exchange through the windward opening is mainly driven by the large momentum of the impinging mean flow. The turbulent flow contributes only an average of 14.8% to the total ventilation rate.

For lateral ventilation, the velocity and pressure fields around the opening are very unsteady and highly time-dependent. The fluctuating reverse and reattachment flows dominate the lateral flow field and, in turn, the airflow exchange through the opening, leading to a highly fluctuating ventilation rate. The turbulent flow contributes an average of 63.4% to the total ventilation rate.

For leeward ventilation, the fluctuating intensity of the velocity, pressure fields, and the ventilation rate fall in between those of the windward and lateral ventilations. The airflow exchange through the opening is mainly driven by the low-pressure, fluctuating, recirculation vortex behind the building. Turbulent flow still plays an important role in airflow exchange, which contributes an average of 37.3% to the total ventilation rate.

The locations of inlets and outlets on an opening can change frequently with time, and they are not necessarily located at the upper and lower parts. This implies that it is not reliable to use a predictive method of single-sided ventilation rates that assumes that the inlet and outlet are regularly located on the upper and lower parts of an opening.

7.5 Interunit dispersion

7.5.1 RANS simulations

A validated RANS model is used to investigate the interunit dispersion around multistory buildings. Mean dispersion patterns and the corresponding reentry ratios are obtained.

- Under a normal incident wind ($\theta = 0^\circ$), the pollutant disperses mainly downwards on the windward side and upwards on the leeward side, respectively. The presence of balconies shifts the most affected units obliquely on the windward side, without obviously increasing the reentry ratios. On the leeward side, their presence significantly decreases the reentry ratios from a source unit to its upper units, as the vertical parapet of a balcony induces and assists the dilution of pollutant into

the downstream low-pressure recirculation vortex.

- Under an oblique incident wind ($\theta = 45^\circ$), the pollutant disperses mainly towards its downstream units on the windward side and upstream units on the leeward side, respectively. The presence of balconies strongly intensifies the reentry. On the windward side, the balconies function as dispersion channels and restrict the dilution of pollutant along vertical directions. On the leeward side, the intensification of such channel effects is still existed, although their presence prevents the vertical reentry when the pollutant is generated from the downstream units (Ed-).
- Under a parallel incident wind ($\theta = 90^\circ$), the pollutant disperses mainly towards its upper and upstream units. The presence of balconies greatly intensifies the dispersion and decreases the pollutant dilution. The reason is similar with that under oblique incident wind.

In general, many reentry ratios appear to be within the range from 5.0% to 10.0%, which suggests that the interunit dispersion is an important pollutant transmission route. On average, the strongest interunit dispersion occurs on the windward wall of the buildings under oblique wind direction (45° & windward side), due to the high ACH values and the unidirectional spread routes. It should be highlighted that the role of protrusive envelope features in interunit dispersion cannot be ignored. The presence of balconies significantly modifies the near-wall flow pattern and the dispersion characteristics. Except under a normal incident wind (0°), a balcony intensifies the interunit dispersion by increasing the reentry ratios. Overall, in case of an outbreak of an infectious disease, distinctive control measures should be implemented depending on the incident wind direction and the fact whether the building has envelope features.

7.5.2 LES simulations

Interunit dispersion around multistory buildings is further investigated using a validated LES model. Transient dispersion characteristics including time scales are obtained.

Continuous release of tracer gas in a source unit results in a quick elevation of concentration level in this unit, and the accumulated tracer gas starts to transmit to its

adjacent units from a later moment. Such an interunit dispersion would eventually achieve a dynamically stable state, with reentry ratios always fluctuating around their mean values. The main dispersion routes always vary with time, implying that the incursion of pollutants into a specific unit is intermittent. In addition, secondary dispersions are observed. These two features regarding dispersion route contribute to extended dispersion scope and increased dispersion uncertainty.

For the pre-stable periods, the nondimensional times required to reach the mean and half mean M_{i-j} values are analyzed. These time scales of a unit are influenced negligibly by its distance from the source unit and the approaching wind direction, which, generally, are larger at windward sides than at leeward sides. The magnitudes of the time scales of reaching the half mean M_{i-j} values are mostly comparable with those of natural ventilation.

For the dynamically stable periods, the mean and maximum reentry ratios as well as their standard deviations are analyzed. LES simulations reveal much broader infectious scopes than previous RANS simulations. A unit holds a very small mean reentry ratio could experience very large reentry ratios occasionally. For many units, the standard deviations of reentry ratios are large enough to be comparable with the mean reentry ratios. These findings demonstrate that the transient characteristics of the interunit dispersion are important and should be considered when formulating intervene measures, even if the RANS results are used.

7.6 Recommendations for future work

Despite of the above useful findings obtained from this thesis, there are still several aspects that are either limit or incomplete in this thesis, which are recommended for the future work.

(a) For LES simulation of atmospheric flow and dispersion, currently there are no existing formulas to take into account the roughness height on the domain ground. Without such formulas, a homogeneous ABL cannot be achieved, and thus the negative effect of an inhomogeneous ABL on numerical solutions cannot be eliminated. Therefore, such formulas for LES simulation should be developed.

(b) The examination of influencing factors for LES simulation of atmospheric

flow and dispersion are limited to an isolated building configuration with normally incident wind. Future research should examine the influence of building configuration and wind direction. In addition, the exhaust opening of the experimental model is located on the leeward façade and thus only wake dispersion is studied. Dispersion from upstream and roof regions should also be examined.

(c) For CFD simulation of single-sided natural ventilation, owing to the limited availability of experimental data, the sensitivity analyses of the computational parameters are conducted only for a windward opening with a specific wind direction (60°). In addition, the physical model used in this study is a single-zone model, which will have different ventilation characteristics with a zone in a multi-zone model. These issues should be explored in future studies.

(d) The observation of the interunit dispersion characteristics is limited by the scope of the building model. Although the basic dispersion routes, such as upward, downward and lateral dispersion, have been observed from the present five-story building model, a model with more stories and more units per floor should be developed in future studies for a more complete observation.

References

- Ai, Z.T., Mak, C.M., Niu, J.L., Li, Z.R., 2011a. Effect of balconies on thermal comfort in wind-induced, naturally ventilated low-rise buildings. *Building Services Engineering Research and Technology* 32(3), 277-292.
- Ai, Z.T., Mak, C.M., Niu, J.L., Li, Z.R., 2011b. The assessment of the performance of balconies using computational fluid dynamics. *Building Services Engineering Research and Technology* 32(3), 229-243.
- Ai, Z.T., Mak, C.M., Niu, J.L., Li, Z.R., Zhou, Q., 2011c. The effect of balconies on ventilation performance of low-rise buildings. *Indoor and Built Environment* 20(6), 649-660.
- Allard, F., 1998. *Natural ventilation in buildings: a design handbook*, James & James Ltd., London.
- Allocca, C., Chen, Q., Glicksman, L.R., 2003. Design analysis of single-sided natural ventilation. *Energy and Buildings* 35(8), 785-795.
- Antonia, R.A., Krogstad, P.-Å., 2001. Turbulence structure in boundary layers over different types of surface roughness. *Fluid Dynamics Research* 28, 139-157.
- ASHRAE, American Society of Heating, Refrigerating and Air-conditioning Engineers: *ASHRAE Handbook, Fundamentals* (SI): Atlanta, GA, 2009, section 10.4.
- ASHRAE, American Society of Heating, Refrigerating and Air-conditioning Engineers. *ASHRAE Handbook, HVAC Applications* (SI), Atlanta, GA, 2011, section 45.3.
- ASHRAE Standard 62-2010, *Ventilation for acceptable indoor air quality*, Atlanta, GA, 2010.
- Bangalee, M.Z.I., Lin, S.Y., Miao, J.J., 2012. Wind driven natural ventilation through multiple windows of a building: A computational approach. *Energy and Buildings* 45, 317-325.
- Barhaghi, D.G., Davidson, L., 2007. Natural convection boundary layer in a 5:1 cavity. *Physics of Fluids* 19(125106), 1-15.
- Barker, J., Stevens, D., Bloomfield, S.F., 2001. Spread and prevention of some common viral infections in community facilities and domestic homes. *Journal of Applied Microbiology* 91, 7-21.
- Ben-Cheikh, N., Hammami, F., Campo Antonio, Ben-Beya B., 2012. A dynamic sub-grid scale model for large eddy simulation of turbulent flows in a lid-driven cubical cavity. *Comptes Rendus Mecanique* 340, 721-730.
- Blocken, B., 2014. 50 years of computational wind engineering: Past, present and future. *Journal of Wind Engineering and Industrial Aerodynamics* 129, 69-102.

- Blocken, B., Gualtieri, C., 2012. Ten iterative steps for model development and evaluation applied to Computational Fluid Dynamics for Environmental Fluid Mechanics. *Environmental Modelling & Software* 33, 1-22.
- Blocken, B., Janssen, W.D., van Hooff, T., 2012. CFD simulation for pedestrian wind comfort and wind safety in urban areas: General decision framework and case study for the Eindhoven University campus. *Environmental Modelling & Software* 30, 15-34.
- Blocken, B., Persoon, J., 2009. Pedestrian wind comfort around a large football stadium in an urban environment: CFD simulation, validation and application of the new Dutch wind nuisance standard. *Journal of Wind Engineering and Industrial Aerodynamics* 97(5-6), 255-270.
- Blocken, B., Stathopoulos, T., Carmeliet, J., 2007. CFD simulation of the atmospheric boundary layer: wall function problems. *Atmospheric Environment* 41, 238-252.
- Blocken, B., Stathopoulos, T., Saathoff, P., Wang, X., 2008. Numerical evaluation of pollutant dispersion in the built environment: comparisons between models and experiments. *Journal of Wind Engineering and Industrial Aerodynamics* 96, 1817-1831.
- Braniš, M., Rezáčova, P., Domasova, M., 2005. The effect of outdoor air and indoor human activity on mass concentrations of PM₁₀, PM_{2.5}, and PM₁ in a classroom. *Environmental Research* 99, 143-149.
- Brundrett, G.W., 1992. *Legionella and Building Services*, Oxford, Butterworth-Heinemann, pp. 129-130.
- BS5925, 1991. Code of practice for ventilation principles and designing for natural ventilation, British Standards Institution, London, UK.
- Burnett, J., Bojic, M., Yik, F., 2005. Wind-induced pressure at external surfaces of a high-rise residential building in Hong Kong. *Building and Environment* 40, 765-777.
- Bu, Z., Kato, S., 2011. Wind-induced ventilation performances and airflow characteristics in an areaway-attached basement with a single-sided opening. *Building and Environment* 46, 911-921.
- Caciolo, M., Cui, S., Stabat, P., Marchio, D., 2013. Development of a new correlation for single-sided natural ventilation adapted to leeward conditions. *Energy and Buildings* 60, 372-382.
- Caciolo, M., Stabat, P., Marchio, D., 2011. Full scale experimental study of single-sided ventilation: analysis of stack and wind effects. *Energy and Buildings* 43, 1765-1773.
- Caciolo, M., Stabat, P., Marchio, D., 2012. Numerical simulation of single-sided ventilation using RANS and LES and comparison with full-scale experiments.

- Building and Environment 50, 2020-2213.
- Casey, M., Wintergerste, T., 2000. Best Practice Guidelines, ERCOFTAC Special Interest Group on Quality and Trust in Industrial CFD, ERCOFTAC, Brussels.
- Castro, I.P., Robins, A.G., 1977. The flow around a surface mounted cube in a uniform and turbulent shear flow. *Journal of Fluid Mechanics* 79(2), 307-335.
- CDCP, Centers for Disease Control and Prevention, 1994. Guidelines for Preventing the transmission of *Mycobacterium tuberculosis* in health-care facilities, *MMWR Recommendations and Reports* 43, 1-132.
- Cebeci, T., Bradshaw, P., 1977. Momentum transfer in boundary layers, Hemisphere Publishing Corporation, New York.
- Celik, I., Cehreli, Z.N., Yavuz, I., 2005. Index of resolution quality for large eddy simulation. *Journal of Fluids Engineering* 127, 949-958.
- Chand, I., Bhargava, P.K., Krishak, B.L.V., 1998. Effect of balconies on ventilation inducing aeromotive force on low-rise buildings. *Building and Environment* 33(6), 385-396.
- Chau, C.K., Hui, W.K., Tse, M.S., 2008. Valuing the health benefits of improving indoor air quality in residences. *Science of the Total Environment* 394, 25-38.
- Chavez, M., Hajra, B., Stathopoulos, T., Bahloul, A., 2011. Near-field pollutant dispersion in the built environment by CFD and wind tunnel simulations. *Journal of Wind Engineering and Industrial Aerodynamics* 99, 330-339.
- Chen, H.C., Patel, V.C., 1988. Near-wall turbulence models for complex flows including separation. *AIAA Journal* 26(6), 641-648.
- Chen, Q., 2009. Ventilation performance prediction for buildings: A method overview and recent applications. *Building and Environment* 44, 848-858.
- Cheng, W.C., Porté-Agel, F., 2013. Evaluation of subgrid-scale models in large-eddy simulation of flow past a two-dimensional block. *International Journal of Heat and Fluid Flow* 44, 301-311.
- Choiniere, Y., Tanaka, H., Munroe, J.A., Suchorski-Tremblay, A., 1992. Prediction of wind induced ventilation for livestock housing. *Journal of Wind Engineering and Industrial Aerodynamics* 41-44, 2563-2574.
- Chu, C.R., Chiang, B.F., 2013. Wind-driven cross ventilation with internal obstacles. *Energy and Buildings* 67, 201-209.
- Cockroft, J.P., Robertson, P., 1976. Ventilation of an enclosure through a single opening. *Building and Environment* 11, 29-35.
- Cole, E.C., Cook, C.E., 1998. Characterization of infectious bio-aerosols in health care facilities: an aid to effective engineering controls and preventive strategies. *American Journal of Infection Control* 26, 453-464.
- Dascalaki, E., Santamouris, M., Argiriou, A., Helmis, C., Asimakopoulos, D.N.,

- Papadopoulos, K., Soilemes, A., 1996. On the combination of air velocity and flow measurements in single sided natural ventilation configurations. *Energy and Buildings* 24, 155-165.
- Dascalaki, E., Santamouris, M., Argiriou, A., Helmis, C., Asimakopoulos, D.N., Papadopoulos, K., Soilemes, A., 1995. Predicting single sided natural ventilation rates in buildings. *Solar Energy* 55(5), 327-341.
- Diapouli, E., Chaloulakou, A., Spyrellis, N., 2007. Indoor and outdoor particulate matter concentrations at schools in the Athens area. *Indoor and Built Environment* 16(1), 55-61.
- Durbin, P.A., Medic, G., Seo, J.-M., Eaton, J.K., Song, S., 2001. Rough wall modification of two-layer $k-\varepsilon$. *Journal of Fluids Engineering* 123, 16-21.
- Duguid, J.P., 1946. The size and duration of air-carriage of respiratory droplets and droplet-nuclei. *Journal of Hygiene* 44, 471-479.
- El-Hougeiri, N., El Fadel, M., 2004. Correlation of indoor-outdoor air quality in urban areas. *Indoor and Built Environment* 13, 421-431.
- EPD-HK, Environmental Protection Department, Hong Kong: Air quality data: <http://epic.epd.gov.hk/ca/uid/airdata/p/1>, Accessed on 10 May 2013.
- EPD-HK, Environmental Protection Department, Hong Kong, Air quality objectives: http://www.epd.gov.hk/epd/english/environmentinhk/air/air_quality_objectives/air_quality_objectives.html, Accessed on 2 September 2014.
- Ernest, D.R., Bauman, F.S., Arens, E.A., 1991. The prediction of indoor air motion for occupant cooling in naturally ventilated buildings. *ASHRAE Transactions* 97, 539-552.
- Etheridge, D.W., 2002. Nondimensional methods for natural ventilation design. *Building and Environment* 37, 1057-1072.
- Etheridge, D.W., 2011. Natural ventilation of buildings: theory, measurement and design, Wiley, UK, Chapter 10.
- Etheridge, D.W., Sandberg, M., 1996. Building ventilation: theory and measurement. Wiley, Chichester, UK.
- Evola, G., Popov, V., 2006. Computational analysis of wind driven natural ventilation in buildings. *Energy and Buildings* 38(5), 491-501.
- Finnegan, M.J., Pickering, C.A., Burge, P.S., 1984. The sick building syndrome: Prevalence studies. *British Medical Journal* 89, 1573-1575.
- Fitzgerald, D., Haas, D.W., 2005. Mycobacterium tuberculosis, In: Mandell, G.L., Bennett, J.E., Dolin, R., eds., Principles and practice of infectious diseases, 6th ed., Philadelphia: Churchill Livingstone, pp. 2852-2886.
- Fluent, 2010. ANSYS FLUENT 13.0 Theory Guide, Turbulence, Canonsburg, PA, ANSYS Inc.

- Franke, J., Hellsten, A., Schlünzen, H., Carissimo, B., 2007. Best practice guideline for the CFD simulation of flows in the urban environment. COST Action 732, COST Office, Brussels, ISBN 3-00-018312-4.
- Franz, D.R., Jahrling, P.D., Friedlander, A.M., McClain, D.J., Hoover, D.L., Bryne, W.R., Pavlin, J.A., Christopher, G.W., Eitzen, E.M.Jr., 1997. Clinical recognition and management of patients exposed to biological warfare agents. *The Journal of the American Medical Association* 278(5), 399-411.
- Gao, C.F., 2011. The study of natural ventilation in residential buildings, Ph.D. Thesis, The Hong Kong Polytechnic University, Chapter 6.
- Gao, N.P., Niu, J.L., Perino, M., Heiselberg, P., 2008. The airborne transmission of infection between flats in high-rise residential buildings: Tracer gas simulation. *Building and Environment* 43, 1805-1817.
- Gao, N.P., Niu, J.L., Perino, M., Heiselberg, P., 2009. The airborne transmission of infection between flats in high-rise residential buildings: Particle simulation. *Building and Environment* 44, 402-410.
- Gao, Y., Chow, W.K., 2005. Numerical studies on air flow around a cube. *Journal of Wind Engineering and Industrial Aerodynamics* 93, 115-135.
- Georgakis, C.H., Santamouris, M., 2006. Experimental investigation of air flow and temperature distribution in deep urban canyons for natural ventilation purposes. *Energy and Buildings* 38, 367-376.
- Germano, M., Piomelli, U., Moin, P., Cabot, W.H., 1991. A dynamic subgrid-scale eddy viscosity model. *Physics of Fluids A* 3, 1760-1765.
- Geurts, B.J., Fröhlich, J., 2002. A framework for predicting accuracy limitations in large-eddy simulations. *Physics of Fluids* 14, L41-44.
- Ghaisas, N.S., Shetty, D.A., Frankel, S.H., 2013. Large eddy simulation of thermal driven cavity: Evaluation of sub-grid scale models and flow physics. *International Journal of Heat and Mass Transfer* 56, 606-624.
- Gorlé, C., van Beeck, J., Rambaud, P., 2010. Dispersion in the wake of a rectangular building: validation of two Reynolds-averaged Navier-Stokes modeling approaches. *Boundary-Layer Meteorology* 137, 115-133.
- Gorlé, C., van Beeck, J., Rambaud, P., Van Tendeloo, G., 2009. CFD modeling of small particle dispersion: the influence of the turbulence kinetic energy in the atmospheric boundary layer. *Atmospheric Environment* 43, 673-681.
- Gousseau, P., Blocken, B., Stathopoulos, T., van Heijst, G.J.F., 2011. CFD simulation of near-field pollutant dispersion on a high-resolution grid: A case study by LES and RANS for a building group in downtown Montreal. *Atmospheric Environment* 45, 428-438.
- Gousseau, P., Blocken, B., van Heijst, G.J.F., 2012. Large-eddy simulation of pollutant dispersion around a cubical building: Analysis of the turbulent mass

- transport mechanism by unsteady concentration and velocity statistics. *Environmental Pollution* 167, 47-57.
- Gousseau, P., Blocken, B., van Heijst, G.J.F., 2013. Quality assessment of large-eddy simulation of wind flow around a high-rise building: Validation and solution verification. *Computers and Fluids* 79, 120-133.
- Habil, M., Taneja, A., 2011. Children's exposure to indoor particulate matter in naturally ventilated schools in India. *Indoor and Built Environment* 20(4), 430-448.
- Haghighat, F., Brohus, H., Rao, J., 2000. Modelling air infiltration due to wind fluctuations – a review. *Building and Environment* 35, 377-385.
- Haghighat, F., Rao, J., Fazio, P., 1991. The influence of turbulent wind on air change rates – a modelling approach. *Building and Environment* 26(2), 95-109.
- Hang, J., Li, Y., 2011. Age of air and air exchange efficiency in high-rise urban areas and its link to pollutant dilution. *Atmospheric Environment* 45, 5572-5585.
- Hargreaves, D., Wright, N., 2007. On the use of the $k-\varepsilon$ model in commercial CFD software to model the neutral atmospheric boundary layer. *Journal of Wind Engineering and Industrial Aerodynamics* 95, 355-369.
- Hasama, T., Kato, S., Ooka, R., 2008. Analysis of wind-induced inflow and outflow through a single opening using LES & DES. *Journal of Wind Engineering and Industrial Aerodynamics* 96, 1678-1691.
- Hinze, J.O., 1975. *Turbulence*. McGraw-Hill Publishing Co., New York.
- Hodgson, M.J., Miller, S.L., Li, Y., McCoy, W.F., Parsons, S.A., Schoen, L.J., Sekhar, C., 2012. *Airborne Infectious Diseases*, ASHRAE Position Document, Atlanta, Georgia.
- Homod, R., Sahari, K.S.M., 2013. Energy savings by smart utilization of mechanical and natural ventilation for hybrid residential building model in passive climate. *Energy and Buildings* 60, 310-329.
- Hölscher, N., Niemann, H.J., 1998. Towards quality assurance for wind tunnel tests: A comparative testing program of the Windtechnologische Gesellschaft. *Journal of Wind Engineering and Industrial Aerodynamics* 74-78, 599-608.
- Horemans, B., Van Grieken, R., 2010. Speciation and diurnal variation of thoracic, fine thoracic and sub-micrometer airborne particulate matter at naturally ventilated office environments. *Atmospheric Environment* 44, 1497-1505.
- Hu, C.H., Ohba, M., Yoshie, R., 2008. CFD modeling of unsteady cross ventilation flows using LES. *Journal of Wind Engineering and Industrial Aerodynamics* 96, 1692-1706.
- Hussein, A.S., El-Shishiny, H., 2009. Influences of wind flow over heritage sites: A case study of the wind environment over the Giza Plateau in Egypt. *Environmental Modelling & Software* 24, 389-410.

- HWFB-HK, Health, Welfare & Food Bureau, Government of the Hong Kong Special Administrative Region, 2003. SARS Bulletin (28 May 2003). Available at: <http://www.info.gov.hk/info/sars/bulletin/bulletin0528e.pdf>, accessed on September 20, 2012.
- IAQMG, Indoor Air Quality Management Group, 2003. A guide on indoor air quality certification scheme for offices and public places. Environmental Prediction Department, Hong Kong.
- Iizuka, S., Kondo, H., 2004. Performance of various sub-grid scale models in large-eddy simulations of turbulent flow over complex terrain. *Atmospheric Environment* 38, 7083-7091.
- Ijaz, M.K., Brunner, A.H., Sattar, S.A., Nair, R.C., Johnson-Lussenburg, C.M., 1985. Survival characteristics of airborne human coronavirus 229E. *Journal of General Virology* 66, 2743-2748.
- ISO 12569, 2012. Thermal performance of buildings and materials – Determination of specific airflow rate in buildings –Tracer gas dilution method, 2nd edition, Switzerland.
- Jiang, Y., Alexander, D., Jenkins, H., Arthur, R., Chen, Q., 2003. Natural ventilation in buildings: Measurement in a wind tunnel and numerical simulation with large-eddy simulation. *Journal of Wind Engineering and Industrial Aerodynamics* 91, 331-353.
- Jiang, Y., Chen, Q., 2001. Study of natural ventilation in buildings by large eddy simulation. *Journal of Wind Engineering and Industrial Aerodynamics* 89, 1155-1178.
- Jiang, Y., Chen, Q., 2002. Effect of fluctuating wind direction on cross natural ventilation in buildings from large eddy simulation. *Building and Environment* 37, 379-386.
- Jiang, Y., Chen, Q., 2003. Buoyancy-driven single-sided natural ventilation in buildings with large openings. *International Journal of Heat and Mass Transfer* 46, 973-988.
- Joint Practice Note No. 1, 2001. Green and Innovative Buildings, Building Department, Lands Department and Planning Department, Hong Kong.
- Karava, P., Stathopoulos, T., Athienitis, A.K., 2006. Impact of internal pressure coefficients on wind-driven ventilation analysis. *International Journal of Ventilation* 5, 53-66.
- Karava, P., Stathopoulos, T., Athienitis, A.K., 2011. Airflow assessment in cross-ventilated buildings with operable façade elements. *Building and Environment* 46, 266-279.
- Katayama, T., Tsutsumi, J., Ishii, A., 1992. Full-scale measurements and wind tunnel tests on cross-ventilation. *Journal of Wind Engineering and Industrial*

- Aerodynamics 41-44, 2553-2562.
- Kato, S., Murakami, S., Mochida, A., Akabayashi, S., Tominaga, Y., 1992. Velocity-pressure field of cross ventilation with open windows analysed by wind tunnel and numerical simulation. *Journal of Wind Engineering and Industrial Aerodynamics* 44, 2575-2586.
- Kim, S.E., 2004. Large eddy simulation using unstructured meshes and dynamic subgrid-scale turbulence models. Technical Report AIAA-2004-2548. 34th Fluid Dynamics Conference and Exhibit, American Institute of Aeronautics and Astronautics.
- Kim, W.W., Menon, S., 1997. Application of the localized dynamic subgrid-scale model to turbulent wall-bounded flows, Technical Report AIAA-97-0210, 35th Aerospace Sciences Meeting, Reno, NV, American Institute of Aeronautics and Astronautics.
- Klein, M., 2005. An attempt to assess the quality of large eddy simulations in the context of implicit filtering. *Flow Turbulence and Combustion* 75, 131-147.
- Klepeis, N.E., Nelson, W.C., Ott, W.R., Robinson, J.P., Tsang, A.M., Switzer, P., Behar, J.V., Hem, S.C., Engelmann, W.H., 2001. The national human activity pattern survey (NHAPS): A resource for assessing exposure to environmental pollutants. *Journal of Exposure Analysis and Environmental Epidemiology* 11(3), 231-252.
- Kobayashi, T., Sagara, K., Yamanaka, T., Kotani, H., Takeda, S., Sandberg, M., 2009. Stream tube based analysis of problems in prediction of cross-ventilation rate. *International Journal of Ventilation* 7, 321-334.
- Kobayashi, T., Sandberg, M., Kotani, H., Claesson, L., 2010. Experimental investigation and CFD analysis of cross-ventilated flow through single room detached house model. *Building and Environment* 45, 2723-2734.
- Kraichnan, R., 1970. Diffusion by a random velocity field. *Physics of Fluids* 11, 21-31.
- Krogstad, P.-Å., Antonia, R.A., 1999. Surface roughness effects in turbulent boundary layers. *Experiments in Fluids* 27, 450-460.
- Lai, M.Y., Cheng, P.K., Lim, W.W., 2005. Survival of severe acute respiratory syndrome coronavirus. *Clinical Infectious Diseases* 41, e67-e71.
- Lakehal, D., Rodi, W., 1997. Calculation of the flow past a surface-mounted cube with two-layer turbulence models. *Journal of Wind Engineering and Industrial Aerodynamics* 67-68, 65-78.
- Larsen, T.S., Heiselberg, P., 2008. Single-sided natural ventilation driven by wind pressure and temperature difference. *Energy and Buildings* 40, 1031-1040.
- Larsen T.S., Heiselberg, P., Sawachi, T., 2003. Analysis and design of single-sided natural ventilation, Proceedings of the 4th International Symposium on HVAC,

- Beijing, China, pp. 159-163.
- Lateb, M., Masson, C., Stathopoulos, T., Bédard, C., 2011. Effect of stack height and exhaust velocity on pollutant dispersion in the wake of a building. *Atmospheric Environment* 45, 5150-5163.
- Launder, B.E., Spalding, D.B., 1972. *Lectures in Mathematical Models of Turbulence*, Academic Press, London, UK.
- Launder, B.E., Spalding, D.B., 1974. The numerical computation of turbulent flows. *Computer Methods in Applied Mechanics and Engineering* 3, 269-289.
- Laussmann, D., Helm, D., 2011. Air change measurements using tracer gases: Methods and results, Significance of air change for indoor air quality. InTechOpen, Rijeka, Croatia.
- Leitl, B., Schatzmann, M., 1998. CEDVAL at Hamburg University. <http://www.mi.uni-hamburg.de/Data-Sets.432.0.html>. Accessed in January 2013.
- Lilly, D.K., 1992. A proposed modification of the Germano subgrid-scale closure method. *Physics of Fluids A* 4, 633-635.
- Lim, H.C., Castro, I.P., Hoxey, R.P., 2007. Bluff bodies in deep turbulent boundary layers: Reynolds-number issues. *Journal of Fluid Mechanics* 571, 97-118.
- Lim, H.C., Thomas, T.G., Castro, I.P., 2009. Flow around a cube in a turbulent boundary layer: LES and experiment. *Journal of Wind Engineering and Industrial Aerodynamics* 97, 96-109.
- Linden, P.F., 1999. The fluid mechanics of natural ventilation. *Annual Review of Fluid Mechanics* 31, 201-238.
- Liu, H., 1991. *Wind engineering: a handbook for structural engineers*. Prentice Hall, USA.
- Liu, X.P., Niu, J.L., Kwok, K.C.S., Wang, J.H., Li, B.Z., 2010. Investigation of indoor air pollutant dispersion and cross-contamination around a typical high-rise residential building: Wind tunnel tests. *Building and Environment* 45, 1769-1778.
- Liu, X.P., Niu, J.L., Kwok, K.C.S., 2011a. Analysis of concentration fluctuations in gas dispersion around high-rise building for different incident wind directions. *Journal of Hazardous Materials* 192, 1623-1632.
- Liu, X.P., Niu, J.L., Kwok, K.C.S., Wang, J.H. and Li, B.Z. (2011b) Local characteristics of cross-unit contamination around high-rise building due to wind effect: Mean concentration and infection risk assessment, *Journal of Hazardous Materials* 192, 160-167.
- Li, W.W., Meroney, R.N., 1983. Gas dispersion near a cubical model building, Part 1, mean concentration measurements, *Journal of Wind Engineering and Industrial Aerodynamics* 12, 15-33.
- Li, X.X., Liu, C.H., Leung, D.Y.C, Lam, K.M., 2006. Recent progress in CFD modeling of wind field and pollutant transport in street canyons. *Atmospheric*

- Environment 40, 5640-5658.
- Li, Z.R., Ai, Z.T., Wang, W.J., Xu, Z.R., Gao, X.Z., Wang, H.S., 2014. Evaluation of airflow pattern in wind-driven naturally ventilated atrium buildings: measurement and simulation. *Building Services Engineering Research and Technology* 35(2), 139-154.
- Lo, L.J., Banks, D., Novoselac, A., 2013. Combined wind tunnel and CFD analysis for indoor airflow prediction of wind-driven cross-ventilation. *Building and Environment* 60, 12-23.
- Loosli, C., Lemon, H., Robertson, O., Appel, E., 1943. Experimental airborne influenza infection: 1. Influence of humidity on survival of virus in air. *Proceedings of the Society for Experimental Biology and Medicine* 53, 205-206.
- Lubcke, H., Schmidt, S., Rung, T., Thiele, F., 2001. Comparison of LES and RANS in bluff-body flows, *Journal of Wind Engineering and Industrial Aerodynamics* 89, 1471-1485.
- Macdonald, R.W., Griffiths, R.F., Cheah, S.C., 1997. Field experiments of dispersion through regular arrays of cubic structures. *Atmospheric Environment* 31(6), 783-795.
- Martinuzzi, R., Tropea, C., 1993. The flow around surface-mounted, prismatic obstacles placed in a fully developed channel flow. *Journal of Fluid Engineering* 115, 85-92.
- Mathey, F., Cokljat, D., Bertoglio, J.P., Sergent, E., 2006. Assessment of the vortex method for large eddy simulation inlet conditions. *Progress in Computational Fluid Dynamics* 6, 58-67.
- Mavroidis, I., Andronopoulos, S., Bartzis, J.G., 2012. Computational simulation of the residence of air pollutants in the wake of a 3-dimensional cubical building: The effect of atmospheric stability. *Atmospheric Environment* 63, 189-202.
- Melaragno, M., 1982. *Wind in architectural and environmental design*. Van Nostrand Reinhold, New York.
- Mendell, M.J., Fisk, W.J., Kreiss, K., Levin, H., Alexander, D., Cain, W.S., Girman, J.R., Hines, C.J., Jensen, P.A., Milton, D.K., Rexroat, L.P., Wallingford, K.M., 2002. Improving the health of workers in indoor environments: priority research needs for a national occupational research agenda. *American Journal of Public Health* 92, 1430-1440.
- Meroney, R.N., 2004. Wind tunnel and numerical simulation of pollution dispersion: A hybrid approach. Invited Lecture, Croucher Advanced Study Institute, Hong Kong University of Science and Technology, 6-10 December.
- Meyers, J., Geurts, B.J., Baelmans, M., 2003. Database analysis of errors in large-eddy simulation. *Physics of Fluids* 15, 2740-2755.
- Mfula, A.M., Kukadia, V., Griffiths, R.F., Hall, D.J., 2005. Wind tunnel modeling of

- urban building exposure to outdoor pollution. *Atmospheric Environment* 39, 2737-2745.
- Mitman, M., 1945. Aerial infection. *British Medical Journal* 1, 71-74.
- Miyake, Y., Tsujimoto, K., Agata, Y., 1999. A DNS of a turbulent flow in a rough-wall channel using roughness elements model. *Japanese Society of Mechanical Engineers International Journal* 43(2), 233-242.
- Miyake, Y., Tsujimoto, K., Nakaji, M., 2001. Direct numerical simulation of rough-wall heat transfer in a turbulent channel flow. *International Journal of Heat and Fluid Flow* 22, 237-244.
- Mochida, A., Tominaga, Y., Yoshie, R., 2006. AIJ guideline for practical applications of CFD to wind environment around buildings. *Proceedings of the Fourth International Symposium on Computational Wind Engineering*, Japan Association for Wind Engineering, Japan, pp. 533-536.
- Morawska, L., 2006. Droplet fate in indoor environments, or can we prevent the spread of infection. *Indoor Air* 16, 335-347.
- Morawska, L., Afshari, A., Bae, G.N., Buonanno, G., Chao, C.Y.H., Hänninen, O., Hofmann, W., Isaxon, C., Jayaratne, E.R., Pasanen, P., Salthammer, T., Waring, M., Wierzbicka, A., 2013. Indoor aerosols: from personal exposure to risk assessment. *Indoor Air* 23, 462-487.
- Murakami, S., 1993. Comparison of various turbulence models applied to a bluff body. *Journal of Wind Engineering and Industrial Aerodynamics* 46-47, 21-36.
- Murakami, S., 1998. Overview of turbulence models applied in CWE-1997. *Journal of Wind Engineering and Industrial Aerodynamics* 74-76, 1-24.
- Murakami, S., Kato, S., Akabayashi, S., Mizutani, K., Kim, Y.D., 1991. Wind tunnel test on velocity-pressure field of cross-ventilation with open windows. *ASHRAE Transaction* 97(1), 525-538.
- Nicas, M., Nazaroff, W.W., Hubbard, A., 2005. Toward understanding the risk of secondary airborne infection: Emission of respirable pathogens. *Journal of Occupational and Environmental Hygiene* 2, 143-154.
- Nicoud, F., Ducros, F., 1999. Subgrid-scale stress modeling based on the square of the velocity gradient tensor. *Flow turbulence and combustion* 62, 183-200.
- Nikuradse, J., 1933. Laws of flow in rough pipes. *VDI Forschungsheft* 361.
- Niu, J.L., Tung, T.C.W., 2008. On-site quantification of re-entry ratio of ventilation exhausts in multi-family residential buildings and implications. *Indoor Air* 18, 12-26.
- Orszag, S.A., Yakhot, V., Flannery, W.S., Boysan, F., Choudhury, D., Maruzewski, J., Patel, B., 1993. Renormalization group modeling and turbulence simulations. *International Conference on Near-Wall Turbulent Flows*. Tempe, Arizona.
- Papakonstantinou, K.A., Kiranoudis, C.T., Markatos, N.C., 2000. Numerical

- simulation of air flow field in single-sided ventilated buildings. *Energy and Buildings* 33(1), 41-48.
- Parente, A., Gorlé, C., van Beeck, J., Benocci, C., 2011. A comprehensive modeling approach for the neutral atmospheric boundary layer: consistent inflow conditions, wall function and turbulence model. *Boundary-Layer Meteorology* 140, 411-428.
- Phaff, H., De Gids, W., 1982. Ventilation rates and energy consumption due to open windows: A brief overview of research in the Netherlands. *Air Infiltration Review* 4(1), 4-5.
- Poupard, O., Blondeau, P., Iordache, V., Allard, F., 2005. Statistical analysis of parameters influencing the relationship between outdoor and indoor air quality in schools. *Atmospheric Environment* 39, 2071-2080.
- Ramachandran, G., Adgate, J.L., Hill, N., Sexton, K., Pratt, G.C., Bock, D., 2000. Comparison of short-term variations (15-min averages) in outdoor and indoor PM_{2.5} concentrations. *Journal of the Air & Waste Management Association* 50, 1157-1166.
- Ramponi, R., Blocken, B., 2012. CFD simulation of cross-ventilation for a generic isolated building: Impact of computational parameters. *Building and Environment* 53, 34-48.
- Raupach, M.R., Antonia, R.A., Rajagopalan, S., 1991. Rough-wall turbulent boundary layers. *Applied Mechanics Reviews* 44, 1-25.
- Richardson, L.F., 1910. The approximate arithmetical solution by finite differences of physical problems involving differential equations, with an application to the stresses in a masonry dam. *Philosophical Transactions of the Royal Society of London* 210, 307-357.
- Richards, P.J., Hoxey, R., 1993. Appropriate boundary conditions for computational wind engineering models using the $k-\varepsilon$ turbulence model. *Journal of Wind Engineering and Industrial Aerodynamics* 46-47, 145-153.
- Richards, P.J., Hoxey, R.P., Short, L.J., 2001. Wind pressures on a 6 m cube. *Journal of Wind Engineering and Industrial Aerodynamics* 89, 1553-1564.
- Richards, P.J., Hoxey, R.P., 2012. Pressures on a cubic building-Part 1: Full-scale results. *Journal of Wind Engineering and Industrial Aerodynamics* 102, 72-86.
- Riddle, A., Carruthers, D., Sharpe, A., McHugh, C., Stocker, J. 2004. Comparisons between fluent and adms for atmospheric dispersion modeling. *Atmospheric Environment* 38, 1029-1038.
- Riley, E.C., Murphy, G., Riley, R.L., 1978. Airborne spread of measles in a suburban elementary school. *American Journal Epidemiology* 107, 421-432.
- Roache, P.J., 1994. Perspective: a method for uniform reporting of grid refinement studies. *Journal of Fluids Engineering* 116, 405-413.
- Robinson, J., Nelson, W.C., 1995. National human activity pattern survey data base,

- US EPA, Research Triangle Park, NC, USA.
- Rodi, W., 1991. Experience with two-layer models combining the $k-\varepsilon$ model with one-equation model near the wall. AIAA-91-0216, 29th Aerospace Science Meeting, January 7-10, Reno, Nevada.
- Rodi, W., 1997. Comparison of LES and RANS calculations of the flow around bluff bodies. *Journal of Wind Engineering and Industrial Aerodynamics* 69-71, 55-75.
- Saathoff, P.J., Stathopoulos, T., Dobrescu, M., 1995. Effects of model scale in estimating pollutant dispersion near buildings. *Journal of Wind Engineering and Industrial Aerodynamics* 54-55, 549-559.
- Sada, K., Sato, A., 2002. Numerical calculation of flow and stake-gas concentration fluctuation around a cubical building. *Atmospheric Environment* 36(35), 5527-5534.
- Salim, S.M., Buccolieri, R., Chan, A., Sabatino, S.D., 2011. Numerical simulation of atmospheric pollutant dispersion in an urban street canyon: Comparison between RANS and LES. *Journal of Wind Engineering and Industrial Aerodynamics* 99, 103-113.
- Sandberg, M., 2004. An alternative view on theory of cross-ventilation. *International Journal of Ventilation* 2(4), 400-418.
- Santos, J.M., Jr., Reis, N.C., Goulart, E.V., Mavroidis, I., 2009. Numerical simulation of flow and dispersion around an isolated cubical building: the effect of the atmospheric stratification. *Atmospheric Environment* 43, 5484-5492.
- Santos, J.M., Mavroidis, I., Reis, Jr N.C., Pagel, E.C., 2011. Experimental investigation of outdoor and indoor mean concentrations and concentration fluctuations of pollutants. *Atmospheric Environment* 45, 6534-6545.
- Schulze, T., Eicker, U., 2013. Controlled natural ventilation for energy efficient buildings. *Energy and Buildings* 56, 221-232.
- Sherman, M.H., 1990. Tracer-gas techniques for measuring ventilation in a single zone. *Building and Environment* 25(4), 365-374.
- Sherman, M.H., Modera, M., 1986. Comparison of measured and predicted infiltration using the LBL infiltration model, in: *Proceedings Measured Air Leakage of Buildings*, Philadelphia, pp. 325-347.
- Smagorinsky, J., 1963. General circulation experiments with the primitive equations. 1. The basic experiment. *Monthly Weather Review* 91, 99-164.
- Smalley, R.J., Leonardi, S., Antonia, R.A., Djenidi, L., Orlandi, P., 2002. Reynolds stress anisotropy of turbulent rough wall layers. *Experiments in Fluids* 33, 31-37.
- Smirnov, R., Shi, S., Celik, I., 2001. Random flow generation technique for large eddy simulations and particle-dynamics modeling. *Journal of Fluids Engineering* 123, 359-371.
- Snyder, W.H., 1981. Guideline for fluid modeling of atmospheric diffusion,

- meteorology and assessment. Research Triangle Park, NC, Division Environmental Sciences Research Laboratory, U.S. Environmental Protection Agency.
- Sofian, N.Z.M., Ismail, M., 2012. Indoor and outdoor relationships of respirable suspended particulate matter at primary schools in Kural Terengganu, Malaysia. *Indoor and Built Environment* 21(3), 423-431.
- Speziale, C.G., Abid, R., Anderson, E.C., 1992. Critical evaluation of two-equation models for near-wall turbulence. *AIAA Journal* 30(2), 324-331.
- Stathopoulos, T., 1997. Computational wind engineering: past achievements and future challenges. *Journal of Wind Engineering and Industrial Aerodynamics* 67-68, 509-532.
- Steffens, J.T., Heist, D.K., Perry, S.G., Zhang, K.M., 2013. Modeling the effects of a solid barrier on pollutant dispersion under various atmospheric stability conditions. *Atmospheric Environment* 69, 76-85.
- Straw, M.P., 2000. Computation and measurement of wind induced ventilation. Ph.D. Thesis, University of Nottingham.
- Swami, M.V., Chandra, S., 1988. Correlations for pressure distribution on buildings and calculation of natural-ventilation airflow. *ASHRAE Transactions* 94, 243-266.
- Tabor, G.R., Baba-Ahmadi, M.H., 2010. Inlet conditions for large eddy simulation: a review. *Computers and Fluids* 39, 553-567.
- Tamura, T., Nozawa, K., Kondo, K., 2008. AIJ guide for numerical prediction of wind loads on buildings. *Journal of Wind Engineering and Industrial Aerodynamics* 96 (10-11), 1974-1984.
- Tang, J.W., Li, Y., Eames, I., Chan, P.K.S., Ridgway, G.L., 2006. Factors involved in the aerosol transmission of infection and control of ventilation in healthcare premises. *Journal of Hospital Infection* 64, 100-114.
- Tellier, R., 2006. Review of aerosol transmission of influenza A virus, *Emerging Infectious Diseases* 12, 1657-1662.
- Tominaga, Y., Mochida, A., Murakami, S., Sawaki, S., 2008a. Comparison of various revised $k-\varepsilon$ models and LES applied to flow around a high-rise building model with 1:1:2 shape placed within the surface boundary layer. *Journal of Wind Engineering and Industrial Aerodynamics* 96, 389-411.
- Tominaga, Y., Mochida, A., Yoshie, R., Kataoka, H., Nozu, T., Yoshikawa, M., Shirawasa, T., 2008b. AIJ guidelines for practical applications of CFD to pedestrian wind environment around buildings. *Journal of Wind Engineering and Industrial Aerodynamics* 96(10-11), 1749-1761.
- Tominaga, Y., Murakami, S., Mochida, A., 1997. CFD prediction of gaseous diffusion around a cubic model using a dynamic mixed SGS model based on composite grid technique. *Journal of Wind Engineering and Industrial*

- Aerodynamics 67-68, 827-841.
- Tominaga, Y., Stathopoulos, T., 2007. Turbulent Schmidt numbers for CFD analysis with various types of flow field. *Atmospheric Environment* 41, 8091-8099.
- Tominaga, Y., Stathopoulos, T., 2009. Numerical simulation of dispersion around an isolated cubic building: comparison of various types of $k-\varepsilon$ models. *Atmospheric Environment* 43, 3200-3210.
- Tominaga, Y., Stathopoulos, T., 2010. Numerical simulation of dispersion around an isolated cubic building: model evaluation of RANS and LES. *Building and Environment* 45, 2231-2239.
- Tominaga, Y., Stathopoulos, T., 2011. CFD modeling of pollution dispersion in a street canyon: Comparison between LES and RANS. *Journal of Wind Engineering and Industrial Aerodynamics* 99, 340-348.
- Tominaga, Y., Stathopoulos, T., 2013. CFD simulation of near-field pollutant dispersion in the urban environment: A review of current modeling techniques. *Atmospheric Environment* 79, 716-730.
- Tsuchiya, M., Murakami, S., Mochida, A., Kondo, K., Ishida, Y., 1997. Development of a new $k-\varepsilon$ model for flow and pressure fields around bluff body. *Journal of Wind Engineering and Industrial Aerodynamics* 67-68, 169-182.
- Vandaele, L., Wouters, P., 1994. The PASSYS Services, Summary Report of the PASSYS Projects. Belgian Building Research Institute, EC DG XII, Brussels.
- van Hooff, T., Blocken, B., 2013. CFD evaluation of natural ventilation of indoor environments by the concentration decay method: CO₂ gas dispersion from a semi-enclosed stadium. *Building and Environment* 61, 1-17.
- van Hooff, T., Blocken, B., 2010. Coupled urban wind flow and indoor natural ventilation modelling on a high-resolution grid: A case study for the Amsterdam ArenA stadium. *Environmental Modelling & Software* 25, 51-65.
- Wang, H., Chen, Q., 2012. A new empirical model for predicting single-sided, wind-driven natural ventilation in buildings. *Energy and Buildings* 54, 386-394.
- Wang, J.H., Niu, J.L., Liu, X.P., Yu, C.W.F., Assessment of pollutant dispersion in the re-entrance space of a high-rise residential building, using wind tunnel simulations. *Indoor and Built Environment* 19(6), 638-647.
- Warren, P., 1977. Ventilation through openings on one wall only. *Proceedings of International Centre for Heat and Mass Transfer Seminar "Energy Conservation in Heating, Cooling, and Ventilating Buildings"*, Washington, pp. 189-209.
- Warren, P., Parkins, L.M., 1985. Single-sided ventilation through open windows, *Proceedings of Conference on Thermal Performance of the Exterior Envelopes of Buildings*, ASHRAE SP 49, Florida, pp. 209-228.
- Wells, W.F., 1934. On air-borne infection, StudyII, Droplets and droplet nuclei. *American Journal of Hygiene* 20, 611-618.

- White, F.M., 1991. Viscous fluid flow, second edition. McGraw-Hill, New York.
- WHO, World Health Organization, 2005. Air quality guidelines, Global update, Geneva, Switzerland.
- WHO, World Health Organization, 2003. First Data on Stability and Resistance of SARS Coronavirus Compiled by Members of WHO Laboratory Network. Available at: http://www.who.int/csr/sars/survival_2003_05_04/en/, accessed 14 August, 2014.
- Wolfshtein, M., 1969. The velocity and temperature distribution of one-dimensional flow with turbulence augmentation and pressure gradient. *International Journal of Heat and Mass Transfer* 12, 301-318.
- Xie, Z.T., Castro, I.P., 2009. Large-eddy simulation for flow and dispersion in urban streets. *Atmospheric Environment* 43, 2174-2185.
- Xie, Z.T., Voke, P.R., Hayden, P., Robins, A.G., 2004. Large-eddy simulation of turbulent flow over a rough surface. *Boundary-Layer Meteorology* 111, 417-440.
- Yakhot, V., Orsag, S.A., 1986. Renormalization group analysis of turbulence: basic theory. *Journal of Scientific Computing* 1(1), 3-51.
- Yamanaka, T., Kotani, H., Iwamoto, K., Kato, M., 2006. Natural, wind-forced ventilation caused by turbulence in a room with a single opening. *International Journal of Ventilation* 5(1), 179-188.
- Yang, Y., Gu, M., Chen, S., Jin, X., Jin, H., 2009. New inflow boundary conditions for modeling the neutral equilibrium atmospheric boundary layer in computational wind engineering. *Journal of Wind Engineering and Industrial Aerodynamics* 97, 88-95.
- Yoshie, R., Jiang, G., Shirasawa, T., Chung, J., 2011. CFD simulations of gas dispersion around high-rise building in non-isothermal boundary layer. *Journal of Wind Engineering and Industrial Aerodynamics* 99, 279-288.
- Yoshie, R., Mochida, A., Tominaga, Y., Kataoka, H., Harimoto, K., Nozu, T., Shirasawa, T., 2007. Cooperative project for CFD prediction of pedestrian wind environment in the Architectural Institute of Japan. *Journal of Wind Engineering and Industrial Aerodynamics* 95(9, 11), 1551-1578.
- Zhang, W., Mak, C.M., Ai, Z.T., Siu, W.M., 2012. A study of the ventilation and thermal comfort of the environment surrounding a new university building under construction. *Indoor and Built Environment* 21(4), 568-582.